DISSERTATION

THE C3HEB/FEJ MICE AS A NOVEL PRECLINICAL MOUSE MODEL FOR *MYCOBACTERIUM TUBERCULOSIS*: AN ANALYSIS OF THE HOST PATHOGENESIS AND THE *IN VIVO* ENVIRONMENT OF THE NECROTIC GRANULOMA

Submitted by

Emily R. Driver

Department of Microbiology, Immunology, and Pathology

In partial fulfillment of the requirements

For the Degree of Doctor of Philosophy

Colorado State University

Fort Collins, Colorado

Spring 2014

Doctoral Committee:

Advisor: Anne Lenaerts

Randall Basaraba
Dean Crick
Daniel Gustafson

ABSTRACT

THE C3HEB/FEJ MICE AS A NOVEL PRECLINICAL MOUSE MODEL FOR *MYCOBACTERIUM TUBERCULOSIS*: AN ANALYSIS OF THE HOST PATHOGENESIS AND THE *IN VIVO* ENVIRONMENT OF THE NECROTIC GRANULOMA

Mycobacterium tuberculosis (MTB), the causative agent of tuberculosis (TB), infects and kills millions each year. Actively infected patients exhibit a heterogeneity of disease lesions in the lungs, which make it difficult for current treatment regimens to effectively cure. Efforts are underway to develop novel pre-clinical drugs, and this requires a thorough re-evaluation of the current animal models used to test these formulations. A new mouse model using C3HeB/FeJ mice, deficient at the sst-1 locus develops a similar heterogeneity of pulmonary lesions to human disease when aerosol infected with MTB.

The studies presented here have found the C3HeB/FeJ mice develop 3 types of lesions: type I) necrotic granulomas delineated with a collagen rim, type II) necrotic alveolitis, and type III) cellular inflammation. Type I lesions, consist of an accumulation of amphophilic cellular debris admixed with numerous extracellular bacilli. At the periphery of the necrotic core on the inside of the collagen rim is a cuff with foamy macrophages of variable size, which contain very large numbers of intracellular bacilli. Type II lesions, the alveolar septal walls remain mostly intact, while the alveolar spaces are filled with high numbers of dying neutrophils, intact cells, extracellular bacteria and debris, creating a honeycomb-like necrosis, which is only seen at very late stage in immunocompetent mouse models. Type III lesions, are disorganized and have a mix

of lymphocytes, macrophages (epitheloid and foamy), and a small number of neutrophils with low numbers of intracellular bacilli.

The necrotic encapsulated type I granuloma creates an environment that promotes hypoxia, creates a physical barrier, and causes physiological changes to the various bacterial populations. The Kramnik mouse model has higher populations of resistant bacteria when drug treated, such as isoniazid (INH), rifampin (RIF), and pyrazinamide (PZA). These drugs are less effective when administered as monotherapies in C3HeB/FeJ mice. The adaptations the MTB undertake in the core of the type I granuloma while under stress not only make drug treatment less effective, but also make standard acid-fast staining techniques, such as auramine-rhodamine less efficient at detecting bacilli. While, Sybr Gold, a novel acid-fast stain that binds to nucleic acid, is capable of staining bacilli throughout infection and in all lesion types. The discrepancy in staining ability of the two acid-fast stains is indicative of the physical target for auramine-rhodamine no longer being present or available for staining in the bacilli in the core of the necrotic granuloma.

The knowledge on histopathology then leads us further to modify the granuloma in the Kramnik mouse model. Firstly, using collagen disrupters we aimed to improve treatment efficacy. Secondly, by using clinical TB strains the goal was to advance disease to potentiate cavitary disease and gain a greater understanding of strain relevance to treatment. Thirdly, by taking advantage of the structural similarity of the necrotic granuloma and solid cancerous tumors allow for the translation of therapy technologies, such as liposomal nanoparticles to be exploited for treatment of MTB. Preliminary findings suggest that the use nanomedicines in TB therapy may be an effective method of drastically reducing treatment as well as potential issues.

The C3HeB/FeJ mouse strain is a highly relevant disease model that can be used for determining the efficacy of novel pre-clinical drugs and drug regimens, to gain a better understanding of disease pathogenesis, to understand the specific immunological events of disease, and to explore alternatives to standard therapy.

ACKNOWLEDGEMENTS

I would like to extend my heartfelt thanks to my advisor, Anne Lenaerts, who has been a wonderful mentor to me. She has spent much of her scarce time exploring novel ideas with me and answering all of my questions. She supported every one of my potential ideas and I cannot express enough gratitude I have for my experience as a graduate student. I cannot imagine a better advisor and I hope to have continued collaborations in the future.

I would also like to thank the members of my committee – Randy Basaraba, Dean Crick, and Dan Gustafson for their insightful questions, encouragement, and suggestions for experiments. They each taught me how to expand and hone my thinking as an investigator. I appreciate the time they have taken from their busy schedules to help me through graduate school.

My warmest thanks go to all current and past members of the Lenaerts and Orme labs, for their help and support throughout this endeavor. Their assistance with experiments, moral support, and friendship has been very important to me and without which this would not have been possible.

Many thanks go to Gavin Ryan who became a dear mentor and friend during his tenure in the Lenaerts Lab. With his encouragement and willing ear I came to understand microscopy and that I needed to be more willing to ask for help.

I would like to thank Donnie Hoff for his helpfulness throughout my experiments and for his friendship.

A special thanks goes to Alan Schenkel and Marta Lishnevsky who have helped me through discussions, moral support, and expertise.

I would like to thank Mercedes Gonzalez-Juarrero and members of her lab for taking the time to for many discussions on immunology and potential future experiments. Also for use of equipment and training of specific techniques I used throughout my thesis.

Many thanks go to Diane Ordway and the members of her lab, Lizzie Creissen, Kristie Capson, Andres Obregon-Henao and Marcela Henao-Tamayo for their expertise in flow cytometry and their generosity in sharing materials and use of equipment.

Finally, I would like to thank my extended family and friends for their unending support throughout this endeavor. They have taken time from their lives to read what I have produced and discuss my work on multiple occasions. I cannot express how much I appreciate their support.

DEDICATION

I dedicate this thesis to my parents, Richard and Patricia Driver,

and my brother, Peter.

They have done more for me than I can express.

TABLE OF CONTENTS

CHAPTER 1: LITERATURE REVIEW

1.1 – INTRODUCTION

The tubercle bacillus is an old world infectious agent that is still thriving in the new world. Currently, *Mycobacterium tuberculosis* (MTB) has latently infected one-third of the world's population. Of the infected individuals, 5-10% will become diseased and can become infectious during their lifetime generally due to either aging or immunosuppression [1]; and co-infection with Human Immunodeficiency Virus (HIV) increases reactivation of tuberculosis by 10% per year. MTB killed nearly 1.3 million people in 2012, and has become one of the Big Three infectious diseases along with HIV and Malaria. In recent years the combined infection with HIV has accelerated mortality rates [2].

The World Health Organization recognizes the problem MTB poses and recommends for drug-susceptible tuberculosis (TB), as the standard treatment, 2 months of daily isoniazid (INH, H), rifampin (RIF, R), ethambutol (EMB, E), and pyrazinamide (PZA, Z) [intensive phase]; followed by 4 months of daily INH and RIF with or without EMB [continuation phase] [3]. Patients within the DOTS program (Directly Observed Therapy Short Course) are carefully monitored to guarantee that they complete the full course of treatment. There are many obstacles that impede the DOTS program, especially within developing countries where it is needed most. To date, estimates suggest that DOTS only reaches a quarter of those in need in some countries [4].

Progress has been made globally in the treatment of TB but is rather slow. The Stop TB Partnership with the World Health Organization put forth goals to reduce the global disease burden by 50% in 2015 and elimination of TB by 2050. This year marks the fifth year that 16 of

22 high burden countries had a treatment success rate of 85% or higher of those patients treated, in large part due to the DOTS program [2].

The lengthy treatment for tuberculosis can result in patient non-compliance; many patients stop taking their medications as their symptoms improve. A consequence of withdrawing the medication before the treatment course is finished has resulted in the increase of mono- and multi-drug resistant TB (MDR-TB). MDR-TB refers to isolates that are resistant to at least the two first line drugs, RIF and INH. In many parts of the world the incidence of MDR-TB can be as high as 14% of all TB cases. Extensively-drug resistant TB (XDR-TB) is defined as those strains that are resistant to both RIF and INH, along with a quinolone and at least one injectable second line drug such as kanamycin, capreomycin or amikacin. Treatment for MDR and XDR-TB rely on second and third line TB drugs that are less effective than regimens for drug susceptible TB, the drugs have greater side-effects and the duration is twice as long as susceptible TB; and in the case of XDR-TB an effective cure is the best case scenario for only 50% of patients [5]. In 2009, cases of TB resistant to all first and second line drug treatment regimens were documented in Iran [6], these cases were deemed totally-drug resistant TB (TDR-TB). TDR-TB patients can remain sputum smear positive after 18 months to 4 years of intensive treatment [7]. The Centers for Disease Control has called TDR-TB “virtually untreatable” [8]. Recent approval of Bedaquiline (BDQ) for use in MDR and XDR-TB patients is a dramatic improvement for potential treatments for these patients [9, 10].

The tubercle bacillus is spread from an infected individual to others by coughing, more specifically by passing infected respiratory droplets from liquefied cavities through the air to another person. Infectiousness is influenced by several factors: the frequency and force of someone’s cough, the number of viable bacilli being expelled, the consistency of sputum and the

size of aerosolized particles. The moisture in the air and the bacillus' waxy coat protect it from drying out while in transmission [11]. After transmission the bacilli are inhaled deep in the lungs and reach the alveoli. The alveolar macrophages ingest the bacilli but are prevented from destroying them through several protective mechanisms induced by the bacterium; such as the bacteria reducing the ability to acidify the phagosome within the macrophages, arresting the maturation of the phagosome and avoiding fusion of the phagosome with the lysosome [12-14]. The bacilli use the macrophage as a host while they continue replicating. The acquired immune system is activated with the development of cell-mediated immunity (CMI), which suppresses the logarithmic bacilli growth [15, 16]. Although TB patients show a heterogeneity in lung lesion types, the 'classical granuloma' is the hallmark of the tuberculosis disease in TB patients, which is characterized by the formation of a necrotic core that develops within granulomatous lesions (Figure 1.1).

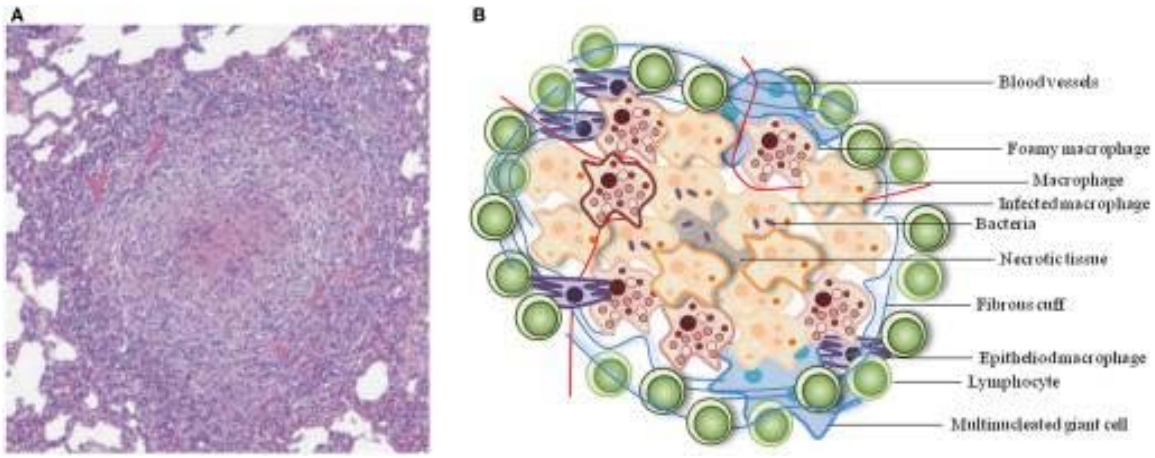

Figure 1.1. Representative architecture of a TB granuloma. A) A representative lesion with central necrosis from minipig lung tissue. Adapted from Gil et al [17]. B) Schematic of the cellular components of a TB granuloma [18].

Necrosis is a process instigated by the lysis of bacteria laden macrophages as well as neutrophils, which ultimately create caseous necrosis in the core of the lung lesion. As the bacilli

invade more macrophages and neutrophils, the lesion continues to expand. Ultimately, the lesion becomes an aggregate of epitheloid cells surrounded by a cuff, which include lymphocytes, plasma cells and fibroblasts. Throughout the newly formed collagen rim, angiogenesis is ongoing. The central region of the human granuloma becomes devoid of blood vessels, which renders it hypoxic, and this hypoxia will further increase the propensity for necrosis [19, 20]. Another characteristic of most human lesions is the progressive collagen deposition around the pulmonary granuloma. At the periphery, Langhans' giant cells can be present. In the core, an acellular, eosinophilic region of caseating necrosis can further progress and mineralize or liquefy later in disease.

1.2 – PERSISTENT BACILLI

1.2.1 Definitions

TTB is difficult to treat and requires extended therapy for effective cure. This long treatment duration is due to 'persister' bacteria, which is a rather elusive and a not well understood bacterial population [21, 22]. We define the persister bacteria as a population which can survive antibiotic treatment but are genetically identical to susceptible TB bacteria. These bacteria are thought to have a distinct physiological state from true susceptible bacteria [23]. Three related terms that describe the phenomenon of these difficult to eradicate bacterial population frequency used are: latency, dormancy and persistence. The terminology for their use in TB is often times disputed and therefore for the purpose of this work, we define these terms more closely. "Latency" is by most, and also here, defined as the clinical state in which a patient is asymptomatic, non-contagious but skin test positive and often by X-ray shows lesions in the lung. Latency can result from infection whereby a vigorous CMI response limits to a great extent

the initial infection. Latency remains to date in large part a mystery. In addition the exact location of the bacteria in a latent infection is unclear. “LTBI” (latent tuberculosis infection) has been a useful term when describing clinical disease for patient management [24]. With more new examinations becoming available that focus on the heterogeneity of lung lesions from active and latent TB in patients [25, 26], proper terminology to describe the spectrum of disease states is imperative. At this time, the incapability to distinguish the several disease states (from sterilizing immunity, subclinical active, fulminant active disease) is seen as a hindrance to the management of patients, and to the development of new drugs and vaccines [24, 25].

“Dormancy”, implies a lack of activity and an almost spore-like state. The MTB bacilli are thought to always have some metabolic activity and therefore the term dormancy seems to be the least appropriate. “Dormant lesions”, which is terminology often times used in the histopathology field, describes a lesion composed mostly of mononuclear phagocytes, dendritic cells, and lymphocytes [27]. The lesion is encapsulated in a fibrotic wall and bacilli within the lesion are low in numbers. These bacilli are in a ‘state of non- to low-replicating persistence’ [27]. Dormancy is also being used as a term associated with an *in vitro* model developed by Wayne that evaluates MTB under depleting oxygen [28, 29].

“Persistence” is the term being used to describe the ability of the bacillus to withstand various environmental pressures and still remain viable. The environmental factors can be *in vivo* stimuli that are encountered within a granuloma, such as low oxygen tension, nutrient starvation, RNI and NO depletion. In addition, many host immune response features can lead to persistence such as certain cytokines and chemokines [30]. On the other hand, persisters are also referred to as the subpopulation of bacteria that can survive antibiotic treatment [23]. These bacteria are genetically drug susceptible but are more drug tolerant. Initially, it was thought that these drug

tolerant bacteria were either non-replicating or slowly replicating [22, 31, 32]. However, more recently, McKinney et al, in an elegant study described drug tolerance for INH independent of the replication [33]. Over time the concept of persisters has evolved from a uniform population to far more complex phenotypes some of which are drug induced, others are stochastic changes through the pulsating activation of catalase-peroxidase (KatG) or can show epigenetic changes [21, 34-36]. All of these persistence factors ensuring the survival of the bacteria population under various environmental pressures.

1.2.2. Host immune response

The host immune response to tuberculosis is complex and not completely elucidated. Certain key aspects of immune control have been characterized which have assisted in the development of new therapies, vaccines, and diagnostic tests. The adaptive immune response plays a critical role in pulmonary host defense against an MTB infection [37]. CD4+ T cells are a major T cell subset, which plays a central role in host immunity to infection. CD4+ T cells are differentiated into two populations, T helper 1 (Th1) and T helper 2 (Th2) [38]. Th1 inflammatory cytokines include interferon-gamma (IFN-γ), interleukin-12 (IL-12) and tumor necrosis factor- alpha (TNF-α), and Th2 suppressive cytokines include IL-4, IL-5, and IL-13. Th1 CD4+ T cells mediate activation of mononuclear phagocytes, such as macrophages [37]. CD8+ T cells (cytotoxic T cells) are also strong producers of IFN-γ, IL-12, and TNF-α in MTB infected individuals and, similar to CD4, CD8+ T cells are critical for macrophage activation [39]. Mice deficient in CD4+ T cells or IFN-γ knockout (GKO) mice, suffer from exacerbated disease; these animals present with lesions of active neutrophils instead of granulomas consisting of macrophages and lymphocytes [40-43]. Therefore, the immunocompromised SCID or mouse

models deficient in interferon gamma (GKO) can in some ways be seen as a reasonable comparison to an HIV patient deficient in CD4 T cells. The lack of CD4+ cells in HIV infected patients is considered to be a major cause of the resurgence of TB in countries with a high HIV burden, resulting in 20-37% increase in co-morbitity [44-47]. During HIV infection the depletion of CD4+ T cells results in the highly decreased production of IFN-γ, IL-12 and TNF-α cytokines [48, 49].

The cytokine IFN-γ has been determined to be a key protective mediator of macrophage activation and resistance to intracellular pathogens [50, 51]. IFN-γ is mainly produced early on by macrophages and later at high levels by CD4 positive T-cells, and is crucial for containing the MTB infection [44, 52, 53]. Within immunocompetent mouse models, the production of IFN-γ and other cytokines result in the generation of inducible nitric oxide synthase (iNOS) and reactive nitrogen intermediates (RNI) [54, 55]. These reactive intermediate species are detrimental and cidal for the bacteria, which has been well established using the murine model. Mice lacking iNOS have an increased pathologic response and an increased recruitment of neutrophils [56]. However, the correlation between human TB and iNOS expressing macrophages is less clear [57-59]. The RNI are toxic to the infected macrophage, which will result in the death of the host cell creating necrosis and progressive disease [20].

The protective activity of IFN-γ against TB has been shown to be dependent on expression of the Th1 cytokine IL-12 [60-62]. Similar to GKO mice, mice lacking a functional IL-12 gene cannot control the growth of the bacterial infection [60, 63]. Another Th-1 cytokine, IL-23 is co-expressed with IL-12 to drive IFN-γ expression and maintains IL-17 production throughout infection. The absence of IL-23 does not impact control of bacterial growth early in infection [64], but in a chronic infection IL-23 KO mice had increased bacterial growth

compared to the wild-type C57Bl/6 mice [38]. Both IL-12 and IL-23 deficiency will result in a reduced IFN-γ cytokine levels in humans. Although there is a deficiency in both of these Th1 cytokines, the TB patients are controlling the infection by developing granulomas with aggregations of lymphocytes and macrophages in infected organs. This suggests that the IL-12 and IL-23 axis is not as important in humans as was demonstrated in mice [20].

Tumor necrosis factor-alpha (TNF-α) is thought to play a key role in latent infection. The cytokine activates macrophages, which will result in the production of inducible nitric oxide synthase (iNOS) and generation of reactivate nitrogen intermediates [57, 65]. Antibodies against TNF-α, or TNF-α suppression by immunomodulators have resulted in fatal reactivation of latent tuberculosis infection [20, 66, 67]. TNF-α has also been shown to play a role in regulating granuloma formation by modulating leukocyte migration. Soluble TNF is a membrane-bound molecule that is essential for normal granuloma formation and survival following tuberculosis infection [14]. In the absence of TNF, there is a delay in the initial recruitment of monocytes into infected tissue, although granuloma formation will occur this is delayed rendering the lesion more necrotic [20, 68, 69].

Interleukin-10 (IL-10) is an anti-inflammatory cytokine expressed by macrophages, dendritic cells, neutrophils, B cells and T cells, and is produced to dampen the highly inflammatory effects of IFN-γ/IL-12 and TNF-α during a tuberculosis infection [70]. Blocking IL-10 expression has been effective in restoring protective immune cytokines, while inhibiting the IL-10 receptor during infection resulted in reduced bacterial burdens and increased T cell recruitment and IFN-γ production [71]. The effects of inhibiting IL-10 production is either transitory as well as mouse strain dependent. Relatively resistant mouse strains, such as Balb/c and C57Bl/6, show no difference in bacterial loads in the lungs when lacking IL-10 [72-74].

Others have reported a temporary increase in IFN-γ levels, which coincided with a decrease of the bacterial load in lungs and spleens [70, 75, 76]. The highly susceptible mice (CBA/J) show increased levels of IL-10 in the lungs with the coinciding decrease of IL-12 and IFN-γ, which appears to exacerbate the susceptibility of the mice and increase their bacterial burdens [77]. Recently, an elegant study by the same group showed that the administration of an anti-IL-10R antibody early in infection promotes the formation of mature necrotic granulomas in CBA/J mice [78]. Lastly, human macrophages infected with MTB produce IL-10, which is able to cause blockage of the phagosome maturation, ultimately resulting in the survival and replication of the bacilli [79, 80]. While IL-10 is produced to protect the host from excessive inflammatory damage from Th1 cytokines, it allows for increased bacterial growth that can be detrimental.

Chemokines are pro-inflammatory mediators also produced after a MTB infection. Chemokines are small molecular weight proteins involved in immuno-regulatory and inflammatory functions [81]. Chemokines are categorized into groups based on their N-terminal cysteine residues, C-, C-C, C-X-C, and C-X_3-C subfamilies, where X represents an amino acid. Many chemokine ligands are inflammatory, such as, CCL2, CCL3, CCL5, CXCL8, CXCL9, CXCL10, and CXCL11. Induction of CCL2, monocyte chemotatic protein-1 (MCP-1), is of particular importance due the high levels expressed in broncho-alveolar lavage from pulmonary TB patients [82]. CCL2 is a strong chemo-attractant of CCR2+ monocytes/macrophages and CD4+ T cells [81]. CCL2 has been shown to be involved in the formation of the granuloma in tuberculosis and even to play a role in protection against the bacilli [20, 83]. In pulmonary TB patients, CCL2 and TNF-α were consistently correlated with increased severity of disease [84].

1.2.3 Bacterial metabolism and transcription profiles

MTB can manifest itself and remain alive under varying conditions and disease states, which makes it one of the most versatile pathogens. Changes in the microenvironment can affect the bacteria in such a way that they adapt to these new conditions by altering their transcription profiles and internal metabolism [85-87]. When the bacterium becomes stressed, whether due to oxygen deprivation, nutrient starvation, or macrophage acidification, it must make adaptations to survive. One important change the bacterium makes is a shift in its energy source. MTB can change to using lipids and fatty acids as a carbon source; the bacteria then use an alternative pathway, the glyoxylate shunt, for metabolism [25, 88-90]. The glyoxylate shunt uses the enzyme isocitrate lyase (ICL) to catalyze the cleavage of isocitrate into succinate and glyoxylate [91, 92]. MTB has two types of ICL, ICL1 and ICL2, both of which are required for growth, survival, and virulence in the macrophage [90, 93] as well as under in vivo conditions [94]. Bacteria deficient in ICL are unable to metabolize fatty acids and are rapidly cleared from infected macrophages [95], a result observed in humans and mice [94]. Pathogenic MTB during a persistent infection have an increased expression of ICL, which increases the production of succinate [89]. The increased succinate under limited O_2 enables the MTB to sustain succinate dehydrogenase activity and oxidative synthesis of ATP, maintain membrane potential, and store the remainder as TCA precursors to resume oxidative activity upon reoxygenation [89, 96]. MTB under metabolic stress have mechanisms that allow for continued survival and energy production.

Specific transcriptional adaptations that allow the bacterium to survive the surrounding environment and maintain virulence are sigma factors [97]. Of importance, one of the 13 sigma factors, *sig*E, controls the bacterial response to external stimuli after phagocytosis [87]. In

addition, the sigE factor regulates gene expression that maintains the mycobacterial envelope to cope with external stress [98]. Other sigma transcripts have shown importance in virulence and intracellular survival, such as *sig*D and *sig*B, *sig*G and *sig*H [99, 100]. SigH is an essential regulator of bacterial to oxidative, nitrosative and heat stresses [101].

To determine the factors and genes of bacterial persistence for MTB have been the center of intense and still ongoing studies. Through microarray and whole genome sequencing techniques, a large set of genes has been shown to become activated in states of hypoxia or environmental stressors. These 48 genes are under the control of a transcription regulator, called the DosR regulon [102-104] (also discussed in detail under 1.2.5 below). One gene induced under hypoxia and potentially involved in persistence is *acr*-2 (also known as hspX controlled by the DosR), which encodes alpha-crystallin [103, 105-107]. Acr localizes to the inner surface of the cell membrane and is a member of the small heat shock protein family that forms high molecular weight aggregates and has chaperone activity *in vitro* [108]. Acr expression dramatically increases under hypoxic conditions and due to the powerful regulation under low oxygen tension could provide insight into the nature and control of the whole genome response [103, 107, 109]. Acr is considered to be an immunodominant protein since it is found in the sera of most pulmonary TB patients [110, 111]. In immunocompetent C57Bl/6 mice there was an increase in bacterial burden, pathogenicity, and increased production of pro-inflammatory cytokines when infected with an acr-gene disrupted MTB strain. The observed increase in bacterial burden may be indicative of acr having a global down-regulating effect to prepare the bacterium for dormancy [112].

1.2.4 In vitro models of persistence

In an elegant experiment by Lawrence Wayne, also called the Wayne Model, determined an *in vitro* model of persistence for MTB [29]. He discovered that when bacteria are grown in culture with a closed cap with a limited headspace for oxygen consumption, MTB enter sequential stages of non-replication. During the transition, Wayne describes two specific non-replicative stages (NRP): the NRP-1 and NRP-2 stages. These stages reflect discrete metabolic and drug susceptibility states compared to log-phase growth. During the NRP-1, there is a slow but logarithmic increase in turbidity that is not reflected in an increase in colony forming units. There is a high rate of production of glycine dehydrogenase and ATP concentrations are maintained during this phase. Once the bacilli transition to the NRP-2 stage, the production of glycine dehydrogenase declines dramatically and ATP decreases slightly. NRP-1 appears to start about the time the O_2-concentration of the medium reaches 1% of the original saturation level. During transitioning from NRP-1 to NRP-2 stage, the O_2 concentration drops below 0.06%. Throughout the NRP-1 and NRP-2 stages, the drug susceptibility profiles of the bacilli change with the change in metabolism of the bacilli. INH and ciprofloxacin had negligible effects in the NRP-1 and NRP-2 stages, while they killed over 90% of actively replicating bacteria. Metronidazole (MET), an antimicrobial known to function against anaerobes, showed most effective killing only during late stage NRP-2. These observations suggest an organized mechanism for dormancy and persistence [29, 113-115]. Current variations of the Wayne model need approximately 21 days for complete oxygen depletion [116]. In 2010, alterations were introduced by Voskuil et al [102] using the “Rapid Anaerobic Dormancy” model, (RAD), which uses a more rapid stirring culture in smaller test tubes. These changes resulted in a more rapid

and uniform oxygen depletion within 7-10 days generating a bacterial population that is more transcriptionally homogenous.

The microarray technology provided a powerful tool to assess expression of many genes in response to changing environmental conditions [107]. Originally observed in the Wayne Model, the genetic profile of MTB changes dramatically under hypoxic conditions. Initial microarray studies showed three genes of particular interest to Schoolnik et al., which were the Rv3134c/Rv3133c/Rv3132c gene cluster. To investigate the role of this gene cluster individual mutations were made to dissect its exact function. It was observed at that time that Rv3133c was required for induction of acr expression under reduced oxygen tension. Since the Rv3133c product mediates the enhanced expression of at least one gene (*acr*) in response to low oxygen tension; it was thought that other genes in the hypoxia regulon could also be under its control [103, 117]. A more detailed description of the DosR regulon is described below under 1.2.5.

Other *in vitro* models of persistence have shown characteristics of the MTB bacilli under reductive stress. The starvation model optimized by Duncan et al [68] showed that bacteria initially grown in rich media, which are then deprived of that environment, have a decreased respiration and a severely shut down metabolic profile [68]. These starved bacteria are not affected when treated with RIF and INH. In contrast, MET has no effect on the starvation phase bacteria, which is different from the Wayne model. The stationary phase model, allows bacteria to remain for an extended amount of time in the culture media without agitation. The bacteria aggregate to the bottom of the flask where a lack of oxygen limits growth [118]. The stationary phase model was used to describe bacterial transcription factors, such as sigA and sigB. It was determined that sigA was unresponsive to stress and constitutively active, whereas sigB was up-

regulated during stationary phase. SigB has been determined to be required for survival and virulence of the bacteria [118].

1.2.5 DosR and its role in persistence

The exact function of the DosR regulon is still being studied by multiple investigators and seems to be more complex than originally thought. Initially, it was thought that the DosR was necessary for survival via the induction of a robust genetic response to reduced oxygen tension [103]. It has since been postulated that DosR is required for the optimal transition for MTB back to aerobic growth and the lack of the DosR regulon is not sufficient to initiate bacteriostasis [102, 104]. Therefore, some have renamed the regulon as "Dormancy Survival Regulator" (or DosR) [103]. DosR is a three-component system regulator; composed of two sensor histidine kinases, DosS or DosT, and a response regulator, DosR [119]. Upon phosphorylation the DosR regulon then leads to the induction of a set 48 co-regulated genes under its direct control [102, 104, 120, 121]. The DosS is potentially activated by two related pathways. Firstly, DosS constitutively binds with oxygen thus suppressing the sensor, when oxygen is depleted the sensor autophosphorylates leading to DosR activation [122-124]. Secondly, DosS acts as a redox sensor and is susceptible to oxidation rates as a signal for activation [125, 126]. Other stressors such as NO and CO gases induce the DosR regulon through these kinase sensors as well. The gases bind to the heme irons of the DosT and DosS, possibly to displace O_2, resulting in activation of the sensor [124, 126, 127].

Further experimentation with the DosR regulon has uncovered more questions in terms of its exact function *in vitro* as well as *in vivo*. The DosR regulon is highly up-regulated in the initial phases of low oxygen tension but as time progresses shows a decreased expression.

During this lag in DosR expression, D. Sherman described, the Enduring Hypoxic Response (EHR), a cluster of upwards of 230 genes are expressed 4-7 days after oxygen depletion [120]. In a recent set of experiments performed by Voskuil et al [102], it has been shown that the DosR regulon is necessary for the shift away from oxygen consumption, to maintain ATP levels and balance the redox state of the cell as oxygen becomes depleted. The induction of the regulon prior to respiration inhibition allows the bacilli to transcribe and translate the DosR regulon before energy becomes limited. While it has been noted that the transcription of the DosR/EHR is ceased within a few weeks after anaerobiosis, it is the initial expression that remains essential to ultimate survival and growth. The DosR regulon bacterial mutant after being exposed to anaerobiosis required an extra week to achieve colonies of countable size as compared to wild type bacteria. A lack of anaerobic survival, non-culturablilty on solid media, and reduced growth post-exposure to anaerobiosis, a DosR mutant bacterial strain does not survive well in a microenvironment that oscillates between oxygenated and hypoxic conditions [128].

The role of DosR *in vivo* is still under investigation. In the chronic immunocompetent C57Bl/6 mouse model the DosR KO, complement, and wild type bacterial strains had similar bacterial burden in the lungs throughout infection [127]. It is not entirely surprising that no difference in bacterial growth was observed in the mouse model, as there is no hypoxia reached in the chronic mouse model [128]. However, we observed significant less pathology in mice infected with the Dos R mutant when compared to the wild-type MTB strain. Converse et al, showed a DosR mutant strain was attenuated in both the guinea pig and rabbit infection models, which were chosen for their ability to produce necrotic granulomas with hypoxic regions [127]. The *in vivo* data suggest that the DosR regulon plays some role in persistence, but it may not the only factor to establishing or maintaining a chronic or persistent infection *in vivo* [129, 130].

1.3 – ANIMAL MODELS OF PERSISTENCE

1.3.1 Wild type mice

The most widely used *in vivo* model to the study of TB has been the chronic infection mouse model [131-137]. The transition to the chronic phase of infection is brought on by the emergence of acquired CMI, which is mediated by antigen specific T cells and macrophage activation, and results in the stabilization of bacterial numbers in the lungs [132]. After infection with TB, macrophages and lymphocytes accumulate in distinct lesions in the lungs of mice as the infection progresses from the acute to chronic phase [138], with macrophages forming the inner core and the lymphocytes surrounding the core area. In chronic stages of disease, the number of epitheloid-type foamy macrophages and lymphocytes increases dramatically. Later in infection, macrophages might degenerate and coalesce into small patches of interstitial fibrosis. It is important to note that bacilli remain intracellular throughout infection, and on rare occasions of necrosis small numbers of bacilli can become extracellular. As infection progresses, pathogenesis shows a thickening of the alveolar septae, and we see accumulation of inflammatory cells in the lung parenchyma. Granulomatous lesions are by then characterized by sheets of epitheloid and foamy macrophages that fill alveoli, which are often demarcated by mild interstitial fibrosis. As disease progresses the granulomatous lesions enlarge to the point that many coalesce, leading to consolidation of as much as half of the lung lobe. Small necrotic foci are often associated with clefts of accumulated cholesterol, which arises from released cytoplasm of dying cells that are especially rich in fatty acids [139]. Fibrosis of alveolar septae is more advanced, as indicated by increasing accumulation of collagen among the foamy macrophages. In late stage chronic disease, extensive remodeling of the lung parenchyma occurs. Chronic interstitial fibrosis and granulomatous involvement of the lung reaches a degree until individual

lesions can no longer be distinguished; many of the macrophages are dead or dying thereby creating foci of purulent cellular debris [140]. While immunocompetent mice form granulomatous lesions these tissues were shown not be hypoxic using hypoxia probes currently available suggesting that the mouse model of persistent TB is not entirely reflective of human disease [138, 141].

This mouse infection model is versatile and can be adjusted for multiple purposes, such as vaccine testing, drug treatment, or immunology studies to evaluate MTB. These mice can endure intravenous infection, a low and high dose aerosol infection, intratracheal and intranasal infection routes to establish an MTB infection [142]. Drug treatment can begin 30 days post infection to test drug efficacy in a chronic infection, or the inoculum can be increased to mimic acute pulmonary TB [143]. Therapy may also begin just a few days after infection to evaluate an acute infection model before adaptive immunity plays a role in the host profile.

McCune and colleagues at Cornell University developed another mouse model during the 1950s, now better known as the Cornell Model [144-146]. After intravenous infection, as early as 20 minutes after, mice are treated with antimycobacterial drugs, which reduce the bacterial burden to nearly undetectable levels. After antibiotic treatment is completed the animals are allowed to reactivate, either naturally by an extended withdrawal of therapeutics or with the help of immunosuppressive agents, such as glucocorticoids. This model is often used as a latent mouse model because of the low bacterial burden [147, 148]. However, it is an drug induced latency which is not necessarily the same as LTBI and the relapse rates are very hard to predict [149]. To date, a mouse model showing a more true latent disease state remains elusive.

1.3.2 GKO mouse model

Immunocompromised mouse strains are often used in TB research in order to study the immune response, or for drug treatment purposes. The susceptible transgenic mouse IFN-γ gene disrupted C57Bl/6 mice (GKO) for instance are being used to rapidly test experimental compounds against a TB infection, as they cannot control a TB infection. The mouse model contains mainly actively replicating bacteria, and the infection remains acute. IFN-γ has been shown to be a protective cytokine secreted by activated T cells and natural killer cells. In the initial stages of infection, the histopathology of the GKO mice is similar as compared to wild type C57Bl/6 mice; however, the granulomas of the GKO mice are far less structured [134]. Twenty days after aerosol infection, the number of bacteria in the lungs of GKO mice was 100-fold higher than in the wild type mice [134]. At this point of infection, the lesions within the lungs consist of mostly polymorphic cells with a low numbers of monocytes. Later in infection in the GKO model, about 4 weeks after aerosol infection, we showed that the pathology progresses significantly [134]. The lungs develop multifocal necrotic areas containing large numbers of intra-cellular acid-fast bacteria with substantial interstitial hemorrhage and cellular infiltrates of granulocytes and eosinophils. Lungs of GKO mice are almost totally devoid of mononuclear cells, have lost their cohesive structure and exhibit advanced caseous necrosis in late stage infection [134]. The extensive necrotic lesions with extracellular bacilli only form about a week prior to the mice succumbing to disease. And therefore as an advanced disease model with necrotic lesions it is not very practical [53].

1.3.3 Other animal models of persistence

Other animal models for the study of TB include the guinea pig, rabbit, NHP, rat, goat, zebrafish, and more recently the minipig [17, 50, 105, 150-155]. For the study of persistent bacilli and vaccination studies, the guinea pig has jumped to the forefront of TB research [156]. The guinea pig model has several advantages; there are many immunological reagents available, and they form necrotic primary granulomas which are similar to certain human lesions. Once infection of the respiratory route occurs, it has been suggested that every inhaled bacterium gives rise to the formation of a lung lesion. After initial exposure by a low dose aerosol, the infected guinea pigs develop primary lesions, characterized by a necrotic core [105, 150, 151, 157-162]. The primary lesions differ from secondary lesions which are non-necrotic and originate from extrapulmonary hematogenous dissemination after the activation of acquired immunity [163]. Vaccination of guinea pigs has shown to produce an overall reduction in size and degree of necrosis, a reduction in the number of bacilli, prevention of the hematogenous reseeding of previously unaffected portions of the lung [150, 164].

The progression of pathogenesis in the guinea pig model has been well studied [11, 105, 136, 151, 158-163, 165, 166]. As early as 15 days after aerosol infection, small aggregations of epitheloid macrophages mixed with granulocytes can be seen. Within one-month post infection the classic granuloma with a prominent necrotic eosinophilic core packed with karyorrhectic debris is present throughout the lung section. By two months post-infection, the guinea pig has necrotizing granulomatous lesions with peripheral fibrosis. Guinea pigs develop distinct regions of necrosis with defined rings of fibrosis that can progress to mineralization or calcification within the centralized core of this area. Surrounding this acellular core is a ring of epithelioid

macrophages, lymphocytes, and small numbers of multinucleated giant cells, neutrophils and eosinophils [162, 163].

While the guinea pig is a suitable medium-sized animal model resembling human pathology features for pathology to date, it does have its disadvantages for preclinical drug testing. The animals are substantial in size and therefore more expensive than mouse models. For drug development purposes, the animals also require substantial drug amounts which are usually not available in early drug discovery efforts. The main disadvantage of using guinea pigs in TB drug development is however their intolerance to broad-spectrum drugs, which disturb their delicate gastrointestinal flora which is required to generate their vitamin-C supply [162, 167]. The vitamin-C deficiency can lead to colitis, and cause gut lesions. To combat the resultant anorexia and in severe cases death an emulsion of drugs in sucrose, vegetable puree, lactobacillus and vitamin C supplement is often given [162], which might affect results and should be controlled for.

The rabbit was historically used by Maxwell Lurie to test the resistance and susceptibility to TB [168]. The granulomas that develop in these particular resistant rabbit strains are highly reflective of human disease in that they can develop various lesion types including cavitary disease. Lurie used an inbred New Zealand White rabbit strain, which was susceptible to TB. However, the strain no longer exists [11]. Other current rabbit strains will clear most of the infection with MTB H37Rv or Erdman, but are more susceptible to *M. bovis* [169]. The rabbits, however, will produce a reliable cavitary model when infected with highly virulent W-Beijing strains, such as HN878 [170]. For the study of latent disease the rabbit model is infected with H37Rv or Erdman [155]. Unfortunately, many immunological reagents for rabbit are not widely available

The study of latent tuberculosis is most successful in NHP [50]. NHP are naturally susceptible to MTB infection and exhibit most characteristics of human disease [171]. After intratracheal infection, about half of NHP develop latent disease, mimicking human pathogenesis [171]. The latent stage in the NHP model is defined as animals that have received an infectious dose, are skin-test positive, show lesions on X-rays but do not develop clinic symptoms [172]. Unfortunately, primates are very expensive and impractical for many scientific programs including early drug development.

Other animal models of tuberculosis disease such as the zebrafish, rat, goat and minipig are useful to specific aspects of the study of TB. Zebrafish are naturally susceptible to *Mycobacterium marinum*, which replicates in macrophages and produces a chronic granulomatous infection with necrotic lesions [152, 173]. Zebrafish are small and are easily manipulated, this allows researchers to develop molecular, genetic, and imaging tools that can be translated to mammalian models [174]. Immunological tools are difficult to obtain making it complicated to explore detailed host-bacteria relationships. Rats are primarily used in drug development and pharmacokinetic testing of new compounds. The Wistar rat and cotton rat models are resistant to MTB and have the potential to be developed for latent drug testing as the rat tends to clear TB infection with the onset of the adaptive immunity [153, 175]. However, the use of more virulent clinical MTB strains give more advanced disease leading to necrotic lesions in the lungs. Goats can be naturally infected with *Mycobacterium caprae*, or experimentally infected with *M. bovis* or *M. tuberculosis*. They develop encapsulated necrotic granulomas, which produce a strong immunological response, such as an increased iNOS and neutrophilic response, which may account for the highly developed necrotic lesions [154, 176]. Again here, the immunological reagents are difficult to obtain. The minipig develops a heterogeneous

infection when MTB is injected intrathoracically. The minipig has been hypothesized to represent human LTBI, they develop early cellular phase I lesions which progress into necrotic encapsulated phase II granulomas by 5-9 weeks post infection [17]. Many of these larger animals models show pathology that is highly representative of human lesions, however more data on drug treatment is required to show whether they can add information for pre-clinical drug investigation, as they are more cost-prohibitive

More recently, various research groups have reported on mouse strains that develop necrotic lesions after an MTB infection. Currently, five genetically diverse mouse strains have been described that show necrosis upon infection with MTB: the IL-13 transgenic mouse [177], CBA/J [178], iNOS -/- [179], I/St [180], and C3HeB/FeJ [181] (summarized in Table 1.1).

The IL-13 transgenic mouse strain was first explored in terms of its pulmonary pathology associated with asthma and other inhaled antigens. It was found that the removal of IL-13 resulted in a reduction in inflammatory response in the lung [182-184]. As of late, there has been interest in the role of IL-4R-alpha/IL-13 axis involved in increasing TB-associated pathology [177]. IL-13 transgenic mice were used to explore TB pathogenesis, and it was seen that mice over-expressing IL-13 developed centrally necrotizing granulomas and peri-necrotic fibrosis while wild type and IL-4Ra deficient mice lacked these features [177] (personal communication with Dr. Ehlers).

Another MTB susceptible mouse strain, CBA/J, which does not have any immunological defects, has been used to study intracellular cytokines after infection [185] as well as lesion development when infected with low aerosol doses of MTB [178]. The CBA/J shares some similarities with human disease with extensive granulomatous infiltration, necrosis, and fibrosis. Studies done by Turner et al [77, 78] have shown increased levels of IL-10 and a decrease in

IFN-γ and IL-12 production. Judicious administration of anti-IL-10R antibody can successfully promote the development of mature necrotic granulomas in the CBA/J mice [78]. The CBA/J mouse model may be helpful in understanding neutrophils in MTB disease progression [178].

Table 1.1 Mouse Strains that Develop Necrotic Granulomas when infected with MTB

STRAIN	DEFECT	LUNG FEATURES	OTHER DISEASES	AVAILABILITY
IL-13 TRANSGENIC	Over-expression of IL-13/IL-4Ra	Necrotic lesions with peri-necrotic fibrosis	Used to evaluate asthma and lung inflammation	Requires in-house breeding colony
CBA/J	No TB related defect. Early parental strain derived from same strain as C3H	Early administration of multiple doses of IL-10 promotes development of necrotic encapsulated granulomas	Interstitial cystitis, cochlear nucleus, thyroiditis, and lung injury	Commercially available *difficult breeders
iNOS -/-	Knock-out of inducible Nitric Oxide production	Uncontrolled bacterial growth and development of abscesses	Lung inflammation and fungal infections	Requires in-house breeding colony
I/St	Deficient gene locus Ts-1 on chromosome 1	Large regions of necrosis with fibrosis	Intracellular pathogens: *Chylamydia pneumoniae* and *Salmonella enterica*	Requires in-house breeding colony
C3HeB/FeJ	Deficient gene sst-1 locus on chromosome 1	3 types of advances lesions with necrotic encapsulated granulomas, necrotizing alveolitis, and cellular infiltrates	Intracellular pathogens: Listeriosis and Leishmaniasis	Commercially available *good breeders

Mice deficient in iNOS (inducible nitric oxide), a key reactive species component, have uncontrolled growth bacilli and develop encapsulated abscesses in the lung [186, 187]. Early in infection, the presence of iNOS is important for the control but it may also be linked to antibacterial activity in chronic infection when induced in foamy macrophages [188]. iNOS KO mice have an increased production of Gr1+, CD4+ and CD8+ cells compared to wild type mice when infected with MTB [179].

The I/St mouse strain described by Apt et al will develop necrotic granulomas when infected with MTB [189]. The functional differences between the I/StSnEgYCit (I/St) and A/SnEgYCit (A/Sn) mouse strains are still being determined but it has been described that the I/St has increased severity of lung pathology [190]. The I/St mouse strain has a recessive allele of a single locus on chromosome 1, the resultant effect are macrophages are no longer efficient at killing MTB. The gene locus has been named the Ts-1 (or tuberculosis sensitivity-1) by Apt et al [189]. It should be noted that the I/St mice that are hypersusceptible to MTB are found to be resistant to *M. avium* [191].

Lastly, the C3HeB/FeJ mouse strain, a sub-strain of the C3H strain able reliably develops necrotic granulomas upon MTB infection. It was Igor Kramnik [181, 192] who performed most of the initial studies for tuberculosis on this mouse strain, hence the tuberculosis mouse model now being addressed by most as the “Kramnik mouse model”. The mouse strain has been found to be susceptible to TB disease but is otherwise completely immunocompetent. The strain is characterized by a de novo mutation of the *Ipr*1 (intracellular pathogen resistance 1) gene of the *sst-1* (super susceptibility to tuberculosis 1) locus on chromosome 1 of the mouse genome [193-195]. Originally, the sst1 locus was thought to be associated with a 12-transmember domain molecule, Nramp (natural resistance-associated macrophage protein 1), also on chromosome 1.

Nramp controls host resistance to intracellular pathogens including *M. bovis* and MTB [192, 196]. This was later however shown not to be the case, and it has since been determined that Ipr1 and Nramp are two distinct genetic locations 10-12 centimorgan apart on chromosome 1 [181].

The sst1 mutation is largely lung specific, and spleen and liver hematogenous dissemination of MTB has been found similar to other mouse strains [192]. After early infection with MTB C3HeB/FeJ mice develop large regions of diffuse necrosis that become organized with time. Later in infection there are distinct regions of acellular necrosis encompassed with epithelioid macrophages, lymphocytes, neutrophils and eosinophils. The mean survival time after an intravenous infection with 10^5 colony-forming units of MTB is 3.5-5.5 weeks whereas for low dose aerosol with 15-30 colony-forming units is 20-30 weeks. *In vitro* in macrophage cultures from C3HeB/FeJ mice, this locus had an effect on macrophage-mediated control of MTB [197]. While the mutation has an effect on innate immunity, it is unclear what exact function the sst-1 controls. It has been determined that iNOS does not seem to play a role, the iNOS levels were unaffected by the sst-1 mutation within the lung. Since the *sst1* gene has such a dramatic effect on the susceptibility in mice, further studies are underway by Kramnik et al. to address whether the human homolog, SP110, also results in susceptibility to pulmonary TB [198, 199].

Potential uses for these mouse models developing advanced pathology are countless. Currently, work is being done to explore positron emission tomography on the Kramnik mouse model and the relation to drug treatment [200]. The Kramnik mouse model can be easily used and lesions visualized using the PET scan equipment and can thereby effectively reduce the numbers of animals needed to evaluate the effectiveness of drug therapy.

1.4 – RATIONALE

This goal of this thesis is to develop and optimize a model more reflective of human TB disease capable of recapitulating clinical outcomes when evaluating drugs and drug regimens. To achieve this objective a small animal model, such as a mouse model, is optimal due to the ease of manipulation and large-scale reproducibility. The C3HeB/FeJ mouse strain develops necrotic encapsulated granulomas similar to those found in human and NHP TB pulmonary disease. Through comprehensive analysis of histopathology, immune response, and drug treatments we aim to propose the C3HeB/FeJ mouse strain as a novel representative mouse model for the study of MTB.

Specific Aim 1: To develop a reliable mouse model that reflects human disease; C3HeB/FeJ mice are infected with MTB, which will develop necrotic encapsulated granulomas with specific pathological features of advanced disease. C3HeB/FeJ mice develop features such as a collagen rim, hypoxia, and neo-angiogenesis, which will create a microenvironment refractory to chemotherapies that are not effective on actively replicating bacteria.

Specific Aim 2: To gain a better understanding of multiple aspects of the Kramnik mouse model in terms of lesion progression, bacterial location, and cell-specific cytokine production. C3HeB/FeJ mice infected with MTB will give us a greater understanding of the role local microenvironment has in the development of a heterogencity of lesion types reflective of human disease.

Specific Aim 3: Utilize the C3HeB/FeJ mouse model as a tool to improve treatment by using various approaches: 1) by indentifying single drugs that are also effective against advanced disease displaying necrotic lesions, 2) by co-treatment that improves pathology, 3) by using alternative delivery systems adapted to advanced lesion types. The adjunctive therapy approaches and knowledge gained from a small animal preclinical cavitary disease model will improve drug therapy and shorten TB treatment duration.

The C3HeB/FeJ mouse model may be an important tool for the field of TB research and other granulomatous diseases. This mouse model fills a gap in the late stage TB pre-clinical drug discovery pipeline. In TB drug development compounds are initially evaluated in an acute mouse model in order to know whether sufficient drug exposure is obtained that can lead to efficacy in the lung. A more chronic infection mouse model is then used to provide drug efficacy information over long treatment durations against an intracellular infection. The Kramnik mouse model provides the TB field with the opportunity to determine the killing kinetic profile of a drug against more advanced disease: under such pressures as *in vivo* hypoxia, against extracellular bacteria, and a higher resistance frequency. The future will tell whether the Kramnik mouse model will fill a niche and add more information than the classical mouse models, or eventually will replace them. However in the meantime, there is much information to be gained from studying this mouse model in terms of pathology, persistence, and immunology that defines the lesion. Eventually, this mouse model will be instrumental in furthering the treatment of the TB epidemic.

CHAPTER 2 – DEVELOPMENT AND EVALUATION OF THE C3HEB/FEJ MOUSE MODEL FORMING NECROTIC GRANULOMAS FOR THE TESTING OF *M. TUBERCULOSIS* DRUGS[*]

2.1 – INTRODUCTION

Mycobacterium tuberculosis (MTB) like other pathogenic bacteria can adapt to a wide variety of microenvironments and survive for many months even following aggressive combination drug therapy. In controlled *in vitro* studies, bacilli have been shown to survive nutrient and oxygen depletion as well as microenvironments with high carbon monoxide and nitric oxide concentrations [29, 130, 201]. These adaptation strategies are thought to facilitate survival of MTB as the pulmonary environment changes due to immune-mediated pressure, sequestration of the bacilli within granulomas, and in response to chemotherapeutic treatment.

One of the hallmarks of human tuberculosis (TB) infection is the development of granulomatous inflammatory lesions with central caseous necrosis that form first in the lungs but can involve essentially any part of the body resulting in extra-pulmonary tuberculosis [202]. In post-primary disease that can occur decades after initial exposure, aggressive and more destructive cavitary lesions often develop in the apical lung lobes, which are significantly less responsive to long-term, combination drug therapy. While cavitary lesions often communicate with conducting airways, necrotic granulomas are thought to be refractory to drug therapy

[*] Portions have been previously published in Antimicrobial Agents and Chemotherapeutics

doi:10.1128/AAC.00217-12

because the microenvironment is hypoxic or microaerophilic, low in nutrients, and has a higher concentration of carbon monoxide than more normal lung parenchyma [203]. These changes in the lung microenvironment are thought to trigger the bacilli to alter their metabolic profile making them more tolerant of drug therapy, especially those therapies that are most effective against actively replicating bacilli [14, 204]. In addition, encapsulation of lesions by fibrous connective tissue may represent a physical barrier to drug penetration which was recently indicated in a study using the rabbit model [205]. We have shown in animal models that develop necrotic lesions that the majority of bacilli are extracellular admixed with debris from necrotic host cells [167]. Because these lesions more closely mimic what occurs in humans with naturally occurring TB, it desirable to evaluate any promising new TB drug regimen under similar, clinically relevant *in vivo* conditions. While the mouse model has proven its usefulness in TB drug development [53, 206-209], the most commonly used mouse strains fail to develop organized granulomas with central necrosis. This has been the main reason other model species have been explored for drug testing [90]. While other TB animal models, such as the guinea pig [162, 210], rabbit [155, 211], and NHP [50] form necrotic granulomas, each has drawbacks that limit their usefulness for preclinical drug testing [212]. The NHP following a natural and experimental MTB infection develops a variety of lesion types that more closely mimic the human disease, but widespread use of this model is cost prohibitive for extensive preclinical drug evaluations [50, 212, 213]. The rabbit model forms necrotic granulomas and cavitary lesions following infection with *M. bovis* and highly virulent clinical MTB strains [155], however, the rabbit model is also expensive to maintain. Additional drawbacks include pathogen containment concerns, since rabbits shed MTB in the urine, and are highly susceptible to concurrent infections with *Pasteurella* and *Bordetella bronchiseptica* [the latter also seen in guinea pigs].

The guinea pig model develops necrotic granulomas and while more cost effective, is limited by the inability to tolerate certain drug classes resulting in dysbacteriosis and vitamin-C deficiency after treatment with broad-spectrum antibiotics [162]. Of practical concern, for the larger animal models a substantial quantity of drug is required to reach therapeutic tissue levels, which is generally not available during the early preclinical stages of TB drug development.

Whereas the most widely used laboratory mouse strains such as Balb/c and C57BL/6 show little evidence of caseous necrosis and fibrosis [181, 214] a mouse strain with a recessive allele, the C3HeB/FeJ mice, which was firstly described by Igor Kramnik *et al*. in context of an MTB infection [192], develops highly organized encapsulated necrotic lesions following a TB infection. We will from this point forward refer to this mouse model, as is also done by others, as the "Kramnik mouse model" [200]. Kramnik's group observed that although C3HeB/FeJ mice had no overt immunodeficiency, they were highly susceptible to infection with TB. More importantly, these mice developed pulmonary granulomas that more closely resembled human lesions, which was a significant limitation of conventional mouse models of TB. Using a forward genetic approach, they identified a region at the 54.0 cM location of chromosome 1, termed the 'super-susceptibility to tuberculosis-1' (*sst1*) locus which was responsible for a decreased ability to control TB multiplication in the lungs. More importantly, the susceptible *sst1* allele was shown to control the formation of caseous necrosis of pulmonary lesions [215]. Further work using positional cloning identified the 'Intracellular pathogen resistance-1' (*Ipr1*) isoform of the 'interferon-inducible-75' (*Ifi75*) gene as responsible for a significant proportion of the increased susceptibility of the C3HeB/FeJ mice [194]. *Ipr1* negative mice fail to control bacterial replication to the same extent as wild-type control mice, even though major pathways controlling macrophage responsiveness (nitric oxide production and upregulation by IFN-γ) were

demonstrated to be intact [197]. More importantly, infected macrophages from *Ipr1* negative mice preferentially die by necrosis as opposed to apoptosis.

In the Kramnik mouse model the bacterial load increases to high numbers and the lung pathology progresses dramatically following a low dose infection with TB. This has been described after an intravenous dose of 10^5 CFU, or an aerosol infection of 15-30 CFU per mouse [181, 193]. Necrotic microfoci are observed after two weeks following infection, and progress to highly organized encapsulated lesions at later stages of disease, when the bacterial load in the lungs can reach 10^8 CFU or higher [181, 216]. The lesion necrosis in the Kramnik mouse model occurs primarily in the lung, whereas the infection appears to be better controlled in other organs such as in the spleen and liver [181].

Since the C3HeB/FeJ mice displayed an increased susceptibility to TB infection but possessed an otherwise intact and functional immune system, and due to the formation of necrotic lung lesions resembling human pulmonary lesions, we hypothesized that the Kramnik mouse model may represent a novel model for preclinical screening of new, desperately needed TB drugs. This mouse model also lends itself to advanced imaging techniques such as Positron Emission Tomography (PET) which allowed the investigators to follow disease progression in real time [200].

In this study, we compared disease progression, pathology, location of bacilli, and responsiveness to monotherapy with multiple drugs in the Kramnik mouse model and Balb/c mice that differ in their response to experimental TB infection.

2.2 – MATERIALS AND METHODS

2.2.1 Animals

Female specific pathogen-free C3HeB/FeJ and Balb/c mice aged 6-8 weeks were purchased from Jackson Laboratories, Bar Harbor ME. Mice were housed in a bio-safety level III animal facility and maintained with sterile bedding, water and mouse chow. Specific pathogen-free status was verified by testing sentinel mice housed within the colony.

2.2.2 Bacteria and drugs

M. tuberculosis Erdman strain (TMCC 107) was used for drug evaluations in mice and prepared as previously described [116, 217]. Briefly, the bacteria were originally grown as a pellicle to generate low passage seed lots [116]. Working stocks were generated by growing to mid-log phase in Proskauer-Beck medium containing 0.05% Tween 80 (Sigma Chemical Co., St. Louis, MO) in three passages, enumerated by colony counting on 7H11 agar plates, divided into 1.5 ml aliquots and stored at -70°C until use.

Isoniazid (INH), rifampin (RIF), pyrazinamide (PZA) and metronidazole (MET) were obtained from Sigma Chemical Co. (St. Louis, MO). Linezolid (LZD) was purchased from 21CEC (East Sussex, United Kingdom). Drugs were prepared for the treatment of the mouse models as described before [116]. Briefly, RIF was dissolved in 100% DMSO, with subsequent dilution in sterile water prior to administration. The final concentration of DMSO in the drug preparation was 5%. INH and PZA were dissolved in sterile water. MET and LZD were formulated in 0.5% methylcellulose (Sigma Chemical Co.).

2.2.3 Aerosol infection and drug treatment schedule

C3HeB/FeJ mice were exposed to a low-dose aerosol infection with *M. tuberculosis* in a Glas-Col inhalation exposure system, as previously described [217], resulting in an average of 55 bacteria in the lungs on the day of exposure. Balb/c mice were exposed to a high-dose aerosol infection with an undiluted logarithmically growing broth culture of MTB (optical density at 800 nm of ~1.0) [218, 219]. Five mice were sacrificed the following day to determine the number of CFU implanted in the lungs.

Both mouse strains were treated with the following drugs: INH (25 mg/kg), RIF (10 mg/kg), PZA (150 mg/kg), MET (200 mg/kg) and LZD (100 mg/kg). For the Balb/c mice, drug treatment with single drugs started two weeks post infection and occurred 5 days per week via oral gavage. Mice were euthanized after 2, 4, 6 and 8 weeks of treatment by CO_2 inhalation. For the Kramnik mouse model, drug treatment with single drugs started 6 weeks post infection and occurred 5 days per week via oral gavage. Mice were euthanized after 2, 4, and 7 weeks of treatment by CO_2 inhalation. For all mice, the left lung lobes were homogenized and the bacterial load determined by serial dilution on 7H11 agar plates.

2.2.4 Enumeration of bacterial load of lungs and spleens

At the time of sacrifice, left and right lung lobes as well as the spleens were aseptically removed. The right caudal lung lobe was perfused with fixative for pathology analysis. The left and right cranial lung lobes were used for bacterial enumeration and disrupted with a tissue homogenizer (Glas-Col Inc., Terra Haute, IN). The number of viable organisms was determined by plating serial dilutions of lung homogenate on Middlebrook 7H11 agar plates supplemented

with OADC (GIBCO BRL, Gaithersburg, MD). Colonies were counted after at least 21 days of incubation at 37°C [116].

2.2.5 Enumeration of drug resistant colonies of the lungs

Upper right lung lobes were collected from the drug treatment trials of the final two treatment time points from both Balb/c and Kramnik mice. The lung lobes were disrupted with a tissue homogenizer, serially diluted and plated on Middlebrook 7H11 agar plates supplemented with OADC as well as on Middlebrook 7H11-OADC agar plates supplemented with specific concentrations of drugs for resistance enumeration. The drug-containing 7H11 plates had the following drug concentrations: 0.4 mg/mL of RIF, 4 mg/mL of INH and 8 mg/mL of LZD. Colonies were counted after at least 21 day of incubation at 37°C and kept for 10 weeks to ensure all viable colonies would be detected. The detection limit of the lung and spleen plating procedure was 150 CFU, and 50 CFU respectively. The viable bacterial counts of whole organs were calculated, converted to logarithms [CFU counts were log-transformed as $Log_{10}(x + .001)$, where x equals the total organ CFU count]. The data were expressed as the mean Log_{10} CFU ± the standard error of the mean for each group.

2.2.6 Statistical analysis

The viable CFU counts were converted to logarithms, which were then evaluated by a one-way analysis of variance and two-way analysis of variance, followed by a multiple comparison analysis of variance by a one-way Tukey test and Dunnett test (SAS Software program, Research Triangle Park, NC). Differences were considered significant at the 95% level of confidence.

2.2.7 Staining procedures

At each sacrifice, the right caudal lung lobe was infused with 10% neutral-buffered formalin and preserved until processed for histopathological assessment. Five micrometer thick paraffin sections were stained with TB Auramine-Rhodamine T as per manufacturer's instructions (Becton-Dickinson, Sparks, MD), with modifications in order to visualize bacteria as well as the surrounding lung tissue [134]. A combination fluorescent staining method was used by combining Auramine O and Rhodamine B to stain the bacteria (AR; Becton Dickinson), Hematoxylin QS for staining tissue (HQS; Vector Laboratories, Inc., Burlingame, CA), and 4'6-diamidino-2-phenylindole dihydrochloride for staining nuclei (DAPI; Sigma Chemical Co.). Briefly, tissue sections were dewaxed in xylene and rehydrated through a graded alcohol series, then stained with TB Auramine-Rhodamine T for 30 min. After washing excess stain with ddH_2O, slides were decolorized with TB Decolorizer TM (BD) until the excess stain dissolved. Counterstaining was performed with Hematoxylin QS for ~5 sec. After washing excess Hematoxylin with ddH_2O, slides were stained for 15 min. with DAPI (200 ng/mL final concentration) and washed in ddH_2O.

Lung tissue sections were stained to visualize the bacteria with the sensitive acid fast staining method with Kinyoun's carbol fuchsin (Rowley Biochemical Institute, Danvers, MA) stain in a method described by the United States Armed Forces Institute of Pathology (AFIP 1968). Five micrometer thick paraffin sections were dewaxed in xylene and rehydrated through a graded alcohol series, rinsed with tap water, then stained with Kinyoun's carbol fuchsin for 30 min at 60°C. Excess stain was rinsed with ddH_2O and slides were decolorized with 3% HCl acid alcohol wash until pale pink. Counterstaining was achieved with TB Methylene Blue (Becton-

Dickinson) for ~10 sec as per manufacturer's recommendations. Excess methylene blue was washed away with ddH_2O.

For staining of collagen deposition, Picrosirius red was used to detect the extent of collagen fibrils made and thickness of collagen as it ages. Picrosirius red can distinguish between new and already established collagen depositions. Newer collagen consists of thin fibrils that stain green to yellow, while older, thicker collagen stains orange to deep red [220]. The staining method used was previously established by Early *et al*. [221]. Briefly, section slides were stained with Vector's formulation of Mayer's Iron Hematoxylin (Vector Laboratories) for 8 min at room temperature then rinsed under tap water until clear. Slides were submerged in a bath of 0.1% Sirius red in saturated picric acid (Electron Microscopy Sciences, Hatfield, PA) in the chemical hood for 1 hr at room temperature. Subsequently, slides were submerged for 2 min into two acidified water baths (0.5% glacial acetic acid). Finally the slides were dehydrated for 2 min in distilled water, 3 min in 70% isopropanol, 3 min in two changes of 96% isopropanol, and 3 min in two changes of 100% isopropanol baths. The slides were cleared once in xylene and mounted with Permount mounting media (Fisher Scientific, Pittsburg, PA).

To visualize hypoxic regions in lung tissues, the pimonidazole Hypoxyprobe (Chemicon, Burlington MA) immunohistochemical staining technique was used. Mice were intraperitoneally injected with pimonidazole hydrochloride at a dose of 60 mg/kg at least 1 hour prior to sacrifice. Antigens were retrieved on deparaffinized tissues with pronase (Fisher Scientific) for 40 min at 40°C. After reduction of endogenous peroxidase activity with 3% hydrogen peroxide for 20 min, the anti-pimonidazole antibody Hypoxyprobe-1MAb1 (dilution 1:50; Chemicon), was added overnight at 4°C with biotinylated reagent (Vector Laboratories). The reaction was visualized by AEC (Vector Laboratories) [141].

2.2.8 Pathology and microscopy

The right caudal lobe from each mouse was collected at necropsy and fixed in 10% neutral buffered formalin in phosphate buffered saline (PBS). Tissue sections were embedded in paraffin and cut to 5 μm thickness on a microtome. Subsequent tissue sections were mounted on glass slides, deparaffinized and stained either with Hematoxylin and eosin (H & E), Picrosirius red, pimonidazole or AR fluorescent stain. Fluorescent sections were visualized using a Nikon Intensilight mercury vapor lamp and scanned using a Nikon TE-I motorized microscope controlled by Nikon NIS Elements software (Nikon, Melville, NY) with FITC, TRITC and DAPI filters. Light microscopy sections were visualized using an Olympus BX41 with Olympus DP70 camera controlled by Olympus DP Software (Olympus, Melville, NY).

2.3 – RESULTS

2.3.1 Disease progression over time

Balb/c mice were infected with a high dose aerosol (4.04 ± 0.06 Log_{10} CFU one day post infection) to achieve a similar pulmonary bacterial load as the highly susceptible Kramnik mice by the initiation of drug treatment (day 12). At day 12 after aerosol infection, the bacterial burden within the lungs had increased to 7.47 ± 0.06 Log_{10} CFU, at which point chemotherapeutic treatment was initiated. At day 17 after aerosol, the lung burden had increased to 8.24 ± 0.14 Log_{10} CFU after which the first mice from the untreated control group began to display clinical symptoms and had to be humanely euthanized. By day 26, only two mice remained from the untreated control group and the pulmonary bacterial load had increased to 8.3 ± 0.7 Log_{10} CFU with both animals exhibiting severe clinical signs of infection (Table 2.1).

Table 2.1. Bacterial numbers in lungs and spleens one day post infection, 12 days post infection (start of drug treatment), and after 2, 4, 6 and 8 weeks of treatment in Balb/c mice[a]

	Log_{10} CFU ± SEM			
Treatment Regimen	Lung Lobe	n[b]/N	Spleen	n[b]/N
Day 1, Balb/c	4.04 ± 0.06	5/5		
Day 12, Balb/c (Pre-Treatment Controls)	7.47 ± 0.06	5/5	3.65 ± 0.20	5/5
Day 17, Balb/c	8.24 ± 0.14	7/7	5.36 ± 0.12	7/7
Day 26, Balb/c	8.30 ± 0.70	2/2	5.65 ± 0.13	2/2
2 weeks INH, Balb/c	5.50 ± 0.08	5/5	1.94 ± 0.24	2/5
2 weeks RIF, Balb/c	5.11 ± 0.11	5/5	2.49 ± 0.24	4/5
2 weeks LIN, Balb/c	5.55 ± 0.08	5/5	4.21 ± 0.12	5/5
2 weeks PZA, Balb/c	6.11 ± 0.00	1/5[c]	4.50 ± 0.13	5/5
2 weeks MET, Balb/c	8.13 ± 0.40	7/7	5.23 ± 0.09	7/7
4 weeks INH, Balb/c	4.98 ± 0.03	5/5	0.00 ± 0.00	0/5
4 weeks RIF, Balb/c	4.56 ± 0.08	5/5	1.90 ± 0.10	3/5
4 weeks LIN, Balb/c	5.18 ± 0.12	5/5	4.14 ± 0.13	5/5
4 weeks PZA, Balb/c	5.58 ± 0.07	5/5	4.82 ± 0.10	5/5
6 weeks INH, Balb/c	4.56 ± 0.09	5/5	0.00 ± 0.00	0/5
6 weeks RIF, Balb/c	3.31 ± 0.02	5/5	0.00 ± 0.00	0/5
6 weeks LIN, Balb/c	4.03 ± 0.06	5/5	3.77 ± 0.12	5/5
6 weeks PZA, Balb/c	5.28 ± 0.07	5/5	4.99 ± 0.09	5/5
8 weeks INH, Balb/c	3.62 ± 0.06	5/5	0.00 ± 0.00	0/5
8 weeks RIF, Balb/c	3.36 ± 0.29	5/5	0.34 ± 0.34	1/5
8 weeks LIN, Balb/c	3.71 ± 0.16	4/5	3.70 ± 0.17	4/5
8 weeks PZA, Balb/c	5.51 ± 0.09	5/5	5.15 ± 0.10	5/5

[a]Data are Log_{10} CFU counts in the lung and spleen.
[b]n/N, number of mice that yielded viable CFU data (n) over the total number of mice that group (N).
[c]One mouse yielded viable colonies due to technician error

For the infection of the Kramnik mouse model, preliminary experiments were performed to establish a non-lethal bacterial inoculum that would still allow progression of the disease to state exhibiting caseous necrotic lesions. These initial experiments showed that an aerosol infection resulting in an average of 84.4 CFU in the lungs on day one after aerosolization gave rise to an average bacterial burden of 9.14 ± 0.17 Log_{10} CFU in the lungs by day 30, however, the study had to be terminated early at day 44 due to mortalities. To reduce the mortality rate of

the infected mice and increase the timeline of the experiment, a final protocol was used where mice were infected with an average of 55 CFU, which resulted in a productive TB infection, generated necrotic lesions after 40 days, showed a stable chronic infection of about 10^8 CFU, and allowed survival of the Kramnik mice to at least 90 days (data not shown).

To test the efficacy of single drug treatments, the Kramnik mice were aerosol infected with an average of 57 bacteria in the lungs per mouse. By 6 weeks of infection, the bacterial load in the lungs of the Kramnik mice had reached 6.85 Log_{10} CFU, at which time drug therapy was initiated. The pulmonary bacterial load continued to increase slowly in the lungs of the untreated Kramnik control mice throughout the duration of the experiment. By 13 weeks of infection, Kramnik mice had an average of 7.92 Log_{10} CFU in their lungs, at which point the experiment had to be terminated due to increased morbidity and clinical signs of disease (Table 2.2).

Table 2.2. Bacterial numbers in lungs and spleens one day post infection, 42 days post infection (start of drug treatment), and after 2, 4 and 7 weeks of treatment in Kramnik mice[a]

	Log_{10} CFU ± SEM			
Treatment Regimen	Lung Lobe	n[b]/N	Spleen	n[b]/N
Day 1, Kramnik	1.57 ± 0.21	5/5		
Day 42, Kramnik (Pre-Treatment Controls)	6.85 ± 0.44	5/5	4.48 ± 0.06	4/5
2 weeks Control, Kramnik	6.77 ± 0.41	5/5	4.57 ± 0.11	5/5
2 weeks INH, Kramnik	5.52 ± 0.54	5/5	2.82 ± 0.09	5/5
2 weeks RIF, Kramnik	5.31 ± 0.19	5/5	3.30 ± 0.23	5/5
2 weeks LIN, Kramnik	6.24 ± 0.31	5/5	4.10 ± 0.12	5/5
2 weeks PZA, Kramnik	6.53 ± 0.39	5/5	4.41 ± 0.24	5/5
2 weeks MET, Kramnik	6.35 ± 0.39	5/5	4.52 ± 0.14	5/5
4 weeks Control, Kramnik	7.25 ± 0.46	5/5	4.94 ± 0.13	5/5
4 weeks INH, Kramnik	5.43 ± 0.62	5/5	4.08 ± 0.16	5/5
4 weeks RIF, Kramnik	4.82 ± 0.61	5/5	2.68 ± 0.18	5/5
4 weeks LIN, Kramnik	5.68 ± 0.46	5/5	3.95 ± 0.26	5/5
4 weeks PZA, Kramnik	6.74 ± 0.71	5/5	4.40 ± 0.29	5/5
4 weeks MET, Kramnik	7.58 ± 0.45	5/5	4.67 ± 0.18	5/5
7 weeks Control, Kramnik	7.98 ± 0.27	4/4	5.46 ± 0.21	4/4
7 weeks INH, Kramnik	6.22 ± 1.61	3/5	1.95 ± 0.49	4/5
7 weeks RIF, Kramnik	5.13 ± 0.48	4/5	0.79 ± 0.49	2/5
7 weeks LIN, Kramnik	4.97 ± 0.68	9/9	3.44 ± 0.36	9/9
7 weeks PZA, Kramnik	6.57 ± 0.44	9/9	4.36 ± 0.21	9/9
7 weeks MET, Kramnik	7.50 ± 0.42	5/5	4.86 ± 0.12	5/5

[a]Data are Log_{10} CFU counts in the lung and spleen.
[b]n/N, number of mice that yielded viable CFU data (n) over the total number of mice that group (N).

2.3.2 Histopathology of the Kramnik mouse model throughout disease progression

At the initiation of drug treatment, the Kramnik mice had small foci of mixed inflammation composed primarily of lymphocytes and macrophages (Figure 2.1A). In the early stages of cell necrosis, macrophage and lymphocytes were accompanied by infiltrates of granulocytes within alveolar spaces (Figure 2.1B). Necrotic foci expanded in size rapidly between 6 and 10 weeks after aerosol infection. The accumulation of necrotic and fragmented

nuclei within the alveolar spaces is evident by basophilic staining with the progression of disease.

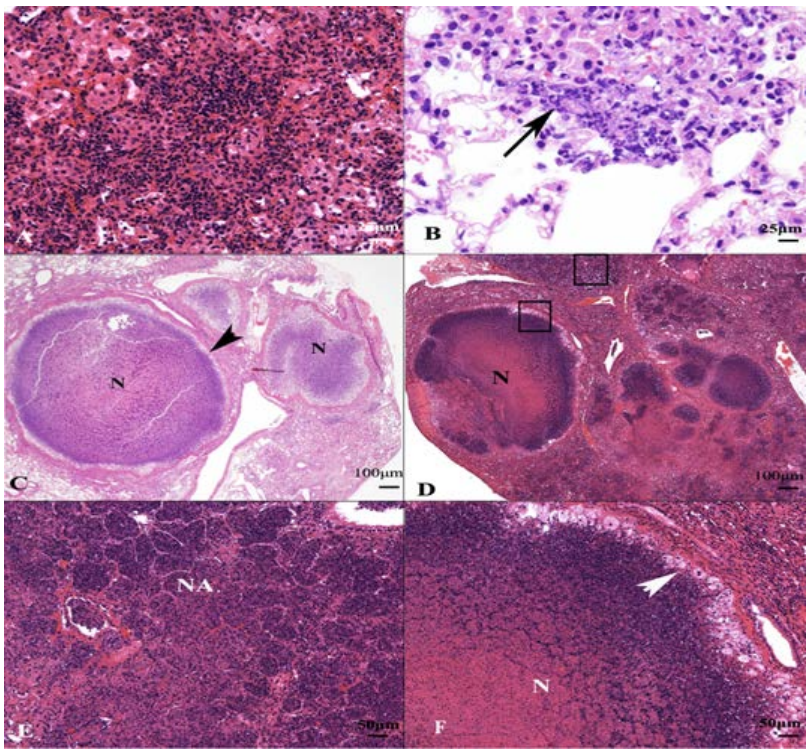

Figure 2.1. Experimental infection of C3HeB/FeJ mice with the Erdman strain of *M. tuberculosis* progresses to form expansive lung lesions with liquefactive necrosis. (A) Non-necrotic lung lesions in the early stages of development are composed primarily of lymphocytes and foamy macrophages (B) With the progression of disease, there is early neutrophil infiltration centered around small foci of lesion necrosis (arrow). (C) At 10 weeks of infection, multiple lesions with central liquefactive necrosis (N) are delineated from the more normal parenchyma by a fibrous capsule (arrowhead). (D) At 13 weeks of infection necrotic lesions extend into the surrounding parenchyma (upper inset) and coalesce. (E) A higher magnification image from upper inset in D, shows severe necrotizing alveolitis (NA) delineated by remnants of intra-alveolar septal walls. (F) A higher magnification image within the lower inset in D showing a fibrous capsule delineating compressed lung parenchyma (upper right corner) from a layer of foamy macrophages (white arrow) and central liquefactive necrosis (N). Stain: Hematoxylin and Eosin.

At 10 weeks of infection, necrotic lesions were demarcated from more normal parenchyma by a capsule of fibrous connective tissue (Figure 2.1C). Besides encapsulated lesions, the alveoli filled with necrotic debris (necrotizing alveolitis) but the inter-alveolar septae were often intact. (Figure 2.1D, E). By 13 weeks of infection, an inner layer of foamy

macrophages separated the necrotic core from the fibrous capsule. Therefore in the Kramnik mouse, two distinct lesion types emerged in the lung, those being encapsulated lesions with liquefactive necrosis (Figure 2.1F), and the more extensive but unencapsulated necrotizing alveolitis (Figure 2.1E). Occasionally, the encapsulated lesions developed central cavities (Figure 2.2D) lined predominately by granulocytes (Figure 2.2E). Other pathology features seen were individual cell necrosis with intracellular and extracellular cholesterol clefts (Figure 2.2C), and the proliferation of blood filled vessels at the periphery of the lesions indicative of early neo-angiogenesis (Figure 2.2A and 2.2B).

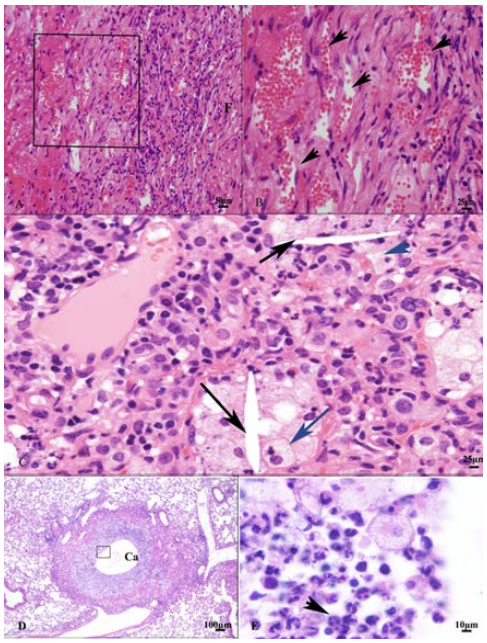

Figure 2.2. Other manifestations of experimental Erdman infection of C3HeB/FeJ mice include neovascularization, individual foamy macrophage necrosis, cholesterol cleft formation and cavitary lesions. (A) Higher magnification of the fibrous capsule from a lung lesions with liquefactive necrosis shows an increase in blood filled capillaries and infiltrates of mixed inflammatory cells. (B) A higher magnification of the region depicted by the square in A showing numerous blood filled capillaries (arrowheads). (C) Besides liquefactive necrosis, lesions have individual foamy macrophage (blue arrow) necrosis with intracellular and extracellular cholesterol clefts (black arrow). (D) Encapsulated lesions with liquefactive necrosis occasionally have central cavitation (Ca). A higher magnification image of the inner surface of the cavitary lesions depicted by the square in D showing a dense accumulation of neutrophils (arrow) admixed with foamy macrophages and lymphocytes. Stain: Hematoxylin and Eosin.

Picrosirius red staining was used to visualize new and established collagen fibrils within the fibrous capsule surrounding necrotic lesions [221]. The Picrosirius stains established a mixture of collagen deposits with thick (1.6-2.4 microns) fibrils that stained dark red/orange, and thin fibrils (0.8 micron or less) that stained bright yellow/green in the later stages of infection (Figure 2.3A, B).

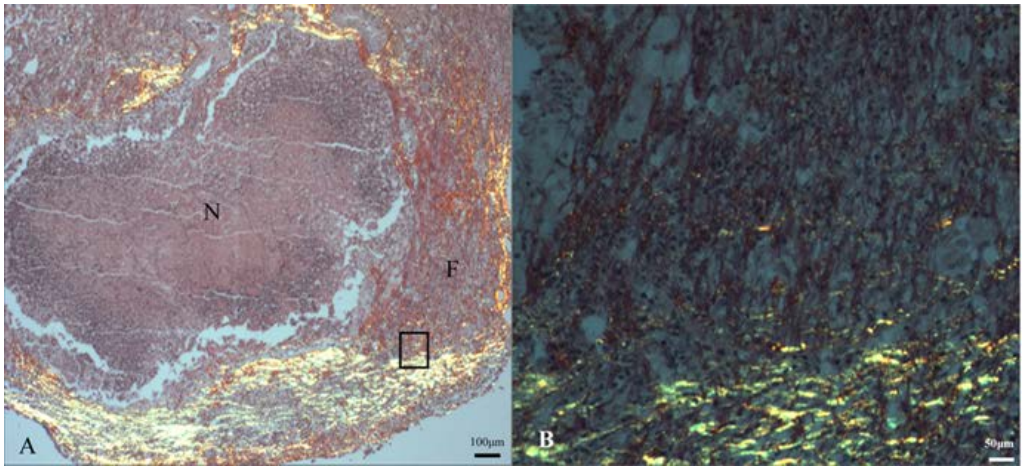

Figure 2.3. Lung lesions with liquefactive necrosis from C3HeB/FeJ mice experimentally infected with the Erdman strain of *M. tuberculosis* are delineated by fibrous connective tissue. (A) Newer, immature collagen fibrils (F) are admixed with more mature collagen (yellow, birefringence). (B) A higher magnification image of the fibrous capsule depicted by the rectangle in (A) showing both immature collagen fibrils (yellow, birefringence) and mature collagen fibers (red staining). Stain: Picrosirius red.

2.3.3 Histopathology of the Balb/c mouse model throughout disease progression

At the initiation of treatment (2 weeks after high dose aerosol), Balb/c mice had small foci of inflammation composed predominately of lymphocytes and smaller accumulations of epithelioid macrophages with no evidence of necrosis. To evaluate the response to the high dose aerosol infection, several untreated animals were euthanized at three and four weeks following infection, which is the time the first mice succumbed to disease. At three-weeks, larger foci of inflammation were accompanied by early individual cell necrosis that occupied approximately

5% of the lung lobe evaluated. Necrotic cells were characterized by nuclear fragmentation (karyorrhexis) and an increase in foamy macrophages. By four-weeks, approximately 15% of the lung parenchyma from Balb/c mice had developed multifocal to coalescing foci of granulomatous inflammation with scattered foci of necrosis (data not shown).

2.3.4 Acid-Fast staining by Kinyoun and Auamine-Rhodamine

Kinyoun Carbol-Fuchsin staining is an acid fast staining technique also used clinically as an alternative to Ziehl-Neelsen [222]. At every stage of infection, the Kinyoun staining method stained high numbers of bacteria in the Kramnik mouse lungs throughout the progression of disease (Figure 2.4). At 6 weeks, primarily extracellular bacteria were concentrated within necrotic lung lesions (Figure 2.4A). Few intracellular bacilli were within foamy macrophages within alveoli and within the necrotic center adjacent to the fibrous capsule. At 10 and 13 weeks of infection, the Kinyoun stain continued to detect very high numbers of extracellular bacilli within the necrotic lung lesions (Figure 2.4B, C).

The Auramine-Rhodamine (AR) stain combined with DAPI and Hematoxylin was also used to visualize acid-fast MTB within the surrounding tissue by fluorescence microscopy. Over the course of the disease in the Kramnik mouse model, AR gradually stained fewer bacteria (as seen in Figure 2.4D, E, and F). This gradual decrease in AR staining is first seen in the center of the necrotic lesion, which then expanded outward ultimately resulting in the majority of bacteria becoming AR negative (Figure 2.4F). At 6 weeks of infection, pockets of intracellular bacilli were seen in inflammatory foci composed of lymphocytes and foamy macrophages (Figure 2.4D). At 10 weeks of infection, extracellular, AR positive bacilli were concentrated at the rim of the necrotic lesions. Very few small foci of intracellular bacilli can be found on the outside of

collagen rim (Figure 2.4E, insert 1 and insert 2). At 13 weeks of infection, few AR positive bacilli were seen within or outside the lesion (Figure 2.4F and inset).

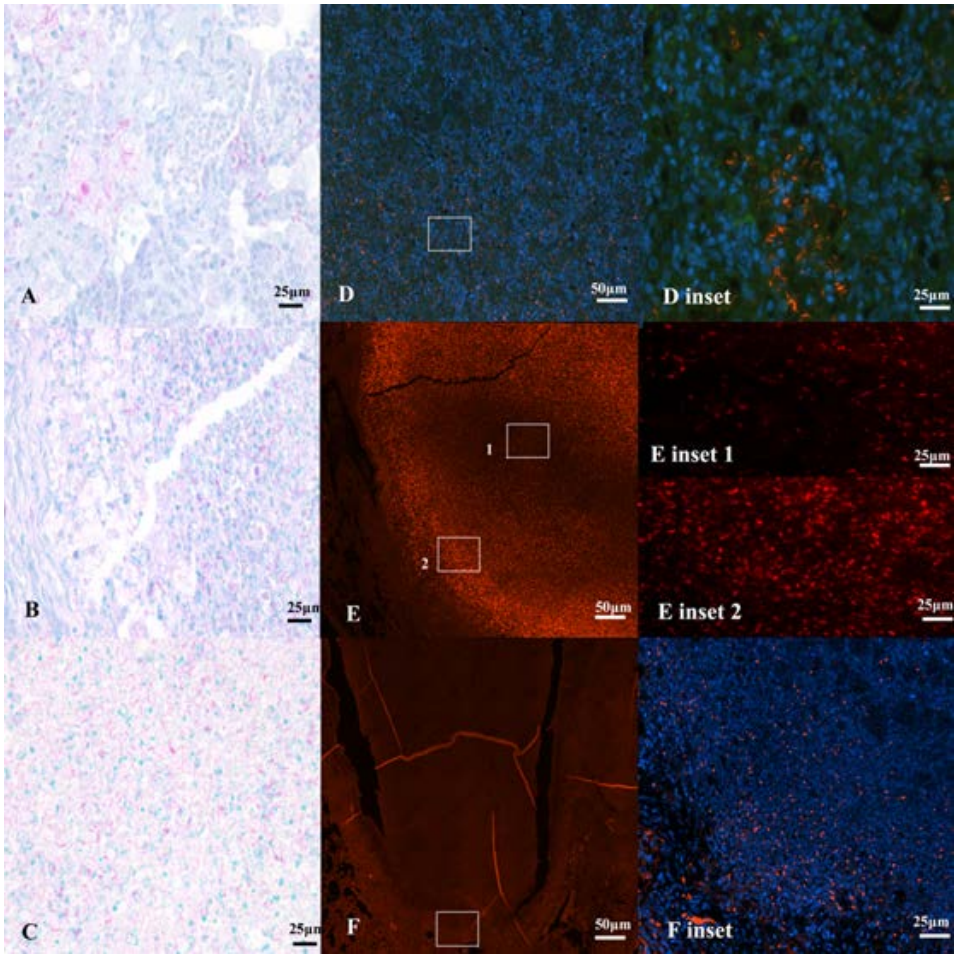

Figure 2.4. Different staining techniques reveal phenotypic differences in bacilli in the late stage of experimental infection of C3HeB/FeJ mice with the Erdman strain of *M. tuberculosis*. Images A and D are serial sections of lesions from mice 6 weeks after infection. B and E are serial sections of lesions from mice 10 weeks after infection and C and F are serial sections of lesions from untreated control mice at 13 weeks after infection. Kinyoun stained sections A, B and C detect numerous intra and extracellular bacilli. (A) At 6 weeks of infection, bacilli are primarily intracellular, whereas at 10 weeks (B) the majority of bacteria are located within necrotic granulomas. (C) 13 weeks post infection showing the center of liquefactive necrotic lung lesion positive for AFB. Auramine-Rhodamine stained sections (D), (E), and (F) lose the ability to detect bacilli over infection. (D) At 6 weeks intracellular bacilli are clearly seen. With magnification inset of intracellular staining. (E) At 10 weeks the central region of necrotic granuloma is devoid of fluorescent bacilli. Inset 1, the center of necrotic lesion has reduction in A/R positive bacilli. Inset 2, the edge of the necrotic lesion retains the majority of detectable staining. (F) At 13 weeks the entirety of the necrotic lung lesion is without stain, save the very edge of the rim, depicted in inset.

2.3.5 Pulmonary granulomas in the Kramnik mouse model are hypoxic

The hypoxic nature of necrotic TB granulomas has been reported in other animal models for TB infection, such as guinea pigs, rabbits and NHP [134, 212], but is generally not observed in the mouse model of infection [223]. We evaluated oxygen tension in the Kramnik model using immunohistochemical detection of pimonidazole hydrochloride (Hypoxyprobe) adducts throughout the progression of disease. The use of Hypoxyprobe identified the presence of hypoxic cells around the edges of caseous granulomas when performed at 10 and 13 weeks post aerosol infection (Figure 2.5A, 2.5B). The hypoxia staining was more prominently centered around alveolar necrosis in areas of pulmonary pneumonia (Figure 2.5C). As the activated intermediate of pimonidazole is only produced within viable cells under conditions of low oxygen tension, the central necrotic tissue does not directly stain with Hypoxyprobe due to a lack of intact, viable cells.

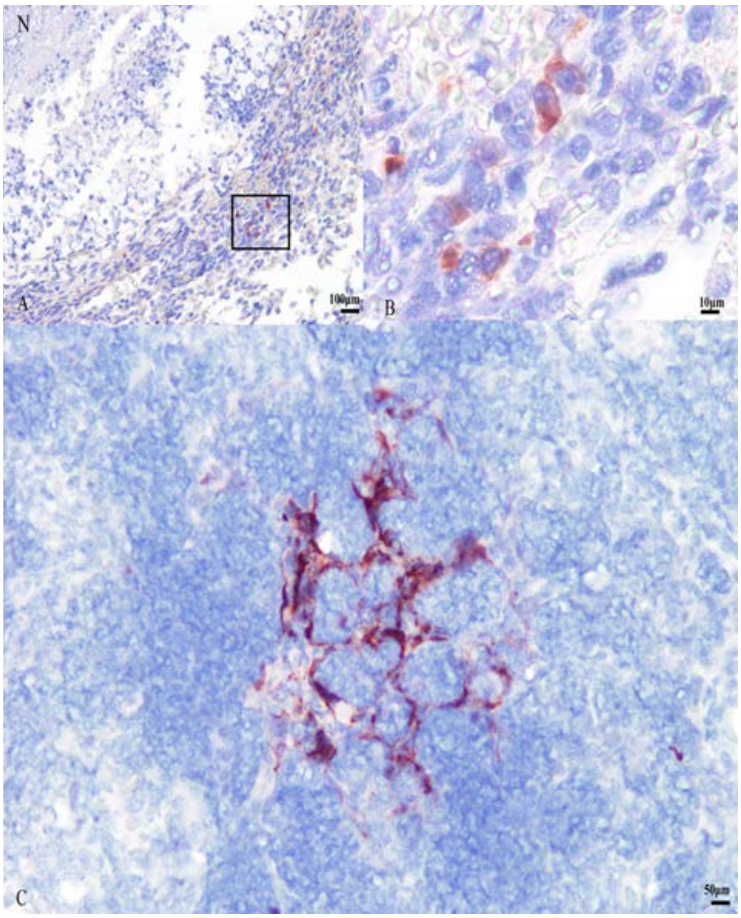

Figure 2.5. Lung lesions with liquefactive necrosis from C3HeB/FeJ mice experimentally infected with the Erdman strain of *M. tuberculosis* show evidence of hypoxia. (A) Immunohistochemical staining for the hypoxia marker pimonidazole within a lung lesion with liquefactive necrosis (N) showing multiple positive stained cells. (B) A higher magnification of the region depicted by the square in (A) showing multiple cells staining positive for pimonidazole adducts. (C) Viable remnants of interalveolar septal walls within a region with necrotizing alveolitis have residual cells that stain positive for pimonidazole. Counter stain: Hematoxylin.

2.3.6 Anti-tuberculosis single drug treatment is less effective in the Kramnik mouse model compared to the Balb/c mouse model

The goal of these experiments was to investigate and compare the killing kinetics of a panel of single TB drugs in the Balb/c and Kramnik mouse models. For the purposes of these experiments, we aimed to achieve similar bacterial numbers in the lungs of both Balb/c and Kramnik mice at the initiation of drug treatment. To achieve this, Balb/c mice were infected with

a high dose aerosol (depositing ~11,000 CFU within the lungs) in order to reach ~10^8 bacilli in the lungs at the start of drug treatment (14 days post infection). This bacterial load is similar to that reached by day 42 in Kramnik mice following a low dose aerosol infection (~80 CFU). Treatment cohorts of Balb/c mice were sacrificed at specific time intervals of 2, 4, 6 and 8 weeks of treatment. Treatment cohorts of the Kramnik mice were sacrificed at specific time intervals of 2, 4, and 7 weeks of treatment. Following aerosol infection but prior to initiating drug treatment, 17 Kramnik mice showed significant weight loss and became moribund as determined by the IACUC regulations. These animals were humanely euthanized and the remaining animals were re-randomized into treatment groups.

All untreated Balb/c mice infected with ~11,000 CFU began to show overt signs of clinical disease (ruffled fur, lethargy, trembling) by 26 days post infection and had to be humanely euthanized. In contrast INH treatment in Balb/c mice showed a significant reduction in the bacterial load in the lungs at all time points versus untreated controls at the start of treatment ($p < 0.0001$; Figure 2.6A). In addition, the bacterial load in the lungs of Balb/c mice continued to decrease statistically for all the time points evaluated ($p < 0.005$). After an initial decrease of approximately 2 Log_{10} CFU in the first two weeks, the bacterial load continued to decrease another 2 logs over the next 6 weeks. When we compared the activity of INH in Balb/c mice with the Kramnik mouse model, the reduction in bacterial load in the lungs was far less pronounced. After 2 weeks of treatment, the Kramnik mice showed a reduction of 1.25 Log_{10} CFU when compared to the untreated controls at the start of treatment ($p = 0.1$; Figure 2.6B). While after 4 and 7 weeks of treatment, the reduction in the bacterial load in lungs was smaller versus the untreated controls at the start of treatment ($p = 0.09$ and $p = 0.5$ respectively). Comparison between treatment time points revealed no significant change in the Kramnik mouse

model over time. Evaluation of Balb/c and Kramnik mice by two-way ANOVA revealed highly significant differences in the lungs following INH treatment ($p < 0.001$).

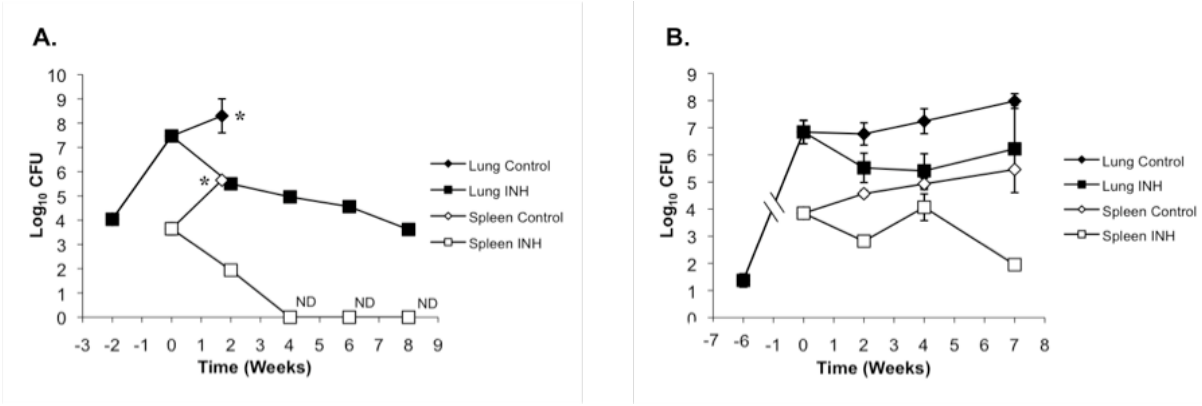

Figure 2.6. Isoniazid (INH) treatment at 25 mg/kg is less effective in C3HeB/FeJ mice against the Erdman strain of *M. tuberculosis* as compared to the Balb/c mouse strain. (A) In Balb/c mice the reduction in CFUs in the lung (filled symbols) and spleen (open symbols) was biphasic, whereas, in the C3HeB/FeJ mouse strain (B) the killing kinetics in the lung were attenuated as was the efficacy in the spleen. (*) Untreated control mice were euthanized at day 26 due to morbidities. (ND) No bacterial colonies detected; detection limit = 50 CFU.

In spleens, INH treatment was highly effective for Balb/c mice resulting in a non-culturable state at 4 weeks of treatment. At all time points the reduction in bacterial load was highly significant when compared to untreated controls at treatment start ($p < 0.0001$; Figure 2.6A). In the Kramnik mouse model, there was a reduction in spleens, however it failed to reach a non-culturable state. The decrease in the bacterial load in the spleen only became significantly different from the untreated controls at the start of treatment after 7 weeks of INH therapy (Figure 2.6B). Surprisingly, after 4 weeks of treatment the bacterial load was higher than that observed after 2 weeks ($p < 0.05$).

Treatment with RIF showed very similar killing kinetics as the ones described for INH. After the initial 2 weeks of RIF treatment, Balb/c mice showed a reduction of the bacterial load in lungs of 2.36 logs versus untreated controls at the start of treatment ($p < 0.0001$). The bacterial load in the lung continued to decrease at a highly significant rate throughout RIF treatment

(Figure 2.7A), except for the 6 and 8 week treatment interval when there was no statistically significant decrease in log CFU ($p = 0.8$). After an initial decrease of ~2.5 Log_{10} CFU in the first two weeks, the bacterial load continued to decrease another 2 logs over the next 6 weeks. After 2 weeks of RIF treatment, the Kramnik mice showed a reduction in bacterial load of 1.47 logs ($p < 0.01$), and after 4 weeks the bacterial number only decreased another ~1 Log_{10}, totaling a 2.43 log reduction versus the untreated controls at the start of treatment ($p < 0.005$; Figure 2.7B). At the final sacrifice point for the Kramnik mouse model, the results showed a significant reduction versus the untreated controls (reduction of 2.85 logs; $p < 0.05$) but there was not a significant change between 2, 4 and 7 weeks of treatment. There was no significant difference seen between Balb/c and Kramnik mice at the 2 week time point, however, for the subsequent timepoints the treatment results for Balb/c and Kramnik mice were significantly different ($p < 0.001$).

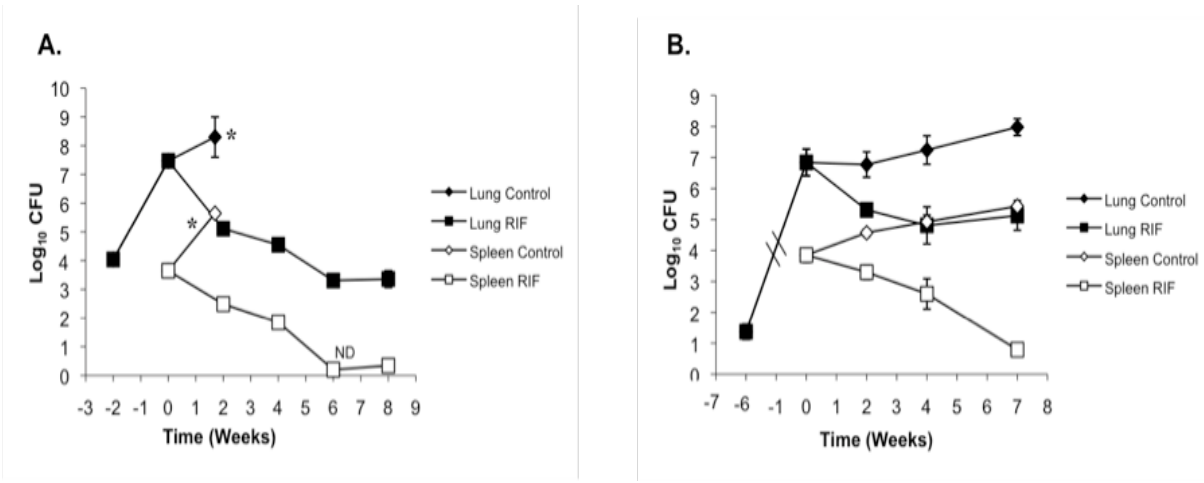

Figure 2.7. Rifampin (RIF) treatment at 10 mg/kg is less effective in C3HeB/FeJ mice against the Erdman strain of *M. tuberculosis* as compared to the Balb/c mouse strain. (A) In Balb/c mice the reduction in CFUs in the lung (filled symbols) and spleen (open symbols) was biphasic, whereas, in the C3HeB/FeJ mouse strain (B) the killing kinetics in the lung were attenuated as was the efficacy in the spleen. (*) Untreated control mice were euthanized at day 26 due to morbidities. (ND) No bacterial colonies detected; detection limit = 50 CFU.

In spleens, similar results were obtained for RIF as those described for the lungs however they were less pronounced. Treatment with RIF was highly effective in the spleens of Balb/c

mice resulting in a non-culturable state at 6 weeks of treatment (only 1 colony was observed in one mouse at 8 weeks). For all time points of the Balb/c mice, the CFU were significantly reduced when compared to untreated controls at the start of treatment ($p < 0.0001$; Figure 2.7A). For the Kramnik mouse model, the spleens also showed a more gradual decrease in the bacterial load over time with a dramatic decrease at the 7-week time point being the only statistically significant time point compared to pretreatment controls ($p < 0.0001$; Figure 2.7B). However, the Kramnik mice failed to reach a non-culturable state. Balb/c and Kramnik mice were not significantly different throughout the course of treatment when compared by two-way ANOVA.

For LZD, superior killing kinetics was observed in Balb/c mice versus Kramnik mice in lungs; however the activity in spleen was static in both mouse models. At all time points throughout the experiment there was an insignificant decrease in the lung bacterial load in the Balb/c strain when compared to the untreated controls at treatment start and between treatment groups. In the Kramnik mouse model there was a lack of significant drug activity early on (after 2 and 4 weeks of treatment) versus the untreated controls at the start of treatment. After 7 weeks of LZD treatment, a significant increase in activity was observed in the Kramnik mice with a bacterial log reduction of 1.85 logs compared to the untreated controls at the start of treatment ($p < 0.005$). Comparison between treatment groups demonstrated a slight reduction in bacterial load from 2 weeks to 7 weeks of treatment ($p < 0.05$) as the activity of LZD increased over time in the Kramnik mouse model. Comparison by two-way ANOVA showed that the Balb/c and Kramnik mice were significantly different throughout infection ($p < 0.01$).

LZD treatment showed in the spleens of Balb/c mice an initial increase of 0.6 logs in bacterial load compared to the untreated controls at the start of treatment ($p < 0.01$) at 2 weeks, but showed no additional statistically significant change after this (Figure 2.8A). For the

Kramnik mice, the bacterial load in the spleen initially showed an increase, followed by a continued decrease at every time point after the start of treatment, none of which were statistically significant when compared to the start of therapy (Figure 2.8B). Spleen data in Balb/c and Kramnik mice were not significantly different throughout the course of treatment when compared to each other through two-way ANOVAs.

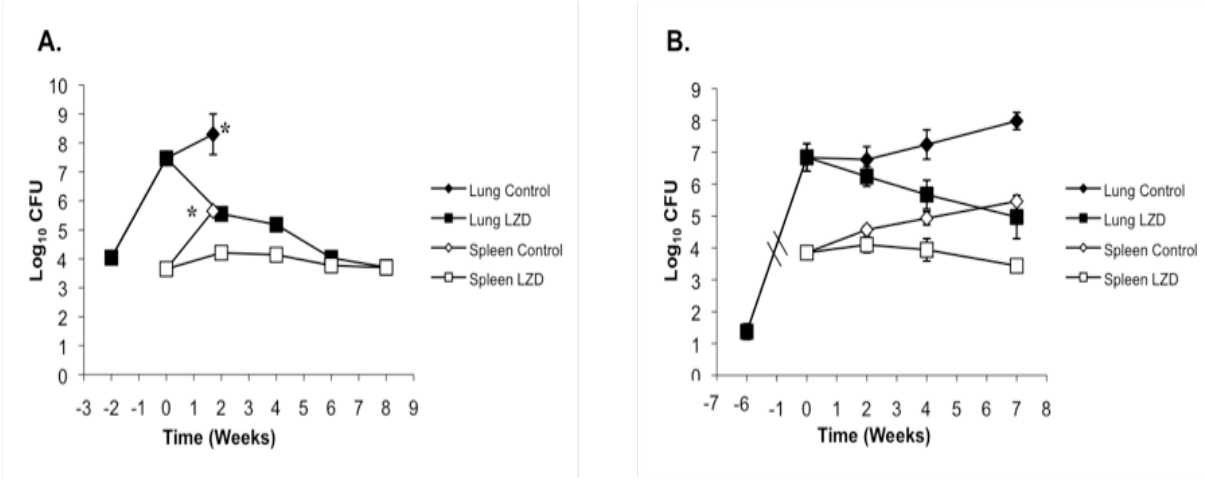

Figure 2.8. Linezolid (LZD) treatment at 100 mg/kg is less effective in C3HeB/FeJ mice against the Erdman strain of *M. tuberculosis* as compared to the Balb/c mouse strain. (A) In Balb/c mice the reduction in CFUs in the lung (filled symbols) and spleen (open symbols) was biphasic, whereas, in the C3HeB/FeJ mouse strain (B) the killing kinetics in the lung were attenuated as was the efficacy in the spleen. (*) Untreated control mice were euthanized at day 26 due to morbidities.

In the lungs, PZA had highly significant activity in Balb/c mice at 2, 4, 6, and 8 weeks of continuous treatment ($p < 0.0001$) when compared to the untreated controls from the start of treatment (Figure 2.9A). When comparing the activity over the different treatment times, there was a significant change ($p < 0.01$) in bacterial load between week 2 and 4 of treatment, whereas the reduction was not statistically significant when comparing treatment groups at 4 versus 8 weeks ($p > 0.5$). In the Kramnik mouse model, there was no significant change in the bacterial load in the lungs over 7 weeks of treatment ($p > 0.5$). The untreated controls of the Kramnik

mouse model continued to have an increase in bacterial load of about 1 Log_{10}CFU in lungs, resulting in a statistically significant reduction of the bacterial load in the PZA treated mice versus the untreated controls ($p \geq 0.03$; Figure 2.9B).

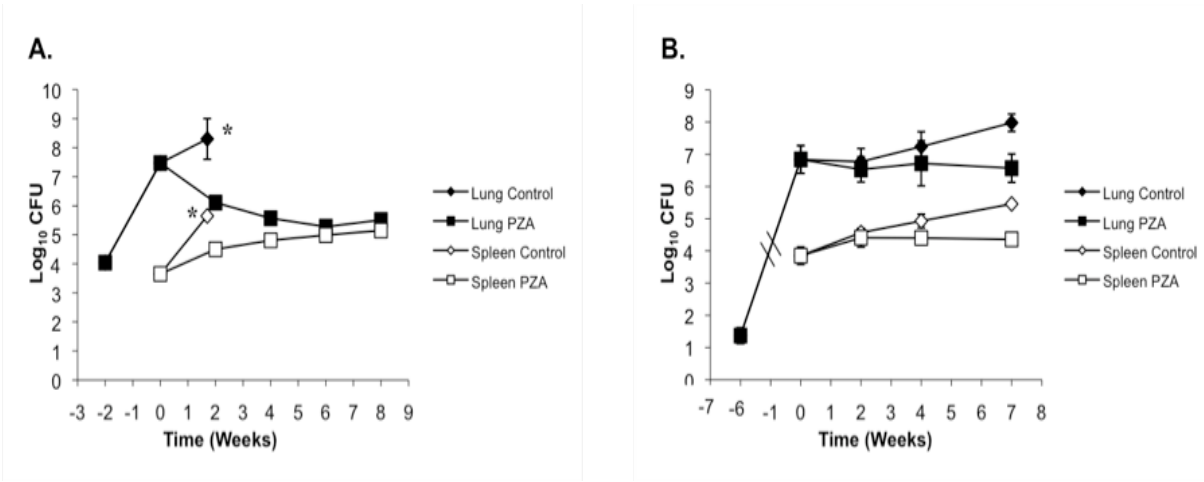

Figure 2.9. Pyrazinoic acid (PZA) treatment at 150 mg/kg is bacteriostatic in C3HeB/FeJ mice against the Erdman strain of *M. tuberculosis* as compared to the Balb/c mouse strain. (A) In Balb/c mice the reduction in CFUs in the lung (filled symbols) and spleen (open symbols) was more pronounced in the early stages of infection but was less effective late. (B) PZA treatment of C3HeB/FeJ mice prevented the progressive bacterial growth seen in control animals (diamonds) and therefore was bacteriostatic in the lung and spleen. (*) Untreated control mice were euthanized at day 26 due to morbidities.

In the spleens of Balb/c mice, PZA treatment showed an initial non-significant increase in bacterial load after 2 weeks (+ 1 Log_{10} CFU), followed by a significant increase at each subsequent time point versus the untreated controls at the start of treatment ($p < 0.01$). At the end of 8 weeks of treatment the bacterial loads in spleens in Balb/c mice showed a highly significant increase (+1.5 Log_{10} CFU) from untreated controls at the start of treatment ($p < 0.001$; Figure 2.9A). In the Kramnik mouse model, PZA activity was not significant at any time point throughout the experiment versus the untreated controls at the start of treatment. There was a ~0.5 Log_{10} CFU increase from the start of treatment to 2, 4 and 7 weeks of therapy, which then remained stable at about 4.4 Log_{10} CFU ($p \geq 0.1$). Comparing the data from Balb/c and Kramnik

mice by means of two-way ANOVAs throughout infection showed a highly significant difference in the lung ($p < 0.005$) and a non-significant result in the spleens of both mouse models.

MET was administered at a high dose of 200 mg/kg in order to maximize the chance of observing drug activity. Previously reported pharmacokinetic data by others described that 15 mg/kg MET was sufficient to reach 4.6-11.3 mg/ml peak serum concentration similar to humans [224-226]. MET did not show any activity in lungs and spleen in both the Balb/c and Kramnik mouse models. Due to the lack of significant activity, Balb/c mice infected by a high dose aerosol became moribund after 2 weeks of therapy with MET and required humane euthanasia. Therefore, only the 2 week time point was available to collect data for the Balb/c mice and the results enumerating the bacterial load were not significantly different when compared to untreated control mice (Figure 2.10A). In the Kramnik mice, MET showed no significant reduction in bacterial load when compared to the untreated control groups from the start of treatment ($p \geq 0.2$).

In both the Balb/c and the Kramnik mice, MET treatment showed no observable activity in the spleen. None of the results were statistically significant when compared to the untreated control groups ($p \geq 0.3$; Figure 2.10B).

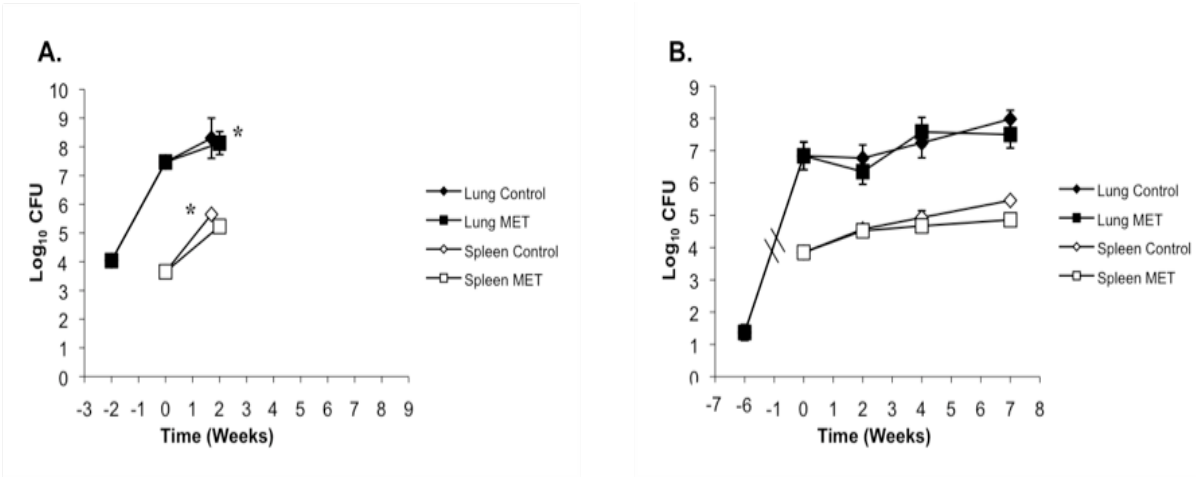

Figure 2.10. Metronidazole (MET) treatment at 200 mg/kg is not effective against the Erdman strain of *M. tuberculosis* in either Balb/c or C3HeB/FeJ mice. (A) In the Balb/c mouse strain MET had no effect in the reduction of CFUs in the lung (filled symbols) and spleen (open symbols) and resulted in early mortality. (B) In the C3HeB/FeJ mouse strain MET had no effect throughout entire study in the lung and spleen. (*) Untreated control mice were euthanized at day 26 due to morbidities.

2.3.7 Kramnik mice have higher numbers of drug resistant colonies

The high bacterial loads in the lungs at the start of drug treatment of both the Balb/c and Kramnik mouse models led us to question whether the frequency of drug resistant mutants would increase following prolonged drug treatment. To quantify drug resistance, serial dilutions of mouse lung homogenates were simultaneously plated on 7H11 agar plates and 7H11 plates containing the drug administered to each group. Balb/c mice (which harbored 7.37 ± 0.09 Log_{10} CFU at the start of drug treatment) showed few resistant colonies over the duration of therapy with INH, RIF or LZD (Table 2.3). At each time point tested for the Balb/c mice, there were only 1-2 animals exhibiting few resistant colonies.

Table 2.3. Numbers of drug susceptible and drug resistant bacterial colonies isolated from lungs[a]

Balb/c Lung Data			Kramnik Lung Data		
Treatment	CFU ± SEM	n[b]/N	Treatment	CFU ± SEM	n[b]/N
Start of Treatment	7.47 ± 0.06	5/5	Start of Treatment	6.85 ± 0.44	5/5
			4 weeks Control 7H11	7.58 ± 0.42	5/5
			7 weeks Control 7H11	8.26 ± 0.52	4/4
6 weeks INH 7H11	4.89 ± 0.09	5/5	4 weeks INH 7H11	4.91 ± 0.67	5/5
6 weeks INH R	0.5 ± 0.5	1/5*	4 weeks INH R	1.26 ± 1.26	1/5†
8 weeks INH 7H11	3.99 ± 0.07	5/5	7 weeks INH 7H11	5.72 ± 1.11	5/5
8 weeks INH R	0.5 ± 0.5	1/5*	7 weeks INH R	4.47 ± 1.83	3/5
6 weeks RIF 7H11	3.53 ± 0.06	5/5	4 weeks RIF 7H11	4.39 ± 0.64	5/5
6 weeks RIF R	0 ± 0	0/5	4 weeks RIF R	0 ± 0	0/5
8 weeks RIF 7H11	3.37 ± 0.24	5/5	7 weeks RIF 7H11	5.47 ± 0.68	4/4
8 weeks RIF R	0.99 ± 0.61	2/5*	7 weeks RIF R	3.57 ± 1.26	3/4
6 weeks LZD 7H11	4.41 ± 0.07	5/5	4 weeks LZD 7H11	5.47 ± 0.46	5/5
6 weeks LZD R	0 ± 0	0/5	4 weeks LZD R	0 ± 0	0/5
8 weeks LZD 7H11	4.24 ± 0.07	5/5	7 weeks LZD 7H11	4.96 ± 0.94	5/5
8 weeks LZD R	0.68 ± 0.68	1/5‡	7 weeks LZD R	0 ± 0	0/5

[a]Data are Log_{10} CFU counts in the lung. Right upper lung lobes were plated on 7H11 plates with and without drugs (INH 4 mg/mL, RIF 0.4 mg/mL and LZD 8 mg/mL). The last two treatment time points for both Balb/c and Kramnik models were plated on drug containing plates.
[b]n/N, number of mice that yielded viable CFU data (n) over the total number of mice that group (N).
(*) Indicates only 1 colony per 1 mouse detected.
(†) Indicates 1 mouse with a high number of colonies, a potential outlier.
(‡) Indicates 1 mouse with 8 colonies

The Kramnik mouse model (which had 6.85 ± 0.44 Log_{10} CFU at the start of drug treatment) showed a dramatic increase in resistant colonies from 4 weeks to 7 weeks of single drug treatment. After treatment with INH for 4 weeks, one mouse out of 5 showed a small number of resistant colonies, whereas after 7 weeks of treatment 3 of 5 mice had a large number (4.47 ± 1.83 Log_{10} CFU) of resistant colonies. Treatment with RIF resulted in the presence of resistant colonies only after 7 weeks on treatment; in which 3 of 4 animals exhibited 3.57 ± 1.26

Log_{10} CFU of resistant colonies. Throughout the duration of treatment with LZD, non-culturable resistant colonies were observed in the Kramnik mice (Table 2.3). For PZA, drug resistance was not evaluated by culturing due to the difficulty of observing robust PZA activity on drug containing plates [227].

2.4 – DISCUSSION

In this study, we compared the response of the novel C3HeB/FeJ Kramnik mouse model to the more conventional Balb/c mouse model following aerosol infection with MTB and monotherapy using a panel of five clinically relevant drugs. This study was driven by the need for a mouse model of TB infection that more closely mimics the pathology of naturally occurring TB in humans, to facilitate more realistic *in vivo* drug testing against non-replicating or slowly replicating persistent TB.

The most unique feature of the lung lesions that developed in Kramnik mice was the formation of multiple discrete encapsulated lesions with central liquefactive necrosis as well as areas of necrotizing alveolitis. In contrast, the more widely used Balb/c strain of mice developed less extensive foci of mixed inflammatory cells with minimal cellular necrosis. Unlike the Balb/c mouse strain, the Kramnik mouse model showed evidence of lesion hypoxia, fibrosis, liquefactive necrosis, and occasional cavity formation. The use of immunohistochemistry to detect adducts of pimonidazole as an indicator of hypoxia showed that residual viable cells within necrotic lesions were under hypoxic stress at the time points tested. For most late timepoints, pimonidazole staining was most often concentrated in clusters of foamy macrophages rather than areas of liquefactive necrosis. This can be explained either by a lack of viable cells

capable of metabolizing pimonidazole or the regions of liquefactive necrosis being anoxic rather than hypoxic.

A critical component of lung lesions of TB infected Kramnik mice was the deposition of collagen that delineated foci of liquefactive necrosis from more normal lung parenchyma. The picrosirius red staining showed a mixture of mature and immature collagen fibrils suggesting that there was continuous remodeling of the capsule and that the granuloma is therefore a highly dynamic structure which is in contrast to common belief. While not investigated in these studies, the formation of a fibrous capsule is likely under the influence of cytokines and chemokines that promote collagen deposition, an important feature of human TB lesions. Further studies to characterize these important immunological mediators are currently underway.

Another important feature of the encapsulated lesions in the Kramnik model was the accumulation of macrophages with abundant foamy cytoplasm that formed the most inner layer of viable cells (located directly on the inside of the fibrous capsule). Foamy macrophages are not only a consistent feature in multiple animal models of TB but are also present in human TB lesions. The role foamy macrophages play in the pathogenesis of lesion formation or persistence of bacilli is unknown but recent studies suggest that they contribute to the deposition of collagen via the production of GM-CSF [228, 229]. In both Kramnik and Balb/c mice, the accumulation of foamy macrophages was often accompanied by cholesterol deposition. Cholesterol derived from the cell membrane of necrotic host cells forms characteristic clear clefts in microscopy sections. The crystallized cholesterol is solubilized and removed by the fixation process; however, the original location between clusters of foamy macrophages and the site of individual cell necrosis is preserved. It has been shown primarily using *in vitro* cultures that bacilli in microenvironments of hypoxia and nutrient deprivation adapt by altering their metabolism to

utilize lipids [139, 230]. It has been hypothesized that host cholesterol is utilized as an energy source for the bacteria in this inhospitable environment of hypoxia and cellular debris. Studies have shown upregulation of genes for lipid sequestration and metabolism in human patients infected with TB, representing pathogen-mediated dysregulation of host lipid metabolism [230].

Although commonly used as an alternative to the mouse model, evaluating drug therapy in the guinea pig model, which develops necrotic granulomas, has presented some challenges. Guinea pigs clear the first-line TB drugs [167] moxifloxacin and PA-824 [210] very quickly [even more rapidly than mice], resulting in the need for much larger drug doses in order to achieve similar drug exposures over time. This leads to substantial drug intolerability, as guinea pigs are especially susceptible to perturbations in the normal intestinal flora caused by broad-spectrum antibiotics. Although many methods have been attempted to add vitamin supplements and probiotics to their diet [162], adverse effects may still occur and could potentially skew study results. Interestingly though, several studies to date have shown that guinea pigs, when compared directly with mice, have greater and faster bacterial killing after drug treatment [157, 162, 210]. This is surprising as one would expect the bacteria within the caseous necrotic lesions of infected guinea pigs to be more drug refractory (due to the slowed metabolism of the bacteria, and/or drug penetration issues) versus the bacilli in the inflammatory lesions of the classical mouse model.

Healing of lesions by dystrophic mineralization, which is a prominent pathological feature in human TB and in the guinea pig TB model [166, 231, 232], is not a response observed readily in the Kramnik mouse model. There are species differences in the rate of mineral deposition and the shortened survival time may explain why mineralization is not seen in the Kramnik and other mouse models of TB.

To visualize the TB bacilli in the lung lesions of the Kramnik mice during disease progression**,** different acid-fast stains were used. In an earlier report, we described a novel triple-staining method which identified TB bacilli as well as the surrounding tissues in the mice and guinea pigs [134]. While the vast majority of bacilli identified in pulmonary lesions of Balb/c mice were intracellular, the majority of bacilli present in the Kramnik mice were extracellular. In addition, comparison of the AR and Kinyoun Carbol-Fuchsin staining methods revealed differences in the number of stained bacteria identified in the Kramnik mouse model over the course of infection. In the Kramnik mice, the bacilli appear to lose their AR acid-fastness as the disease progressed into large hypoxic, liquefactive, necrotic granulomas. The decrease in AR positive bacilli is noticeable starting from the center of the necrotic lesion and continuing outward throughout disease progression until eventually all bacteria within the lesion core become AR negative. This is in sharp contrast with the results obtained after Kinyoun staining where the bacteria within the granulomas remain positively stained over time. Although the exact target of both staining methods is still being debated [136], these results suggest that the lack of detection with AR over time is due to a change in the bacterial phenotype. As AR still stains bacteria under hypoxic conditions *in vitro* [136], as well as in guinea pig lung lesions [134], it is unclear why the particular bacterial population in the Kramnik mice causes these negative staining results. Genetic approaches will be required to examine the changes in the bacterial phenotype in the lungs of the Kramnik mice.

To assess the suitability of the Kramnik mouse model for evaluation of new TB drugs and treatment regimens, the efficacy of a panel of five single drugs was compared in Kramnik mice that form necrotic lesions versus Balb/c mice solely forming non-necrotic or inflammatory lesions. Mice were infected via aerosol with pursuant chemotherapeutic treatment for 7 to 8

weeks. Examination of the bacterial load in the lungs and the spleens revealed that the Kramnik mice had a significantly refractory response to drug treatment using INH, RIF, LZD, or PZA monotherapy when compared to Balb/c mice. This refractory effect in the Kramnik mice was most pronounced for PZA, as PZA treatment was highly effective in the Balb/c mice [99% of bacteria were eradicated in 4 weeks], whereas no decrease in bacterial CFU was observed in the lungs of the Kramnik mice from the start of treatment. At 150 mg/kg, PZA contained the bacterial load in the lungs of the Kramnik mouse model over the course of treatment whereas in the untreated Kramnik controls there was a slowed but continuous growth observed [1 Log_{10} over 7 weeks]. This study was limited as only one single PZA drug dose was tested, and therefore it is possible that a higher drug dose might show clear bactericidal activity *in vivo*. As the lack of PZA activity in the Kramnik mouse model might have significant clinical implications, it will be crucial to investigate a higher dose range in this mouse model. Overall, the data obtained showed that the reduction in bacterial load in the Balb/c model far exceeded the results seen in the Kramnik mouse model. This is in contrast to what we expected from previous *in vitro* data describing PZA as primarily active against persistent bacilli [233]. Earlier *in vitro* data identified some of the conditions required for potentiating PZA activity. Anaerobic conditions have been shown to enhance the activity of PZA, and older cultures of TB are somewhat more sensitive to PZA [234, 235]. PZA is known to show better *in vitro* activity at lower pH [235], and to have better efficacy against intracellular bacilli in the macrophage infection model [236]. To date, limited information is available on what bacterial population PZA may target *in vivo.* A few earlier reports showed activity of PZA against TB using mouse models infected via different routes and with different inoculum sizes (reviewed in [237]). The reason for the failure to observe any cidal activity in the Kramnik mouse model cannot merely be

attributed to the extracellular nature of the bacteria or penetration across the granuloma as PZA has been shown to have activity in the guinea pig model of infection [238]. It is remarkable that the mechanism of action for PZA, one of the three pillar TB drugs, remains largely a mystery after many years. As these results would have significant clinical implications, more studies are required to assess PZA resistance frequencies *in vivo*, evaluate multiple PZA doses, and measure PZA penetration in lung lesions using the Kramnik mouse model.

Metronidazole on the other hand did not show any activity in either mouse infection model even though excessively high doses were administered. MET, a drug which requires anaerobic conditions for activation, has been previously reported to lack demonstrable activity in mice [225, 226] whose lesions fail to become hypoxic [138], but has shown demonstrable activity in rabbits against *M. bovis* [212] and is currently being evaluated in non-human primates. Metronidazole also lacked activity in guinea pigs, but the conclusions were limited due to the increased inflammation in the lung and toxicity of the drug [167]. While there are currently no clinical data confirming the activity of MET in TB patients, the additional evaluation in other animal models might indicate which conditions are required in order to observe MET activity *in vivo*.

In the drug studies described here, the bacillary burden in the lungs of both mouse models was high at the start of treatment [6.85 Log_{10} in Kramnik and 7.45 Log_{10} in Balb/c mice], which increases the likelihood of drug resistance following single drug treatment. To measure the appearance of INH, RIF, and LZD resistance, plating of tissue homogenates was performed on 7H11 agar plates as well as on agar plates containing the respective drugs. Although the bacterial load at the start of treatment in Balb/c mice was approximately four times higher than in the Kramnik model, only few single resistant mutants in a minority of Balb/c mice were observed for

INH and RIF after 6 and 8 weeks. This is in great contrast with the drug resistance observed in the Kramnik mouse model, where we observed a substantial increase in the number of bacilli that were drug resistant after 7 weeks of treatment with INH (up to 4.47 Log_{10} resistant CFU) or RIF (up to 5.72 Log_{10} resistant CFU). The exact reason for the higher number of drug resistant bacteria following treatment in the Kramnik mouse model is not clear, but it is crucial to understand the mechanism as this could have significant clinical implications.

We speculate that the high prevalence of resistant mutants might be due to multiple causes; such as having sub-therapeutic drug exposure levels, a weakened immune response, or an altered bacterial mutation rate in the Kramnik mice. First, due to the highly organized and encapsulated nature of the granulomas observed in the Kramnik mice, it is possible that bacteria within the granulomas received subtherapeutic exposure levels of drug due to poor drug penetration. This could facilitate survival and selection of low level drug resistant mutants in Kramnik mice, which would not be observed in the primarily inflammatory lesions of Balb/c mice. For moxifloxacin, a recent elegant study measured an increased drug distribution in cellular regions of granulomas and uptake by macrophages, but a decreased penetration into the cores of necrotic rabbit lesions [205]. The same was predicted for the standard clinical drugs via a recent mathematical modeling study and confirmed through plasma and tissue pharmacokinetic studies by the same group [239]. A second explanation for the increased frequency of drug resistance in Kramnik mice might be that the precursor mutation frequency in both mouse models is in fact the same, but the immune pressure in the Balb/c mice selectively kills drug resistant mutants which are less fit for *in vivo* survival than their drug susceptible counterparts due to its fully activated immune response. Although the C3HeB/FeJ mice do not have any broadly systemic immune deficiencies, an altered or weakened immune response as the result of

inactivation of the *Ipr1* gene may selectively decrease immune-mediated pressure on drug resistant mutants. Recent studies in athymic nude mice support this finding revealing a remarkable propensity to select drug-resistant mutants. Daily treatment with human-equivalent doses of RIF-INH-PZA for 2 months followed by RIF-INH selected INH-resistant mutants in the majority of mice, and was only prevented by the addition of EMB [240]. In support of this hypothesis, clinical studies of individuals co-infected with HIV and TB, and treated with INH and rifapentine [241] or rifabutin and INH [242] were significantly more likely to develop rifamycin monoresistance, especially in patients with the lowest CD4 T cell counts. Rifamycin resistance is rarely observed in immunocompetent individuals, even under conditions of poor treatment compliance which facilitates the emergence of drug resistance, implicating a positive role for host immunity in suppression of acquired drug resistance. If the weakened immune response of the Kramnik mouse model is the cause of the increased resistant bacterial numbers, the Kramnik mouse model would have the additional benefit of assessing resistance frequencies of single drugs and drug regimens before advancing to clinical trials. Besides efficacy and sterilizing potential of drug regimens, the assessment of the potential for bacterial resistance is the most important criteria for a new regimen. A third explanation, and perhaps the most intriguing one, is the occurrence of a heightened bacterial mutation frequency within the hypoxic regions of necrotic granulomas found in the Kramnik mouse model. Recently, a study using latently infected non-human primates described that hypoxic conditions can suppress the expression of DNA repair enzymes, thereby resulting in higher mutation frequencies [243]. A recent study done by McKinney, et al., that may further complicate determining the cause of INH resistance showed that KatG pulses in the presence of INH [33]. This pulsating bursting of KatG expressions creates divergent populations of bacilli that can and cannot be killed by INH

independent of replication. Further studies examining the specific mutations of the drug-resistant colonies and the mutation frequencies at different times following treatment are necessary to answer these questions, and are currently underway. Spontaneously resistant mutants will be isolated and sequenced, and compared to published mutations observed *in vitro* and in clinical isolates. This will allow us to assess the frequency of each mutation and to determine whether a loss of fitness is observed for some of the selected mutants *in vivo*. For instance certain frequent *katG* mutants isolated from clinical specimens can only be collected *in vitro* but are not observed in the classical mouse model or in the guinea pig [157].

Mice have many advantages as an animal model for preclinical screening of desperately needed anti-TB drugs, and the Kramnik mouse model in particular, has unique pathologic features that have similarities to human TB. Based on the morphologic features and the host-pathogen relationship, the Kramnik mouse model has a critical advantage over the more commonly used mouse strains to evaluate novel preclinical therapies against persisting bacteria. Another advantage of using the Kramnik mouse compared to other larger species is that parallel drug killing kinetics can be achieved using an acute (Balb/c; actively replicating bacteria) and chronic (C3HeB/FeJ; slowly replicating bacteria) mouse model which will generate useful information regarding the *in vivo* pharmacodynamics of a drug in both models. This information may well prove essential for screening novel drugs against persistent, slowly replicating bacilli, and can be used to further define the role poor drug penetration has in failed drug responses. To our knowledge this is the only small animal model that can provide this at this point. Moreover, the Kramnik model minimizes the need to reevaluate PK kinetics and perform cross-species bridging experiments [157, 167, 210].

In these studies we showed that the Kramnik mouse responded to aerosol infection with the formation of hypoxic, encapsulated lung lesions with liquefactive necrosis, which contained numerous extracellular bacilli that were less susceptible to drug therapy as compared to Balb/c mice. In contrast, Balb/c mice developed less extensive foci of mixed inflammatory cells that harbored primarily intracellular bacilli and had minimal individual cellular necrosis. Using these two models we examined the effect lesion morphology had on the response to treatment with a panel of clinically relevant TB drugs that differed in their mode of action. Enumeration of the pulmonary bacterial load showed that most single drugs tested were highly effective in the Balb/c mouse model with primarily intracellular bacilli, whereas Kramnik mice had mostly extracellular bacilli that were refractory to treatment. Overall, the results from the experiments presented here demonstrate that the Kramnik mouse model has great promise to evaluate novel preclinical drugs in a more stringent animal model possessing liquefactive necrotic granulomas containing persistent bacteria.

2.5 – FUNDING

This work was supported by the Bill and Melinda Gates Foundation under Drug Accelerator grant ID number 42589, “Assay Standardization.” and the National Institutes of Health (NIH) Contract NO1 AI-95385 at Colorado State University, Fort Collins

CHAPTER 3 – COMPREHENSIVE ANALYSIS OF THE PROGRESSION OF DISEASE IN THE NECROTIC GRANULOMA MICROENVIRONMENT OF C3HEB/FEJ MICE INFECTED WITH *MYCOBACTERIUM TUBERCULOSIS*

3.1 - INTRODUCTION

Mycobacterium tuberculosis (MTB) is the causative agent of the highly insidious disease tuberculosis that infected 8.4 million new people and killed 1.4 million in 2011 alone [2]. According to the World Health Organization, progress has been made in both the treatment and control of tuberculosis (TB); however, the overall burden remains a substantial obstacle to eradication [2]. Current therapy consists of a multi-drug cocktail administered up to 9 months for susceptible TB. While the current treatment regimen is effective against drug susceptible tuberculosis when followed completely, it is cumbersome for patients and often results in noncompliance [244]. Many of the TB drugs were discovered more than 50 years ago, just recently great strides have been made in drug discovery with a new TB drug being approved for use in MDR-TB patients, Bedaquiline (BDQ) by Johnson and Johnson [9, 10]. According to the last report of the Working Group for New TB Drugs (June 2013), there are currently 21 drugs in the pipeline ranging from animal model preclinical testing to Phase III clinical trials. The renewed effort to develop effective and safe drugs for the expedient treatment of TB has also required a thorough evaluation of current animals models used in preclinical development to evaluate and prioritize these compounds as single agents as well as drug combinations.

TB is a uniquely difficult disease to model in animals due to the heterogeneity in lesion types and disease manifestation in TB patients. For human pulmonary TB, a true hallmark of active disease is the encapsulated caseous necrotic granuloma and cavity formation [203]. While

NHP may most closely replicate tuberculosis disease (the active as well as the latent disease state), they are prohibitively expensive and are not conducive to large-scale early pre-clinical drug trials [50, 213, 245]. Mice have the distinct advantage of being easy to handle and house, and are economical, allowing researchers to investigate novel compounds as well as multiple drug regimens on a larger scale. However, the most widely used mouse models do not develop the advanced pathology seen in TB patients, and does not form the characteristic encapsulated necrotic granulomas after MTB infection. The standard mouse model forms non-necrotic inflammatory granulomas that contain predominantly intracellular bacteria [134, 160]. Other animal models, such as the guinea pig, develop the necrotic primary granulomas and their lesions trend toward sclerotic healing [246], containing low numbers of bacilli per lesion [167]. Though guinea pigs can develop the desired pathological features they are often intolerant to treatment with broad-spectrum antibiotics [162, 167, 245]. We, and others, described earlier a mouse model that shows remarkable similar lung pathology to that observed in humans when in infected with MTB [131, 181, 192, 200, 247, 248], the so-called Kramnik mouse model. This mouse model, using the C3HeB/FeJ mouse strain, develops liquefactive necrotic encapsulated lesions upon a TB infection [131, 181, 192, 200, 247, 248]. This model gives researchers a rare opportunity to study TB in a heterogeneity of lesions as related to human disease etiology in a small animal model.

The Kramnik mouse is characterized by a *de novo* mutation in the sst-1, super susceptibility to tuberculosis-1 region [193]. In animals that lack a functional sst-1 a large subset of macrophages are non-functional allowing for rapid progression of early infection [195]. There is a significant early inflammatory response with a high numbers of neutrophils infiltrating. Bacteria are shown to reside within the macrophages and neutrophils in mid- to late infection. It

is this large influx of inflammatory cells, which precedes the onset of the necrotic response [131]. Innate immunity appears not to be affected, however, T-cell recruitment is greatly impaired and a strong pro-inflammatory response is being promoted [179]. The Kramnik mouse model when infected with a very low aerosol dose (50-75 CFU/mouse) will develop consistent necrotic lesions 6-8 weeks post aerosol infection [131]. We showed in this earlier publication that the Kramnik mouse model has high numbers of both intracellular as well as extracellular bacilli. The heterogeneity in lesion types observed in the Kramnik mouse model which contain both intracellular and extracellular bacilli per lesion, is again similar to what is seen in human lesions [14]. This model provides an economical alternative of other animal models with necrotic lesions (such as guinea pigs, rabbits, rats and NHP, [50, 155, 162, 175]), most of which have far fewer bacteria numbers per lesion or per gram of tissue [212].

In order to locate and study the bacterial population in the various lesion types, we employed a novel acid-fast staining method that utilizes the same principles as the clinically used auramine-rhodamine fluorescent dye but is significantly more sensitive [249]. Using the fluorochrome Sybr ® Gold (Ryan et al., submitted) in a phenol based diluent; we can reliably stain the majority of mycobacterial phenotypes as compared to other current acid fast staining methods (Ryan et al., submitted). Using the Sybr Gold staining method on *in vitro* samples, we were able to detect 99% of the bacilli in actively replicating, hypoxic and sputum cultures versus auramine-rhodamine (54-74%) and carbol-fuschin (66-85%) staining methods (Ryan et al., submitted). This report is the first in showing the results of this novel Sybr Gold acid-fast staining approach on *in vivo* processed samples by using the dye in Kramnik mouse and human tissues.

The progression of the pathology in the Kramnik mouse model is indicative of changes in the host immune response and the pathogen-host interaction. Most studies evaluating the immune response after a MTB infection were performed in mouse models while evaluating the cytokine profiles systemically in sera or on a whole lung homogenate [72, 77, 250]. More recent studies in non-human primates showed a distinct cytokine microenvironment in individual lesions by using immunohistochemistry and ELISA [24]. They found cellular populations that surround the granuloma that produce specific markers that are reminiscent of germinal centers in lung tissue such as B-lymphocyte markers CD20 and CXCR5. The discrete lesions in the Kramnik mouse model will allow for isolation of specific lesions thereby studying the immune environment and the precise location of immune cells and cytokine production.

Our goal is to give a detailed evaluation of the pathological response of the Kramnik mouse model when infected with MTB. By sampling animals throughout infection, we are able to obtain a comprehensive assessment of the pathological features over time and compare it to known human pathological data. By using the highly sensitive novel acid-fast approach we were able to locate the bacteria throughout infection. By combining the data from the histopathology analysis and from the immunology studies it showed that the early inflammatory response might determine the progression of disease. The Kramnik mouse model seems to show several parallels to human disease in terms of pathology and importance of early, inflammatory neutrophilic response compared to the immunocompetent mouse strains and therefore a reasonable representation of TB disease.

3.2 – MATERIALS AND METHODS

3.2.1 Animals

See Methods in Chapter 2

3.2.2 Bacteria

See Methods in Chapter 2

3.2.3 Aerosol Infection

See Methods in Chapter 2

3.2.4 Enumeration of bacterial load of lungs and spleen

See Methods in Chapter 2

3.2.5 Pathology and microscopy analysis of tissue samples

Infection matched whole lung and spleen samples were collected at necropsy and fixed in 4% paraformaldehyde in phosphate buffered saline (PBS). Tissue sections were embedded in paraffin and sectioned to 5μm thickness. Subsequent tissue sections were mounted on glass slides, deparaffinized and stained either with: Hematoxylin and eosin (H & E), auramin-rhodamine fluorescent stain, Masson's Trichrome collagen stain, or the Sybr Gold fluorescent stain (Ryan et al., submitted) as described below. Sections stained with fluorescence dyes were visualized using a Nikon Intensilight mercury vapor lamp and scanned using a Nikon TE-I motorized microscope controlled by Nikon NIS Elements software (Nikon, Melville, NY) with FITC, TRITC and DAPI filters. Light microscopy sections were visualized using an Olympus

BX41 with Olympus DP70 camera controlled by Olympus DP Software (Olympus, Melville, NY) [131, 136].

3.2.6 Human lung samples

Human lung samples were acquired from Dr. Edward Chan from National Jewish Hospital (Denver, CO). Six anonymized patients with MDR-TB had re-sected lung tissue fixed and embedded in paraffin blocks.

3.2.7 Staining procedures

At each terminal sacrifice, the whole mouse lung lobes were infused with 4% paraformaldehyde (EMS, Hatfield, PA) and preserved for 48 hours in paraformaldehyde, then washed and kept in 70% ethanol until processed for histopathological assessment. The novel acid-fast staining method using the Sybr Gold fluorescent dye was used as previously described by our laboratory. Briefly, the dye is diluted 1:1000 in a stain solution of phenol (8 g), glycerin (60 mL), isopropanol (14 mL), and distilled water (26 mL). The slides were heated on a block at 65^{o}C for 5 minutes and then cooled at room temperature for an additional 5 minutes. The tissue sections were washed with acid alcohol (0.5% HCL, 70% isopropanol, 29.5% water) for three minutes, then washed with water and counterstained with Hematoxyin QS for 5-10 seconds. The excess hematoxyin was washed away with ddH2O and slides were subsequently stained with DAPI (200 ng/mL final concentration) ~10 minutes and washed again with water. Slides were mounted with Prolong Gold antifade mounting media.

Collagen was stained in the mouse tissue sections using the Masson's Trichome Kit (American MasterTech, California) using the manufacturer's procedure. Briefly, tissue sections

were dewaxed in xylene and rehydrated through a grades alcohol series. The sections were briefly rinsed in water and heated at 56^{o}C for 1 hour with Bouin's Fluid. Slides were washed then stained with Weigert's Hematoxylin. Rinse slides, stain in Biebrich Scarlet-Acid Fuchsin for 15 minutes, after which they were rinsed. Slides were stained with phosphomolybdic / phosphotungstic acid for 5 minutes and placed directly into Aniline Blue stain for 10 minutes, then rinsed. Slides were then placed in 1% acetic acid for 3 minutes followed and dehydrated by a graded alcohol series and xylene. Slides were hard mounted with Surgipath MM24 Mounting Media (Leica Biosystems, Richmond VA).

3.2.8 Cytometric Bead Array Analysis

For this experiment, five infected C3HeB/FeJ mice (10 weeks after low dose aerosol infection) and 5 naïve C3HeB/FeJ mice were used and organs were aseptically collected. Tissue from whole lung, isolated granulomas, infected lung tissue without gross lesions (non-granulomatous), spleen, lymph nodes, and serum from each animal were collected. Tissues were disrupted using the Bullet Blender from Next Advance (Avervill Park, NY). Cytokine profiles were measured by using the mouse inflammation CBA kit from BD Biosciences (Franklin Lakes, NJ), which analyzed IL-6, IL-10, IL-12, TNF-α, IFN-γ, and MCP-1. A FACSCanto II and FloJo software were used for analysis. The cytokine levels of samples were calculated by extrapolating the mean fluorescence intensity (MFI) by using the standard curves for every cytokine respectively.

3.2.9 Immunohistochemistry

Paraffin embedded blocks from each group of mice were cut in sections of 5-7 μm using a microtome and placed onto slides. Thereafter, the paraffin was removed from the tissue sections using EZ-DeWax solution (Biogenex Lab, San Ramon, CA) and were rehydrated by passing the sections through graded ethanol solutions and finally transferred into a bath containing PBS. Following this step, sections were washed and after blocking the tissue endogenous peroxidase with Peroxidased 1 (Biocare, CA) during 5 min at room temperature. Thereafter the sections were treated with antigen retrieval using the citrate buffer (Dako, CO) and pressure cooker standard procedure. The unspecific binding of antibodies was blocked by incubating the sections for 5 mintues at room temperature in background eraser (Biocare, CA) and then each section was incubated overnight at room temperature with a primary antibody raised against murine F4/80, lysozyme, and IL-10 antigens. After washing the slides three times for 5 min in PBS at RT, the slides were incubated again with the appropriate secondary antibody for 60 min at RT. Thereafter the specific antibody binding reaction was amplified using one of the Tyramide Signal Amplification (TSA) system using a kit purchased from PerkinElmer Life and Analytical Sciences Inc, (Boston, MA). This step was done with an adaptation of the manufacturer's instructions, briefly, when the TSA system was performed, after incubation with the secondary antibody, the sections were incubated with strept-aviding conjugate to horseradish peroxidase (SA-HRP) at a dilution 1/100 for 30 min at RT followed by a 2 min incubation at RT with the biotinylated TSA reagent. After the amplification step, the slides were washed and incubated again for 5 min with the chromogen substrate for HRP either 3,3'-diaminobenzidine (Impact DAB; VectorLab, MI) or aminoethycarbazole (Impact AEC; VectorLab, MI). Finally the slides were counter stained by immersing the sections for 1 min in Mayer's Hematoxylin

(DakoCytomation, Carpenteria, CA) and mounted for microscopic observation using coverslip and Histomount mounting media (Zymed, San Francisco, CA). As a negative control the procedure described above was also carried out omitting the primary antibody step. Sections were examined using an Olympus X70 microscope.

3.2.10 Statistical analysis

See Methods in Chapter 2

3.3 - RESULTS

3.3.1 Survival of mice after M. tuberculosis Erdman infection

When infected with MTB, the C3HeB/FeJ mouse strain showed a wide range of outcomes in terms of disease progression. Between 25-42 days post aerosol infection, 25-40% of the infected animals progress with rapid disease, and will succumb to disease (Figure 3.1).

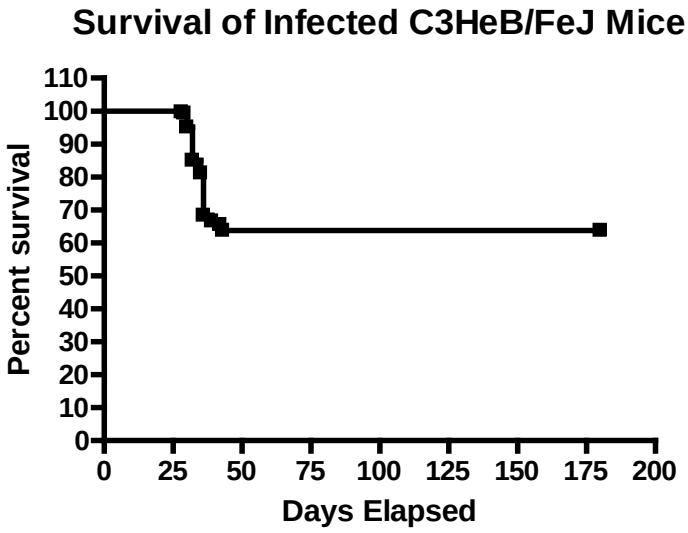

Figure 3.1. Survival curve of mortality of untreated C3HeB/FeJ mice infected with *Mycobacterium tuberculosis*. 183 mice of 280 survived initial 50 days of infection resulting in a 35% mortality rate.

These animals were humanely euthanized per IACUC requirements based on more than 20% weight loss. The remaining mice after 42 days post aerosol infection show a very different outcome in that they either have no external signs of infection or their weight and other indicators stabilize. This distinct mouse population that succumbs to disease was studied for pathology and shows very few to none defined necrotic, fibrotic lesions but in contrast shows mainly a vast neutrophilic infiltration and extensive collapse of the lung parenchyma. Due to the early mortality of the mice with predominantly the uncontrolled neutrophillic lesions, the remaining mice were more likely to show the necrotic, fibrotic lesions.

3.3.2 Kramnik Mouse Model Lesion Pathology

3.3.2.1 Temporal development of lesion pathology

The C3HeB/FeJ mouse strain when aerosol infected with a low inoculum of MTB (of approx. 50 bacteria per mouse) develops cellular lesions early on which are consisting of mixed mononuclear cells. After one-month post aerosol, a clear distinction in lesion types is already visible mainly based on the proportion of three distinct cell types of neutrophils, macrophages and lymphocytes seen in the histological examination of lung tissue. The early cellular composition appears to determine the progression to the various lesion types throughout further disease. Three lesion types can be distinguished: I) the classical granuloma with discriminative necrotic core and fibrotic collagen rim, II) the uncontrolled, highly inflammatory lesion with neutrophilic dominance, and III) the cellular lesion with mixed mononuclear cell composition (lymphocytes/macrophages).

3.3.2.2 Granuloma formation

The lung bacterial load at 4 weeks post-aerosol infection rapidly increases to 6.47 ± 0.34 log_{10}CFU. The early lesion development shows alveolar thickening and inflammation of septal walls (Figure 3.2E), however the extent of lung lesion involvement is limited and most of the lung is still uninvolved lung parenchyma (Figure 3.2B). At this early stage in infection beginning stages of lesions are visible with karyorrhectic nuclei and foamy macrophages (Figure 3.2D). The various characteristics of the three lesion types are becoming apparent. The early type I lesion show an organized assembly of epitheloid and foamy macrophages with neutrophils infiltration and pockets throughout the affected parenchyma. The early type II lesion development is less organized and a massive number of neutrophils are attracted (Figure 3.2A). The early type III lesion develops as a result of the accumulation of lymphocytes, epithelioid and foamy macrophage as well as neutrophil accumulation. This is very similar as what has been described for other immunocompetent mouse strains such Balb/c and C57BL/6 mice [134].

At 6 weeks post infection at 7.53 ± 0.21 log10, overall the lung histopathology is becoming more severe and the various lesion types are heterogeneous within the different lung lobes of one animal as well as between groups of animals. Figure 3.3A represents the distinct heterogeneity encountered in one animal throughout the lung lobes at 6 weeks post infection. Two of the five lobes have the encapsulated necrotic type I lesion while the other three lobes have type II and III lesions showing inflammatory lesions. The lung involvement is still limited at this time point with several regions of normal lung parenchyma (Figure 3.3B). The heterogeneity in lesion types within one animal is a common occurrence in early infection. During this time span there is also a greater variance in the severity of the lesions. There are the more severe encapsulated necrotic type I lesions with the beginnings of a highly eosinophilic

core and a well-developed collagen rim as seen in (Figures 3.3D and E), whereas other type I lesions have yet to progress to the more liquefactive state of necrosis. From Figure 3.3C the mixed composition of foamy macrophages and neutrophils that are necrotizing is apparent but is still retaining some shape.

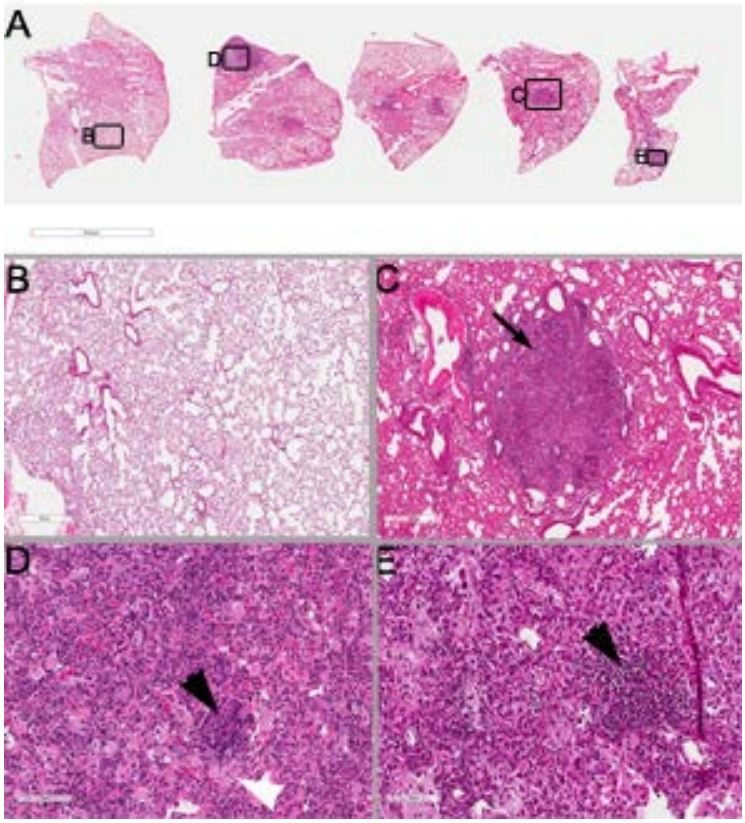

Figure 3.2. Early lung lesion heterogeneity at 4 weeks post aerosol infection (PAI). (A) 5 lung lobes of one representative mouse (0.4x). (B) Normal lung parenchyma (4x). (C) Early clustering of necrotic debris and lesion foci (Arrow) (20x). (D) Predominantly cellular lesion, majority foamy macrophages (white arrow head) with lymphocytes and pockets of necrotic cells (black arrow head) (20x). (E) Cellular lesion with predominantly necrotic cells (black arrow head) and some lymphocytes (20x). Stain: hematoxylin and eosin.

Also the type II lesion becomes apparent at this time in infection, showing necrotizing alveolitis (Figure 3.3E). The alveolar septal walls remain mostly intact, while the alveolar spaces are filled with high numbers of dying neutrophils, intact cells, bacteria and debris, creating a

honeycomb-like necrosis, which is only seen at very late stage in immunocompetent mouse models [134]. These lesions seem to develop in conjunction with the encapsulated necrotic lesions (in Figure 3.3A, indicated by a black arrow). In a proportion of the mice, the type II lesions can involve the entirety of the lung lobe leaving limited normal lung parenchyma in that lung lobe. This is likely resulting in a proportion of the mice starting to lose body weight and succumb to disease between day 35 - 45 post aerosol (peak at 42 days).

At eight weeks post-aerosol infection the bacterial load was stabilized at 7.96 ± 0.42 $\log_{10}$CFU (as shown in Figure 3.6 and Figures 3.4A and 3.7), and more than 67% of the lung lobes have necrotic, or type III lesions. The histopathology shows a similar distribution in lesion types as described for the earlier time point, with progression of the severity of the lesion types. Especially for type II lesions, the necrotizing alveolitis can expand significantly at this stage of disease. The encapsulated necrotic granulomatous lesions are large and multi-lobulated that may suggest the coalescing of multiple necrotic lesions. At this later time point the necrotic lesions type I are composed of an eosinophilic core with a large area of necrotic cell debris with mainly extracellular bacilli. It should be noted that even with the large regions of lung destruction there remains whole sections of lung, even whole lobes, unaffected by disease (Figure 3.4B). These uninvolved lung lobes contribute to the large heterogeneity and variation that is seen when measuring levels of necrosis and bacterial burden (shown in Figures 3.6 and 3.7).

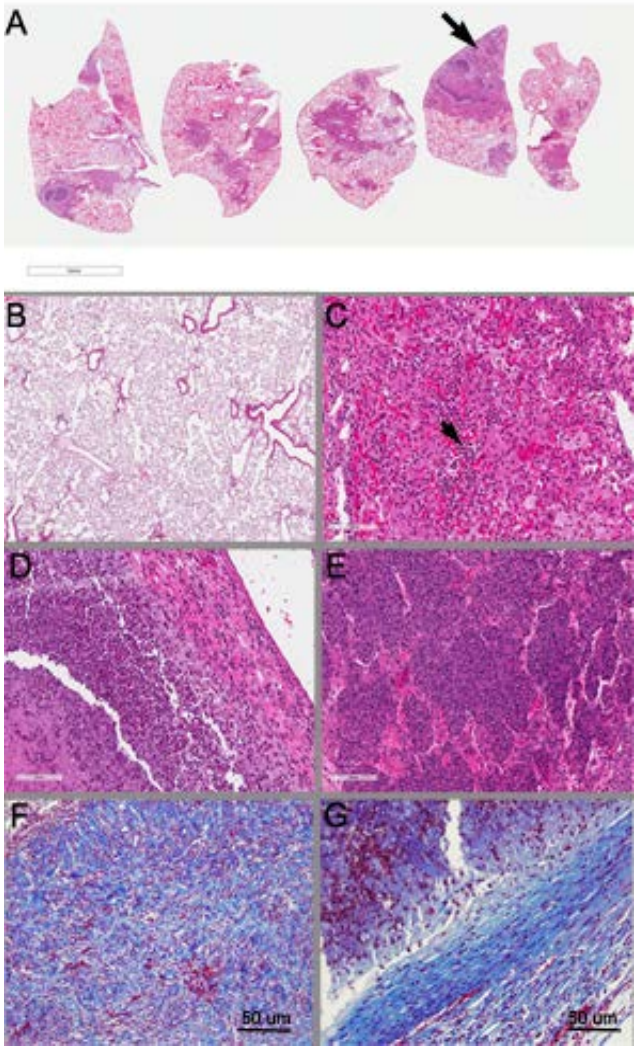

Figure 3.3. All lesion types represented at 6 weeks PAI with host response. (A) 5 lung lobes of one representative mouse (0.4x). (B) Normal lung parenchyma (4x). (C) Type III lesion, cellular lesion with high numbers foamy macrophages, lymphocytes (small arrow head) and small numbers of neutrophils (20x). (D) The edge of Type I lesion, collagen capsule with foamy macrophage rim, necrotic neutrophil region and central eosinophilic core (20x). (E) Type II lesion, necrotic material filling the alveolar spaces (large arrow in A) (20x). (F) Large region of diffuse collagen fibrils stained with Masson's Trichrome (20x). (G) Collagen surrounding a type I lesion stained with Masson's Trichrome (20x). Stain: hematoxylin and eosin.

From ten to twelve weeks post aerosol infection the bacterial load in the lungs is maintained around 8.09 ± 0.09 $\log_{10}$CFU, and the mice show developed lesions with liquefactive necrosis (Figure 3.5A). These lesions, the majority type I lesions, consist of an accumulation of

amphophilic cellular debris admixed with numerous extracellular bacilli. At the periphery of the necrotic core on the inside of the collagen rim is a cuff with foamy macrophages of variable size, which contain very large numbers of intracellular bacilli. In Figure 3.5B a distinct line of functional macrophages delineated by the collagen border of the necrotic granuloma is observed. The numbers of intracellular bacteria in especially foamy cells can become numerous, as seen in serial sections of H&E (Figure 3.5C) and acid-fast stained tissue (Figure 3.10B).

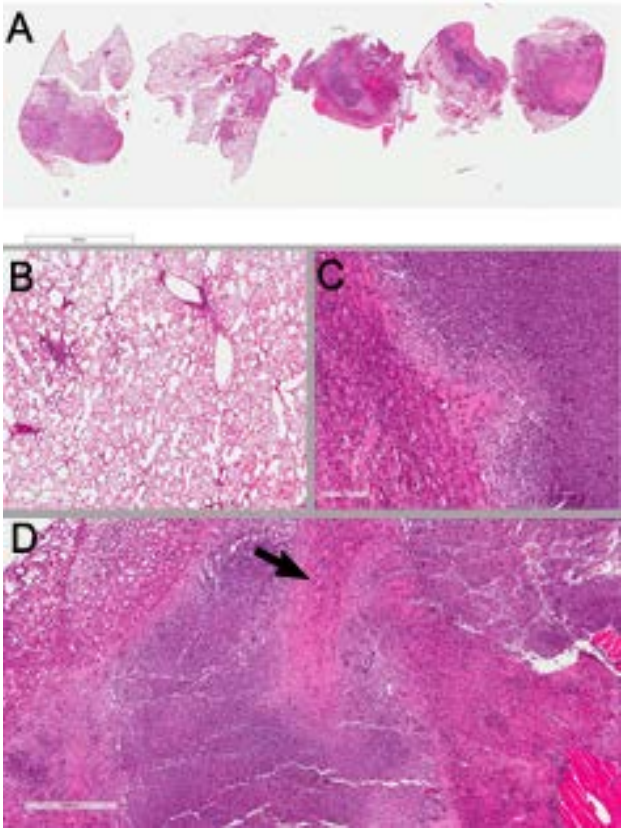

Figure 3.4. 8 weeks PAI, majority of lesions are necrotic. (A) 5 lung lobes of one representative mouse (0.4x). (B) Normal lung parenchyma (4x). (C) Type I lesion with large collagen capsule and necrotic karyorrhectic neutrophils (20x). (D) Large type I lesion coalesce with collagen insets (black arrow) (20x). Stain: hematoxylin and eosin.

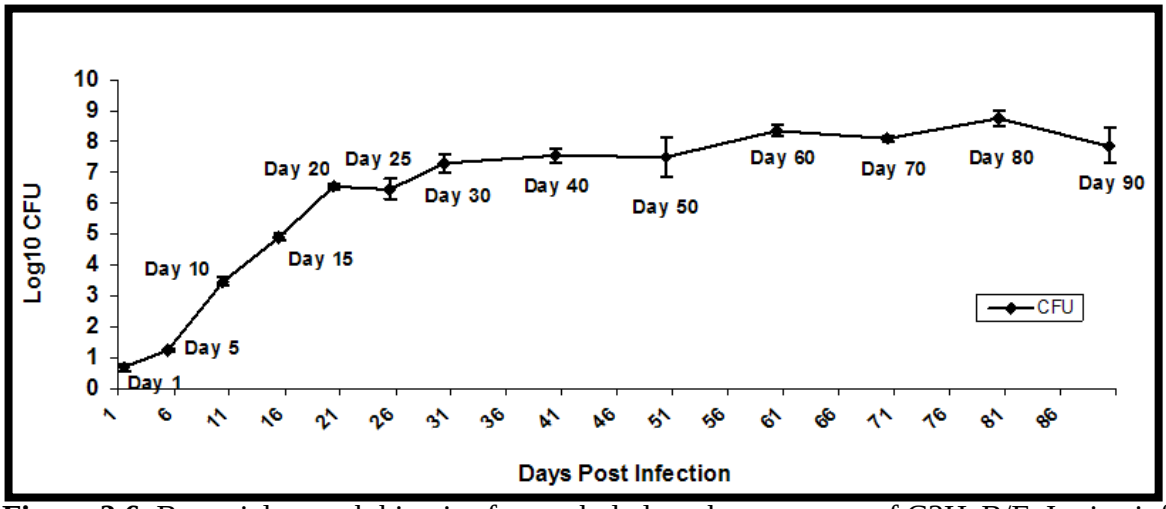

Figure 3.6. Bacterial growth kinetics from whole lung homogenate of C3HeB/FeJ mice infected with a low dose aerosol with *M. tuberculosis*. Low dose aerosol infection results in rapid bacterial growth in the initial 20-30 days then to stabilize. The remainder of the experimental duration there is slow continued bacterial growth of 1-1.5 $\log_{10}$ CFU.

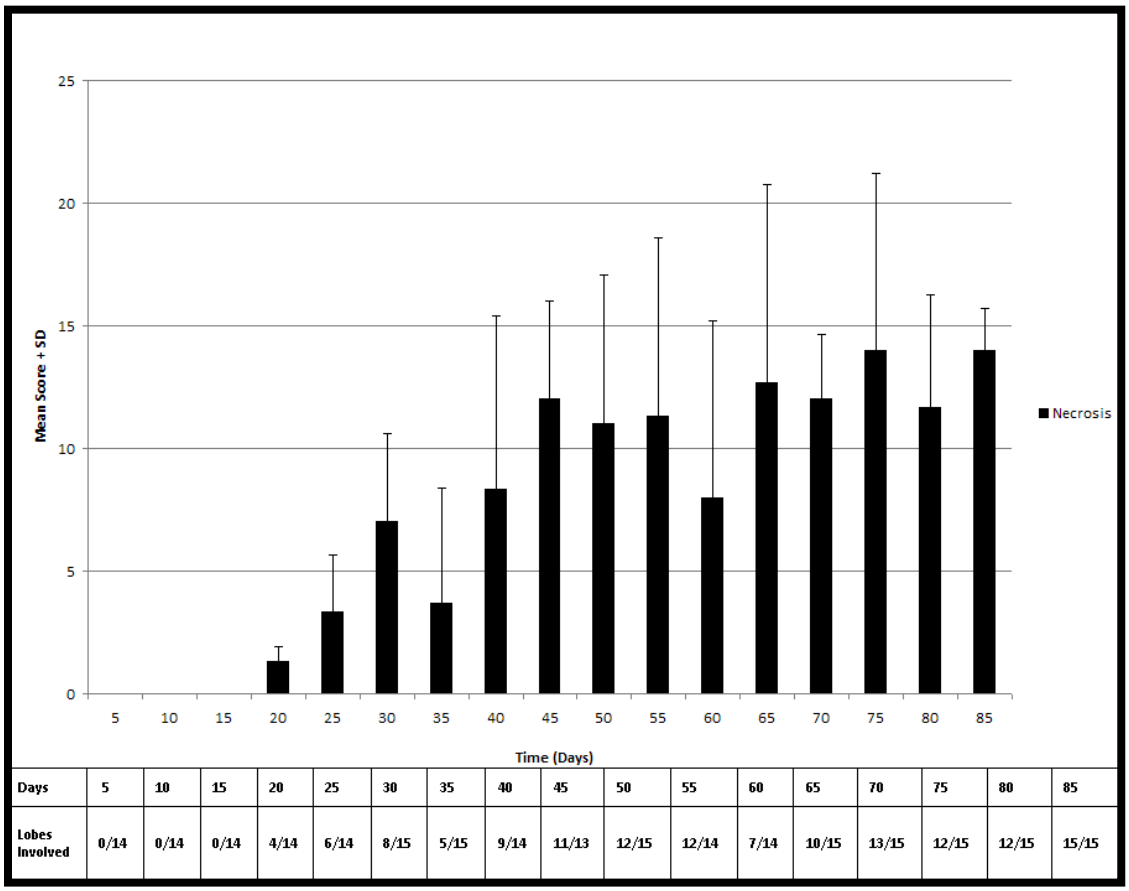

Days	5	10	15	20	25	30	35	40	45	50	55	60	65	70	75	80	85
Lobes Involved	0/14	0/14	0/14	4/14	6/14	8/15	5/15	9/14	11/13	12/15	12/14	7/14	10/15	13/15	12/15	12/15	15/15

Figure 3.7. Increasing lung necrosis and lobe involvement over time of C3HeB/FeJ mice when infected with MTB.

3.3.2.3 Granuloma fibrosis

Early in disease at the edges of the cellular lesion, early deposition of collagen is already visible based on Masson's trichome staining. There is a thickening surrounding the areas of disease in Figure 3.2C. As lesions develop the fibrosis takes different forms, at 6 weeks post aerosol infections the collagen can surround the type I lesion (Figure 3.3G) and also be intermixed in the lung parenchyma (Figure 3.3F). In Figure 3.4D is the presence of a well-defined collagen inset acting as a division of two lesions that have coalesced as disease as progressed. By 10 weeks post aerosol infection, the further encapsulation of lesions is observed as a fibrous matrix as seen with trichrome collagen staining which indicative of lesion healing (Figure 3.5D).

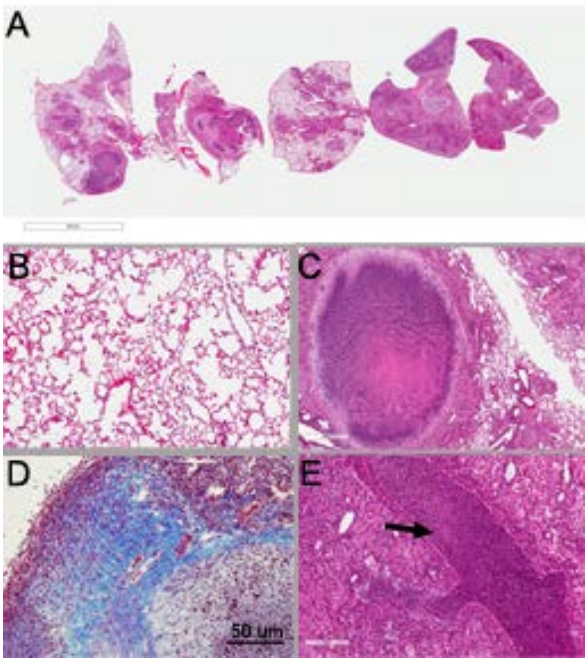

Figure 3.5. 10 week PAI, type I and II lesions represented with continued presence of normal lung tissue. (A) 5 lung lobes of one representative mouse (0.4x). (B) Normal lung parenchyma (4x). (C) Type I lesion (20x). (D) Large section of collagen fibrils stained with Masson's Trichrome (10x). (E) Type II lesion with airway obstructed with necrotic debris (black arrow) (20x). Stain: hematoxylin and eosin.

3.3.3 Bacterial Location in Lung Lesions of the Kramnik mouse model over time

3.3.3.1 Comparison side by side of the acid-fast staining of bacteria by the fluorescent auramine-rhodamine method and detection of bacilli in tissues via a novel fluorescent acid staining method using Sybr Gold

As we have shown before MTB bacteria can survive intra- as well as extracellular environment within the lung in mice and guinea pigs [131, 134]. We have already described that the AR staining method gradually stained fewer bacteria over the course of the disease in the Kramnik mouse model [131]. In this study we further demonstrate that that acid fast with Sybr Gold staining results in enhanced detection of the MTB bacteria when compared to AR staining. For this purpose early and late lesions were stained using the AR staining method. The bacteria were visualized easily in the early lesions however; it becomes more difficult to stain all bacteria with the AR method as infection progresses (Figure 3.9A) [131]. Serial sections of the same lesion were also used for staining with the novel Sybr Gold staining method

Figure 3.8 shows lung sections with the location of bacteria visualized via the green fluorescent Sybr Gold staining method, a newly developed acid-fast staining protocol (Ryan et al., submitted). Early in infection (from 4-8 weeks), the bacilli were found mostly intracellular in macrophages or neutrophils surrounding airways and vessels (Figure 3.8A and B). The bacteria are clustered in lesions consisting of immune cells, which were visualized by DAPI nuclei staining.

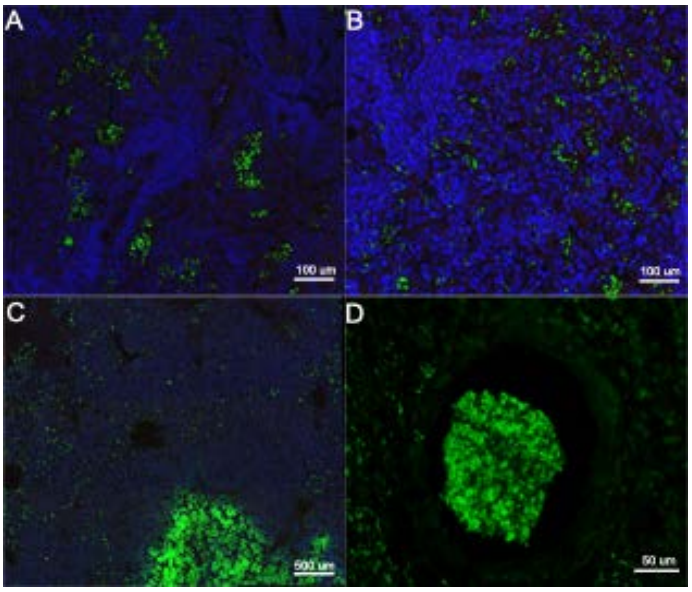

Figure 3.8. Sybr Gold stain revel the bacterial location in Type II and Type III lesions at late stage of infection with the Erdman strain *M. tuberculosis* (10-12 weeks post aerosol infection). (A) Bacterial clustering intracellular in lung tissue near bronchioles at 10 weeks post aerosol infection, Type III lesion (20x). (B) Diffuse intracellular bacteria at 12 weeks post aerosol infection, Type III lesion (20x). (C) High concentration of extracellular stained bacteria in necrotic debris, Type II lesion (10x). (D) Large mass of stained extracellular bacteria, necrotic debris and cellular remanants in a bronchiole (40x). Stain: Sybr Gold and Dapi.

As the type I lesion develops liquefactive necrosis the bacteria in the center of the lesion transition to an extracellular environment as the host cells become necrotic. In these late stages of disease in the Kramnik mouse model (10-12 weeks post aerosol infection), very high numbers of extracellular bacteria are being detected within the necrotic granuloma using the Sybr Gold staining protocol. In addition, a sizeable concentration of bacteria is also present intracellularly in the foamy macrophages that surround the karyorrhectic nuclei (Figure 3.9B). The remaining bacteria are present in the center of the necrotic lesion (Figure 3.9D). At this time we can only estimate and speculate that most bacteria in lesion type I are extracellular in late stages of infection due to the high bacterial burden concentrated in the lesions. For the type II lesion which is characterized by necrotizing alveolitis, high burdens of extracellular bacteria are detectable

using the Sybr Gold staining method in the necrotic debris within the intact alveolar spaces (Figure 3.8C). Even in airways the necrotizing alveolitis is visible, and extensive necrotic debris is seen comprising of high numbers of extracellular bacteria blocking the airways (Figure 3.8D).

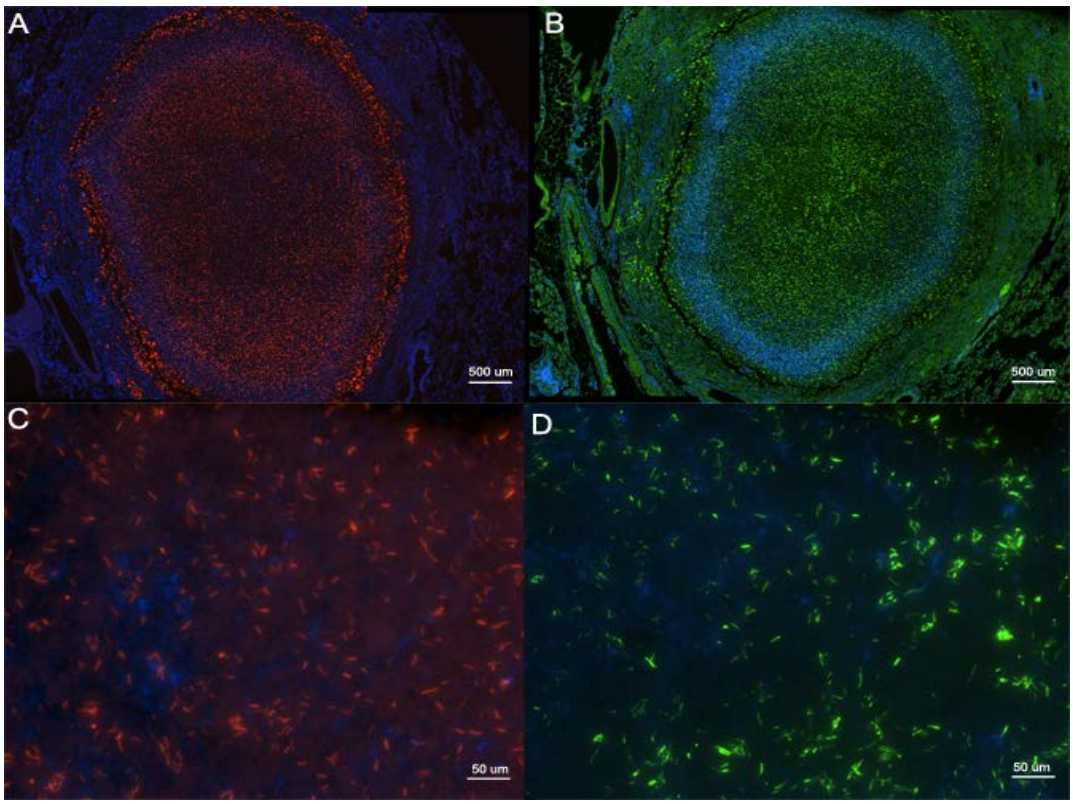

Figure 3.9. Differences in bacterial detection by acid-fast staining techniques. Images A and C have been stained with auramine-rhodamine. Serial sections B and D have been stained with Sybr Gold. (A) Type I lesion stained with auramine-rhodamine with reduced staining in the center of the lesion (10x). (B) Serial section of A, Type I lesion stained with Sybr Gold (10x). (C) Central region of necrotic lesion, type I lesion, stained with auramine-rhodamine (40x). (D) Serial section of C, central region of necrotic lesion, type I lesion, stained with Sybr Gold (40x).

3.3.3.2 Human lesion bacterial populations

Lung sections were derived from re-sected human lung tissue of MDR-TB patients that were on treatment for a significant amount of time were used to determine the presence of MTB

bacteria using the Sybr Gold method of staining large excised necrotic granulomas obtained from human lungs stained by the Sybr Gold approach, demonstrated a high bacterial number.

Using the Sybr Gold staining technique described above on the lung tissue, we were able to visualize the large numbers of bacteria in human TB cavitary lesions. Fig 3.10 shows the morphology of the human TB lesion with a center necrotic region, the excised lesion is large and diffuse. The surrounding tissue is composed of an intermix of collagen and other infiltrates. Throughout the lesion we can see the presence of foamy macrophages. When stained with Sybr Gold the only region that detects bacilli is the necrotic core of the dissected lesion, with primarily extracellular bacteria.

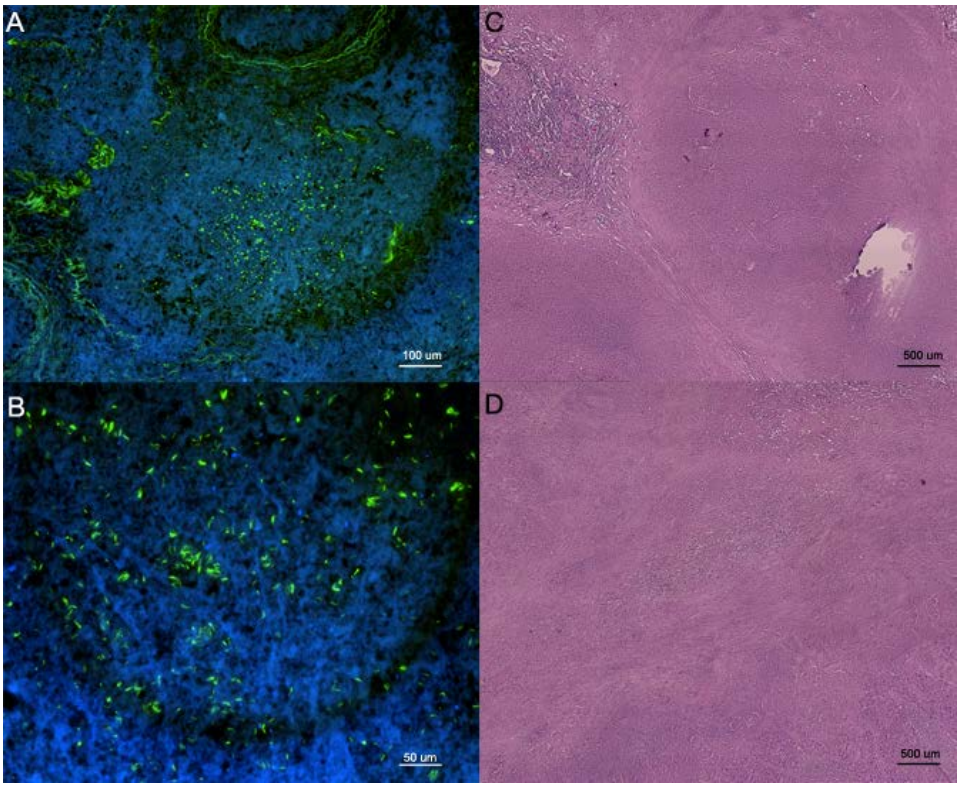

Figure 3.10. Excised human necrotic lesion from patients with MDR-TB. Images A and B bacterial location detected with sybr gold staining and Images C and D tissue architecture stained by H&E. (A and B) Necrotic lesion with extracellular bacteria stained with sybr gold and dapi, 10x and 40x, respectively. (C and D) Necrotic human lung tissue with remnant of lung parenchyma stained with hematoxylin and eosin (10x).

3.3.4 Immunohistochemistry localization of macrophage activity

In late stage disease, as described above, the type I lesions have distinct populations of cells types that surround the necrotic lesion. To determine the phenotypic characteristics of the of specific cell types within a tissue section we used F4/80, IL-10 and lysozyme immunohistochemistry (IHC). Lysozyme is a constitutive enzyme of macrophage with effective antimicrobial activity including activity against MTB [251]. Using IHC we demonstrated that interstitial macrophages within the parenchyma and macrophages within the type II and III lesions (Figure 3.11) have strong staining for lysozyme, an antimicrobial enzyme. However, it is important to notice that that the foamy macrophages, which contain large numbers of bacilli, are negative for lysozyme production. Similar IHC staining for F4/80 marker, indicative of functional macrophages, demonstrated that some macrophages but not all within type I and type II lesions were positive for the F4/80 marker. Furthermore it was interesting to find that a cuff of macrophages surrounding the foamy cell layer in the type I lesions have strong staining for the F4/80 marker. Interestingly the foamy cells in any of the three types of lesions were negative for the F4/80 marker. (Figure 3.11), Previous report from our lab [72, 77] demonstrated that foamy cells are positive for IL-10 cytokine. Thus, we performed IHC for IL-10 cytokine. IL-10 is strongly expressed by the foamy macrophages within the type I and II and III lesions. Altogether, the IHC staining demonstrated that the IL-10 is in the interior rim of the necrotic encapsulated lesion (Figure 3.11) while functional macrophages, positive for lysozyme and F4/80 are segregated on the outer rim of the lesion. This staining pattern creates a distinct microenvironment of the type I lesion not seen in lesion types II or III.

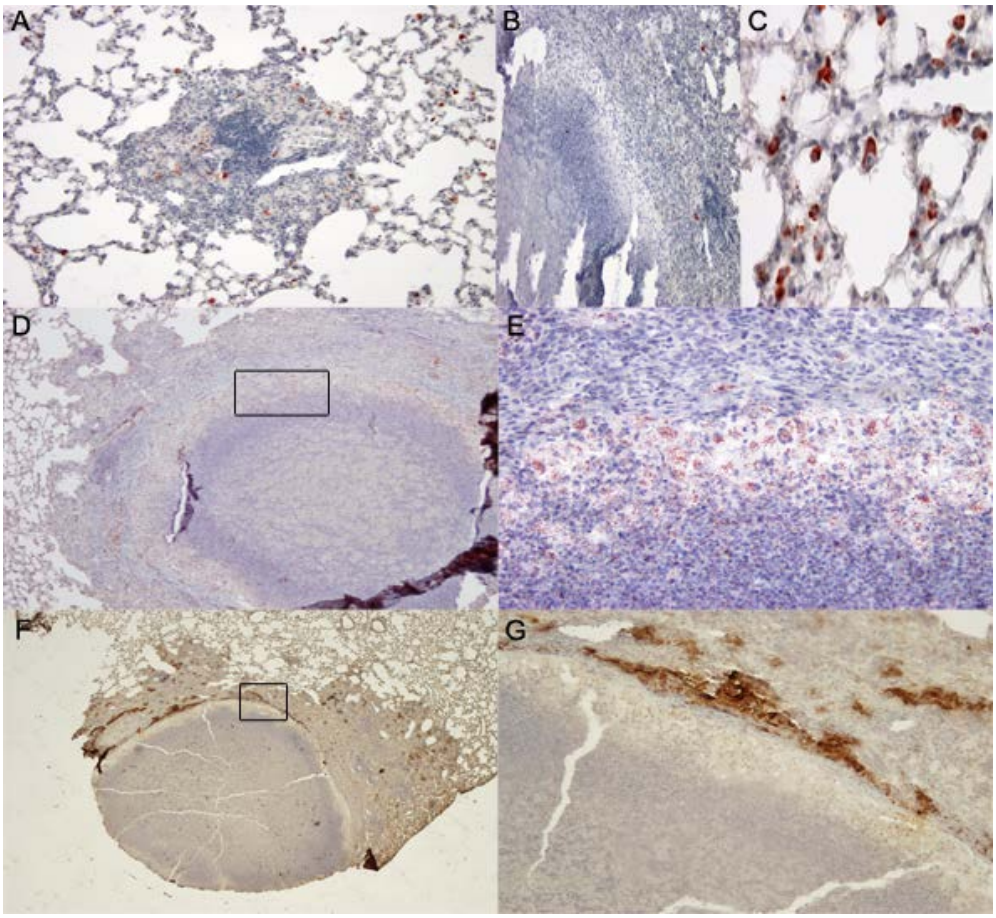

Figure 3.11. Cytokine expression is shown to microenvironment specific based on immunohistochemistry staining. A, B and C positive staining for lysozyme (red): A: interstitial Mo in parenchyma strongly positive for lysozyme B: type II lesion showing very few MO positive for lysozyme and foamy cells negative for lysozyme C: type I lesion with foamy cell rim and MO (compare to F4/80 positive MO in F and G) negative for lysozyme D and E: positive staining for IL-10 (red) in type I lesion and in foamy cells in rim of Type lesion (E) F and G: F4/80 staining in macrophages over the foamy cell rim in a type I granuloma.

3.3.5 Cytokine and Chemokine Analysis: Significantly distinct cytokine production in isolated granulomas

In order to better understand the development of the unique pathologic features in the Kramnik mouse model, we performed a preliminary immune assay to identify key immune events. Through the use of a cytometric bead analysis (CBA) we were able to measure the levels

of inflammatory cytokines produced by diseased animals. The cytokines measured by this assay were IL-6, IL-10, IL-12, IFN-γ, TNF-α, and MCP-1.

The results from the CBA assay showed an upregulation of the inflammatory profile of cytokines locally at the granuloma itself when compared to non-granulomatous tissue. There were increased protein levels of MCP-1, TNF-α, IL-6, and IL-10 in the granuloma versus the whole lung tissue, and a decreased level IFN-γ in the isolated granuloma ($p < 0.05$). IL-12 levels were not significantly different in all studied tissue samples (data not shown). The opposing cytokine expression profiles of IL-10 and IFN-γ were most striking. IL-10 protein levels were significantly greater within the granuloma and IFN-γ levels were significantly greater outside the granuloma, as compared to whole lung cytokine levels ($p < 0.0005$ and $p < 0.05$, respectively). When we examined the cytokine levels in the excised granulomas the increased cytokine levels of MCP-1, IL-6, IL-10 and TNF-α were highly concentrated in the granulomatous lesions as shown in Figure 3.12.

In the CBA assay, Figure 3.12, the expression of MCP-1 from the isolated granulomas was found highly significant ($p < 0.0001$) when compared to both the naïve lung and non-granulomatous tissue. MCP-1 levels from granuloma show more than a 40-fold increase from the naïve lung tissue. Comparing the MCP-1 level of the isolated granulomas to the whole lung with lesions there is an increase of cytokine production of 1.5-fold, which is not a significant finding ($p > 0.2$). Further analysis showed the cytokine produced by the non-involved lung tissue is nearly a third less compared to the isolated granulomas ($p < 0.0001$).

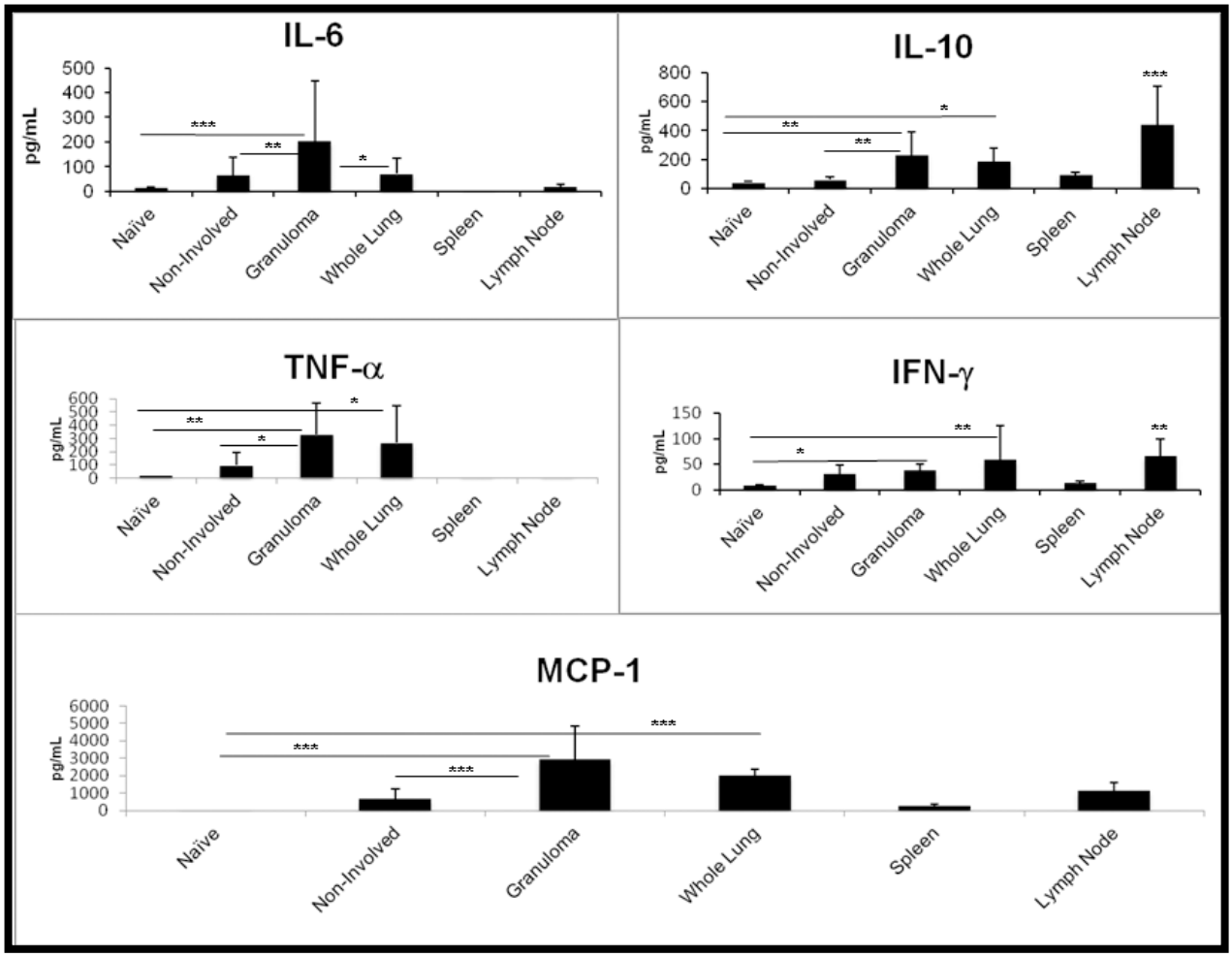

Figure 3.12. Cytokine expression is specific to microenvironment. IL-6 is highly significantly expressed in the granuloma compared to naïve lung ($p<0.0001$), whole lung ($p<0.001$), and non-involved lung ($p<0.05$). TNF-α, inflammatory cytokine, has increased expression in the whole lung and granuloma, both significantly higher than naïve ($p<0.01$) and non-involved lung ($p<0.05$). TNF-α low level expression in the lymph node not significant to naïve lymph node. IL-10 expression is higher but not significant in granuloma than whole lung. Both whole lung and granuloma are significant higher than naïve lung ($p<0.001$) and non-involved lung ($p<0.001$). IL-10 is highly significant ($p<0.0001$) expressed in the lymph node compared to naïve lymph node. IFN-g expression is higher in the whole lung but not significant than expression in the granuloma. Whole lung IFN-g expression is significantly higher ($p<0.001$) than naïve lung. IFN-g lymph node expression is significant ($p<0.001$) compared to naïve lymph node. MCP-1 expression is highly significant in the granuloma compared to whole lung ($p<0.0001$), naïve lung ($p<0.0001$), and non-involved lung ($p<0.0001$). All cytokine expression in the spleen was not significant to naïve spleen.

Other inflammatory cytokines, such as IL-6 and TNF-α, gave a similar trend in cytokine profile to that of MCP-1. The excised granuloma has 3-fold the level of IL-6 and TNF-α when compared to infected non-involved lung tissue. These are highly significant differences of cytokine production that are localized to specific regions of infected tissue ($p < 0.001$ and 0.0005, respectively). The results show that the local microenvironment of the granuloma has an increased production of inflammatory cytokines as well as down regulation of IFN-γ production, when compared to the whole lung.

3.4 – DISCUSSION

The main goals of this study were to perform an in-depth examination of the progression of pathology in the Kramnik mouse model for its potential future use in TB drug development, with a special focus on the location of bacteria within the lung lesions. In addition, this study aimed to compare the characteristic pathology features in the mouse model to published human data to assess to what extent it reflects features of human disease.

The lung pathology in the Kramnik mouse model shows prominent heterogeneity in lung lesion types across the lung lobes in a single mouse, as well as between mice infected for the same amount of time. This heterogeneity in lesion types is also seen in TB patients as described in a comprehensive color atlas of pulmonary TB [252]. This is, for the ultimate use of this model in TB drug development, both an advantage in that an optimal treatment regimen should be effective under all conditions, as well as a disadvantage as the heterogeneity of lesions results in larger standard deviations between mice from treatment groups and therefore require a higher number of animals per group. For current drug trials in our laboratory using the Kramnik mouse model, treatment is started at 8 weeks post aerosol infection to ensure the development of more

mature, encapsulated necrotic lesions within the majority of the mice in at least one of the lung lobes. We identified three lesion types in the Kramnik mouse model that can best be described as; type I, the classical granuloma with a necrotic core, type II, the uncontrolled rapid bacterial growth with large neutrophilic accumulation, and type III, the cellular lesion with a mixed mononuclear cell composition.

The genetic mutation in the *sst-1* loci [195] of chromosome 1 in the C3HeB/FeJ mice, infected macrophages have been described to die by necrosis rather than apoptosis, which result in the typical encapsulated lesions that are characteristic for this strain [131, 192-195, 197]. Our experimental conditions using 50-75 CFU of MTB Erdman per mouse, produce advanced type I lesions by 8-10 weeks after aerosol infection. Type II lesions have a high bacterial burden, similar to type I lesions, without organization of the extracellular matrix. The animals that have a predominantly type II lesions tend to succumb to disease early, 28-45 days after infection, and result in approximately 35% of the mortality seen in experimental animals prior to the initiation of the adaptive immunity (Figure 3.1). Other uniquely susceptible mouse strains have shown similar survival curves when infected with MTB, such as the CBA/J and IL-10-/- knockout mice [71, 178, 250]. For type III lesion, a cellular lesion composed of mononuclear cell types (macrophages/lymphocytes). This lesion is disorganized and has a mix of lymphocytes, macrophages (epitheloid and foamy), and a small number of neutrophils. The early signals in the innate immune response likely trigger these various responses, but the mechanism is unclear. The rate of lesion progression can be accelerated by increasing the infectious dose or by using a more virulent MTB challenge strain, similar to what is seen in the guinea pig [165]. Also early experimentation done by Igor Kramnik [194] showed that these mice were able to develop the liquefactive necrotic lesions in the lungs within 4 weeks when infected intravenously with a

higher dose. Other laboratories using the H37Rv MTB strain show less mortality over the course of infection, slower progression of disease but more heterogeneity due to a higher variance of the three lesion types across mice. To establish the experimental conditions is important when determining the type of disease progression sought and the use of the model.

The early immune events seem to determine what lesion type will develop, unlike our earlier belief that one lesion type will likely advance to another. In addition, the recruitment of high numbers of neutrophils towards the site of infection in this mouse model is the dominant cell type and likely the cause of the massive necrosis that is so characteristic to the mouse strain. For a type I lesion, the early lesion consists of a mixed macrophage and neutrophilic composition in an organized manner, and even at the early stage epitheloid cells are observed with some minor collagen deposition. In later stages of the progression type I lesion a thickening and an ongoing remodeling of the collagen rim occurs and neo-vascularization within the fibrous rim is observed. Based on earlier work we are able to surmise from picrosirius red staining techniques, which visualize collagen that the host is constantly adapting to infection [131]. This stepwise progression in pathology of disease is in many aspects similar to what is seen in cancer field for solid tumors where the development of hypoxia, necrosis, and collagen depositions are common features [253]. Therefore, certain treatments options directed towards hypoxia, neo-angiogenesis, and remodeling of the collagen rim like vascular endothelial growth factor (VEGF), anti-TGF-β, and Losartan Potassium from the field of oncology should be investigated as augmentation to treatments or treatments themselves due to the similarities to TB [253-255].

The type I lesion can evolve and form a cavity after expelling its liquefied content [131]. The cavity formation in the Kramnik mouse model is characterized by loss of normal lung parenchyma, which is replaced by neutrophilic infiltrates and the necrotic material from center of

granuloma lesion have eroded into an airway [14, 204]. The cavitary lesion is then an opening in the center of the lesion that allows for transmission of the bacilli to another person or experimental animal [159]. This is currently an infrequent event under the current experimental conditions (0.5-1%). Cavitary disease is known to be an important cause for treatment failure in TB patients by increase of relapse of infection in cavitary cases, showing higher incidences of resistance, and it's important in transmission of the disease [256]. Knowledge regarding the progression of disease in the Kramnik mouse model is assisting us with our attempts to increase cavitation, currently experiments are underway to change the course of disease by influencing the cytokine environment as well as drug treating the animals to increase the healing process of the necrotic lesions and allow for relapse of infection.

Two prominent cell types are observed in the lesions characterizing the Kramnik mouse model: foamy macrophage and the significant neutrophilic response. Both cell types appear to be ineffective in bacterial killing and permissive to bacterial growth thereby carrying a substantial number of bacteria. Other groups have shown macrophages and neutrophils infected with MTB are prevented from undergoing apoptosis and allow for intracellular growth of the bacterium, possibly providing a source of nutrition [257-260]. Human TB granulomas have been described as having central caseous necrosis surrounded by a large cuff of epithelioid histiocytes mixed with lymphocytes [252]. Peripheral to this cuff, which shows similarity to what is observed in the Kramnik mouse model, is the fibrous collagen encapsulation and vascular remodeling. This collagen matrix encompasses a network of neo-vascularization. This lesion while technically a granuloma is more appropriately described as pyogranulomatous due to co-localization of macrophages and neutrophils. Also similar to the Kramnik model in the alveolar spaces surrounding the necrotic granuloma there are numerous alveolar macrophages. In the Kramnik

mouse model these macrophages stain positive for the marker F4/80. While the microscopic structural features are comparable between the human and Kramnik mouse model, there are differences in the relative proportion of cell types. Most notable is the distinct lack of lymphocytic recruitment in the Kramnik mouse model, which are prominent in chronic human TB lesions.

Human disease, like the Kramnik mouse model, has been shown to produce similar heterogeneity of lesions. It is known that human lesions contain a lymphocytic infiltration early in infection as well as macrophages [14]. Early lesions are similar to what is seen in the Kramnik mouse model; septal wall swelling and desquamation, vasodilatation of capillaries and early influx of inflammatory cells [203, 252]. As infection progresses several types of lesions have been described in the literature. Georges Canetti in 1944 performed some of the most complete assessment of the wide range of lesion types from cadavers of patients who died from primary TB and other diseases. TB patients tend to develop what is described as a fibrino-macrophagic alveolitis [203], which has similar characteristics to the necrotizing alveolitis seen in the Kramnik mouse model. The septal walls of infected lung remain mostly intact with addition of fibrin in bundles; there are large numbers of macrophages and the occasionally neutrophils. Necrotizing alveolitis in the Kramnik model is more neutrophil dominated and has fewer macrophages but the high bacterial load is similar to what was seen by Dr. Canetti [203]. In more recent publications, more extensive reports on the larger exudative aggregates are described to be composed of lymphoid cells and these have been defined as TB pneumonia due to the obstruction of the alveolar spaces [252, 256, 261-263].

A disease feature thoroughly described by Dr. Canetti and only recently re-evaluated in current literature is the prominence of neutrophil involvement in human disease [203, 264]. In

the Kramnik mouse model the neutrophilic response dominates, in human disease neutrophils do play a role in those lesion types depicted as polymorphonuclear alveolitis. A lesion where the alveoli are filled with neutrophils and the occasional macrophage, have the highest bacterial numbers relative to other lesion types. This is also evident in the Kramnik model where especially the type II lesion consists of high numbers of neutrophils and enormous bacterial burden. Other groups have been showing the importance of neutrophils in bacillary transport especially in the transmission stage of disease in humans [265].

In recent years the focus on bacillary location in disease has gained more interest especially in light of the applications in drug delivery and questions concerning drug penetration across granulomas [205]. Other animal models, which develop necrotic lesions, such as the rabbit, the guinea pig or the NHP model, all of which have low bacterial numbers per lesion or per gram of tissue. For the NHP, extensive work was performed to correlate specific microenvironments of necrotic, non-necrotic, and suppurative lesions with the bacillary burden and cytokines levels present in those lesions [24]. Unfortunately, in the macaque model the overall low numbers of bacilli present make it very difficult to reach conclusions about the environments in which the bacteria are thriving. One of the major advantages of the Kramnik mouse model is the highly organized suppurative lesions containing high bacteria burdens. In an earlier paper, we showed the results of classical acid fast staining methods [131, 134]. We stated that the fluorescent AR showed reduced staining of bacilli within the core of the lesion, although with the Ziehl Neelsen staining method it was clear that the caseum was also packed with bacteria [131]. In this paper, we report for the first time the staining results using a novel acid-fast staining method based on Sybr Gold on *in vivo* sections. Sybr Gold is a fluorescent nucleic acid stain, which visualizes a significantly greater number of bacilli *in vitro* that are acid-fast

negative with current clinically used acid fast stains (Driver et al., submitted). The new staining method is highly sensitive, has far less background as it only becomes fluorescent when binding to nucleic acids. The stain is then solely retained by the bacteria due to the acid wash at the end of the staining protocol. *In vitro* cultures, Sybr Gold detects 99% of bacteria in both actively replicating aerobic and NRP hypoxic cultures (Ryan et al., submitted). Transmitted light microscopy with Ziehl-Neelsen fuchsin stain and fluorescence microscopy with auramine O and AR stains detected only 54% to 86% of cultured MTB. Because of Sybr Gold's ability to distinguish more phenotypes of bacilli we now have found it to be a superior stain to auramine-rhodamine both *in vivo* and *in vitro*. In type III lesions and early in infection the bacteria are easily distinguished as intracellular in Figure 3.8A and B; they are surrounded by cells with large nuclei, lymphocytes and macrophages. As in the other lesion types the bacteria survive predominantly within the foamy macrophages. The uncontrolled inflammation and necrotic debris in the alveolar spaces in the type II lesion have a high burden of acid-fast bacteria (Figure 3.8C and D). The necrotic neutrophils and macrophages with high numbers of extracellular bacteria also fill the airway creating obstruction. The type I lesions, like type II lesions, have a high bacterial burden that are detected by the Sybr Gold stain. The necrotic core of the encapsulated lesion contain extracellular bacilli while the predominantly foamy macrophage rim contain large numbers of intracellular bacilli. The foamy macrophages that surround the lesion are not only permissive to bacilli survival but seems to allow for growth and replication. The MTB modulate macrophage lipid-sensing receptors to create a foamy environment to allow the bacteria to thrive [266]. Compared to the auramine-rhodamine stain in Figure 3.9A and C the staining ability of the Sybr Gold to comprehensively stain the acid-fast bacteria in the necrotic core is depicted in Figure 3.9B and D. The change in auramine-rhodamine acid-fast bacteria is

indicative of a conformational change in the central most bacteria. This may be due to the hypoxic environment [131, 247] and/or the environmental and oxidative stress [243].

Human cytokine production has shown intriguing results with IFN-γ, IL-10 and TNF-α all being predictive of disease and disease outcome [78, 267, 268]. Several studies [268, 269] point to IFN-γ as being a reliable marker for active disease that will become reduced after treatment. In standard mouse models whole lung homogenate is used on non-necrotic granuloma forming models to gain single cell suspensions for either flow cytometry or ELISA [78, 267] resulting in data that may not be representative of natural disease states. A great benefit of the Kramnik mouse model is the ability to use a small animal model that develops these encapsulated necrotic granulomas which can be dissected from the rest of the uninvolved lung. We were able to obtain serum, tissue sections of whole lung with lesions, individual lesions, and infected lung tissue without grossly visible lesions from individual animals at 10 weeks post aerosol infection. This isolation technique allowed us to analyze the distinct environments of either the lung as a whole, the local environment of the granuloma as well as the systemic cytokine profiles. The use of the whole lung has resulted in the assertion that the control of bacterial growth begins earlier in more resistant a mouse strain, such as the C57Bl/6. This data may contribute the lack of growth control seen in the Kramnik mouse model. The C57Bl/6 mice had significantly high levels of TNF-α and IL-12 when after being exposed to infection for a short period of time, within the first week. At this time it is difficult to speculate the cytokine profile of the Kramnik mice at early infection. To date, we have only explored the cytokine expression late in infection.

In the NHP model, Joanne Flynn and colleagues have examined B cell function and other T cells [24]. They, too, isolated granulomatous tissue to examine and correlate

microenvironments with cytokine, T cell and B cell flow cytometry data. They found distinct cellular populations that surround the granuloma that produce specific markers that are reminiscent of germinal centers in lung tissue such as B-lymphocyte markers CD20 and CXCR5 [270]. By fluorescent IHC staining the B cell markers are positioned around the lymphocytic cuff corresponds to our CBA data of the distinct microenvironment determined by the excising of discreet necrotic granulomas. This data also corresponds with the IHC data in Figure 3.11, which demonstrate the functionality of specific cell types within lesions.

IL-10 is highly expressed by foamy macrophages, as seen in Figure 3.11, by using the CBA assay we are able to confirm significant IL-10 expression from the granuloma. The foamy macrophages are located on the inner cuff of the granuloma, while the whole lung and non-involved lung have significantly lower levels of IL-10 expression. IFN-γ is a protective Th1 cytokine which is known to inhibit the expression of IL-10 [78, 271, 272]. IL-10 was expressed at significantly higher levels in samples derived from granuloma than in samples derived from whole lung and non-involved lung. Conversely, the levels of IFN-γ expression in samples derived from granuloma were lower than in samples derived from whole lung and non-involved lung. Furthermore the levels of IFN-γ measured in the granuloma samples were statistically no different from those derived from naïve animals. However, the levels of expression of IFN-γ found in the non-granulomatous lung and whole lung have 5x and 10x more cytokine than naïve mice, respectively. With the use of a CBA assay we are able to measure actual cytokine protein expression levels from tissue homogenate and plasma samples that are then correlated to IHC. While modulated foamy macrophages are located on the inner cuff of the granuloma, functional or activated macrophages are designated to the outer rim of the granuloma. Stains F4/80 and lysozyme in Figure 3.11 distinguished this activity. F4/80 is useful marker of macrophage

“interaction with tissue microenvironment in situ, e.g. in granuloma formation” as described by S. Gordon [273]. The clear functional line of F4/80 and lysozyme positive and negative cells is very distinct; this change in functional macrophages may be the interface of cytokine interaction, drug interaction and nutrient exchange of type I lesions that make them difficult to treat. This distinctive line of foamy and ‘functional’ macrophages prompts speculation the foamy macrophages are a barrier created by the bacilli to prevent destructive inflammatory cytokine action.

The Kramnik mouse model continues to be a useful model to study the pathological features of MTB infection. Through the use of this mouse model we have been able to determine three distinct lesion types present in late stage infection. With the use of advanced and novel acid-fast techniques we are able to characterize well-defined bacterial populations for these lesions. The discreet microenvironments defined by cytokine analysis give us insight into the immunological events that help form the pathological features in late disease. These finding suggest that modulating those cytokines may augment the disease to be more amenable to treatment and therefore shortening the duration.

3.5 – FUNDING

This work was supported by The Bill and Melinda Gates Foundation grant ID number 1033596 “Evaluation of a New Murine Model Testing Tuberculosis Chemotherapy” at Colorado State University.

CHAPTER 4 – THE USE OF LIPOSOMAL NANOPARTICLES AS A NOVEL DRUG DEVILERY VEHICLE IN C3HEB/FEJ MICE INFECTED WITH *MYCOBACTERIUM TUBERCULOSIS*

4.1 – INTRODUCTION

Mycobacterium tuberculosis (MTB) has infected 8.6 and killed 1.3 million people in 2012 [2]. Current treatment protocols for susceptible tuberculosis (TB) disease require 2 months of intensive daily isoniazid (H), rifampicin (R), pyrazinamide (Z), and ethambutol (E) followed by a continuation phase of 4 months of daily isoniazid and rifampicin (Table 4.1) [3].

Table 4.1. Recommended Treatment Regimens for New Cases of Tuberculosis

Patient Category	Diagnostic Category	Treatment regimens[a]	
		Initial phase	Continuation phase
I	New smear-positive patients, new smear-negative patients with extensive parenchymal involvement, concomitant HIV-related diseases or severe forms of extrapulmonary TB	Preferred 2 HRZE[b]	Preferred 4 HR 4 $(HR)_3$
		Optional 2 HRZE	Optional 6 HE
		Optional 2 $(HRZE)_3$	Optional 4 $(HR)_3$

[a] Numbers preceding regimens indicate the length of treatment in months. Subscript numbers following regimens indicate the frequency of administration per week. When no subscript numbers are given, the regimen is daily

[b] Streptomycin may be used instead of ethambutol and it should replace ethambutol in tuberculosis meningitis

* Adapted from *Implementing the stop TB strategy: A handbook for national tuberculosis control programmes*, Geneva, World Health Organization, 2008 (WHO/HTM/TB/ 2008.401) [3]

Susceptible TB can be effectively cured if these medications are taken in full and correctly; unfortunately, treatment can have severe side effects and patient compliance is difficult to maintain for the necessary 6-9 months.

Recent progress has been made in developing new treatments to shorten the duration and reduce resistance; there are currently 21 drugs in the “pipeline” from the animal model preclinical testing phase to Phase III clinical trials (Working group for New TB Drugs 2013). Among these new TB drugs, one drug has been recently approved by the FDA for clinical use against MDR-TB, which is Bedaquiline (BDQ), by Johnson and Johnson [9, 10, 274, 275]. Despite these recent achievements, the majority of the drugs used today were discovered over 50 years ago. Due to the increase in drug resistant TB, it has become imperative to also explore novel approaches to improve the current treatment regimens.

The extensive length of treatment is thought to be caused by a proportion of bacilli that are refractory to treatment due their surroundings in the lung [14]. Bacteria are located within heterogeneous lesion types, and the advanced necrotic, fibrous lesions create a hostile environment for the bacteria that can reduce their susceptibility to drugs and can affect drug penetration throughout the lesion [205]. The salient characteristic of active TB in patients is the development of necrotic lesions that can progress to cavitation in the lung. The necrotic lesion consists of a central caseous necrosis region which is surrounded by a large cuff of epithelioid histiocytes mixed with lymphocytes [252]. Peripheral to the cellular cuff is the fibrous collagen matrix and within the collagen deposition signs of vascular remodeling can be observed. Other lesion types exist in human disease such as post primary tuberculosis lipid pneumonia, which is presented by an accumulation of foamy macrophages in alveoli typically found in the upper lung lobes [262], and polymorphonuclear alveolitis where the alveoli are filled with neutrophils with

the occasional macrophage [203]. Animal models that recapitulate the necrotic granuloma pathology tend to be large, cost-prohibitive, or difficult to work with, such as non-human primates, rabbits, minipigs, goats, and guinea pigs [17, 50, 154, 155, 162]. In order to model multiple lesion types seen in TB patients in an animal model, which is small and easily manipulated, a novel mouse model using the C3HeB/FeJ mouse strain, has been shown to present caseous necrotic lesions when aerogenically or intravenously infected with MTB [181, 193]. The mouse strain is characterized by a *de novo* mutation in the sst-1, which is the super susceptibility to tuberculosis-1 region [192]. In mice that lack a functional sst-1 allele, a large subset of macrophages are non-functional which allows for a rapid progression of early infection. This results in a high inflammatory response and influx of neutrophils in the lungs of infected animals [131, 197].

C3HeB/FeJ mice infected with MTB will develop three distinctive lesion types after about 6-8 weeks of aerosol infection. The three lesions types can be histologically distinguished as follows. Type I lesion is observed as the classical necrotic granuloma with a defined eosinophilic core, fibrotic collagen rim, and neo-angiogenesis. Lesion type II is observed as the highly inflammatory, uncontrolled lesion with neutrophilic dominance. Types I and II lesions have been shown to have distinct regions of hypoxia, the core of the necrotic granuloma is possibly nearly anoxic [131, 247]. And type III lesions are observed as cellular lesions with a mixed composition of mononuclear cells (lymphocytes / macrophages) (Driver, chapter 3 manuscript in preparation). We described earlier that C3HeB/FeJ mice when infected with a low aerosol dose (50-75 CFU/mouse) will develop consistently necrotic lesions 6-10 weeks post infection [131] (Driver et al. submitted, Irwin et al. submitted). These mice have a refractory

response to single drug treatment and a higher frequency of resistant bacteria in the lung and spleen [131].

Certain pathological features as seen in the lesion type I in lungs after TB infection are remarkably similar to what is seen in solid tumors, such as carcinomas, melanomas, and neuroblastomas [276]. These neoplastic tumors are hypoxic, centrally necrotic, develop a complex capillary network, and show an inflammatory mononuclear response [253, 277]. The tumor stroma is a supportive structural capsule around the tumor made of an extracellular matrix, consisting of cancer-associated fibroblasts (CAF), tumor-associated macrophages (TAMs), tumor-associated neutrophils (TANs), fibronectin, and collagen [278, 279]. The stroma is a contributing factor to drug resistance by creating a physical barrier to treatment [280, 281]. Solid tumors have attributes that create a specific environment such as non-functioning lymphatics and neo-angiogenesis which is characterized by the tumor blood vessels being tortuous and highly irregular [282, 283]. The tumor blood vessels are composed of defective endothelial cells with wide fenestrations, they have irregular vascular alignment, lack a smooth muscle layer and innervations [284-288]. This leaky vasculature leads to a phenomenon known as enhanced permeability and retention (EPR). These abnormal blood vessels proliferate predominately at the tumor periphery and this phenomenon leaves many central areas of the tumor avascular [284]. This lack in vascularity leads to un-perfused regions, which creates microenvironments that are devoid of oxygen, are low in pH, and gives rise to necrosis [289, 290] which ultimately leads to decreased drug efficacy and tumor progression.

To compensate for the physical barriers in solid tumors, over 20 nanomedicines have been approved for use in oncology by the FDA [291]. Nanomedicines have the advantage of extended drug-exposures, controlled drug-release kinetics, and improved patient compliance due

to less frequent dosing schedule [292-294]. Also many chemotherapeutics have adverse side effects that are diminished with more direct delivery approaches of the nanoparticles to tumors [289]. The liposomal formulations increase the therapeutic index of many antineoplastic drugs, such as the pegylated liposomal doxorubicin and liposomal daunorubicin [291, 295]. Liposomal formulations have had moderate success in the treatment of ovarian cancer and Kaposi's sarcoma [296, 297]. A recent study has shown improved tumor penetration of doxorubicin in a dextran-aldehyde nanocarrier formulation [293].

In order to target a liposome to a certain organ, tissue or cell type, the amphiphile bilayer of the liposomal nanoparticle allows for conjugation of different types of targeting ligands. Antibodies and antibody fragments, small molecules such as folate, sugars, and even nucleic acids can be conjugated to nanoparticles (Figure 4.1) [298, 299].

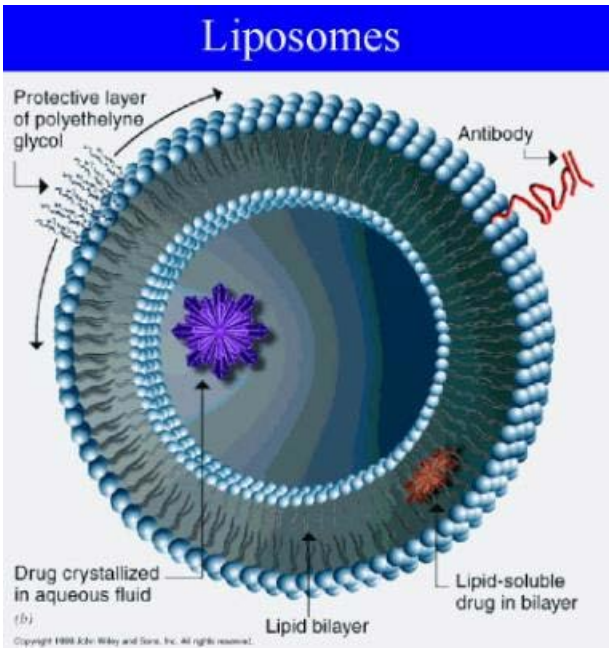

Figure 4.1. Example of a targeted drug containing nanoliposome [300].

Folic acid antagonists have been used as an important co-factor in cancer treatments even prior to the era of nanoparticles [301]. The folate binding protein, a glycosylphosphatidyl-inositol-anchored cell surface receptor for the vitamin folic acid, is overexpressed in many human cell types, such as macrophages during inflammation [302, 303]. This overexpression of folate binding protein can be exploited as a homing target for folic acid bound liposomes. This creates an effective targeting mechanism to direct liposomes to the site of inflammation.

The morphology of solid tumors and type I necrotic granulomas observed in C3HeB/FeJ mice show striking similarities, which may result in similar challenges in terms of drug delivery to the caseum of the necrotic tumor/lesion. Necrotic lesions of TB infected Kramnik mice have similar characteristics of hypoxia, central necrosis, a decreased drug responsiveness, lack in vacularization as solid tumors that are devoid from blood flow due to interstitial fluid pressure (IFP). Like solid tumors, TB granulomas contain non-functional, foamy macrophages surrounding the central core of the necrotic granuloma. The cellular layer of foamy macrophages is delineated with a collagen rim, which contain functional macrophages through the collagen depositions as well on the exterior. It is also within the collagen rim that signs of neo-vasularization are apparent. These morphological similarities of collagen deposition, macrophage accumulation, and neo-angiogenesis of a cancerous tumor, which is also seen in a TB granuloma, piqued the interest of Merrimack Pharmaceuticals, a pharmaceutical company based in Cambridge, MA, in evaluating the potential application of liposomal nanoparticle drug delivery in order to treat TB. As with cancerous tumors, they hypothesized that the liposomes would accumulate mainly within macrophages (activated/foamy) and would directly deliver drug to the site of the granuloma. Scientists at Merrimack have previously shown benefit from targeted and

non-targeted delivery of liposomal formulations of chemotherapeutics including doxorubicin and irinotecan against solid tumors [304-307].

By using a folate-targeted liposomal nanoparticle drug delivery approach to TB our long-term goal is to achieve a highly, sustained drug release at the site of infection, thereby shortening extensively the treatment duration, and potentially reducing side effects of drug treatment. In this preliminary study, we evaluated the pharmacokinetics profiles of empty liposomes over time in plasma and different tissues of infected and uninfected Balb/c and Kramnik mice. In addition, we aimed to evaluate our hypothesis to show that the liposomal nanoparticles will predominantly target the macrophages of the necrotic granuloma in the lungs of TB infected Kramnik mice. To our knowledge this is the first experiment to evaluate liposomal nanoparticles as a drug delivery system for the treatment of TB.

4.2 – METHODS AND MATERIALS

4.2.1 Animals

See Methods in Chapter 2

4.2.2 Bacteria

See Methods in Chapter 2

4.2.3 Liposomal formulations

Proprietary information from Merrimack Pharmaceutical Inc. Cambridge MA

4.2.4 Aerosol infection and drug treatment schedule

For a preliminary tissue distribution study, C3HeB/FeJ mice were exposed to a low-dose aerosol infection with MTB. The mice were placed in a Middlebrook Aerosol Generation Device (Glas-Col Inc., Terra Haute, IN) [217]. Compressed air is pumped into the chamber through a venturi nebulizer, in which we placed 5 ml of suspension of bacteria at a concentration of 10^6/ml. After 30 minutes the nebulizer will be emptied and the mice will have inhaled to 50-100 bacilli into their lungs, which resulted in an average of 70, 133, and 84 (day 28, 60, and 90, respectively) bacteria at day 1 for three separate infections. In a subsequent, more extensive pharmacokinetic study with both C3HeB/FeJ and Balb/c, mice were exposed to a low-dose aerosol infection with MTB, which resulted in 43 average bacteria at day 1.

The goal was to study the liposomal distribution at various stages of lesion developed; an early time point when only cellular lesions were present, an intermediate time point when necrosis had developed and a late time point with severe and highly necrotic, fibrotic lesions. Thereto, in the initial study C3HeB/FeJ mice were separated into three infection groups (28, 60 and 90 days post-aerosol infection) resulting in three stages of infection at sacrifice. Ten days prior to sacrifice mice receiving the targeted liposomes are transitioned to a sterile folic acid free diet (Dyets, Bethlehem, PA). Mice were injected (IV) with either untargeted or folate-targeted liposomes Cy-5 (fluorescently far red) 24 or 48-hour prior to sacrifice by CO_2 inhalation.

A more thorough pharmacokinetic experiment was performed on C3HeB/FeJ and Balb/c mice after 10 weeks of infection. Both mouse strains are IV injected with a combination of non-targeted Cy-3 and targeted Cy-5 (fluorescent orange and far red, respectively), non-targeted Cy-5 and targeted Cy-3, and a control dual non-targeted Cy-5 and Cy-3 (data not shown). The dual injection allows for tracking of the targeted liposomes. Mice were sacrificed by CO_2 inhalation

after 6, 24, 48, 96 and 168 hours post injection. Mice with targeted liposomes were on a folic acid free diet (Dyets, Bethlehem, PA) 10 days prior to injection with liposomes.

4.2.5 Enumeration of bacterial load of the lungs

See Methods in Chapter 2

4.2.6 Pathology and microscopy

At every sacrifice point, the animal is centrally perfused first with phosphate buffered saline (PBS) with 0.04% EDTA, followed by perfusion with 4% paraformaldehyde in PBS placing an 18 gauge needle in the right atrium. Whole lung, excised granuloma, spleen, left liver lobe, left kidney, and heart are collected from all animals. After 48 hours of fixation, tissues were sent to Merrimack Pharmaceuticals for further processing, immunostaining, and imaging of liposomes.

Tissue sections were embedded in paraffin and cut to 5 μm thickness on a microtome. Subsequent tissue sections were mounted on glass slides, deparaffinized and stained either with Hematoxylin and eosin (H & E) and Sybr gold fluorescent stain. Fluorescent sections were visualized using a Nikon Intensilight mercury vapor lamp and scanned using a Nikon TE-I motorized microscope controlled by Nikon NIS Elements software (Nikon, Melville, NY) with FITC, TRITC and DAPI filters. Light microscopy sections were visualized using an Olympus BX41 with Olympus DP70 camera controlled by Olympus DP Software (Olympus, Melville, NY) at Colorado State University.

Slides immunohistological stained with anti-CD31 and Cy-5 were visualized at Merrimack Pharmaceuticals (Cambridge, MA).

4.2.7 Staining procedures

Lung tissue sections were stained at Merrimack by Violette Paragas to visualize the liposomes, endothelial cells, and nuclei. The slides were rehydrated in phosphate buffered saline (PBS) for five minutes followed by incubation with rat anti-mouse CD31-Cy3 (1:100) in DaVinci antibody diluent for 4 hours at room temperature. After wash with PBS, a secondary incubation with goat anti-rat Alexa 555 (1:500) in DaVinci antibody diluent for 30 minutes at room temperature. Excess stain was rinsed with PBS, and then stained with Hoechst for 5 minutes at room temperature. Wash excess stain with PBS and mount with ProLong Gold mounting media (Invitrogen, Grand Island, NY).

The novel acid-fast staining method using the Sybr Gold (Invitrogen, Grand Island, NY) fluorescent dye was used as previously described by our laboratory. Briefly, the dye is diluted 1:1000 in a stain solution of phenol (8 g), glycerin (60 mL), isopropanol (14 mL), and distilled water (26 mL). The slides were heated on a block at 65^0C for 5 minutes and then cooled at room temperature for an additional 5 minutes. The tissue sections were washed with acid alcohol (0.5% HCL, 70% isopropanol, 29.5% water) for three minutes, then washed with water and counterstained with Hematoxyin QS for 5-10 seconds. The excess hematoxyin was washed away with ddH2O and slides were subsequently stained with DAPI (200 ng/mL final concentration) ~10 minutes and washed again with water. Slides were mounted with Prolong Gold antifade mounting media.

All drug measurements of fluorescently tagged liposomes in plasma and organs of infected mice was performed at Merrimack by Dmitri Kirpotin.

4.3 – RESULTS

4.3.1 Preliminary results on liposomal distribution in mouse tissues

4.3.1.1 Bacterial burden

To determine the distribution of liposomes post intravenous injection, we used macrophage folated-targeted and non-targeted liposomes in infected C3HeB/FeJ mice. To study liposomal distribution at different stages of lesion pathology, mice were sacrificed at either 28, 60 and 90 days after three separate aerosol infections. The mice, at these three distinct stages of infection, were injected with the liposomes and allowed to rest for either 24 or 48 hours to allow maximum distribution. At the time of sacrifice the mice had reached a bacterial load ranging from 6.5 - 8.8 log10 CFU in the lungs (Table 4.2).

Table 4.2. Bacterial burden in *M. tuberculosis* infected C3HeB/FeJ mice at sacrifice

Infection Group	Log10 CFU
Day 28	8.89
Day 60	6.40
Day 90	6.64

4.3.1.2 Advanced lung pathology of tuberculosis infection over time in C3HeB/FeJ mice

The goal was to study the liposomal distribution at various stages of lesion developed. Liposomes were injected either at 24 or 48 hours prior to sacrifice in order to find the timepoint giving the most optimal liposomal distribution in the lesion. The tissue from the 48-hour post injection time point yielded the most distinctive signal for both the day 60 and 90 days post-aerosol infection.

At the early time point (28 days post aerosol), mice show only one single lesion type which are the small, early inflammatory lesions as expected [131, 308].

At the later time points (60 and 90 days after aerosol infection), we can distinguish three different lesion types in the lungs of the C3HeB/FeJ mice. The distinct lesion types can be distinguished by the proportions of specific cell types in the early lesions, such as neutrophilic infiltrates, macrophages, and lymphocytes. We have classified the lesions in the C3HeB/FeJ mice into three morphologically distinct types, as follows: I) the classical granuloma with discrete necrotic core and fibrotic collagen rim, II) the highly uncontrolled inflammatory lesion with neutrophilic dominance, and III) the cellular lesion with mixed mononuclear cell composition (lymphocytes/macrophages).

For this particular study, we focused primarily on the type I necrotic lesions at later timepoints post aerosol infection. From the day 60 time point on, the type I lesions are well developed, with prominent large, necrotic granulomas with a complex collagen rim (Figure 4.2A, B, and C). The type I lesions have a large central necrotic region, which is surrounded by a rim of karyorrhectic neutrophils and an outer ring a foamy macrophages. The lesion is encased with fibrils of collagen and sporadic blood vessels. The collagen fibrotic rim is lined on the inside by the foamy macrophages, and dispersed throughout the rim as well as outside functional macrophages are located. The foamy macrophages within the necrotic granuloma are heavily burdened with acid-fast bacteria.

At 90 days post infection, the mice had predominantly type I lesions and there were also a small number of type II lesions in the lung parenchyma. Type II lesions consists of high neutrophilic accumulation and high macrophage burden, do not show the collagen rim or the foamy macrophage layer (Figure 4.2D).

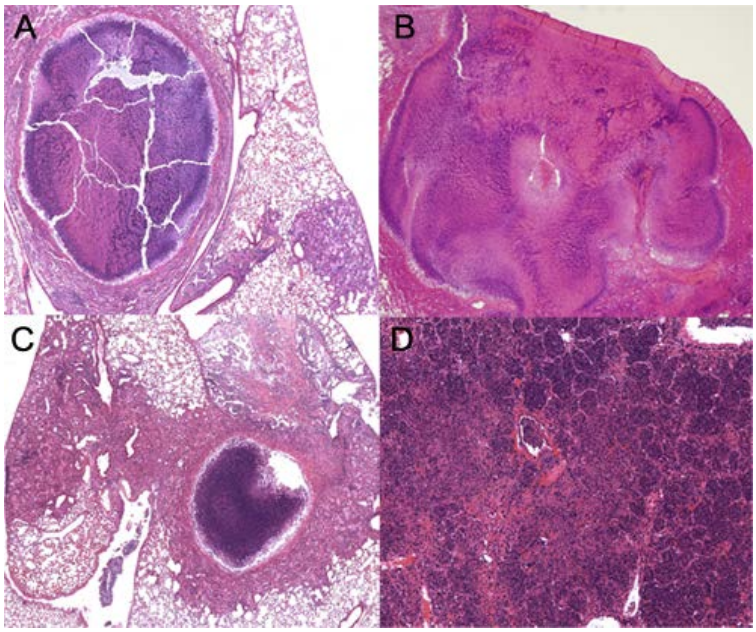

Figure 4.2. Late stage necrotic lesions from C3HeB/FeJ mice infected with Mycobacterium tuberculosis. (A) Type I necrotic granuloma with well-developed collagen rim and necrotic core 4x. (B) Coalesced necrotic granuloma, type I, less organized but retains collagen rim and foamy macrophages ring 4x. (C) Early necrotic granuloma, core consists entirely of necrotic cellular debris with large extracellular matrix 4x. (D) Highly destructive type II necrotic alveolitis 4x. Hematoxylin and Eosin.

4.3.1.3 Bacterial location in the necrotic granulomas

Late stage lung tissue was stained with fluorescent Sybr Gold stain to detect acid-fast bacteria in the necrotic granulomas. In figure 3 is the clear observation of bacteria in the cellular layer of foamy macrophages (Figure 4.3A) and throughout the necrotic core (Figure 4.3B) of the necrotic type I granuloma. The type II lesion had a high bacterial burden throughout the lesion (Figure 4.3C).

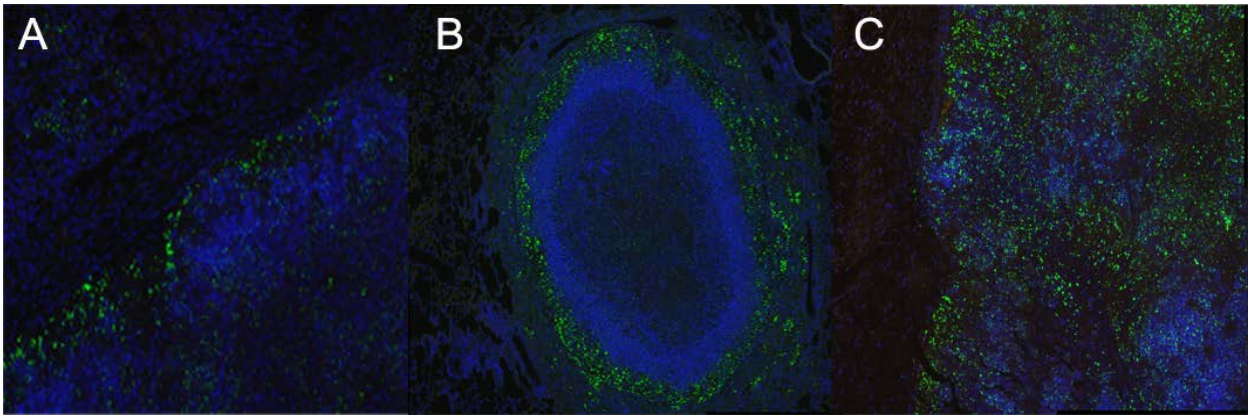

Figure 4.3. High concentration of bacteria stained with Sybr Gold (fluorescent green) in type I and II lesions. (A and B) Acid-fast Sybr Gold stained bacteria in the foamy macrophages of the rim of the type I lesion 20x (A) and the whole necrotic granuloma 10x (B). (C) Type II lesion with uncontrolled bacterial growth and cellular debris within the alveolar spaces 20x. Sybr Gold and DAPI

4.3.1.4 Liposomal distribution in necrotic granuloma tissue

Lung tissues were also processed by Merrimack Pharmaceuticals to study the spatial location of the liposomal nanoparticles within the necrotic granuloma at 60 and 90 days post aerosol infection after 48 hours post injection. Targeted liposomes containing folic acid in their outer lipid layer were used to bind to the folic acid receptors expressed on endothelial cells surrounding the lesions by coating the nanoparticle with folic acid [309]. Feeding the mice a folic acid free mouse chow will leave the binding receptors on macrophages surrounding and within the necrotic granulomas open. The liposomes with folic acid moieties are the only available source of 'free' folic acid and easily target and bind to the open receptors on the macrophages. The non-targeted the liposomes were expected to be more prevalent in the vasculature of the tissue. These microscopic assessments are preliminary, as more sections and more have to be studied to make firm conclusions.

At 60 days post aerosol infection, the initial assessment showed that both the targeted and the non-targeted liposomes could be distinguished in the lung sections of the TB infected mice

(Figure 4.4). In figure 4.4A, the non-targeted liposomes are visualized as pink staining and remain in the vasculature, which surround the necrotic lesion within the lung parenchyma. The folate-targeted liposomes in figure 4.4B demonstrate that the liposomes have migrated from the vasculature to the cellular matrix surrounding the necrotic type I lesion. The targeted liposomes appear to remain in the active macrophages that surround the granuloma (Figure 4.4C). These macrophages have been determined to be active based on positive F4/80 IHC staining performed by Dr. Gonzalez-Juarrero (data not shown). Directly interior of the functional macrophages are the heavily bacterial burdened foamy macrophages which has shown preliminary data of liposomal penetration.

Liposomal distribution at 90 days post aerosol infection was largely similar to 60 days post aerosol infection. The non-targeted liposomes in figure 4.5A seem to remain largely within the endothelial tissue surrounding a blood vessel on the outside of a necrotic lesion. The targeted liposomes are shown to more likely to penetrate the type II necrotic lesion in figure 4.5B. The targeted liposomes are present throughout the tissue. Type I lesions with targeted liposomes have distinct liposome penetration to the inner rim before the necrotic central core. At this time it is not possible to determine if the liposomes are in the foamy macrophages or the functional macrophages external to the collagen rim (Figure 4.5C).

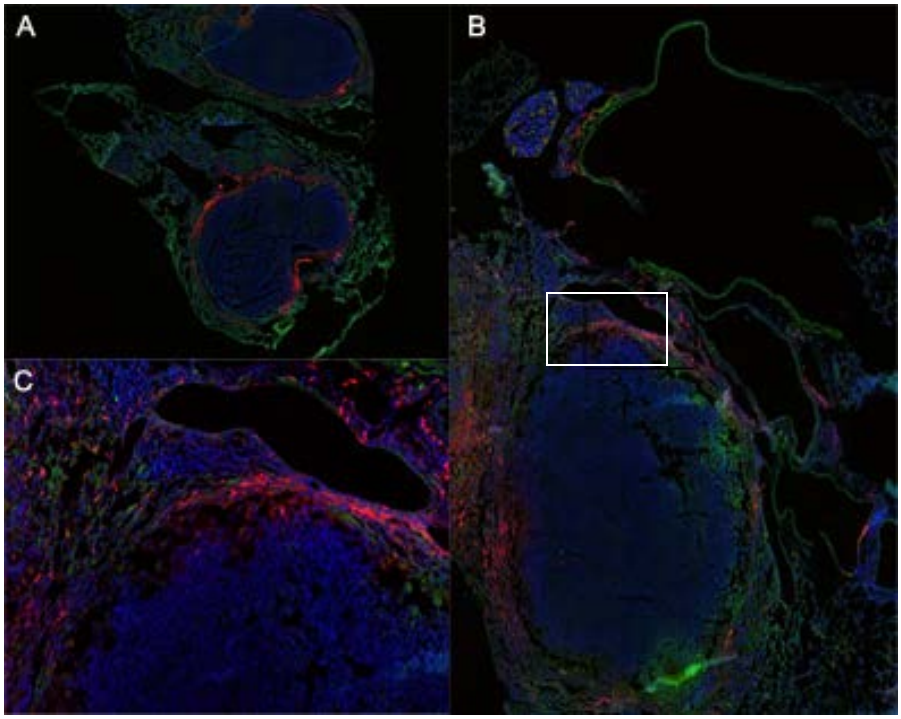

Figure 4.4. Liposomal distribution of non-targeted and targeted 60 days post aerosol infection. (A) Non-targeted Cy-5 liposome distribution remains within the endothelium1x (B) Targeted Cy-5 liposomes into the macrophages surrounding the necrotic granuloma 2x (C) Inset of targeted Cy-5 liposomes in the macrophages 10x (Images Propriety of Merrimack Pharmaceuticals, Cambridge, MA)

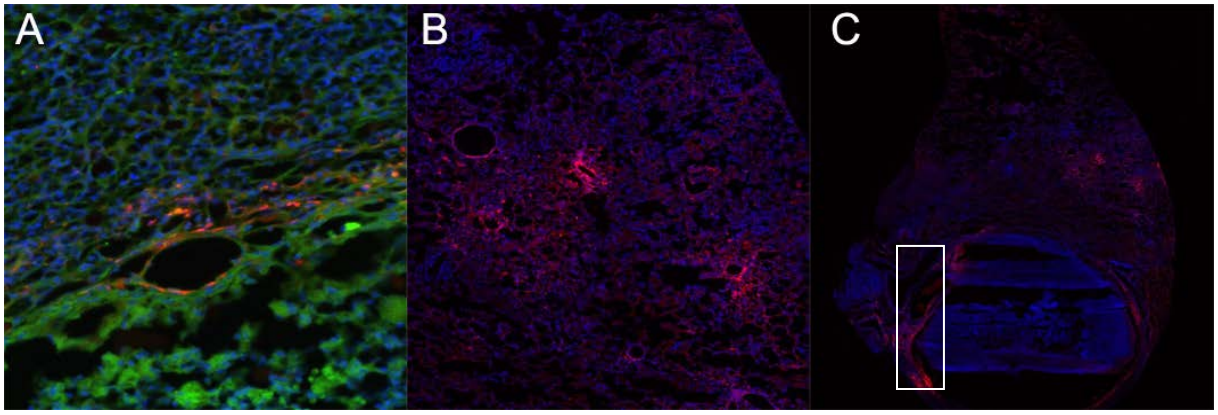

Figure 4.5. Liposomal distribution of non-targeted and targeted 90 days post aerosol infection. (A) Non-targeted Cy-5 liposomes trapped within the vessels surrounding the lesion 20x (B) Targeted Cy-5 liposomes in a type II necrotic alveolitis lesion 4x (C) Targeted Cy-5 liposomes in late stage type I granuloma 1x (Images Propriety of Merrimack Pharmaceuticals, Cambridge, MA)

4.3.2 Extensive pharmacokinetic evaluation of liposomal levels in C3HeB/FeJ and Balb/c mice

4.3.2.1 Liposomal tissue distribution

To examine the ADME properties (absorption, distribution, metabolism, and excretion) of the liposomes, a pharmacokinetic study was performed using infected C3HeB/FeJ and Balb/c mice at 10 weeks post aerosol infection. Mice were sacrificed at 6, 24, 48, 72, and 168 hours after injection of the liposomal formulation, and plasma and various organs collected.

The results showed the highest liposomal levels in plasma and livers of the infected animals at the first measured time point (6 hours after injection). High liposomal levels were maintained in the liver. In the C3HeB/FeJ mice, both the targeted and non-targeted liposomes are cleared from the plasma by 24 hours post injection. There are detectable levels of non-targeted liposome in the plasma at 24 hours but these are greatly reduced compared to the 6 hour time point. The targeted liposomes are cleared after 6 hours in plasma (Figure 4.6). The Balb/c mice show a similar profile of tissue distribution, prominent accumulation in the liver throughout 168 hours and a peak in the plasma at 6 hours for both non-targeted and targeted (data not shown).

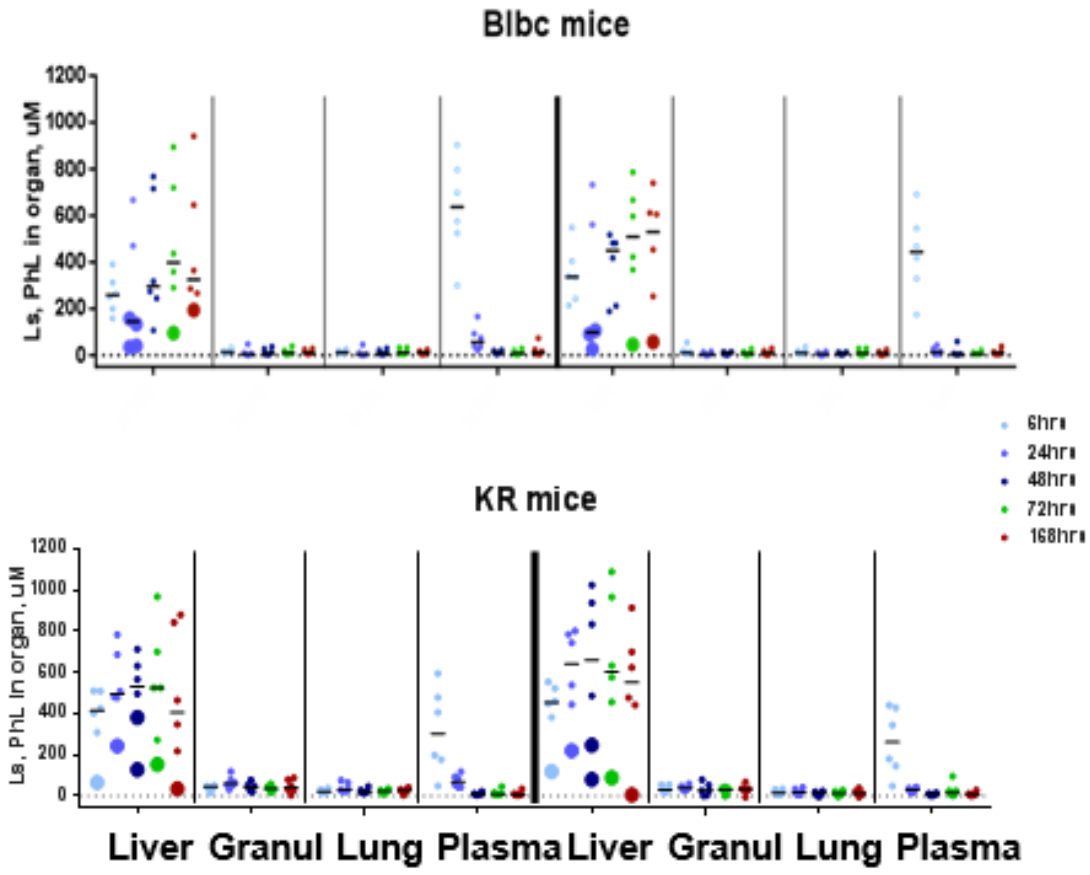

Figure 4.6. Liposome tissue distribution is predominantly in the liver for both C3HeB/FeJ and Balb/c mice for targeted and non-targeted liposomes. Balb/c mice and C3HeB/FeJ mice have measureable liposomes in the liver and 6 hour plasma collection in both targeted and non-targeted liposomes. (Data Propriety of Merrimack Pharmaceuticals, Cambridge, MA)

4.3.2.2 Rapid liposome clearance in infected mice

The next goal of this study was to assess tissue distribution of the liposomes over time in both infected Balb/c and C3HeB/FeJ mice. For this purpose, mice were sacrificed at 6, 24, 48, 72, and 168 hours and plasma and whole lung and excised granulomas were collected. The results showed that both C3HeB/FeJ and Balb/c mice had significantly increased clearance of the liposomes in the plasma (Figure 4.7) for all groups. The liposomal formulations used for the MTB infected C3HeB/FeJ and Balb/c mice had a reduced half-life of approximately 10 hours.

Measuring liposomes within excised granulomas and grossly uninvolved lung tissue showed similar liposomal levels for all tissue types and for both mouse strains. The measureable percentage of the injected liposomes at the first time point (6 hours) was less than 4% ID/g (Injected Dose/gram) for all targeted/non-targeted combinations (Figure 4.8). The low measurements may be due to the sample size, early clearance prior to first measurement, or poor targeting of the folate liposome.

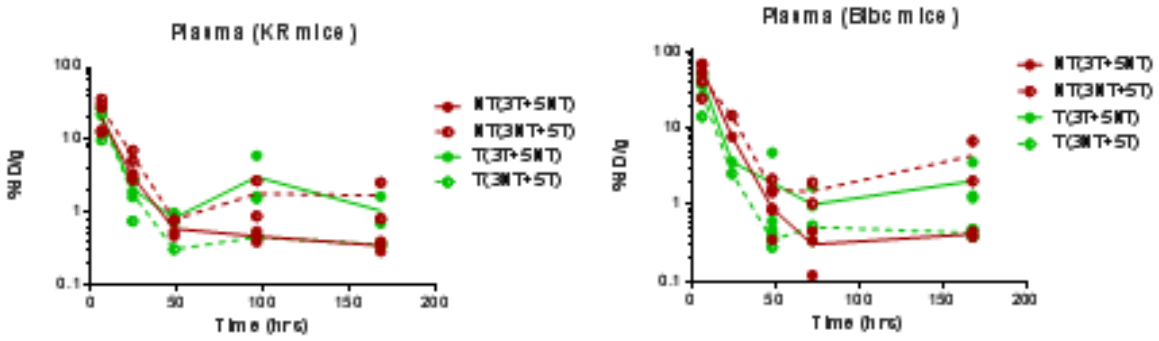

Figure 4.7. Rapid liposomal clearance in infected C3HeB/FeJ and Balb/c mice in the plasma. Combination of Cy-3 and Cy-5, targeted and non-targeted labeled liposomes measured as % injected dose per gram of tissue over hours in animal. (Data Propriety of Merrimack Pharmaceuticals, Cambridge, MA)

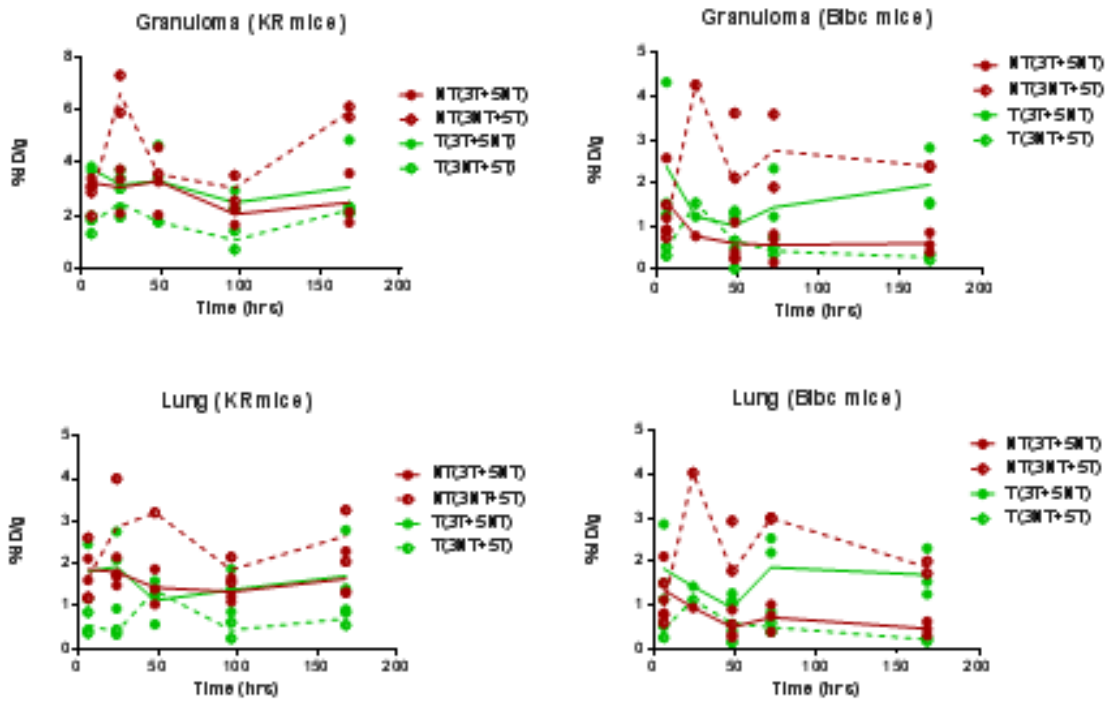

Figure 4.8. Low-level liposome detected in C3HeB/FeJ and Balb/c mice in both granuloma and healthy lung tissue throughout all time points. Combination of Cy-3 and Cy-5, targeted and non-targeted labeled liposomes measured % injected-dose per grams of tissue over hours in animal. (Data Propriety of Merrimack Pharmaceuticals)

4.4 – DISCUSSON

In this pilot study, and in collaboration with Merrimack Pharmaceuticals, we aimed to evaluate the distribution of a novel liposomal delivery approach at the cellular level in lung lesions by microscopy, and at the tissue level in TB infected animals using analytical tools. The liposomal formulations used for this study were pegylated liposomes targeted to macrophages by folic acid, were prepared by Merrimack Pharmaceuticals specialized in using liposomes for cancer therapies. For these initial studies, the liposomal formulations did not encapsulate drugs but fluorescent dyes in order to track the distribution. The striking similarities of the lung lesion types observed in TB infections and in solid tumors instigated this study. By using a mouse model, the C3HeB/FeJ strain, which more closely resembles the specific pathologic features of

human TB disease, we opted to evaluate this novel liposomal nanoparticle drug delivery system in a relevant *in vivo* TB mouse model.

The most prominent lesion in the C3HeB/FeJ mice (type I necrotic granuloma lesion) has many similarities to solid tumors in oncology. They both present with hypoxia, necrotic cellular material, fibrous collagen outer rim, and the development of a surrounding capillary network. C3HeB/FeJ mice were injected with the fluorescently labeled liposomes at different stages of infection with MTB with progression of pathology. To target liposomes towards macrophages, folic acid was anchored to the lipid bilayer of the liposomal formulation, which will bind to macrophages that over-express folic acid binding protein. Based on the fluorescent microscopic images, the location of the liposomes was studied within the different lesion types in the lungs. The specific location of targeted and non-targeted liposomes was ascertained in both the type I and II necrotic granulomatous lung lesions. At later stages of infection, we saw clear liposomal presence both in the lung and lesions [Figure 4.4 and 4.5]. It appeared as if the non-targeted liposomes remained predominantly in the vasculature surrounding the lesions, while targeted liposomes might have extravasated from the vessels into the foamy macrophages cell layer. These observations are preliminary at best and will need further thorough investigation by studying more sections per mouse and more animals. Initial confocal microscopy data suggests liposomes crossing the collagenous fibrils and entering the foamy macrophages, which is where large numbers of bacteria reside (data not shown). In our previous work, we showed that there are clearly two distinct macrophage populations (Driver et al., submitted). On the periphery of the necrotic lesion, there are functional macrophages that can be distinguished by expression of F4/80 [273] and lysozyme [251]. This is in contrast to the foamy macrophages which show high

expression levels of IL-10 [72] and the DEC-205 marker [310], and appear to be permissive to bacterial growth.

It has been shown that after intravenous injection, both the targeted and non-targeted liposomes achieve high levels in the liver as well as in the plasma, before liposomal levels reach the lungs and lung lesions. The first pharmacokinetic study determined the concentration of liposomes in plasma, liver, spleen, lung, and excised granuloma over a 4-day period in uninfected mice. The results showed that initially the liposomes enter the plasma with a peak at 6 hours that is absent by 24 hours. In the liver, the liposomal level is highest and maintained throughout analysis (Figure 4.6). It should be noted that at the earliest measured time point of 6 hours there was little to no measureable liposomes in the grossly non-involved lung and granuloma tissue.

This lack of measurable liposomes in the lung and granuloma even at 6 hours might be problematic. By examining the % injected dose of the liposome over time, a very short half-life is observed in the plasma (Figure 4.7). This short half-life in the plasma translates to low levels of liposomes in the lung tissue throughout time (Figure 4.8) for both C3HeB/FeJ and Balb/c mice. This rapid clearance of the liposomes was a surprising finding and is not entirely clear at this time. We speculate that this may due to the primed immune system of the infected animals. This may also indicate that the liposome were in fact not reaching the target since both targeted and non-targeted had similar detectable low-levels. Based on shared information from Merrimack Pharmaceuticals Inc., it has been determined that liposomes IV injected into tuberculosis infected mice are cleared from the mice much faster than in cancer mouse models previously tested. In previously determined liposomal formulations the half-life of the liposomes in the plasma is approximately 60 hours for neoplastic models (data not shown). A phenomenon

known as accelerated blood clearance (ABC) is seen in multi-dose PEGylated liposomes and is due to an increased IgM antibody response [311-313]. This is likely not the reason to explain the more rapid clearance in our study as we only used a single dose. A more likely rationale is the presence of immune cells (such as Kupffer cells, specialized macrophages) in the liver which are known to easily trap nanoparticles and lower tissue penetration [314]. To confirm this hypothesis another pharmacokinetic study was performed on naïve and infected Balb/c mice. This study did indeed confirm that infected mice had an accelerated rate of clearance in the plasma and organs (data not shown). To counter the rapid clearance of the liposomes, adjustments are now being made to the exterior of the liposomes to prevent early phagocytosis. Delaying this response will allow for greater drug exposure and keeping the intermittent dosing schedule to fewer dosages. These approaches are currently underway.

Liposomal nanoparticles as a novel method for drug delivery for specific infectious diseases might have promise for more local drug delivery with fewer side effects. For an MTB infection, we were able to show that liposomes track to the lungs and are able to accumulate near the vicinity of the necrotic granuloma in the lungs of the infected C3HeB/FeJ mice. Changing the composition of the liposomes may be needed to extend the liposome distribution allowing for longer drug exposure and better-controlled drug release. Further research is currently being performed to determine the bactericidal efficacy of liposomes carrying TB drugs. At this time it is believed that drug delivery by liposomes could have an effect on treatment duration, reduction of bacterial resistance and medication side effects, thereby improving patient compliance.

4.5 – FUNDING

Funding provided by Merrimack Pharmaceuticals Inc., Cambridge, Massachusetts Grant "Assessment of liposomal drugs alone and in combination for TB efficacy".

CHAPTER 5 - ALTERNATIVE TREATMENT APPROACHES TO AUGMENT CLASSICAL THERAPY BY ALTERING HISTOPATHOLOGY

5.1 – INTRODUCTION

In active tuberculosis (TB) disease, one of the most prominent lesion types is the necrotic granuloma The granuloma can be seen as a way for the host to sequester the bacteria in an isolated region in the lung, whereas it is hypothesized, by some, to be a successful feature of survival for the MTB [260]. A granuloma in the initial stages of disease is recruiting high numbers of cellular infiltrates of NK cells, neutrophils, activated macrophages, non-activated macrophages, lymphocytes and others [160]. These immune cells produce high levels of cytokine and chemokines to recruit more inflammatory cells [315]. All of these immune cells promote inflammation and remodeling of the lung tissue to cope with the infection [265, 316, 317]. The constant remodeling of the lung tissue can be seen by the perpetual changes to collagen as we observed earlier by picrosirius red staining which stains recently deposited as well as established collagen in the C3HeB/FeJ mouse model when infected with MTB [131]. For certain drugs it has been shown very elegantly by Veronique Dartois et al. using MALDI-MRM-MS [205], that a drug such as Moxifloxacin (MXF), accumulates in the tissue surrounding a necrotic lesion and that the collagen rim, angiogenesis, and cellular make up of the granuloma may be acting as a barrier to allow drug penetration

Necrotic granulomas, in particular cavitary lesions, are problematic for treatment of TB patients on this on several levels: cavitary disease has been shown to give high levels of transmission [159], they are more difficult to treat with a higher rate of relapse, and have a higher resistance frequency within the cavitary lesion [256]. NHP can produce cavitary lesions

but do so variably [204, 213]. Rabbits, goats, and pigs are able to produce cavitary lesions more reliably but are still cost prohibitive to work with for pre-clinical drug development [160, 176].

The C3HeB/FeJ mouse strain or Kramnik mouse model has the ability to develop the key necrotic granulomas with a high frequency [181]. Usually these necrotic lesions do not progress further into cavitary disease and this remains an infrequent event (only one or two mice out 100 develop a cavitary lesion). If we would be able to increase this frequency, this would better recapitulate all aspects of human disease. These would create new opportunities to study aspects of TB disease treatment largely left unanalyzed at this time.

The effects of collagen disruptors have been researched with increasing regularity for chronic diseases like myocardial fibrosis [318], idiopathic fibrosis [319], cirrhosis [320, 321] and for cancer [254]. These compounds have the ability to prevent the development of host collagen which allows for more normal lung function and thereby increasing the efficacy of drug treatment. Losartan potassium (LK), an angiotensin II receptor antagonist, is being used clinically for chronic heart failure and hypertension by altering the renin-angiotensin-aldosterone axes which prevents vasoconstriction [322]. Further downstream effects of blocking the AGTR1 (angiotensin II receptor, type 1) (Figure 5.1) include the inhibition of fibrinogen, collagen I, fibronectin, and collagen II production and suppression of TGF-β1 from thrombospondin-1 [323].

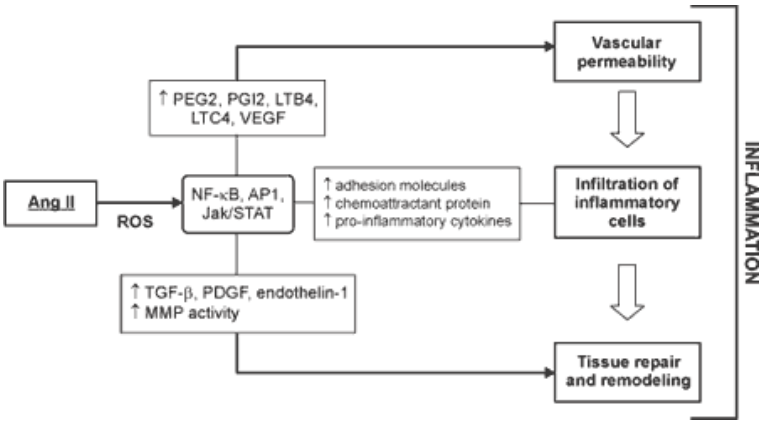

Figure 5.1. Schematic of the angiotension receptor II pathway showing the downstream effects of upregulation of TGF-β and the eventual increase of fibrinogenesis [324]

It has been shown that LK is able to significantly reduce the fibrotic rim from human fibrosarcoma implanted in mice when injected intraperitoneally for 2 weeks [325]. LK has an oral bioavailability of 35% [326], due to first pass metabolism. LK is metabolized by CYP3A4 and CYP2C9 into a highly active carboxylic acid metabolite E-3174 [327]. This would mean that in light of TB treatment, this could result in the faster clearance of compounds affected by CYP enzymes, such as rifampin. Mice treated with a single dose of damaging bleomycin (another fibrolytic compound) with follow up treatment of LK showed conflicting results in different studies [328, 329]. One of the studies showed effect of LK to reduce the fibrotic effects of bleomycin [328], whereas the second study determined that using LK limited the effect of treatment of pulmonary fibrosis [329]. To our knowledge collagen disruptors have not been used in the treatment of TB. Another research group using an indirect approach to alter the collagen deposition has used anti-TNFα therapy in combination with standard drug treatment, which showed that anti-TNF therapy hastened bacterial clearance with standard drug therapy [330].

Over the last years, more information has become available on the epidemiology, immunology, virulence, transmittability as well as the lung pathology of the diverse clinical TB

strains [331]. Many clinical strains show extensive cavitary disease in TB patients [332]. W-Beijing strains are thought to have increased pathogenicity, an inclination towards drug resistance, and appear less response to the BCG vaccination [169, 333]. In order to generate cavitary disease, animals such as rabbits, goats, and pigs, require infection with highly virulent clinical strains [154, 160, 176]. The geographic locations and epidemiological studies have divided MTB strains into six major phylogenic clades [334-338], East African, East Asian, Euro-American, Indo-Oceanic, and 2 West African (*M. africanum*) clades [336]. Significant clade specific differences have been performed more recently studied in animal models by studying the survival, bacterial burden, histopathological changes, and immunological response [232, 339].

W-Beijing strains are within the East Asian clade and are the source of several recent virulent, outbreaks worldwide [340]. Currently, W-Beijing strains are identified by their regions of difference (RD), which are large regions of sequences prone to polymorphisms. Over 30 RDs have been described and strains have been classified based on genomic deletions [341]. For the mouse studies described below, we opted to use TB strains with known diverse characteristics regarding transmittability and progression of disease. Several reports on population studies based in San Francisco, CA [341, 342] and Houston, TX [343] have reported several TB strains that cause pulmonary disease with a high incidence of cavitary formation. The sublineages from San Francisco (RD): RD207 and RD181 produced advanced necrotic granulomas in experimental guinea pig infections [165]. RD207 sublineage was reported to be highly virulent and highly transmissible. The population studies showed RD207 had the highest incidence of secondary infection [165]. In the guinea pig model, it produces multiple highly necrotic lesions within 30 days [165]. The RD181 sublineage is a less virulent sublineage in humans and in the guinea pig under experimental conditions [165]. The strains from the RD181 sublineage are able to control

inflammation, and the pathogenicity is milder. In 1995, a W-Beijing strain, now known as HN878, caused 3 disease clusters and infected over 60 people in Houston [170]. HN878 is highly virulent and is commonly used in rabbit models of TB infection [204] and has been shown to be hypervirulent in mice [344, 345].

Host immunogenic responses to W-Beijing strains have shown a reduced overall Th1 profile, specifically in IFN-γ expression levels [346]. It has since been determined that mice infected with HN878 initially produce a strong IFN-γ response that wanes and there is an increase in T regulatory cells, such as Foxp3+ [333]. There is considerable early Th1 expansion of CD4+ cells in mice infected with HN878. This phenomenon is seen in other W-Beijing strains, a large increase of mRNA expression of IFN-γ that wanes over time and showing a delayed upsurge in mRNA expression of Foxp3+ and other Th2 cytokines [345]. For other RD sublineages a similar pattern is observed. Highly virulent RD207 have high expression levels of Foxp3+ and low IFN-γ, whereas RD181 has increased expression of IFN-γ later in infection [165]. The significant differences observed in cytokine profiles observed within the W-Beijing East Asian clade in different animal models demonstrates that the importance of using clinical strains for pre-clinical testing and model development.

5.2 Study of an angiotensin II inhibitor to disrupt the collagen rim of a necrotic granuloma

As discussed in the introduction, LK is potent angiotensin II inhibitor with downstream effects to fibrinogen and collagen formation. LK has shown great promise in altering the fibrotic rim of cancerous tumors and idiopathic pulmonary fibrosis. We hypothesize that the same effects of LK on the disruption of collagen deposition in necrotic lung lesions could be translated into an augmentation of treatment efficacy for MTB. ***Our hypothesis is that the use of LK will disrupt***

the collagen rim of the necrotic lung lesions to allow for greater drug penetration thereby resulting in a greater efficacy by reducing the bacterial burden of the TB infected C3HeB/FeJ mice. Our approach will include the administration of LK prior to and in combination with TB drug therapy. Comprehensive analysis of the effects of LK treatment will include the enumeration of the bacterial load in the lungs, histopathology of the lung, distribution of collagen as well as the location of bacteria using staining techniques.

5.2.1 – MATERIALS AND METHODS

5.2.1.1 Animals

See Methods in Chapter 2

5.2.1.2 Bacteria and drugs

See bacterial preparation in Chapter 2

Isoniazid (INH) and moxifloxacin (MXF) were obtained from Sigma Chemical Co. (St. Louis, MO). Losartan Potassium (LK) was purchased from Santa Cruz Biotechnology, Inc. (Dallas, TX). Drugs were prepared for the treatment of the mouse models as described before [116]. INH, MXF, and LK were dissolved in sterile water.

5.2.1.3 Aerosol infection and drug treatment schedule

C3HeB/FeJ mice were exposed to a low-dose aerosol infection with MTB in a Glas-Col inhalation exposure system, as previously described [217], resulting in an average of 15 bacteria in the lungs for the first experiment and undetectable for the second experiment on the day of

exposure. Five mice were sacrificed the following day to determine the number of CFU implanted in the lungs.

For the first experiment the mice were treated with the following drugs: INH (25 mg/kg), LK (50 mg/kg), and INH+LK (25+50 mg/kg) for 6 weeks. There was a necessary drop in dose due to acute mortality for LK from 50 to 20 mg/kg at week 2 of treatment for the remainder of the first experiment, as a combination and single treatment. Drug treatment started 3 weeks post infection and occurred 5 days per week via oral gavage. Mice were euthanized after 3 and 6 weeks of treatment by CO_2 inhalation. For all mice, the whole lungs were homogenized and the bacterial load determined by serial dilution on 7H11 agar plates.

For the second experiment, 4 weeks post aerosol infection mice were treated with LK (20 mg/kg) for 2 weeks prior to drug treatment. After two weeks of treatment, mice were given the following drugs: MXF (100 mg/kg), LK (20 mg/kg), MXF without LK pre-treatment (100 mg/kg). Mice were euthanized after 2 and 5 weeks of treatment by CO_2 inhalation. For all mice, the whole lungs were homogenized and the bacterial load determined by serial dilution on 7H11 agar plates.

5.2.1.4 Enumeration of bacterial load of lungs and spleens

See Methods in Chapter 2

5.2.1.5 Pathology and microscopy

See Methods in Chapter 2

5.2.1.6 Staining procedures

See Methods in Chapter 2 for picrosirus red stain and Chapter 3 for H&E and Sybr Gold Methodologies

5.2.1.7 Stereology

Stereo Investigator 8.2 (MBF Biosciences, Williston, VT) was used to analyze lung tissue features: lung, lesion and collagen deposition, described in Ordway et al [162]. Briefly, stereological analyses of tissue sections were performed with the investigator blind to treatment groups. The stereology workstation consisted of a Nikon 80i Research Microscope equipped for brightfield and fluorescence microscopy with CFI objectives (2x/0.01 Plan Apo, 4x/0.2 Plan Apo, 10x/0.30 Plan Fluor, 20x/0.75 Plan Apo, 40x/0.75 Plan Fluor, 100x/1.40Plan Apo), 3-zxis computer-controlled stepping stage with linear grid encoders, Z-axis motorized specimen stage for automated sampling, PC with frame grabber board, color digital camera, 24-in monitor and stereology and virtual slice Zoomify software with the following; 3D serial section reconstruction, solid modeling, virtual slice, confocal and MRI modules. The lung and lesion area were determined using the area fraction factionator (AFF) method on representative hematoxylin and eosin (H & E) stained sections. The area of inflammation and collagen relative to the normal lung parenchyma was estimated from representative lung sections evaluated at 40X. A total of 7-10 fields are selected randomly by the computer (Figure 5.2) and a counting frame (550 μm^2) containing probe points with a grid spacing of 40 µm is used to define lesion, collagen, and lung. The data was expressed as the mean ratio of lesion area to lung area of all the animals within a treatment group.

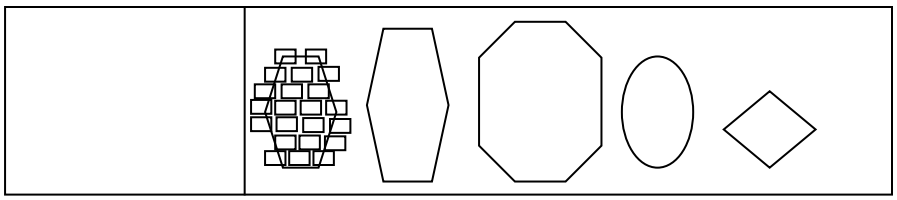

Figure 5.2. Schematic of stereology approach to lung slides using Stereo Investigator.

5.2.1.8 Statistical analysis

See Methods in Chapter 2

5.2.2 – RESULTS

5.2.2.1 Treatment of C3HeB/FeJ mice with Losartan Potassium alone as well as in combination in an initial small scale study

Susceptible C3HeB/FeJ mice infected with MTB Erdman began treatment at 3 weeks post-infection. At the start of treatment the bacterial burden was 6.73 ± 0.22 log10 in the whole lungs of five sample mice. At 6 weeks post aerosol infection untreated mice peaked at 8.75 ± 0.55 log10 with a 0.5 log decrease at 9 weeks to 8.27 ± 0.48 log10. Mice treated with INH alone for 3 weeks reduced the load to 8.01 ± 0.38 log10 in the lungs and further reduction to 6.29 ± 0.34 log10 after 6 weeks of treatment. LK treatment alone resulted in 8.57 ± 0.58 log10 after 3 weeks of treatment and reduced to 6.01 ± 0.45 log10 after 6 weeks of treatment. The LK group had a high mortality resulting in a survival bias of the remaining mice. These mice have a low bacterial burden and less severe histopathology. Combination treatment of INH+LK resulted in 6.6 ± 0.69 log10 after 3 weeks of treatment and 7.19 ± 0.47 log10 after 6 weeks of treatment (Figure 5.3).

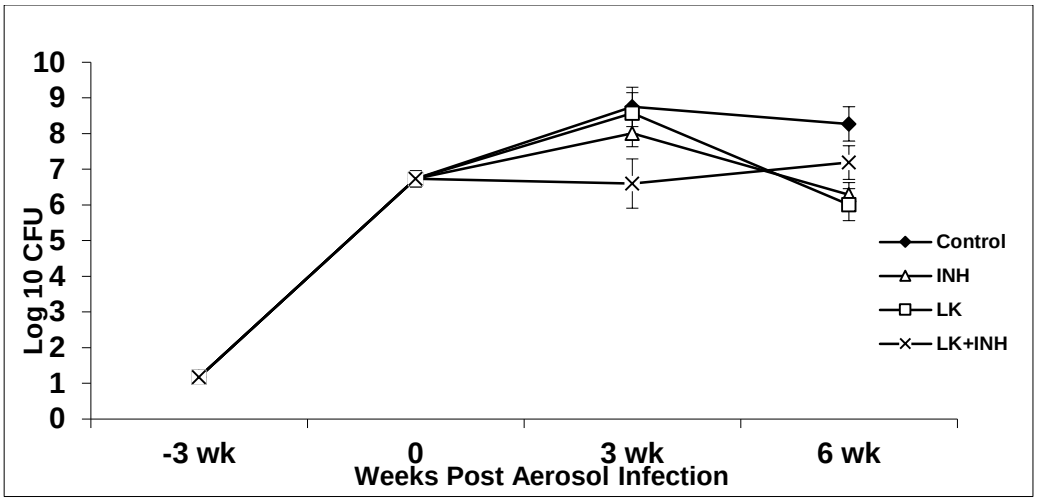

Figure 5.3. Losartan Potassium treatment, alone and in combination, in the lungs show no difference in the bacteria load in the lungs of TB infected mice.

The bacterial burden in the spleen was also investigated after 3 and 6 weeks of treatment. The bacterial numbers in spleens increased, from 5.52 ± 0.2 to 5.94 ± 0.25 log10 in the control mice. Mice treated with INH showed a reduction in bacterial burden of <1.5 logs from 4.2 ± 0.12 to 2.49 ± 0.13 log10. There was a 2-log reduction in bacterial burden in the spleen of mice treated with LK alone (5.89 ± 0.45 dropped to 3.85 ± 0.54 log10), as a result of the survival bias also observed in the lungs. Combination treatment of INH+LK resulted in 5.13 ± 0.19 log10 at 6 weeks and 4.8 ± 0.04 log10 at 9 weeks post aerosol infection (Figure 5.4).

At 4 weeks post aerosol infection (1 week of treatment) mice from all groups and controls began losing significant weight. Within 40 days post infection 13.88% of the mice needed to be humanely euthanized or succumbed to disease. At 45 days 11.78% and at 50 days 8.69% of the remaining mice required euthanasia due to declining weight and overall health condition (Table 5.1).

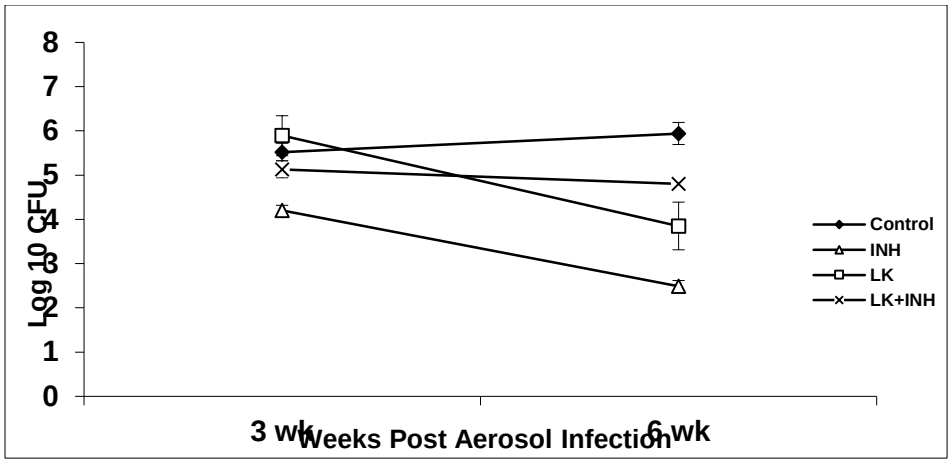

Figure 5.4. Losartan Potassium treatment, alone and in combination, in the spleen show no difference between treatment groups.

Table 5.1. Percentage of C3HeB/FeJ mouse mortality after infection with *M. tuberculosis*

Days Post Aerosol Infection	% Mortality
20 days	0
30 days	0
40 days	13.88
45 days	11.76
50 days	8.69
60 days	4.76

Large numbers of animals designated to treatment groups succumbed to disease within the 40-50 day timeframe, likely caused by the LK treatment. Twenty-nine percent of the control mice, 50% of LK single treatment, and 29% of combination of INH+LK mice required euthanasia or succumbed to disease within 60 days post aerosol infection (Table 5.2). The large number of mouse mortality in all treatment groups makes it difficult to draw conclusions on the efficacy of adjunctive therapy in combination or alone. The mice at the end of the trial showed lower bacterial burdens and had less pathological inflammation.

Table 5.2. Mouse mortality separated into specific treatment groups after the start of treatment at 3 weeks post aerosol infection

Treatment Group	# animals	% of group
Control	10	29
INH	0	0
LK	12	50
INH+LK	7	29

5.2.2.2 Stereological analyses of LK treated mice show no difference in collagen deposition

To calculate the area of disease and collagen in the lungs throughout treatment, the stereology approach was used to determine if there were relevant differences between the groups. As described in the Methods the Stereo Investigator 8.2 (MBF Biosciences, Williston, VT) was used to analyze lung tissue features: lung, lesion and collagen deposition. The lung and lesion area was determined using the area fraction factionator (AFF) method H&E stained sections. The area of inflammation and collagen relative to the normal lung parenchyma will be estimated from representative lung sections evaluated at 40X. A total of 7-10 fields are selected randomly by the computer (Figure 5.2) and a counting frame (550 μm^2) containing probe points with a grid spacing of 40 µm is used to define lesion, collagen, and lung. The data is expressed as the mean ratio of lesion area to lung area of all the animals within a treatment group.

Analysis of the stereology results showed the mice at the start of treatment, 3 weeks post aerosol infection; the pre-treatment group lung tissue was composed of 85% healthy lung parenchyma, 11% early lesion necrosis and 4% collagen. Three weeks of treatment results in relatively equivalent amounts of lesion (red bars) and collagen (green bars) in all treatment groups, 61%, 45%, 49%, and 52% and 8%, 8%, 9%, and 10% in control, INH, LK and INH+LK, respectively. By 6 weeks of treatment the lesion and collagen composition remained stable for all groups at 54%, 53%, 67%, and 52% and 16%, 14%, 8%, and 12%, for the control, INH, LK and INH+LK

groups, respectively (Figure 5.5). In summary, the stereology results from the different treatment groups were inconclusive in terms of observed differences in amount of necrotic lesion, collagen, and lung tissue.

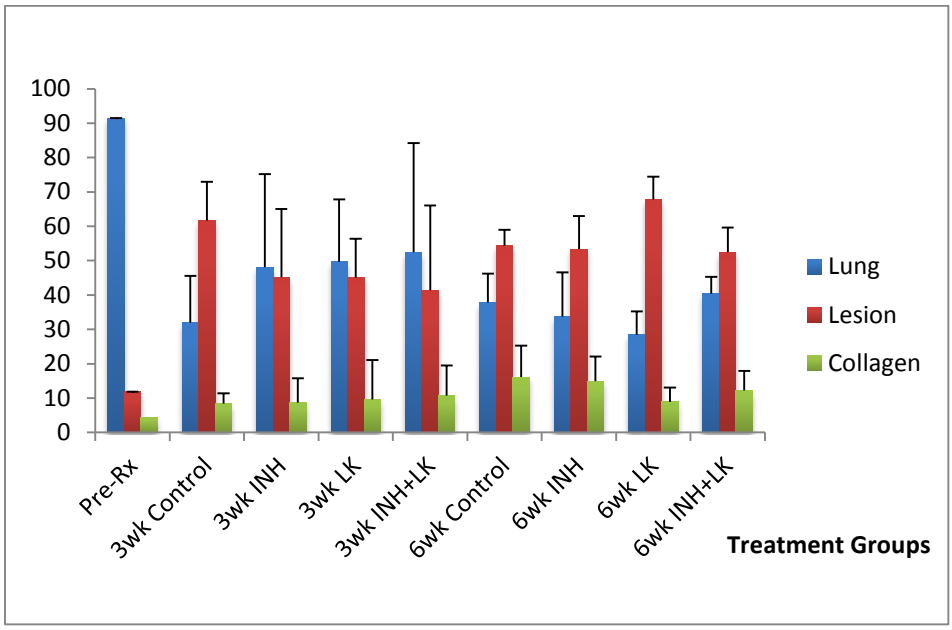

Figure 5.5. Average percent of tissue types show no difference between treatment groups over time. Collective measurement of lung parenchyma, necrosis, and collagen by stereology throughout infection.

5.2.2.3 Pathological analysis

Besides the quantitative histopathology analysis via stereology, we also assessed more qualitatively the potential changes in pathology by LK treatment. To investigate histopathology staining with H&E, picrosirus red, and acid-fast Sybr Gold staining techniques were used to study lesion progression, collagen deposition, and bacterial location. At the start of treatment the animals showed mainly cellular lesions consisting of foamy and epithelioid macrophages, lymphocytes, and neutrophils (Figure 5.6A and B).

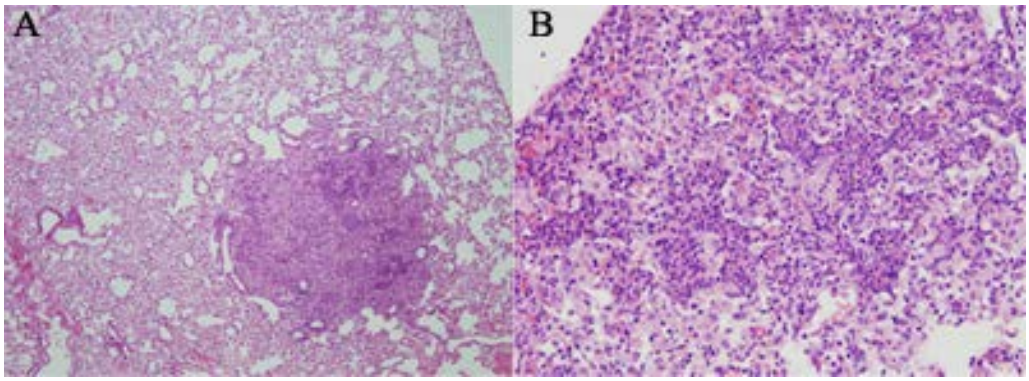

Figure 5.6. Cellular infiltrates with accumulation of neutrophils at the start of treatment. (A) A cellular lesion of foamy macrophages, lymphocytes, and neutrophils 10x. (B) A larger lesion of early necrosis, a high number of neutrophils with lymphocytes and foamy macrophages 10x

Three weeks of treatment resulted in a heterogeneous pathological response in the C3HeB/FeJ mice. Figure 5.7A is a visual representation of type III cellular lesions, composed of lymphocytes, epithelioid and foamy macrophages, as well as neutrophils, (as defined in chapter 3). Three weeks of LK treatment also showed type I lesions (as shown in Figure 5.7B) with a large necrotic lesion with a highly eosinophilic core, a foamy macrophage rim surrounded by collagen and neo-angiogenesis. Mice treated with INH alone and with INH+LK combination appear to have more type I lesions compared to the other lesion types at 3 weeks of treatment (Figure 5.7C and D).

After six weeks of treatment, the animals from drug treatment groups had a heterogeneous pathological response (data not shown). The control mice (Figure 5.8), showed a highly necrotic response that was very eosinophilic when stained with H&E. In Figure 5.8A, a large accumulation of neutrophils is seen in a region of amorphous debris. While, in figure 5.8B, a representative of a classic type I lesion is seen.

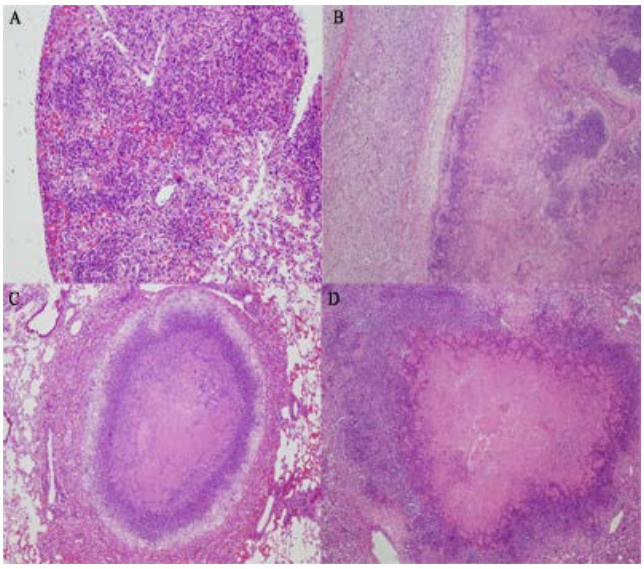

Figure 5.7. Varied lesion development at 6 weeks post aerosol infection, 3 weeks of treatment, from different treatment groups. (A) Type III cellular lesion from 3 weeks of Losartan Potassium (LK) treatment 4x. (B) LK treatment produces type I lesion with the thick collagen rim and necrotic core 10x. (C) A representative type I lesion from 3 weeks of INH treatment 4x. (D) A more diffuse lesion, highly necrotic with collagen deposition around the outside. Representative of type II and type I lesions from combination INH+LK treatment 10x.

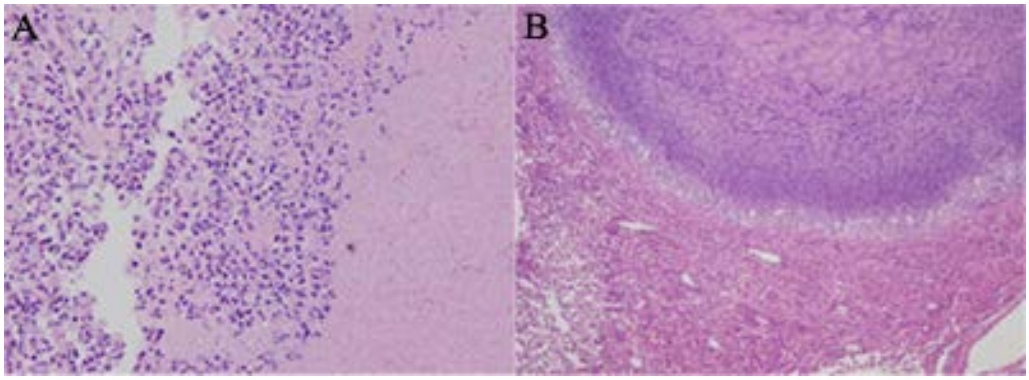

Figure 5.8. Highly necrotic lesions at 9 weeks post aerosol infection. (A) Core of a necrotic lesion from control mice shows distinct neutrophils and an eosinophilic core 20x. (B) The edge of a type I lesion with necrotic core with foamy macrophage rim 10x.

To determine any effects of the drug treatments on collagen depositions, we used picrosirius red stain. As stated in chapter 2, dark red and orange stain is indicative of larger, thicker and therefore older collagen fibrils, as seen in control animals (Figure 5.9A), while the yellow and green stain are indicative of smaller, thinner, and newer collagen fibrils, as were observed in our INH and LK treated animals (5.9B and C). In the combination INH+LK treated mice, there seemed to be a trend towards seeing less collagen deposits at 3 weeks of treatment (Figure 5.9D). Although these preliminary observations showed to be interesting, they are not quantitative and should be interpreted with care.

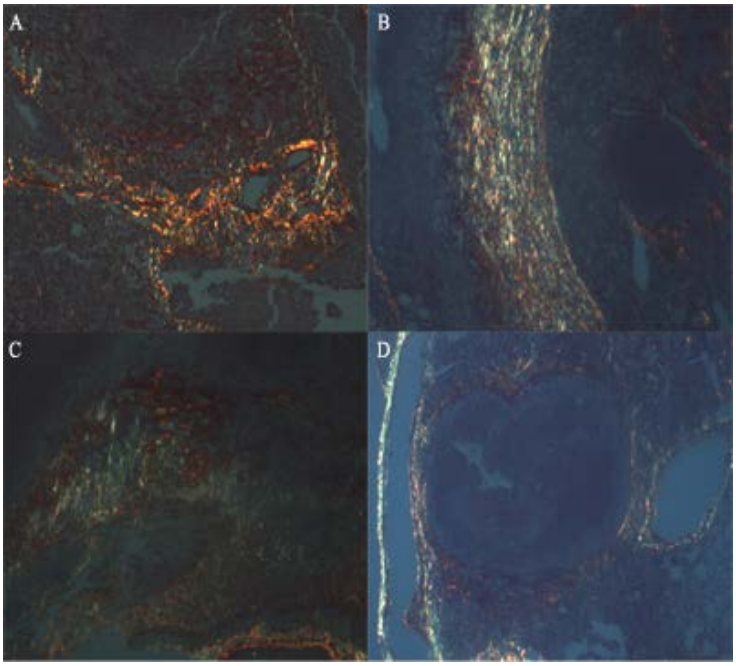

Figure 5.9. Combination treatment visually seems most effective in disrupting collagen rim. (A) Red/orange stained collagen surrounding a lesion at 6 weeks post aerosol infection in control mice 10x. (B) The advanced collagen rim from INH treated mice for 3 weeks is mostly made from thin collagen fibrils determined from the yellow/green stain 10x. (C) The mix of red and yellow collagen fibrils in the LK treated mice 10x. (D) Combination INH+LK treated mice qualitatively has the least amount of collagen. The collagen fibrils present are thicker red/orange 4x

In order to determine whether the LK treatment alone or in combination had any effect on the bacterial location in the lungs, we used the acid-fast fluorescent stain, Sybr Gold. Early on, the Sybr Gold staining showed that bacterial location mainly clustered around nuclei and pockets of lymphocytes (Figure 5.10A and B). Control mice at 3 weeks of treatment, which is 6 weeks post aerosol infection, has a large number of bacteria that concentrate in border of foamy macrophages in the rim of a type I lesion (Figure 5.10C). At 6 weeks of treatment, which is 9 weeks post infection, mice from the LK treatment group showed a well defined type I lesion (Figure 5.10D), with a high concentration of acid-fast positive bacteria in the foamy macrophage rim and a large accumulation of bacteria throughout the necrotic lesion.

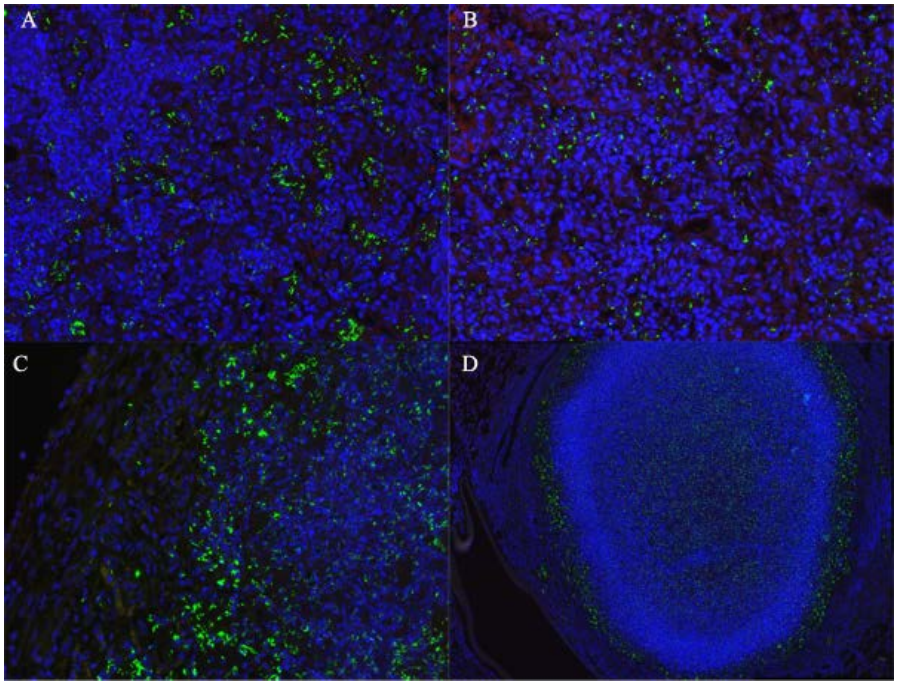

Figure 5.10. Sybr gold fluorescent staining show the transition from intracellular to extracellular at late stage. (A and B) Clusters of bacteria (green) around pockets of nuclei stained with DAPI (blue) for pre-treatment mice 20x. (C) The bacteria are concentrated around the rim of the necrotic lesion and throughout the core of control mice at 6 weeks post aerosol infection 20x. (D) Type I lesion from 6 weeks post-treatment of LK show bacteria in the rim and throughout the core of the necrotic lesion 10x.

Two important lessons were learned from this initial trial were to lower the LK dose in order to reduce adverse effects, and instead of co-treatment of LK and chemotherapy to study pre-treatment of LK prior to TB treatment.

5.2.2.4 Losartan Potassium as a pre-treatment to chemotherapy

Due to the catastrophic mortality of the first pilot study, a lower infectious dose and a shorter, pre-treatment course of LK was used. To explore the benefit of collagen breakdown prior to chemotherapy, LK was used as a pre-treatment. Infected C3HeB/FeJ mice were either initially treated with LK or untreated for 2 weeks with follow up treatment with MXF, LK, or untreated for an additional 3 weeks. The experimental design resulted in the following groups: LK alone (2 wks), LK (2wks) + MXF (3 wks), MXF (3 wks), and an untreated group. C3HeB/FeJ mice were infected with MTB Erdman and allowed to reach peak infection 5.91 ± 0.32 log10 in the lungs for 4 weeks before the start of treatment. At the start of treatment, mice were treated with LK alone for 2 weeks whereas a control group was left untreated. At the end of 2 weeks pre-treatment with LK, the mice reached a bacterial burden of 7.49 ± 0.38. Untreated mice had a bacterial burden of 7.27 ± 0.4 log10. The results of the treatment groups versus the untreated controls were not statistically significantly different ($P > 0.05$) (Figure 5.11).

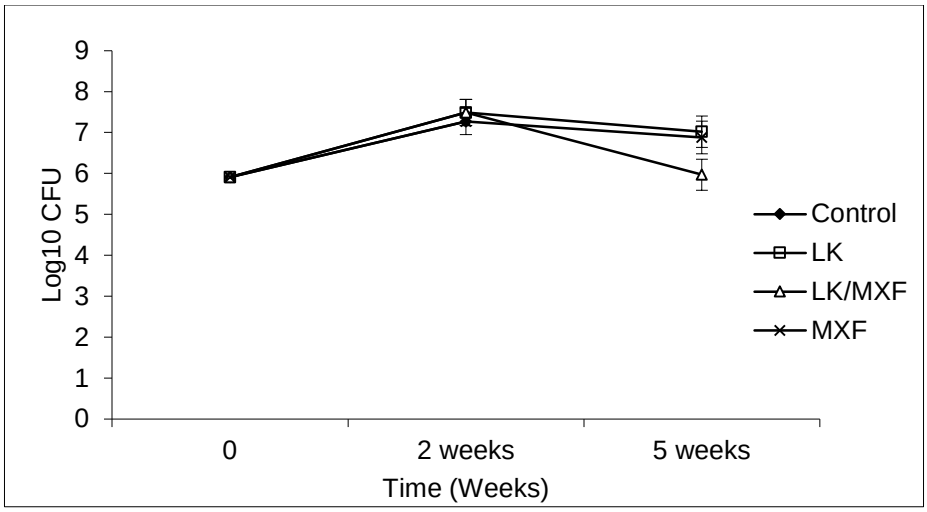

Figure 5.11. Pre-treatment with Losartan potassium does not have a significant change in bacterial burden in C3HeB/FeJ mice.

The spleens of C3HeB/FeJ mice at the start of pre-treatment had a bacterial burden of 4.7 ± 0.23 log10. After 2 weeks of LK treatment or untreated the mice reached 4.53 ± 0.27 or 4.47 ± 0.23 log10, respectively. Mice continually treated with LK for a further 3 weeks were terminated with a bacterial load of 4.10 ± 0.15 log10, while mice treated only with MXF (3 wks) had a 0.5 log reduction to 3.52 ± 0.14 log10 CFU ($p < 0.05$) to the control mice. The combination of pre-treatment of LK followed by MXF had a 1 log reduction to 3.04 ± 0.17 log10 CFU ($p < 0.01$) from the control mice (Figure 5.12). Pre-treatment with LK had no effect on the efficacy of MXF, When groups LK (2 wks) + MXF (3 wks) to MXF (3 wks) were compared, there was no statistically significant difference ($p = 0.11$).

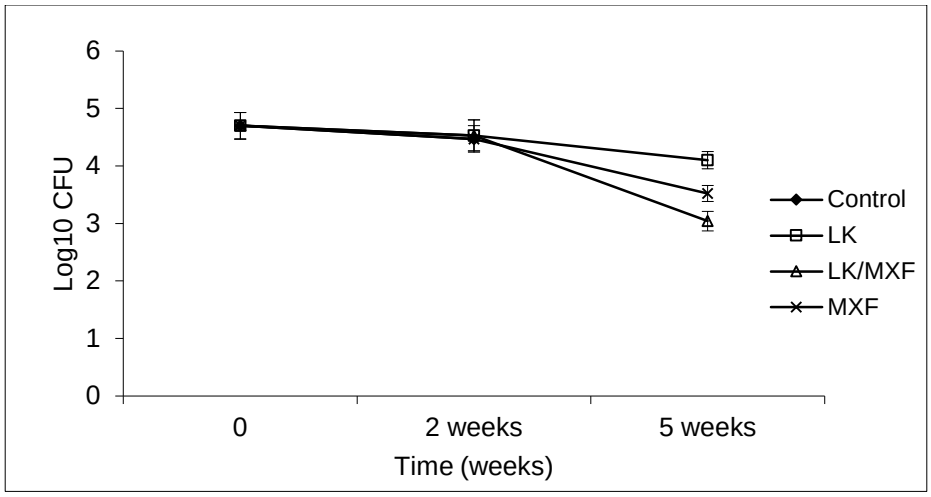

Figure 5.12. Moxifloxacin treatment has a statistically significant bacterial reduction in the spleen, LK pre-treatment does not have an effect. After 5 weeks of treatment, 9 weeks post aerosol infection; mice treated with LK had 4.10 log10, MXF had 3.52 log10* (p=0.03), and LK/MXF 3.04 log10* (p=0.01).

5.2.3 Result summary and conclusions of Losartan potassium as treatment augmentation

Our goal was to use an anti-fibrolitic to manipulate the collagen rim of the granuloma and increase chemotherapeutic efficacy. To achieve this objective LK was given to C3HeB/FeJ mice, which are capable of developing necrotic granulomas, alone and in combination with a highly effective first line TB drug, INH. To draw final conclusions from the data set of the first experiment has been complicated by a few factors. First, we saw a high mortality rate of the Kramnik mice caused by a highly virulent infection, which we and others have seen (Driver et al. submitted, Irwin et al. manuscript submitted), and by the adverse of LK treatment. The mortality was highest in the LK group alone group (50% mortality); and therefore it is possible that the results of the remaining mice were skewed to those with lower bacterial numbers (Figure 3). In the histopathology analysis using stereology, there was little change seen in the percentage of lesion involvement and collagen deposition between the treatment groups in the 3 and 6 weeks of

treatment groups. The high mortality in the LK group may be the result of the healing/resolving of the granulomatous lesions, releasing organisms in the lung, causing an uncontrolled inflammatory response. We can speculate that this resolved lesion may have been the biological equivalent of 'opening Pandora's Box' and without a highly effective combination therapy to counteract the upsurge in bacteria and cytokines the mice might succumb quickly. As a consequence of the high mortality the animals able to survive had a lower bacterial burden, less pathological changes, and fewer clinical symptoms, such as weight loss. In contrast, the mortality might just be caused by the LK treatment itself and therefore lower dosages might be utilized in future experiments.

Due to the catastrophic mortality of the first pilot study, a lower infectious dose and a shorter, pre-treatment course of LK was used. We hypothesized that pre-treatment with a low dose, short course LK treatment would modify the collagen rim in order to have more efficient drug penetration, especially for those drugs known to accumulate outside the lesion such as MXF. Using LK as a pre-treatment in the second experiment showed some promise, but the results of the study with the current design were not statistically significant reducing the bacterial load in the lung. A future study with longer durations of the treatment lengths of LK as well as MXF may result in greater effects in CFU reductions as well as in altering pathology, increase the could answer that question.

5.3 Aim to increase the frequency of cavitary disease in C3HeB/FeJ mice after aerosol infection of clinical *M. tuberculosis* strains

W-Beijing clinical strains are of the most virulent and highly transmittable East Asian lineages of MTB in the world. ***The hypothesis of this study was to use W-Beijing clinical***

strains for mouse infection to produce higher incidences of cavitary disease in susceptible C3HeB/FeJ mice, thereby creating a reliable cavitary model to test future drug treatment protocols. This will be accomplished by using W-Beijing strains known to produce disease progression, ranging from moderate to severe in other mouse and guinea pigs models [333]. These strains evaluated also have shown a history of producing cavitary disease in human patients [165]. The outcome of the proposed mouse study will aim to assess bacterial burden, histopathological evaluations of tissue, and performing flow cytometry of T cells responses in the lungs of these infected animals.

5.3.1 – MATERIALS AND METHODS

5.3.1.1 Animals

See Methods in Chapter 2

5.3.1.2 Bacteria and aerosol infections

M. tuberculosis Erdman strain (TMCC 107) was used for drug evaluations in mice and prepared as previously described [116, 217]. Briefly, the bacteria were originally grown as a pellicle to generate low passage seed lots [116]. Working stocks were generated by growing to mid-log phase in Proskauer-Beck medium containing 0.05% Tween 80 (Sigma Chemical Co., St. Louis, MO) in three passages, enumerated by colony counting on 7H11 agar plates, divided into 1.5 ml aliquots and stored at -70˚C until use.

W-Beijing strains of MTB characterized by the region of difference (RD) were acquired from Kato-Maeda laboratory in San Francisco [165]. We used three strains 4147 and 3507 (RD181) and 5097 (RD207) (Table 5.3). Briefly, strains were grown in 7H9 media containing

0.05% Tween-80 and frozen in aliquots at -70ºC until use. Strain HN878, a W-Beijing strain, recovered from patients in Houston, TX [170] provided by the Kreiswirth laboratory, has been used to reliably produce cavitary lesions in the rabbit model. The W-Beijing strains (5097, 3507, and 4147) from Kato-Maeda laboratory have shown a large necrosis to lesion ratio in previous guinea pig experiments by 30 days of infection. The RD207-5097 grew quickly and was the most severe, while the RD181 sublineage was less severe.

Table 5.3. Lineages and infectivity of clinical strains

Lineage	Laboratory	Transmission	Chest X-ray
Erdman	TMCC	Low	No cavities
HN878	Kreiswirth	High	Cavities
RD207-5097	Kato-Maeda	High	Abnormal; no cavities
RD181-3507	Kato-Maeda	Low	Cavities
RD181-4147	Kato-Maeda	Moderate	Cavities

In the first experiment, the C3HeB/FeJ and Balb/c mice were exposed to a low-dose aerosol infection with MTB RD207-5097 or RD181-3507, via a Glas-Col inhalation exposure system, as previously described [217], which resulted in 266 and 89 CFU/mouse, respectively. In the second experiment, the C3HeB/FeJ and Balb/c mice were exposed to a low-dose aerosol infection of MTB Erdman, RD181-3057, RD181-4147, or HN878 which resulted in an average of 8.3, 86.6, 25, and 33.3 CFU, respectively, in the lungs on the day of exposure. In order to enumerate the bacteria implanted in the lungs, for every MTB strain three Balb/c mice were sacrificed the following day.

5.3.1.3 Enumeration of bacterial load of lungs and spleens

See Methods in Chapter 2

5.3.1.4 Pathology and microscopy

See Methods in Chapter 2

5.3.1.5 Staining procedures

See Methods in Chapter 2

5.3.1.6 Flow cytometry

Cells were harvested from the lungs as described before [347]. Briefly, during necropsy, lungs were perfused with heparin (Sigma, St. Louis, MO). Thereafter, organs were minced and incubated for 30 min at 37°C with collagenase and DNAseI (Sigma), passed through a cell strainer and harvested by centrifugation. For antibody staining, cells were initially incubated with 10 µg/ml of FcBlock (anti-CD16/CD32, clone 93) for 20 min at 4°C. Thereafter, cells were stained with the following antibodies (all antibodies were from eBioscience, San Diego, CA) for 20 min at 4°C in the presence of FcBlock: anti-Gr1 (clone RB6-8C5), anti-CD11b (clone M1/70), anti-CD11c (clone N418), anti-CD4 (clone GK1.5), or anti-CD8 (clone 53-6.7).

For intracellular cytokine staining [179] lung cells were stimulated for 4 hrs with anti-CD3 and anti-CD28 in the presence of Golgi-Stop (BDsciences). Cells were resuspended in permeabilization buffer using a commercial kit (Foxp3 Staining BufferSet; eBiosciences) and incubated for 30 min at room temperature. Cells were washed again and resuspended in Perm/Wash buffer containing labeled mAbs against Foxp3 (FJK-16s, Rat IgG2a), IL-17A

(eBio17B7, Rat IgG2a, K) and IL-17F (eBio18F10, Rat IgG2a), or IFNg (XMG1.2, rat IgG1), and incubated for 30 min at 4 _C. The cells were resuspended in PBS containing 0.05% sodium azide prior to analysis. Data acquisition was performed on a LSR-II flow cytometer (BD) and 100,000 events were analyzed. Data was analyzed using FACSDiva version 6 (Becton Dickinson Instrumentation).

5.3.2 – RESULTS

5.3.2.1 Survival of mice infected with W-Beijing strains from San Francisco

A small pilot study was performed initially to evaluate the growth kinetics of clinical strains RD181-3507 and RD207-5097. Both C3HeB/FeJ mice and immunocompetent Balb/c mice were infected with each strain. Day one post aerosol infection, the mice infected with RD207-5097 showed an average of 266 CFU per mouse, and the bacterial load of RD181-3507 was 89 CFU.

For strain RD207-5097, the C3HeB/FeJ mice continued to gain weight for two weeks but rapidly began to lose weight thereafter. The rapid weight loss resulted in the need for humane euthanasia of the mice within a month post-aerosol infection (Figure 5.13). For the immunocompetent Balb/c mice infected with RD207-5097, the mice were able to control infection for 3 months post-aerosol infection. Bacterial plating of day 1 infection of RD207-5097 showed however contamination in the bacterial stock used for infection (gift from a collaborator), and therefore the results with this strain cannot be used for any data interpretation.

Both the C3HeB/FeJ and Balb/c mice infected with RD181-3507 continued to gain weight and remain healthy during the 3-month experimental duration (Figure 5.13).

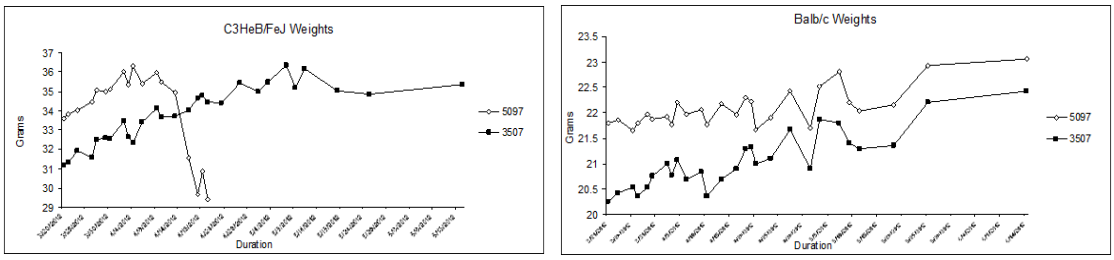

Figure 5.13. Highly virulent clinical strain RD207-5097 has increased mortality in susceptible C3HeB/FeJ mouse strain. C3HeB/FeJ mice infected with RD207-5097 have increased weight loss and morbidity versus mice infected RD181-3507. Balb/c mice infected with either RD207-5097 or RD181-3507 are able to continue thrive until the conclusion of the experiment.

5.3.2.2 Evaluation of histopathology in the lungs of C3HeB/FeJ mice infected with W Beijing strains

Based on the data from the pilot study, a new experiment was conducted to evaluate the histopathology after infection with several Beijing strains. For this purpose, C3HeB/FeJ and Balb/c mice were infected with Erdman, RD181-4147, RD181-3507 and HN878. Three Balb/c mice for each strain were used to determine the infection exposure on day one. The results showed an expected CFU per mouse for the various MTB strains; Erdman, RD181-3507, RD181-4147, and HN878 giving an average of 8.3, 86.6, 25, and 33.3 CFU in the whole lungs, respectively.

MTB Erdman, our main laboratory strain, showed an expected growth curve over 6 weeks from the time of infection (Figure 5.14A), growing exponentially to 8 logs even with a low infectious dose. The RD181 sublineages began with a slow growth in the lungs, however at 6 weeks post aerosol infection also reached 8 logs. HN878 followed a similar growth kinetic as Erdman but was more virulent reaching 8 logs at 4 weeks and remaining at that bacterial load at

6 weeks. The already high bacterial load at 4 weeks resulted in increased mortality of mice infected with HN878 with 8% of the mice needing to be humanely euthanized early.

The bacterial burden of the spleens for all strains was increasing over time but largely similar for all the strains evaluated, with approximately 1.75, 4.8, and 5.3 Log10 CFU at 2, 4, and 6 weeks, respectively (Figure 5.14B).

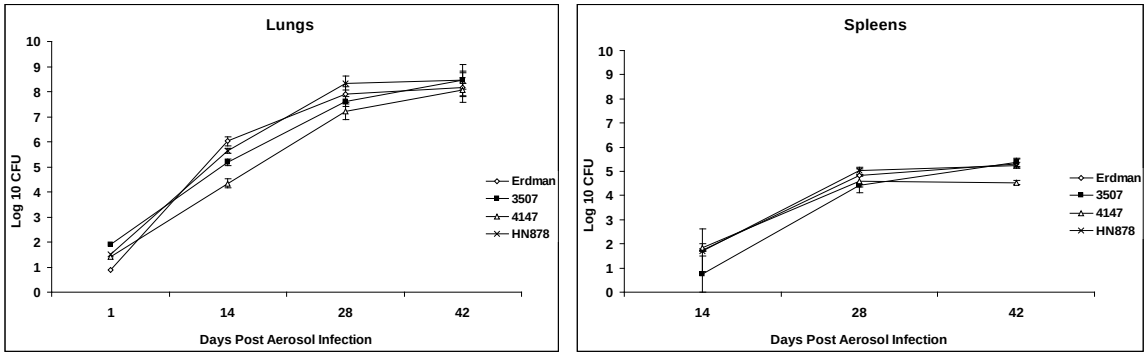

Figure 5.14. C3HeB/FeJ mice infected with clinical strains of *M. tuberculosis* show no statistical difference in bacterial burden in the lung (A) and spleens (B).

5.3.2.3 Pathological progression in the lungs and virulence of clinical strains in C3HeB/FeJ mice

The progression of disease highly depends on virulence of the MTB strain used to infect the susceptible C3HeB/FeJ mouse strain. At 2 weeks after aerosol, MTB Erdman, as well as the RD181-3507 and 4147 strains, showed moderate alveolar thickening in the lungs, an accumulation of lymphocytes, and a small number of neutrophils being recruited (Figure 5.14A and B, respectively). The W-Beijing strain, HN878, showed for all three mice at 2 weeks post aerosol already the presence of large regions of type I and type II lesions (lesion types are more detail described Chapter 3) (Figure 5.15C).

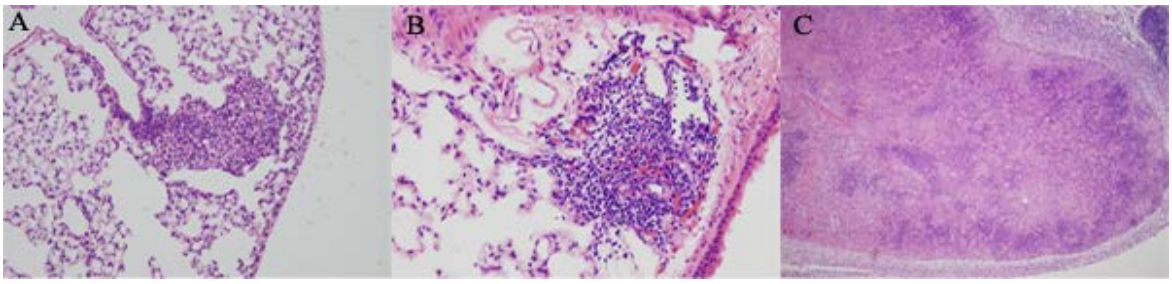

Figure 5.15. Virulent HN878 has early severe pathological features. (A) Midori strain 3507 and (B) Midori strain 4147, at 2 weeks post-aerosol infection results in accumulation of cellular infiltrates with neutrophils and early necrosis 20x. (C) HN878 at 2 weeks post-aerosol infection has type I necrotic lesions with moderately developed collagen rim 4x.

At four weeks post aerosol infection, the lesions from the mice infected with MTB Erdman, 3507, or HN878 strains have progressed predominantly to type II lesions (Figure 5.16). These lesions show extended cellular necrosis with cellular accumulation of lymphocytes, foamy macrophages, and neutrophils. Mice infected with RD181-4147 show mainly cellular type III lesions (Figure 5.16D). The inset from figure 5.16D shows an airway of the cellular lesion with a high number of intact neutrophils obstructing the bronchiole.

At six weeks post-aerosol infection, all strains showed developed advanced lung pathology in the C3HeB/FeJ mice. Mice infected with MTB Erdman showed all three types of lesions in the lungs; type I granulomas with central necrosis and collagen rim (Figure 5.17A), type II lesions with neutrophilic infiltrates and necrotic alveolitis, and the cellular type III lesions (not shown). The W-Beijing strain HN878 produced multi-lobulated type I necrotic lesions (Figure 5.17B). The strain RD181-3507 continued to predominantly result in heavily necrotic disorganized type II lesions (not shown). RD181-4147 showed pathology very similar to MTB Erdman in developing all three types of lesions with a predominance of type I (Figure 5.17D) and type II lesions. In summary, the clinical strains showed a range in pathology that mainly

depends on virulence of the strain, as is observed in the guinea pig model [348]. The highly virulent strains with high transmission had a rapid acceleration of pathological features with increased mortality. The lower transmission strains did develop more advanced pathology but the low inoculums slowed progression.

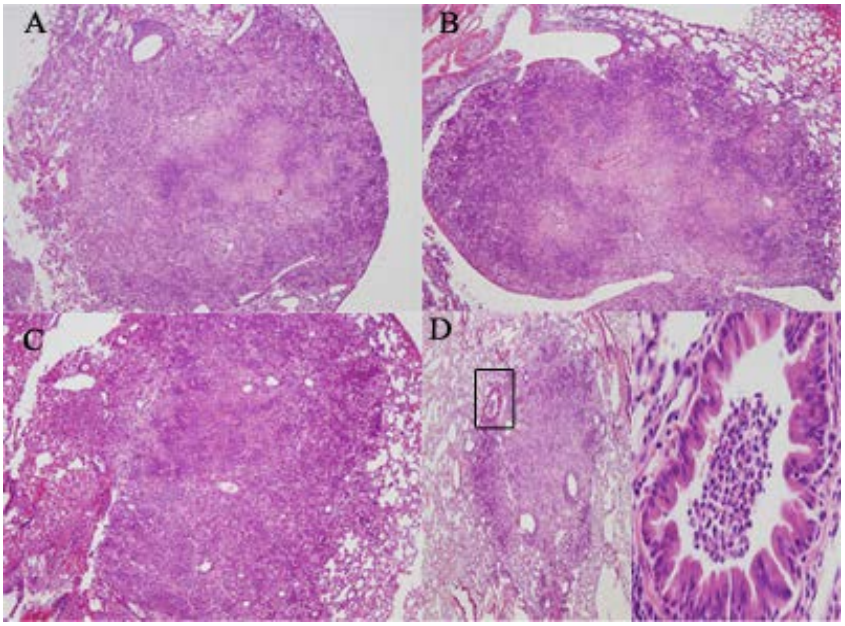

Figure 5.16. Four weeks post-aerosol infection results in type II necrotic lesion for Erdman, 3507, and HN878 in C3He/FeJ mice. (A, B, and C) At 4 weeks post aerosol infection mice infected with Erdman, 3507, and HN878, respectively, result in predominantly type II lesions 10x. (D) Mice infected with 4147 at 4 weeks post infected predominantly result in type III cellular lesion 10x, (Inset) airway with cellular debris composed of neutrophils 20x

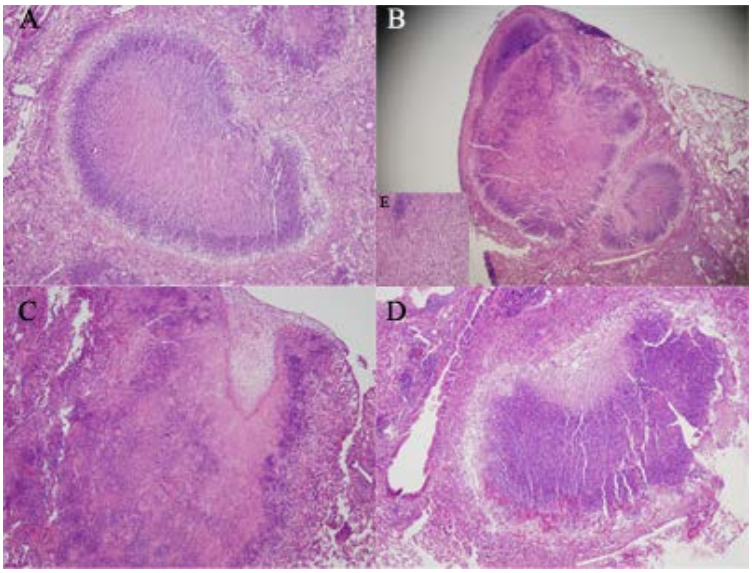

Figure 5.17. Six weeks post aerosol infection mice developed advanced lesions with both laboratory and clinical strains. (A) Type I lesion in mice infected with laboratory strain Erdman 4x. (B) Large multilobulated type I lesion from HN878 W-Beijing strain 2x. (C) Loosely formed collagen fibrils from W-Beijing strain HN878 20x. (D) Strain 4147 produced type I lesions at 6 weeks post aerosol infection 4x.

5.3.2.4 Studying the cytokine profiles in the lungs of C3HeB/FeJ mice after infection with various clinical M. tuberculosis strains

In order to assess whether these differences in growth kinetics and in pathology progression were also reflected by a difference in cellular immune profiles, we were interested in measuring the cytokine profiles after infection with the various clinical strains. At the four and six week time points, 3 mice were sampled from every group for flow cytometry, if mice were available. Due to the high virulence of the HN878 strain lung samples, were only available for 4 weeks post aerosol infection. Erdman, 3507, and 4147 had samples analyzed for 4 and 6 weeks post aerosol infection.

To obtain a preliminary view of the predominant immune response elicited from each TB strain, we focused on IFN-γ expression, IL-17 expression, Foxp3+ expressing cells, and Gr1+^{hi} cell composition profiles (Figure 5.18).

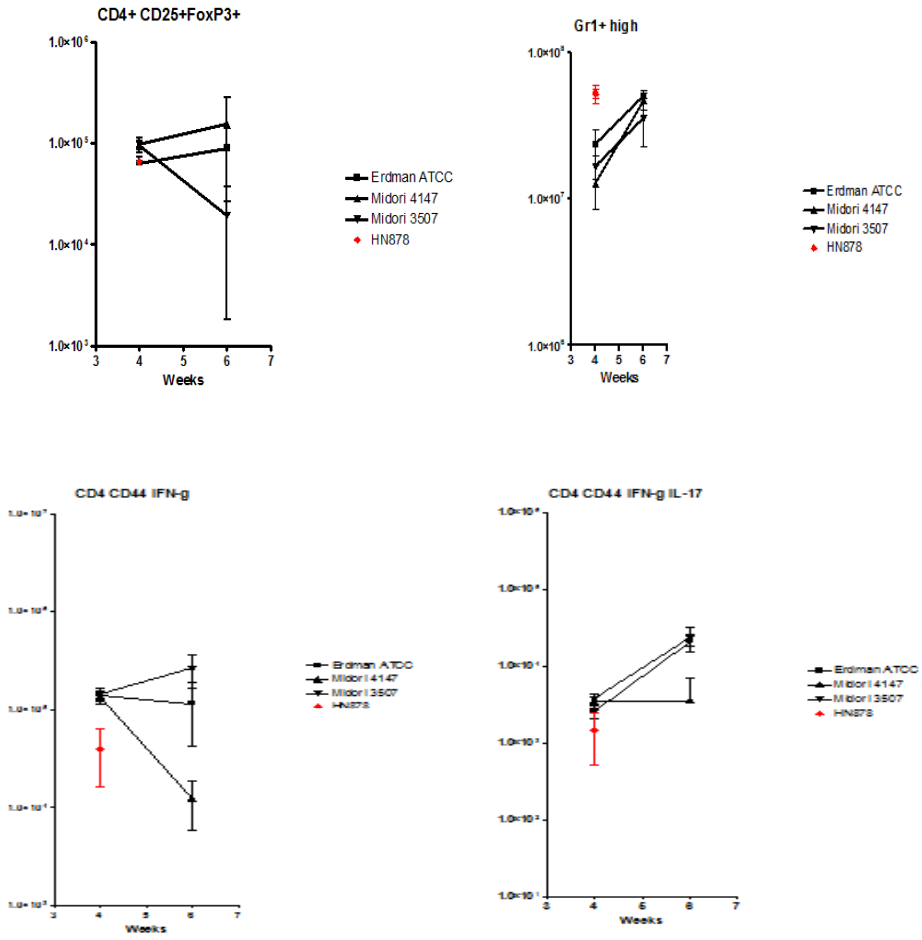

Figure 5.18. Cellular expression profiles of W-Beijing strains show distinct characteristics of each strain. HN878 (red square), highly virulent has high expression of myeloid Gr1+^{hi} only. RD181-4147 (triangle) shows an increase in Foxp3+ and Gr1+ trending toward a repressive cytokine expression. RD181-3507 (upside down triangle) shows a decrease in Foxp3+, an increase in IFN-γ and IL-17, trending toward a more inflammatory profile. Erdman (square) shows a balanced expression of moderate increase of Foxp3+ and an increase in IL-17.

These specific cytokines were chosen to study the Th1 IFN-γ response, Th17 protective response measured by IL-17, T regulator cells measured by Foxp3+, and a myeloid progenitor marker Gr1+ to measure granulocyte infiltration. The highly virulent, high transmission strain HN878 had low expression of IFN-γ, IL-17, and low numbers Foxp3+ cells. HN878 had the highest levels of $Gr1+^{hi}$ (myeloid granulocytes) at 4 weeks than the other strains at either sacrifice. From 4 weeks to 6 weeks post aerosol infection with either the MTB Erdman, 3507, and 4147 strains showed a 0.5 log increase in $Gr1+^{hi}$ cells, which is also confirmed pathologically. There is a large increase in necrotic lesions within the 2-week period for those strains. The higher virulence of HN878 correlated with decreased Th1 response (lower IFN-γ and IL-17), increase in T reg cells (Foxp3+) and increase in neutrophil recruitment ($Gr1+^{hi}$). RD181-3507 W-Beijing strain has been reported to have low transmission and low virulence in human and in previous guinea pig models [165]. Based on the C3HeB/FeJ flow cytometry data, there was a decrease in cells expressing Foxp3+, and a ~0.5 log an increase in IFN-γ and IL-17 expression. Conclusions are confounded by the large standard deviations from the Foxp3 and IFN-γ levels there may be little and therefore difference in cytokine expression over time is likely not statistically significant. In general, infection with the RD181-3507 strain showed more a Th1 expression profile.

RD181-4147 W-Beijing strain is also of the same sublineage as the 3507 strain but had more moderate growth and infectivity in the guinea pig model. The 4147 strain showed a cytokine profile that was the converse of the profile seen for the 3507 strain; showing a moderate increase (~0.2 log) of Foxp3+, a steady expression of IL-17, and a 1 log decrease of cells expressing IFN-γ. As infection progresses, the strain 4147 showed an increase of Treg and a decrease of inflammatory cytokines, which could lead to greater uncontrolled bacterial growth.

When evaluating the MTB Erdman strain, a slight increase of Foxp3+ expression was observed with a large standard deviation (Figure 5.18). From 4 weeks to 6 weeks IFN-γ expression remains steady but also has a large standard deviation and therefore may transition more over time. IL-17 had a distinct increase of ~0.5log at 6 weeks post aerosol infection. Overall, the MTB Erdman showed a predominant Th1 response.

The HN878 strain had a highly inflammatory response with high expression of $Gr1+^{hi}$ and low expression of Foxp3+. RD181-3507 and Erdman have similar Th1 expression profiles of small inflammatory increase, IFN-γ, Gr1+, and IL-17, and a 0.25 log decrease of suppressor Foxp3+. Strain RD181-4147 has an increase in Foxp3+ expression and a large granulocyte Gr1+ expression both IFN-γ and IL-17 expression are low.

5.3.3 Results summary and conclusions of infecting C3HeB/FeJ after infection with clinical Beijing strains

Our goal was to use virulent clinical strains to promote cavitary lesion production in C3HeB/FeJ mice already capable of developing necrotic granulomas. A range of W-Beijing strains were chosen, from the highly virulent HN878 to less virulent RD181-3507 strain to allow for a varied pathological response over a 6 week period after infection. Highly virulent HN878 strain had a neutrophilic response. This was observed by 2 and 4 weeks post aerosol infection histopathology, the samples had predominantly type II neutrophilic lesions, which correlated with the highest expression of $Gr1+^{hi}$ at 4 weeks. HN878 was the only strain that had mortality within 25-40 days post aerosol infection, 8% of the mice were humanely euthanized. Erdman and RD181-3507 followed a similar pathogenesis. Large standard deviations in IFN-γ and Foxp3+ expression confound the small changes in expression observed in both Erdman and RD181-3507.

Both strains have a trend to a Th1 inflammatory profile with an increase in Gr1+^{hi} expression. The two strains have a similar cytokine profile also have a similar histopathogenesis. Initially, both strains have early cellular lesions at 2 weeks post aerosol infection, followed by predominantly type II lesions with the occasional type I necrotic granuloma at 4 weeks. By 6 weeks the infected mice had an intermix of all three lesion types, I, II, and III. RD181-4147 did not begin to develop type I or type II lesions until 6 weeks post-aerosol infection. At 4 weeks post aerosol infection mice infected with 4147 had predominantly type III cellular lesions. This correlated with dramatic 1.0 log decrease of IFN-γ from 4 to 6 weeks post-aerosol infection. There was also an increase in Foxp3+ with a large standard deviation and an increase in Gr1+^{hi} expression.

While cavitary lesions were not produced from this pilot trial many new aspects of TB disease can be learned. This was the first attempt to use clinical strains to infect C3HeB/FeJ mice. We learned that the hyper-virulent strains are too severe for the highly susceptible mouse strain and precautions should be taken. We are particularly excited with the results obtained with the more moderately virulent clinical strains as these could also be used to confirm pre-clinical drug data from the Kramnik mouse model from laboratory strains. If a drug or drug regimen would also perform well against a clinical strain in the Kramnik mouse model, this would increase confidence to advance the drug forward in TB drug development. Also we come away with the knowledge that each clinical strain has its own unique pathology and immune response characteristics. It may be more reasonable to adapt the immunological profile of the animal through siRNA or neutralizing antibodies to create a host environment more amenable to cavitary disease.

5.4 – Overall Summary Chapter 5

In this chapter the overall goal was to change the pathology of the lung lesions in the C3HeB/FeJ mice by altering the necrotic granuloma: first to resolve the necrotic lesion in order to enhance treatment, and second to direct the model towards cavitary disease as this reflects more pathology features from human disease. The necrotic granuloma is difficult to treat, it encapsulates the majority of the bacteria, and much is still unknown about its formation and core environment at this time. The goals of this chapter included using a collagen disrupter to attempt to resolve, at least in part, the granuloma, thereby changing the oxygen and nutrient content, which may ultimately alter the bacterial metabolic state potentially making them more amenable to drug treatment. The next goal consisted of using clinical strains to drive the Kramnik mouse model into producing cavitary lesions, reliably, which would give researchers a resource to investigate new preclinical drugs against a specific lesion type in a small animal model.

LK as a collagen disruptor does show promise when used as a pre-treatment for a short duration. Using LK for extended periods of time in an infectious disease, like TB, is problematic as was observed. The inhibition or break down of collagen deposition in a TB granuloma will not only allow drugs that have penetration problems into the granuloma, but it also may allow for bacterial dissemination into previously unaffected lung parenchyma. This upsurge in bacterial dissemination could then cause a large influx of inflammatory cytokines, which may do more damage to lung tissue than disease if not controlled by drug treatment. Observationally, the mice from the LK group, which were humanely euthanized due to severe clinical symptoms, had exceedingly congested lung tissue compared to other mice euthanized early. The issue of bacterial dissemination has been raised by others that are using techniques such as neutralizing

TNF-α therapy to enhance treatment efficacy [330]. Success was dependent upon aggressive multi-drug treatment.

The usage of clinical strains to manipulate the granuloma environment of the C3HeB/FeJ mouse was informative. Each individual clinical strain had a distinct cytokine response despite all the strains being of the W-Beijing lineage, this information needs to be taken into consideration when using clinical strains. We observed that C3HeB/FeJ mice infected with highly virulent strains had increased inflammatory response and increased mortality. The moderately virulent clinical strains 3507 and 4147 show promise for future to confirm drug efficacy data already established for laboratory strains. Additional efficacy data may be obtained from using both 3507 and 4147 since they seem to have opposing immune responses. RD181-3507 has a predominantly Th1 inflammatory response and RD181-4147 has a more Th2 response with necrotic lesions developing later in infection. These differences can be exploited to determine the efficacy of drugs and drug regimens on the different infectious cytokine profiles. Other groups have worked extensively with guinea pigs but due to their sensitivity to broad-spectrum antibiotics [162, 333]; a mouse model may give more insight into novel drugs activity.

5.5 – FUNDING

This work was supported by The Bill and Melinda Gates Foundation grant ID 1033596 “Evaluation of a New Murine Model Testing Tuberculosis Chemotherapy” at Colorado State University and National Institute of Allergy and Infectious Disease (NIAID) Indefinite Delivery Quantity (IDIQ) Task Order HHSN272201000009I/01 “Mouse models for the early stage of lead drug candidates against mycobacterial species”.

CHAPTER 6 – CONCLUDING REMARKS AND FUTURE DIRECTIONS

Mycobacterium tuberculosis (MTB) continues to kill 1.3 million and infects 8.6 million individuals every year and effective eradication is complicated by the presence of MDR-TB and XDR-TB. Tuberculosis (TB) patients suffer from wide-ranging disease manifestations that result in diverse lung pathology. The lung pathology shows highly heterogeneous lesion formation caused by the bacterium. Lesions in TB patients can present as fibrotic, highly cellular, necrotic, liquefactive, to cavitary disease. Successful treatment should address all these disease states. Current preclinical drug development is mostly achieved through the use of the standard mouse model, C57Bl/6 or Balb/c. These mice develop a chronic infection and have proven be useful in determining the efficacy of novel preclinical drugs. Other animal models are also being used in TB research; such as guinea pigs, rabbits, minipigs, and NHP, among other animal models, all of which can develop necrotic granulomas, which are more similar to human disease. However, of these larger animal models have their own strengths and weaknesses for preclinical drug discovery. The guinea pig is highly intolerant to broad-spectrum antibiotics and proactive steps need to be taken to ensure the health of the animal during treatment. The rabbit and minipig both regularly develop cavitary disease but are large, cost prohibitive, and it is difficult to acquire the amount of necessary experimental compound for drug efficacy studies early in drug development. NHP is by far the most relevant model to human disease, as 30% will become latently infected; but again they are cost prohibitive and not practical for high throughput testing of novel compounds. The Kramnik mouse model, using the C3HeB/FeJ mouse strain, shows lung pathology that is more similar to human disease in pathology when compared to the more classical mouse models.

The C3HeB/FeJ mouse strain is a substrain of the C3H/HeN parental mouse strain and is highly susceptible to TB. It was determined through forward genetic analysis that the C3HeB/FeJ substrain was deficient at "the super susceptible to tuberculosis-1" (*sst1*) locus, which is responsible for the uncontrolled bacterial growth in the lungs [215]. In the studies discussed here, we evaluated whether the C3HeB/FeJ strain can add beneficial information to TB drug development and whether it has a role in the evaluation of new compounds and drug regimens, host pathology, and the interaction between bacteria and drug.

In a first set of studies, we evaluated whether the C3HeB/FeJ mouse strain would develop the relevant lung pathology consistently that was previously described to be similar to several pathology features seen in human TB patients. By means of a low dose aerosol infection of 50-75 CFU per mouse, we achieved a consistent infection with the presence of well-developed necrotic lung lesions at 8 weeks post aerosol infection. The resulting lung lesions had an inherent heterogeneity, which required further investigation. Comprehensive evaluation of multiple experiments determined three distinct lesion types in lungs of C3HeB/FeJ mice which develop after a low dose aerosol infection. We defined these lesions as: 1) the type I lesion which is the classic encapsulated necrotic granuloma, a highly necrotic core with neutrophil dominance and a fibrotic collagen rim; 2) the type II lesions which shows rapid necrotic alveolitis, consisting of large numbers of neutrophils and bacteria that congest the alveolar spaces with remnants of the alveolar septa remaining in the lesion, and 3) a type III lesion which presents itself as a cellular lesion, consisting of mononuclear cells (lymphocytes/macrophages) and which is similar to the lesions found in other immunocompetent mouse models.

The development to the three distinct lesion types appears to develop early on, and seems to not be based on a sequential progression of the disease from lesion type II to lesion type I as

we originally thought or as what is seen in other animal models such as the guinea pig [167]. The type I lesion has a well-defined necrotic core that is surrounded by a rim of collagen that eventually progresses to a fibrotic capsule surrounding the lesion. Even early on (6 weeks post infection), the initial development of this well-structured, controlled lesion type can be visualized. On the inside of the collagen rim, we see a multicellular layer of distinct foamy macrophages. More closely to the core of the lesion there is evidence of recent necrotic (karyorrhectic) neutrophils, where in the core only cellular debris without any cellular distinctions can be seen. C3HeB/FeJ mice are infected with MTB, they develop other lesions than a type I lesion and it became clear these other lesions were indicative of an alternative immune pathway in the host. An early lesion, which is largely composed of lymphocytes as well as macrophages, will progress further into a type III lesion, resembling closely the lesions types found in immunocompetent mouse strains. It is then also not surprising that this type III lesion is best controlled by the immune response and has low bacterial numbers. On the other hand, when lesions have a higher neutrophil content early on, these progress to either a type I or II lesion. The factors that determine the differentiation between type I or type II lesions are unknown at this time, but could be the rate of the neutrophilic influx and time for the host to respond. We speculate the difference in lesion development may be due to the variation in genetic distribution in the animals. The functional gene within the sst-1 locus encompasses a region known for being highly repetitive, the HSR (homogenously stained region repeat), and chromosome 1 has approximately 40 copies of the HSR. The high copy number may have a high number of incomplete copies or a heterogeneous distribution of the sst-1 in the mice that predominantly develop type III lesions. This heterogeneity of lesion development and overall survival is also seen in the CBA/J model of MTB [178] and DBA/2 model of avian influenza [349]. To evaluate

this hypothesis genetic analysis could be used, such as RT-PCR, to determine the functional sst-1 copy number in mice that develop type I, II and III lesions.

Due to the inherent finality of our studies (using terminal sacrifice to collect tissues), it is difficult to establish the trajectory of the progression of the disease towards the specific lesion types. Advanced imaging techniques could be used to track the advancement of lesions throughout infection in the same animals. Imaging such as x-ray imaging, magnetic resonance imaging (MRI) and positron emission topography (PET) are all successful techniques used in tracking lesion size and location in mice and other species for MTB and other diseases. Currently, x-ray has been used to track disease modeling in goats aerosol infected with *Burkholderia pseudomallei* [350] and TB infection in humans and NHP [171]. Decades ago, x-ray technology was used to determine the relationship of TB lesion and lung distribution from *ex vivo* guinea pig lungs, which for instance demonstrated that similar to humans, guinea pig lesions also developed in the apical lung lobes [351]. Comparing the ability of x-ray and MRI to detect early lesions in rhesus macaques infected with a range of bacterial inocula, it was determined MRI was more sensitive. MRI was used to detect lesions prior to onset of clinical manifestations [171]. PET has been used detect and monitor TB disease and treatment through [^{18}F]fluoro-dexyglucose activity in the tissue in mice, rabbits, NHP and humans but has a detection limit for lesions greater than 1mm [200, 352-355]. Recently, Jain et al. has adapted the technology to use a radiolabeled ligand with higher specificity than [^{18}F]. The translocator protein (TSPO) with radiolabeled DPA-713, [^{25}I]iodo-DPA-713, is highly expressed in the lung and specifically in macrophages during inflammation. This marker has shown great promise in mice for early lesion detection, as it is able to detect smaller lesions in mice within 3 weeks of infection [353].

Imaging techniques in conjunction with immunological assays may allow us a greater understanding of the various lesion types in disease over time in the same animal.

For drug development purposes, drug efficacy of a novel compound requires sufficient drug exposure at the site of infection, where the bacteria are located. By means of several acid-fast staining techniques, we located the various bacterial locations within the lung lesions throughout infection in the Kramnik mouse model. By comparing the results of diverse staining techniques it became clear that the majority of bacilli are located in the type I and type II lesions. Commonly used stains such as kinyoun carbol-fuchsin and AR revealed large numbers of bacteria within the foamy macrophages and within the necrotic core of the granuloma. Once the lesions expand over time the lesions can coalesce into one large lesion. With several acid-fast stains we were able to locate intra-as well as extracellular bacterial populations within the type I lesion. The foamy macrophages are heavily infected with bacteria and seem to be permissive to bacterial replication and/or persistence. In the core, high bacterial numbers can be visualized extracellularly within the cellular debris. With the clinically used acid-fast stains, the bacterial population in the center of the core showed to be less fluorescent which we speculate is indicative of a bacterial metabolic change. In addition, some intracellular bacteria are present in the functional macrophages on the outside of the collagen rim. However, these bacterial numbers seem to be low when compared to the numbers observed in the core and foamy macrophage layer. At the current time, the exact proportion of intracellular versus extracellular in the lungs of the C3HeB/FeJ mice is difficult to quantify. As these are important questions to answer in terms of drug development, future experiments using the Nikon software could be used to quantify the staining intensity and enumerate the extracellular bacteria numbers within the necrotic granuloma and intracellular bacteria in foamy macrophages that surround the type I lesion. In the

type II lesions, the majority of bacteria were found extracellularly within neutrophilic debris in the remnants of the alveolar spaces of the lung parenchyma. The high numbers of neutrophils in these lesions is remarkable. Generally neutrophils are short-lived but the high neutrophil numbers suggest that they might be non-functional and persistent. To account for this high number, it also not clear whether there is initially replication of the neutrophils are whether throughout disease there is continuous recruitment of these cells to the core of the lesions. The latter is suggested by some preliminary microscopic analysis whereby neutrophils are being observed to enter type I lesions through the collagen fibrils. More recent evidence shows the importance of neutrophils in human disease [265]. Barry et al, have shown that neutrophils are the predominant cell type with intracellular bacteria from broncho alveolar lavage and sputum samples. We further speculate that the neutrophils may be behaving similarly as infected macrophages. Evidence has shown when macrophages are infected with MTB there is an upregulation in factors that inhibit apoptosis, promote necrosis, and allow the bacteria to evade elimination and promote bacterial growth [259]. When in the macrophage MTB suppresses PGE_2, which has non-inflammatory function, and increases LXA_4, which is a pro-necrotic factor, the macrophage will undergo necrosis [356]. In order to study these aspects in neutrophils, the expression of PGE_2, LXA_4, and other factors that inhibit apoptosis, such as BAX and BAK could be studied, and the sustainability and functionality of the neutrophils examined. Also studying the neutrophilic response by modulating and timing of the influx of neutrophils in the Kramnik mouse model could initiate a new line of research reflective of human disease [308, 357].

Staining with the AR acid-fast protocol showed a distinct lack of stained bacteria in the most centralized center of the necrotic granuloma. At this time the exact target of the AR stain is unknown but early results suggest that this a cell wall component of the mycobacteria (personal

communication, Dr. Dean Crick). This lack of staining in the center of the necrotic core suggests that the bacterial target is either masked (e.g. by thickening of cell wall as has been described, [358]) or might not be expressed under the environmental conditions where the bacteria are located. In the center of the lesion core it is believed to be hypoxic, low in nutrients, and containing mostly cellular debris which could render the bacteria in a transcriptionally altered persistent state. A major part of this work was performed with a novel acid-fast staining method from our laboratory, the Sybr Gold acid-fast stain which binds to nucleic acids. Sybr Gold staining is highly sensitive able to reliably stain 99% of in vitro cultures (Ryan et al., submitted). It was shown to have greater long-term stability and less overall background fluorescence. Sybr Gold staining showed the presence of acid-fast positive bacteria within the necrotic core of serial histopathology sections that AR was unable to detect. Sybr Gold staining in the core was also not as bright as for the bacteria within the foamy macrophages on a per bacterium basis. We speculate bacteria within the foamy macrophages are/were actively replicating in permissive hosts, with a nutrient supply from lipids provided by the macrophage. While bacteria within the necrotic core are less likely to replicate and are rather in a persistent state, exposed to anoxia, nutrient starvation, and oxidative stress. Therefore the mycolic acids in the persistent might be packed differently and more difficult to bind.

The use of immunological tools have helped the TB field tremendously in understanding the key cytokines and other immune molecules that have a pro-inflammatory (Th1) or a anti-inflammatory role (Th2) in the progression of disease. We utilized this knowledge to determine the immune microenvironment of the lung and of specific lesion types in the lungs of the C3HeB/FeJ mouse model at late stages of infection. Preliminary examination of inflammatory cytokines and IHC staining analyzed the immune environment of the encapsulated type I

necrotic granuloma. With the CBA, we showed in the whole lung a predominant pro-inflammatory response observed by an increased expression of monocyte chemoattractant protein-1 (MCP-1, CCL2), interferon-gamma (IFN-γ), tumor necrosis factor-alpha (TNF-α), interleukin-6 (IL-6), and interleukin-10 (IL-10) cytokines. This increased expression was more predominant in the excised necrotic granuloma; high levels of cytokines IL-6, TNF-α, and chemokine MCP-1 were observed. The CBA showed higher levels of IFN-γ in non-granulomatous lung and whole lung tissue. IL-10, an immune dampening cytokine, showed high levels of expression in the excised granuloma. The IHC staining data correlated nicely with the CBA results and determined that the IL-10 expression was nearly exclusive to the foamy macrophages within the necrotic granuloma. These foamy macrophages also house high bacterial numbers, potentially due to dampened immune response. Markers that are specific for functional macrophages, such as F4/80 and lysozyme, show distinct cellular locations directly outside of the foamy macrophage rim of the necrotic granuloma. F4/80 staining shows a sharp delineation of positive cells outside of the foamy macrophage layer the necrotic granuloma. The foamy macrophages from all three lesions types were negative for F4/80 staining. Lysozyme, an enzyme that is constitutively expressed by activated macrophages, was also not expressed by foamy macrophages indicating a lack of (phagocytic) activity. The results of the CBA and the IHC showed a specific cellular composition and cytokine expression profile for the type I necrotic granuloma creating a distinct local microenvironments. The production of specific cytokines may be driven by the bacteria themselves, we speculate the bacteria within the foamy macrophages may be creating an environment inclined to produce IL-10 that dampens inflammatory cytokines allowing for growth and survival. In vitro analysis of IL-10 and lysozyme production from pre-infected and post-infected macrophages to determine the

transition from pro-inflammatory to anti-inflammatory cytokine profile may be useful in establishing the bacilli role.

The knowledge of the specific immune environment could also be useful in immunotherapy which when combined with classical drug treatment has been hypothesized to augment treatment regimens. Various research groups are currently exploring this option by using immunomodulators, small interfering RNA (siRNA), corticosteroids, and non-steroidal anti-inflammatory drugs [359]. The use of siRNA treatments of specific cytokines for instance may be useful in preventing or resolving the formation of the necrotic granuloma thereby allowing for more effective treatment [360]. Corticosteroids reduce inflammation and fibrosis, and have been used as beneficial adjunctive therapy for TB [361, 362]. Ibuprofen and aspirin have shown to enhance the activity of PZA in MTB infected mice and reduce lung pathogenesis [363]. Promising work is already being achieved with anti-TNF-α in combination with multidrug therapy in C3HeB/FeJ mice by Johns Hopkins University [330] and adding IL-10 to reduce inflammatory cytokine expression at key points during infection have been shown to regulate the formation of the granuloma in CBA/J mice [78]. Reducing MCP-1 levels may change the cellular composition of the granuloma and prevent the development of a large, permissive reservoir of foamy macrophages for intracellular bacterial replication.

The described pathological features of the Kramnik mouse model make it an appropriate model to investigate further for preclinical drug evaluation purposes. The ultimate goal of the model is to study drugs and drug regimen in a mouse model with advanced pathology in order reproduce human drug trial results more accurately. Initial studies using single drug treatments demonstrate that the C3HeB/FeJ mouse strain has generally a more refractory response to most drugs. Importantly, compounds such as INH and RIF rapidly kill the majority of bacteria in the

first two weeks, but it takes months to kill the remaining persisting bacteria. PZA shows to be less effective in the Kramnik mouse model where it is highly effective in the Balb/c mouse model. Interestingly, PZA shows more activity in some Kramnik mice than others within the same treatment group. We speculate that PZA is less effective against those mice that show mostly type I lesions.

Currently in our laboratory, there are multiple drug studies being conducted using the C3HeB/FeJ mice examining more experimental single drug treatments and drug combinations. These also include the recapitulation of clinical trial data, such as the REMOX trial in the Kramnik mouse model. In the ongoing REMOX clinical trial, the role of a fluoroquinolone, MXF, is being studied in the standard regimen for drug susceptible TB whereby MXF is replacing INH, or is replacing EMB in the standard combination treatment of MTB. In both the Kramnik mouse model and Balb/c mice, the bactericidal activity of MXF-containing regimens was similar as this of the standard regimen in both mouse strains, whereas for the relapse studies the MXF-containing regimens showed to be superior to the standard regimen and again for both mouse strains.

Recently, novel therapeutics (Bedaquiline [10], PA-824 [364]) and those of renewed interested (Clofazimine [365]) have been evaluated in human EBA trials conducted by the Global Alliance of TB Drug Development in NC-002 (published) and NC-003 (recent data, presented at World Lung Health meeting Oct. 2013). One of the most important findings of the NC-003 clinical trial was the lack of activity of CFZ alone and when added to other drugs (such as PA-824, BDQ) in the two-week clinical trial. A clinical EBA trial is only assessing the activity of a novel drug in sputum samples during the first two weeks of treatment, and therefore the sterilizing activity after long-term exposure is not being studied in such a trial. However, the

lack of activity was in fact recapitulated in the Kramnik mouse model, where CFZ showed no to little activity alone as well as in combination with BDQ, and this in contrast to seeing strong activity in the classical Balb/c mouse model. At this point, further investigation is being conducted to try and understand the lack of activity. Our current hypotheses are twofold: CFZ may be unable to penetrate the necrotic granuloma or the state of bacilli and environment are unresponsive to CFZ treatment. We have preliminary data that shows that both hypotheses might be responsible for the lack of CFZ activity. This new data evaluating CFZ in the Kramnik mouse model affirms the potential benefit for a model that represents the human disease condition The Kramnik mouse model could be an additional tool that can answer focused questions and increase the confidence of a drug or identified drug regimen prior to advancing into a human trial.

The bacterial tolerance to drug treatment has become an area of contention as to the cause. We consider that the inability of AR stain to detect specific bacteria within the necrotic core and the inability of specific drugs to penetrate the type I granuloma are indicative of the environment within the inner core. The MTB are undergoing drastic physiological changes within the necrotic type I granuloma due to the environment. There is evidence to suggest there is an increase in mutation rate due to DNA damage from oxidative stress from the necrotic core [243]. In the Kramnik mouse model the large population of macrophages and we speculate the subsequent production of iNOS may be partially responsible for contributing to the hostile mutagenic environment. This could be determined by measuring the functional NOS production of infected macrophages from C3HeB/FeJ mice.

The unique pathology of the Kramnik mouse model make the C3HeB/FeJ mouse strain a useful resource for exploring a plethora of alternative approaches to treatment. An example of

this is reflected by our pilot study conducted with the pharmaceutical company Merrimack Pharmaceuticals Inc., specialized in oncology treatments, using a liposomal drug delivery system for tuberculosis. The preliminary work conducted with the company, is the start of a larger project, which aims to explore how the physical environment of the necrotic granuloma, which is remarkably similar to solid cancerous tumors, can be exploited to enhance treatment of MTB. Preliminary results, which mainly focused on the type I lesions so far, show active tracking of fluorescently labeled liposomal formulations to the functional macrophages on the outside of the collagen rim as well as in the foamy macrophages on the inside of the collagen capsule. Cursory evaluation with confocal microscopy showed that the liposomal nanoparticles appear to cross to some extent the collagen fibrils into the foamy macrophages, which contain high numbers of bacteria. However, most liposomal accumulation could be observed on the outside of the fibrous capsule within the functional macrophages. More confocal analysis is required on a larger sample size as well as expanding the results to other lesion types. At this early stage in the project, one drawback encountered by our studies is the overall rapid clearance of the liposomes primarily in infected animals. The liposomal nanoparticles used have a specific pegylated makeup and this may actually make the liposomes a target for increased phagosomal digestion. Currently, pharmacokinetic evaluations are being performed on a library of various liposomal formulations to delay phagosome uptake of the liposomes. In a coordinated effort, investigation of the hypothesis is ongoing that due to infection, activated macrophages and other immune cells more readily take up and destroy the liposomes is also being performed.

Further experimentation involving the liposomal nanoparticles is to assess drug efficacy of drug-encapsulated nanoparticles and compare this to free drug. A mouse drug study is currently ongoing in our laboratory that is evaluating a first liposomal formulation that

encapsulates a TB drug in order to evaluate its efficacy when given intermittently and compare to the efficacy of the free drug when given daily. As the liposomal formulations are to be administered by injection route, the practical implications of this approach remain to be seen. The goal of the nanoparticles is therefore aimed to drastically reduce treatment duration, from several months to weeks with direct delivery of drug with sufficient accumulation at the site of infection. These liposomal formulations could also be applied for other difficult to treat infectious diseases, such as *Pseudomonas aeruginosa*, which is a biofilm forming bacterium that is a tremendous problem for the medical field by contaminating equipment thereby infecting patients. A directed, high dose of medication could potentially result in faster treatments and reduced resistance.

Another alternative approach to the classical tuberculosis treatment is to improve lung pathology to increase drug exposure at the site of infection. Disruptors of the physical barrier, which is the fibrous capsule of the necrotic lesion, could be a viable alternative to facilitate drug therapy. Elegant work by Dartois, et al. looking at drug penetration has shown by MALDI imaging of rabbit lesions infected with MTB, that MXF accumulates mainly in macrophages on the outside of the necrotic lesions and that less drug reaches the cores of these lesions. A pilot study has been performed with the Kramnik mouse model by V. Dartois (Rutgers Institute, NJ) using MALDI imaging, showed very similar results for CFZ. As discussed above, an improvement of the pathology may be achieved with immuno-modulators but could potentially also be achieved with, for instance, anti-fibrolitics currently on the market. A pilot study was performed to assess the potential of LK as a collagen disruptor. LK is currently clinically being used as an anti-fibrolitic agent in cases of idiopathic pulmonary fibrosis, liver cirrhosis, and myocardial fibrosis. When LK was used as a pre-treatment, prior to treatment with MXF, we saw

some added activity when compared to MXF alone. There were however some technical issues with the experiment regarding dosages of the LK compound and high mortality rate of mice. A longer-term treatment of mice with established infection with an adjusted dose of LK might give the answer. In addition other anti-fibrolitic compounds could be included in the follow-up study, such as pirfenidone [366]. This compound has shown clinical success in the treatment of idiopathic pulmonary fibrosis. This goal could also be accomplished with techniques used in oncology, such as the judicious addition of VEG-F to restore proper vasculature to the hypoxic necrotic granuloma to allow for better drug penetration [367].

In summary, the Kramnik mouse model is an exciting new mouse model. The C3HeB/FeJ mouse strain has gained considerable interest throughout the field and is based on I. Kramnik's work and ours being utilized by researchers around the globe to study many facets of TB disease. Pathologically, it is more representative of tuberculosis disease and this allows us to explore the cellular composition, immunological function, bacterial status and location, response to drug treatment, and alternatives to traditional therapy on a large scale. Substantial research has been done on the optimization of the TB infected C3HeB/FeJ mouse model itself but there are many research areas of MTB that still need further investigation, such as those outlined in this chapter. The Kramnik mouse model may be instrumental in answering lingering questions and furthering our knowledge about TB in man.

CITED REFERENCES

1. Parrish, N.M., J.D. Dick, and W.R. Bishai, *Mechanisms of latency in Mycobacterium tuberculosis.* Trends Microbiol, 1998. **6**(3): p. 107-12.
2. WHO, *Global Tuberculosis Report*. 2013: Geneva.
3. WHO, *Implementing The Stop TB Strategy: A handbook for national tuberculosis control programmes*. 2008: Geneva.
4. WHO, *Tuberculosis Fact Sheet*. 2013.
5. WHO, *Global Tuberculosis Report*. 2009: Geneva.
6. Velayati, A.A., et al., *Emergence of new forms of totally drug-resistant tuberculosis bacilli: super extensively drug-resistant tuberculosis or totally drug-resistant strains in iran.* Chest, 2009. **136**(2): p. 420-5.
7. Velayati, A.A., P. Farnia, and M.R. Masjedi, *The totally drug resistant tuberculosis (TDR-TB).* Int J Clin Exp Med, 2013. **6**(4): p. 307-9.
8. Klopper, M., et al., *Emergence and spread of extensively and totally drug-resistant tuberculosis, South Africa.* Emerg Infect Dis, 2013. **19**(3): p. 449-55.
9. Gras, J., *Bedaquiline for the treatment of pulmonary, multidrug-resistant tuberculosis in adults.* Drugs Today (Barc), 2013. **49**(6): p. 353-61.
10. Grosset, J.H. and N.C. Ammerman, *Dose-ranging activity of the newly registered antituberculosis drug bedaquiline (TMC207).* Expert Rev Anti Infect Ther, 2013. **11**(7): p. 649-51.
11. Dannenberg, A.M. and American Society for Microbiology. *Pathogenesis of human pulmonary tuberculosis : insights from the rabbit model*. 2006; xiv, 453 p.].
12. MacMicking, J.D., *Recognizing macrophage activation and host defense.* Cell Host Microbe, 2009. **5**(5): p. 405-7.
13. Rohde, K., et al., *Mycobacterium tuberculosis and the environment within the phagosome.* Immunol Rev, 2007. **219**: p. 37-54.
14. Russell, D.G., et al., *Foamy macrophages and the progression of the human tuberculosis granuloma.* Nat Immunol, 2009. **10**(9): p. 943-8.
15. Kaufmann, S.H., *Protection against tuberculosis: cytokines, T cells, and macrophages.* Ann Rheum Dis, 2002. **61 Suppl 2**: p. ii54-8.
16. Kolls, J.K., *CD4(+) T-cell subsets and host defense in the lung.* Immunol Rev, 2013. **252**(1): p. 156-63.
17. Gil, O., et al., *Granuloma encapsulation is a key factor for containing tuberculosis infection in minipigs.* PLoS One, 2010. **5**(4): p. e10030.
18. Guirado, E. and L.S. Schlesinger, *Modeling the Mycobacterium tuberculosis Granuloma - the Critical Battlefield in Host Immunity and Disease.* Front Immunol, 2013. **4**: p. 98.
19. Russell, D.G., et al., *Mycobacterium tuberculosis wears what it eats.* Cell Host Microbe, 2010. **8**(1): p. 68-76.
20. Saunders, B.M. and W.J. Britton, *Life and death in the granuloma: immunopathology of tuberculosis.* Immunol Cell Biol, 2007. **85**(2): p. 103-11.
21. Zhang, Y., *Advances in the treatment of tuberculosis.* Clin Pharmacol Ther, 2007. **82**(5): p. 595-600.
22. Bigger, J.W., *Treatment of staphylococcal infections with penicillin - By intermittent sterilisation.* Lancet, 1944. **2**: p. 497-500.

23. Zhang, Y., W.W. Yew, and M.R. Barer, *Targeting persisters for tuberculosis control.* Antimicrob Agents Chemother, 2012. **56**(5): p. 2223-30.
24. Phuah, J.Y., et al., *Activated B cells in the granulomas of nonhuman primates infected with Mycobacterium tuberculosis.* Am J Pathol, 2012. **181**(2): p. 508-14.
25. Barry, C.E., 3rd, et al., *The spectrum of latent tuberculosis: rethinking the biology and intervention strategies.* Nat Rev Microbiol, 2009. **7**(12): p. 845-55.
26. Lin, P.L. and J.L. Flynn, *Understanding latent tuberculosis: a moving target.* J Immunol, 2010. **185**(1): p. 15-22.
27. Gengenbacher, M. and S.H. Kaufmann, *Mycobacterium tuberculosis: success through dormancy.* FEMS Microbiol Rev, 2012. **36**(3): p. 514-32.
28. Gomez, J.E. and J.D. McKinney, *M. tuberculosis persistence, latency, and drug tolerance.* Tuberculosis (Edinb), 2004. **84**(1-2): p. 29-44.
29. Wayne, L.G. and L.G. Hayes, *An in vitro model for sequential study of shiftdown of Mycobacterium tuberculosis through two stages of nonreplicating persistence.* Infect Immun, 1996. **64**(6): p. 2062-9.
30. Ehlers, S., *Immunity to tuberculosis: a delicate balance between protection and pathology.* FEMS Immunol Med Microbiol, 1999. **23**(2): p. 149-58.
31. Hobby, G.L., K. Meyer, and E. Chaffee, *Observations on the mechanism of action of penicillin.* Proc soc. exp. biol. med, 1942. **50**: p. 281-285.
32. McDermott, W., et al., *Isonicotinic acid hydrazide in tuberculosis in man.* Trans Assoc Am Physicians, 1952. **65**: p. 191-202.
33. Wakamoto, Y., et al., *Dynamic persistence of antibiotic-stressed mycobacteria.* Science, 2013. **339**(6115): p. 91-5.
34. Li, Y. and Y. Zhang, *PhoU is a persistence switch involved in persister formation and tolerance to multiple antibiotics and stresses in Escherichia coli.* Antimicrob Agents Chemother, 2007. **51**(6): p. 2092-9.
35. Luidalepp, H., et al., *Age of inoculum strongly influences persister frequency and can mask effects of mutations implicated in altered persistence.* J Bacteriol, 2011. **193**(14): p. 3598-605.
36. Ma, M.J., et al., *Toll-like receptors, tumor necrosis factor-alpha, and interleukin-10 gene polymorphisms in risk of pulmonary tuberculosis and disease severity.* Hum Immunol, 2010. **71**(10): p. 1005-10.
37. Chen, K. and J.K. Kolls, *T cell-mediated host immune defenses in the lung.* Annu Rev Immunol, 2013. **31**: p. 605-33.
38. Khader, S.A., et al., *IL-23 is required for long-term control of Mycobacterium tuberculosis and B cell follicle formation in the infected lung.* J Immunol, 2011. **187**(10): p. 5402-7.
39. Woodworth, J.S. and S.M. Behar, *Mycobacterium tuberculosis-specific CD8+ T cells and their role in immunity.* Crit Rev Immunol, 2006. **26**(4): p. 317-52.
40. Flynn, J.L. and J. Chan, *Immunology of tuberculosis.* Annu Rev Immunol, 2001. **19**: p. 93-129.
41. Mogues, T., et al., *The relative importance of T cell subsets in immunity and immunopathology of airborne Mycobacterium tuberculosis infection in mice.* J Exp Med, 2001. **193**(3): p. 271-80.
42. Pearl, J.E., et al., *Inflammation and lymphocyte activation during mycobacterial infection in the interferon-gamma-deficient mouse.* Cell Immunol, 2001. **211**(1): p. 43-50.

43. Cooper, A.M., *Cell-mediated immune responses in tuberculosis.* Annu Rev Immunol, 2009. **27**: p. 393-422.
44. Cooper, A.M., et al., *Disseminated tuberculosis in interferon gamma gene-disrupted mice.* J Exp Med, 1993. **178**(6): p. 2243-7.
45. Getahun, H., et al., *HIV infection-associated tuberculosis: the epidemiology and the response.* Clin Infect Dis, 2010. **50 Suppl 3**: p. S201-7.
46. Kalsdorf, B., et al., *HIV-1 infection impairs the bronchoalveolar T-cell response to mycobacteria.* Am J Respir Crit Care Med, 2009. **180**(12): p. 1262-70.
47. Mukadi, Y., et al., *Spectrum of immunodeficiency in HIV-1-infected patients with pulmonary tuberculosis in Zaire.* Lancet, 1993. **342**(8864): p. 143-6.
48. Geldmacher, C., et al., *Preferential infection and depletion of Mycobacterium tuberculosis-specific CD4 T cells after HIV-1 infection.* J Exp Med, 2010. **207**(13): p. 2869-81.
49. Geldmacher, C., et al., *Early depletion of Mycobacterium tuberculosis-specific T helper 1 cell responses after HIV-1 infection.* J Infect Dis, 2008. **198**(11): p. 1590-8.
50. Flynn, J.L., et al., *Non-human primates: a model for tuberculosis research.* Tuberculosis (Edinb), 2003. **83**(1-3): p. 116-8.
51. Tufariello, J.M., J. Chan, and J.L. Flynn, *Latent tuberculosis: mechanisms of host and bacillus that contribute to persistent infection.* Lancet Infect Dis, 2003. **3**(9): p. 578-90.
52. Flynn, J.L., et al., *An essential role for interferon gamma in resistance to Mycobacterium tuberculosis infection.* J Exp Med, 1993. **178**(6): p. 2249-54.
53. Lenaerts, A.J., et al., *Rapid in vivo screening of experimental drugs for tuberculosis using gamma interferon gene-disrupted mice.* Antimicrob Agents Chemother, 2003. **47**(2): p. 783-5.
54. McDonough, K.A., Y. Kress, and B.R. Bloom, *The interaction of Mycobacterium tuberculosis with macrophages: a study of phagolysosome fusion.* Infect Agents Dis, 1993. **2**(4): p. 232-5.
55. Orme, I.M., et al., *Cytokine secretion by CD4 T lymphocytes acquired in response to Mycobacterium tuberculosis infection.* J Immunol, 1993. **151**(1): p. 518-25.
56. Cooper, A.M. and S.A. Khader, *The role of cytokines in the initiation, expansion, and control of cellular immunity to tuberculosis.* Immunol Rev, 2008. **226**: p. 191-204.
57. Chan, J. and J. Flynn, *The immunological aspects of latency in tuberculosis.* Clin Immunol, 2004. **110**(1): p. 2-12.
58. MacMicking, J.D., et al., *Identification of nitric oxide synthase as a protective locus against tuberculosis.* Proc Natl Acad Sci U S A, 1997. **94**(10): p. 5243-8.
59. Nathan, C. and M.U. Shiloh, *Reactive oxygen and nitrogen intermediates in the relationship between mammalian hosts and microbial pathogens.* Proc Natl Acad Sci U S A, 2000. **97**(16): p. 8841-8.
60. Cooper, A.M., et al., *Interleukin 12 (IL-12) is crucial to the development of protective immunity in mice intravenously infected with mycobacterium tuberculosis.* J Exp Med, 1997. **186**(1): p. 39-45.
61. Khader, S.A., et al., *Interleukin 12p40 is required for dendritic cell migration and T cell priming after Mycobacterium tuberculosis infection.* J Exp Med, 2006. **203**(7): p. 1805-15.
62. Cooper, A.M., K.D. Mayer-Barber, and A. Sher, *Role of innate cytokines in mycobacterial infection.* Mucosal Immunol, 2011. **4**(3): p. 252-60.

63. Orme, I.M. and A.M. Cooper, *Cytokine/chemokine cascades in immunity to tuberculosis.* Immunol Today, 1999. **20**(7): p. 307-12.
64. Khader, S.A., et al., *IL-23 compensates for the absence of IL-12p70 and is essential for the IL-17 response during tuberculosis but is dispensable for protection and antigen-specific IFN-gamma responses if IL-12p70 is available.* J Immunol, 2005. **175**(2): p. 788-95.
65. Ulrichs, T. and S.H. Kaufmann, *Mycobacterial persistence and immunity.* Front Biosci, 2002. **7**: p. d458-69.
66. Botha, T. and B. Ryffel, *Reactivation of latent tuberculosis infection in TNF-deficient mice.* J Immunol, 2003. **171**(6): p. 3110-8.
67. Chakravarty, S.D., et al., *Tumor necrosis factor blockade in chronic murine tuberculosis enhances granulomatous inflammation and disorganizes granulomas in the lungs.* Infect Immun, 2008. **76**(3): p. 916-26.
68. Fenhalls, G., et al., *In situ detection of Mycobacterium tuberculosis transcripts in human lung granulomas reveals differential gene expression in necrotic lesions.* Infect Immun, 2002. **70**(11): p. 6330-8.
69. Flynn, J.L., et al., *Tumor necrosis factor-alpha is required in the protective immune response against Mycobacterium tuberculosis in mice.* Immunity, 1995. **2**(6): p. 561-72.
70. Redford, P.S., P.J. Murray, and A. O'Garra, *The role of IL-10 in immune regulation during M. tuberculosis infection.* Mucosal Immunol, 2011. **4**(3): p. 261-70.
71. Beamer, G.L., et al., *Interleukin-10 promotes Mycobacterium tuberculosis disease progression in CBA/J mice.* J Immunol, 2008. **181**(8): p. 5545-50.
72. Higgins, D.M., et al., *Lack of IL-10 alters inflammatory and immune responses during pulmonary Mycobacterium tuberculosis infection.* Tuberculosis (Edinb), 2009. **89**(2): p. 149-57.
73. Jung, Y.J., et al., *Increased interleukin-10 expression is not responsible for failure of T helper 1 immunity to resolve airborne Mycobacterium tuberculosis infection in mice.* Immunology, 2003. **109**(2): p. 295-9.
74. North, R.J., *Mice incapable of making IL-4 or IL-10 display normal resistance to infection with Mycobacterium tuberculosis.* Clin Exp Immunol, 1998. **113**(1): p. 55-8.
75. Redford, P.S., et al., *Enhanced protection to Mycobacterium tuberculosis infection in IL-10-deficient mice is accompanied by early and enhanced Th1 responses in the lung.* Eur J Immunol, 2010. **40**(8): p. 2200-10.
76. Roach, D.R., et al., *Endogenous inhibition of antimycobacterial immunity by IL-10 varies between mycobacterial species.* Scand J Immunol, 2001. **54**(1-2): p. 163-70.
77. Turner, J., et al., *In vivo IL-10 production reactivates chronic pulmonary tuberculosis in C57BL/6 mice.* J Immunol, 2002. **169**(11): p. 6343-51.
78. Cyktor, J.C., et al., *IL-10 inhibits mature fibrotic granuloma formation during Mycobacterium tuberculosis infection.* J Immunol, 2013. **190**(6): p. 2778-90.
79. O'Leary, S., M.P. O'Sullivan, and J. Keane, *IL-10 blocks phagosome maturation in mycobacterium tuberculosis-infected human macrophages.* Am J Respir Cell Mol Biol, 2011. **45**(1): p. 172-80.
80. Shaw, T.C., L.H. Thomas, and J.S. Friedland, *Regulation of IL-10 secretion after phagocytosis of Mycobacterium tuberculosis by human monocytic cells.* Cytokine, 2000. **12**(5): p. 483-6.
81. Rollins, B.J., *Chemokines.* Blood, 1997. **90**(3): p. 909-28.

82. Sadek, M.I., et al., *Chemokines induced by infection of mononuclear phagocytes with mycobacteria and present in lung alveoli during active pulmonary tuberculosis.* Am J Respir Cell Mol Biol, 1998. **19**(3): p. 513-21.
83. Kipnis, A., et al., *Role of chemokine ligand 2 in the protective response to early murine pulmonary tuberculosis.* Immunology, 2003. **109**(4): p. 547-51.
84. Hasan, Z., et al., *CCL2 responses to Mycobacterium tuberculosis are associated with disease severity in tuberculosis.* PLoS One, 2009. **4**(12): p. e8459.
85. Kendall, S.L., et al., *What do microarrays really tell us about M. tuberculosis?* Trends Microbiol, 2004. **12**(12): p. 537-44.
86. Marrero, J., et al., *Gluconeogenic carbon flow of tricarboxylic acid cycle intermediates is critical for Mycobacterium tuberculosis to establish and maintain infection.* Proc Natl Acad Sci U S A, 2010. **107**(21): p. 9819-24.
87. Schnappinger, D., et al., *Transcriptional Adaptation of Mycobacterium tuberculosis within Macrophages: Insights into the Phagosomal Environment.* J Exp Med, 2003. **198**(5): p. 693-704.
88. Bloch, H. and W. Segal, *Biochemical differentiation of Mycobacterium tuberculosis grown in vivo and in vitro.* J Bacteriol, 1956. **72**(2): p. 132-41.
89. Eoh, H. and K.Y. Rhee, *Multifunctional essentiality of succinate metabolism in adaptation to hypoxia in Mycobacterium tuberculosis.* Proc Natl Acad Sci U S A, 2013. **110**(16): p. 6554-9.
90. Munoz-Elias, E.J. and J.D. McKinney, *Mycobacterium tuberculosis isocitrate lyases 1 and 2 are jointly required for in vivo growth and virulence.* Nat Med, 2005. **11**(6): p. 638-44.
91. Lorenz, M.C. and G.R. Fink, *Life and death in a macrophage: role of the glyoxylate cycle in virulence.* Eukaryot Cell, 2002. **1**(5): p. 657-62.
92. Vanni, P., et al., *Comparative structure, function and regulation of isocitrate lyase, an important assimilatory enzyme.* Comp Biochem Physiol B, 1990. **95**(3): p. 431-58.
93. Sharma, V., et al., *Structure of isocitrate lyase, a persistence factor of Mycobacterium tuberculosis.* Nat Struct Biol, 2000. **7**(8): p. 663-8.
94. McKinney, J.D., et al., *Persistence of Mycobacterium tuberculosis in macrophages and mice requires the glyoxylate shunt enzyme isocitrate lyase.* Nature, 2000. **406**(6797): p. 735-8.
95. Blumenthal, A., et al., *Simultaneous analysis of multiple Mycobacterium tuberculosis knockdown mutants in vitro and in vivo.* PLoS One, 2010. **5**(12): p. e15667.
96. Norman, E., et al., *Lipid synthesis in mycobacteria: characterization of the biotin carboxyl carrier protein genes from Mycobacterium leprae and M. tuberculosis.* J Bacteriol, 1994. **176**(9): p. 2525-31.
97. Cole, S.T., *Comparative mycobacterial genomics.* Curr Opin Microbiol, 1998. **1**(5): p. 567-71.
98. Fontan, P.A., et al., *Mycobacterium tuberculosis sigma factor E regulon modulates the host inflammatory response.* J Infect Dis, 2008. **198**(6): p. 877-85.
99. Cappelli, G., et al., *Profiling of Mycobacterium tuberculosis gene expression during human macrophage infection: upregulation of the alternative sigma factor G, a group of transcriptional regulators, and proteins with unknown function.* Res Microbiol, 2006. **157**(5): p. 445-55.

100. Raman, S., et al., *Transcription regulation by the Mycobacterium tuberculosis alternative sigma factor SigD and its role in virulence.* J Bacteriol, 2004. **186**(19): p. 6605-16.
101. Raman, S., et al., *The alternative sigma factor SigH regulates major components of oxidative and heat stress responses in Mycobacterium tuberculosis.* J Bacteriol, 2001. **183**(20): p. 6119-25.
102. Leistikow, R.L., et al., *The Mycobacterium tuberculosis DosR regulon assists in metabolic homeostasis and enables rapid recovery from nonrespiring dormancy.* J Bacteriol, 2010. **192**(6): p. 1662-70.
103. Voskuil, M.I., et al., *Inhibition of respiration by nitric oxide induces a Mycobacterium tuberculosis dormancy program.* J Exp Med, 2003. **198**(5): p. 705-13.
104. Minch, K., T. Rustad, and D.R. Sherman, *Mycobacterium tuberculosis growth following aerobic expression of the DosR regulon.* PLoS One, 2012. **7**(4): p. e35935.
105. Kashino, S.S., et al., *Guinea pig model of Mycobacterium tuberculosis latent/dormant infection.* Microbes Infect, 2008. **10**(14-15): p. 1469-76.
106. Yuan, Y., et al., *The 16-kDa alpha-crystallin (Acr) protein of Mycobacterium tuberculosis is required for growth in macrophages.* Proc Natl Acad Sci U S A, 1998. **95**(16): p. 9578-83.
107. Sherman, D.R., et al., *Regulation of the Mycobacterium tuberculosis hypoxic response gene encoding alpha -crystallin.* Proc Natl Acad Sci U S A, 2001. **98**(13): p. 7534-9.
108. Yuan, Y., D.D. Crane, and C.E. Barry, 3rd, *Stationary phase-associated protein expression in Mycobacterium tuberculosis: function of the mycobacterial alpha-crystallin homolog.* J Bacteriol, 1996. **178**(15): p. 4484-92.
109. Vasudeva-Rao, H.M. and K.A. McDonough, *Expression of the Mycobacterium tuberculosis acr-coregulated genes from the DevR (DosR) regulon is controlled by multiple levels of regulation.* Infect Immun, 2008. **76**(6): p. 2478-89.
110. Lee, B.Y., S.A. Hefta, and P.J. Brennan, *Characterization of the major membrane protein of virulent Mycobacterium tuberculosis.* Infect Immun, 1992. **60**(5): p. 2066-74.
111. Verbon, A., et al., *The 14,000-molecular-weight antigen of Mycobacterium tuberculosis is related to the alpha-crystallin family of low-molecular-weight heat shock proteins.* J Bacteriol, 1992. **174**(4): p. 1352-9.
112. Stewart, J.N., et al., *Increased pathology in lungs of mice after infection with an alpha-crystallin mutant of Mycobacterium tuberculosis: changes in cathepsin proteases and certain cytokines.* Microbiology, 2006. **152**(Pt 1): p. 233-44.
113. Wayne, L.G., *Dormancy of Mycobacterium tuberculosis and latency of disease.* Eur J Clin Microbiol Infect Dis, 1994. **13**(11): p. 908-14.
114. Wayne, L.G. and K.Y. Lin, *Glyoxylate metabolism and adaptation of Mycobacterium tuberculosis to survival under anaerobic conditions.* Infect Immun, 1982. **37**(3): p. 1042-9.
115. Wayne, L.G. and H.A. Sramek, *Metronidazole is bactericidal to dormant cells of Mycobacterium tuberculosis.* Antimicrob Agents Chemother, 1994. **38**(9): p. 2054-8.
116. Lenaerts, A.J., et al., *Preclinical testing of the nitroimidazopyran PA-824 for activity against Mycobacterium tuberculosis in a series of in vitro and in vivo models.* Antimicrob Agents Chemother, 2005. **49**(6): p. 2294-301.
117. Boon, C. and T. Dick, *Mycobacterium bovis BCG response regulator essential for hypoxic dormancy.* J Bacteriol, 2002. **184**(24): p. 6760-7.

118. Hu, Y. and A.R. Coates, *Transcription of two sigma 70 homologue genes, sigA and sigB, in stationary-phase Mycobacterium tuberculosis.* J Bacteriol, 1999. **181**(2): p. 469-76.
119. Roberts, D.M., et al., *Two sensor kinases contribute to the hypoxic response of Mycobacterium tuberculosis.* J Biol Chem, 2004. **279**(22): p. 23082-7.
120. Rustad, T.R., et al., *The enduring hypoxic response of Mycobacterium tuberculosis.* PLoS One, 2008. **3**(1): p. e1502.
121. Voskuil, M.I., *Mycobacterium tuberculosis gene expression during environmental conditions associated with latency.* Tuberculosis (Edinb), 2004. **84**(3-4): p. 138-43.
122. Ioanoviciu, A., et al., *DevS oxy complex stability identifies this heme protein as a gas sensor in Mycobacterium tuberculosis dormancy.* Biochemistry, 2009. **48**(25): p. 5839-48.
123. Ioanoviciu, A., et al., *DevS, a heme-containing two-component oxygen sensor of Mycobacterium tuberculosis.* Biochemistry, 2007. **46**(14): p. 4250-60.
124. Sousa, E.H., et al., *DosT and DevS are oxygen-switched kinases in Mycobacterium tuberculosis.* Protein Sci, 2007. **16**(8): p. 1708-19.
125. Cho, H.Y., et al., *Structural insight into the heme-based redox sensing by DosS from Mycobacterium tuberculosis.* J Biol Chem, 2009. **284**(19): p. 13057-67.
126. Kumar, A., et al., *Mycobacterium tuberculosis DosS is a redox sensor and DosT is a hypoxia sensor.* Proc Natl Acad Sci U S A, 2007. **104**(28): p. 11568-73.
127. Converse, P.J., et al., *Role of the dosR-dosS two-component regulatory system in Mycobacterium tuberculosis virulence in three animal models.* Infect Immun, 2009. **77**(3): p. 1230-7.
128. Bartek, I.L., et al., *The DosR regulon of M. tuberculosis and antibacterial tolerance.* Tuberculosis (Edinb), 2009. **89**(4): p. 310-6.
129. Gill, W.P., et al., *A replication clock for Mycobacterium tuberculosis.* Nat Med, 2009. **15**(2): p. 211-4.
130. Rustad, T.R., et al., *Hypoxia: a window into Mycobacterium tuberculosis latency.* Cell Microbiol, 2009. **11**(8): p. 1151-9.
131. Driver, E.R., et al., *Evaluation of a mouse model of necrotic granuloma formation using C3HeB/FeJ mice for testing of drugs against Mycobacterium tuberculosis.* Antimicrob Agents Chemother, 2012. **56**(6): p. 3181-95.
132. Flynn, J.L. and J. Chan, *Tuberculosis: latency and reactivation.* Infect Immun, 2001. **69**(7): p. 4195-201.
133. Henao-Tamayo, M., et al., *A mouse model of tuberculosis reinfection.* Tuberculosis (Edinb), 2012. **92**(3): p. 211-7.
134. Hoff, D.R., et al., *Location of intra- and extracellular M. tuberculosis populations in lungs of mice and guinea pigs during disease progression and after drug treatment.* PLoS One, 2011. **6**(3): p. e17550.
135. Khader, S.A., et al., *In a murine tuberculosis model, the absence of homeostatic chemokines delays granuloma formation and protective immunity.* J Immunol, 2009. **183**(12): p. 8004-14.
136. Ryan, G.J., et al., *Multiple M. tuberculosis phenotypes in mouse and guinea pig lung tissue revealed by a dual-staining approach.* PLoS One, 2010. **5**(6): p. e11108.
137. Reisfeld, B., et al., *A physiologically based pharmacokinetic model for capreomycin.* Antimicrob Agents Chemother, 2012. **56**(2): p. 926-34.

138. Tsai, M.C., et al., *Characterization of the tuberculous granuloma in murine and human lungs: cellular composition and relative tissue oxygen tension.* Cell Microbiol, 2006. **8**(2): p. 218-32.
139. Miner, M.D., et al., *Role of cholesterol in Mycobacterium tuberculosis infection.* Indian J Exp Biol, 2009. **47**(6): p. 407-11.
140. Rhoades, E.R., A.A. Frank, and I.M. Orme, *Progression of chronic pulmonary tuberculosis in mice aerogenically infected with virulent Mycobacterium tuberculosis.* Tuber Lung Dis, 1997. **78**(1): p. 57-66.
141. Aly, S., et al., *Oxygen status of lung granulomas in Mycobacterium tuberculosis-infected mice.* J Pathol, 2006. **210**(3): p. 298-305.
142. Franzblau, S.G., et al., *Comprehensive analysis of methods used for the evaluation of compounds against Mycobacterium tuberculosis.* Tuberculosis (Edinb), 2012. **92**(6): p. 453-88.
143. Kelly, B.P., et al., *Low-dose aerosol infection model for testing drugs for efficacy against Mycobacterium tuberculosis.* Antimicrob Agents Chemother, 1996. **40**(12): p. 2809-12.
144. McCune, R.M., et al., *The influence of streptovaricin used alone and with isoniazid in an experimental tuberculous infection in animals, and some clinical observations.* Am Rev Tuberc, 1957. **75**(4): p. 659-66.
145. McCune, R.M., et al., *Microbial persistence. I. The capacity of tubercle bacilli to survive sterilization in mouse tissues.* J Exp Med, 1966. **123**(3): p. 445-68.
146. McCune, R.M., F.M. Feldmann, and W. McDermott, *Microbial persistence. II. Characteristics of the sterile state of tubercle bacilli.* J Exp Med, 1966. **123**(3): p. 469-86.
147. Miyazaki, E., R.E. Chaisson, and W.R. Bishai, *Analysis of rifapentine for preventive therapy in the Cornell mouse model of latent tuberculosis.* Antimicrob Agents Chemother, 1999. **43**(9): p. 2126-30.
148. Scanga, C.A., et al., *Reactivation of latent tuberculosis: variations on the Cornell murine model.* Infect Immun, 1999. **67**(9): p. 4531-8.
149. Lenaerts, A.J., P.L. Chapman, and I.M. Orme, *Statistical limitations to the Cornell model of latent tuberculosis infection for the study of relapse rates.* Tuberculosis (Edinb), 2004. **84**(6): p. 361-4.
150. Basaraba, R.J., et al., *Decreased survival of guinea pigs infected with Mycobacterium tuberculosis after multiple BCG vaccinations.* Vaccine, 2006. **24**(3): p. 280-6.
151. Basaraba, R.J., et al., *Pulmonary lymphatics are primary sites of Mycobacterium tuberculosis infection in guinea pigs infected by aerosol.* Infect Immun, 2006. **74**(9): p. 5397-401.
152. Cosma, C.L., et al., *Zebrafish and frog models of Mycobacterium marinum infection.* Curr Protoc Microbiol, 2006. **Chapter 10**: p. Unit 10B 2.
153. Elwood, R.L., et al., *The American cotton rat: a novel model for pulmonary tuberculosis.* Tuberculosis (Edinb), 2007. **87**(2): p. 145-54.
154. Gonzalez-Juarrero, M., et al., *Experimental aerosol Mycobacterium bovis model of infection in goats.* Tuberculosis (Edinb), 2013. **93**(5): p. 558-64.
155. Manabe, Y.C., et al., *The aerosol rabbit model of TB latency, reactivation and immune reconstitution inflammatory syndrome.* Tuberculosis (Edinb), 2008. **88**(3): p. 187-96.
156. Lenaerts, A.J., M.A. Degroote, and I.M. Orme, *Preclinical testing of new drugs for tuberculosis: current challenges.* Trends Microbiol, 2008. **16**(2): p. 48-54.

157. Ahmad, Z., et al., *Biphasic kill curve of isoniazid reveals the presence of drug-tolerant, not drug-resistant, Mycobacterium tuberculosis in the guinea pig.* J Infect Dis, 2009. **200**(7): p. 1136-43.
158. Basaraba, R.J., et al., *Lymphadenitis as a major element of disease in the guinea pig model of tuberculosis.* Tuberculosis (Edinb), 2006. **86**(5): p. 386-94.
159. Dharmadhikari, A.S., et al., *Natural infection of guinea pigs exposed to patients with highly drug-resistant tuberculosis.* Tuberculosis (Edinb), 2011. **91**(4): p. 329-38.
160. Helke, K.L., J.L. Mankowski, and Y.C. Manabe, *Animal models of cavitation in pulmonary tuberculosis.* Tuberculosis (Edinb), 2006. **86**(5): p. 337-48.
161. Lenaerts, A.J., et al., *Location of persisting mycobacteria in a Guinea pig model of tuberculosis revealed by r207910.* Antimicrob Agents Chemother, 2007. **51**(9): p. 3338-45.
162. Ordway, D.J., et al., *Evaluation of standard chemotherapy in the guinea pig model of tuberculosis.* Antimicrob Agents Chemother, 2010. **54**(5): p. 1820-33.
163. Turner, O.C., R.J. Basaraba, and I.M. Orme, *Immunopathogenesis of pulmonary granulomas in the guinea pig after infection with Mycobacterium tuberculosis.* Infect Immun, 2003. **71**(2): p. 864-71.
164. McMurray, D.N., *Recent progress in the development and testing of vaccines against human tuberculosis.* Int J Parasitol, 2003. **33**(5-6): p. 547-54.
165. Kato-Maeda, M., et al., *Beijing sublineages of Mycobacterium tuberculosis differ in pathogenicity in the guinea pig.* Clin Vaccine Immunol, 2012. **19**(8): p. 1227-37.
166. Shang, S., et al., *Activities of TMC207, rifampin, and pyrazinamide against Mycobacterium tuberculosis infection in guinea pigs.* Antimicrob Agents Chemother, 2011. **55**(1): p. 124-31.
167. Hoff, D.R., et al., *Metronidazole lacks antibacterial activity in guinea pigs infected with Mycobacterium tuberculosis.* Antimicrob Agents Chemother, 2008. **52**(11): p. 4137-40.
168. Lurie, M.B., P. Zappasodi, and C. Tickner, *On the nature of genetic resistance to tuberculosis in the light of the host-parasite relationships in natively resistant and susceptible rabbits.* Am Rev Tuberc, 1955. **72**(3): p. 297-329.
169. Tsenova, L., et al., *Virulence of selected Mycobacterium tuberculosis clinical isolates in the rabbit model of meningitis is dependent on phenolic glycolipid produced by the bacilli.* J Infect Dis, 2005. **192**(1): p. 98-106.
170. Manca, C., et al., *Mycobacterium tuberculosis CDC1551 induces a more vigorous host response in vivo and in vitro, but is not more virulent than other clinical isolates.* J Immunol, 1999. **162**(11): p. 6740-6.
171. Rayner, E.L., et al., *Early lesions following aerosol infection of rhesus macaques (Macaca mulatta) with Mycobacterium tuberculosis strain H37RV.* J Comp Pathol, 2013. **149**(4): p. 475-85.
172. Capuano, S.V., 3rd, et al., *Experimental Mycobacterium tuberculosis infection of cynomolgus macaques closely resembles the various manifestations of human M. tuberculosis infection.* Infect Immun, 2003. **71**(10): p. 5831-44.
173. Tobin, D.M. and L. Ramakrishnan, *Comparative pathogenesis of Mycobacterium marinum and Mycobacterium tuberculosis.* Cell Microbiol, 2008. **10**(5): p. 1027-39.
174. Egen, J.G., et al., *Macrophage and T cell dynamics during the development and disintegration of mycobacterial granulomas.* Immunity, 2008. **28**(2): p. 271-84.

175. Singhal, A., et al., *BCG induces protection against Mycobacterium tuberculosis infection in the Wistar rat model.* PLoS One, 2011. **6**(12): p. e28082.
176. Sanchez, J., et al., *Microscopical and immunological features of tuberculoid granulomata and cavitary pulmonary tuberculosis in naturally infected goats.* J Comp Pathol, 2011. **145**(2-3): p. 107-17.
177. Jung, Y.J., et al., *Evidence inconsistent with a negative influence of T helper 2 cells on protection afforded by a dominant T helper 1 response against Mycobacterium tuberculosis lung infection in mice.* Infect Immun, 2002. **70**(11): p. 6436-43.
178. Major, S., J. Turner, and G. Beamer, *Tuberculosis in CBA/J mice.* Vet Pathol, 2013. **50**(6): p. 1016-21.
179. Obregon-Henao, A., et al., *Gr1(int)CD11b+ myeloid-derived suppressor cells in Mycobacterium tuberculosis infection.* PLoS One, 2013. **8**(11): p. e80669.
180. Majorov, K.B., et al., *Different innate ability of I/St and A/Sn mice to combat virulent Mycobacterium tuberculosis: phenotypes expressed in lung and extrapulmonary macrophages.* Infect Immun, 2003. **71**(2): p. 697-707.
181. Kramnik, I., et al., *Genetic control of resistance to experimental infection with virulent Mycobacterium tuberculosis.* Proc Natl Acad Sci U S A, 2000. **97**(15): p. 8560-5.
182. Lewis, C.C., et al., *Unique and overlapping gene expression patterns driven by IL-4 and IL-13 in the mouse lung.* J Allergy Clin Immunol, 2009. **123**(4): p. 795-804 e8.
183. McKenzie, G.J., et al., *Simultaneous disruption of interleukin (IL)-4 and IL-13 defines individual roles in T helper cell type 2-mediated responses.* J Exp Med, 1999. **189**(10): p. 1565-72.
184. Padilla, J., et al., *IL-13 regulates the immune response to inhaled antigens.* J Immunol, 2005. **174**(12): p. 8097-105.
185. Junqueira-Kipnis, A.P., et al., *Interleukin-10 production by lung macrophages in CBA xid mutant mice infected with Mycobacterium tuberculosis.* Immunology, 2005. **115**(2): p. 246-52.
186. Guirado, E., et al., *Intragranulomatous necrosis in pulmonary granulomas is not related to resistance against Mycobacterium tuberculosis infection in experimental murine models induced by aerosol.* Int J Exp Pathol, 2006. **87**(2): p. 139-49.
187. Scanga, C.A., et al., *The inducible nitric oxide synthase locus confers protection against aerogenic challenge of both clinical and laboratory strains of Mycobacterium tuberculosis in mice.* Infect Immun, 2001. **69**(12): p. 7711-7.
188. Cooper, A.M., et al., *IFN-gamma and NO in mycobacterial disease: new jobs for old hands.* Trends Microbiol, 2002. **10**(5): p. 221-6.
189. Nikonenko, B.V., et al., *Comparative analysis of mycobacterial infections in susceptible I/St and resistant A/Sn inbred mice.* Tuber Lung Dis, 2000. **80**(1): p. 15-25.
190. Nikonenko, B.V., et al., *[Genetic aspects of experimental tuberculosis in mice]*. Genetika, 1986. **22**(5): p. 851-4.
191. Kondratieva, E.V., et al., *I/St mice hypersusceptible to Mycobacterium tuberculosis are resistant to M. avium.* Infect Immun, 2007. **75**(10): p. 4762-8.
192. Kramnik, I., P. Demant, and B.B. Bloom, *Susceptibility to tuberculosis as a complex genetic trait: analysis using recombinant congenic strains of mice.* Novartis Found Symp, 1998. **217**: p. 120-31; discussion 132-7.
193. Kramnik, I., *Genetic dissection of host resistance to Mycobacterium tuberculosis: the sst1 locus and the Ipr1 gene.* Curr Top Microbiol Immunol, 2008. **321**: p. 123-48.

194. Pan, H., et al., *Ipr1 gene mediates innate immunity to tuberculosis.* Nature, 2005. **434**(7034): p. 767-72.
195. Yan, B.S., et al., *Genetic architecture of tuberculosis resistance in a mouse model of infection.* Genes Immun, 2006. **7**(3): p. 201-10.
196. Medina, E. and R.J. North, *Resistance ranking of some common inbred mouse strains to Mycobacterium tuberculosis and relationship to major histocompatibility complex haplotype and Nramp1 genotype.* Immunology, 1998. **93**(2): p. 270-4.
197. Yan, B.S., et al., *Progression of pulmonary tuberculosis and efficiency of bacillus Calmette-Guerin vaccination are genetically controlled via a common sst1-mediated mechanism of innate immunity.* J Immunol, 2007. **179**(10): p. 6919-32.
198. Babb, C., et al., *SP110 polymorphisms are not associated with pulmonary tuberculosis in a South African population.* Hum Genet, 2007. **121**(3-4): p. 521-2.
199. Tosh, K., et al., *Variants in the SP110 gene are associated with genetic susceptibility to tuberculosis in West Africa.* Proc Natl Acad Sci U S A, 2006. **103**(27): p. 10364-8.
200. Davis, S.L., et al., *Noninvasive pulmonary [18F]-2-fluoro-deoxy-D-glucose positron emission tomography correlates with bactericidal activity of tuberculosis drug treatment.* Antimicrob Agents Chemother, 2009. **53**(11): p. 4879-84.
201. Ehlers, S., *Lazy, dynamic or minimally recrudescent? On the elusive nature and location of the mycobacterium responsible for latent tuberculosis.* Infection, 2009. **37**(2): p. 87-95.
202. Hunter, R.L., C. Jagannath, and J.K. Actor, *Pathology of postprimary tuberculosis in humans and mice: contradiction of long-held beliefs.* Tuberculosis (Edinb), 2007. **87**(4): p. 267-78.
203. Canetti, G., *The tubercule bacillus in the pulmonary lung lesion of man.* . 1955, New York: Springer.
204. Kaplan, G., et al., *Mycobacterium tuberculosis growth at the cavity surface: a microenvironment with failed immunity.* Infect Immun, 2003. **71**(12): p. 7099-108.
205. Prideaux, B., et al., *High-sensitivity MALDI-MRM-MS imaging of moxifloxacin distribution in tuberculosis-infected rabbit lungs and granulomatous lesions.* Anal Chem, 2011. **83**(6): p. 2112-8.
206. Davies, G.R., et al., *Evaluation of new antituberculosis drugs in mouse models.* Antimicrob Agents Chemother, 2007. **51**(1): p. 403; author reply 403-4.
207. Jain, S.K., et al., *Accelerated detection of Mycobacterium tuberculosis genes essential for bacterial survival in guinea pigs, compared with mice.* J Infect Dis, 2007. **195**(11): p. 1634-42.
208. Nuermberger, E.L., et al., *Moxifloxacin-containing regimens of reduced duration produce a stable cure in murine tuberculosis.* Am J Respir Crit Care Med, 2004. **170**(10): p. 1131-4.
209. Rosenthal, I.M., et al., *Potent twice-weekly rifapentine-containing regimens in murine tuberculosis.* Am J Respir Crit Care Med, 2006. **174**(1): p. 94-101.
210. Ahmad, Z., et al., *Comparison of the 'Denver regimen' against acute tuberculosis in the mouse and guinea pig.* J Antimicrob Chemother, 2010. **65**(4): p. 729-34.
211. Nedeltchev, G.G., et al., *Extrapulmonary dissemination of Mycobacterium bovis but not Mycobacterium tuberculosis in a bronchoscopic rabbit model of cavitary tuberculosis.* Infect Immun, 2009. **77**(2): p. 598-603.
212. Via, L.E., et al., *Tuberculous granulomas are hypoxic in guinea pigs, rabbits, and nonhuman primates.* Infect Immun, 2008. **76**(6): p. 2333-40.

213. Lin, P.L., et al., *Early events in Mycobacterium tuberculosis infection in cynomolgus macaques.* Infect Immun, 2006. **74**(7): p. 3790-803.
214. Keller, C., et al., *Genetically determined susceptibility to tuberculosis in mice causally involves accelerated and enhanced recruitment of granulocytes.* Infect Immun, 2006. **74**(7): p. 4295-309.
215. Pichugin, A.V., et al., *Dominant role of the sst1 locus in pathogenesis of necrotizing lung granulomas during chronic tuberculosis infection and reactivation in genetically resistant hosts.* Am J Pathol, 2009. **174**(6): p. 2190-201.
216. Sissons, J., et al., *Multigenic control of tuberculosis resistance: analysis of a QTL on mouse chromosome 7 and its synergism with sst1.* Genes Immun, 2009. **10**(1): p. 37-46.
217. Orme, I.M., *Immune responses in animal models.* Curr Top Microbiol Immunol, 1996. **215**: p. 181-96.
218. De Groote, M.A., et al., *Comparative studies evaluating mouse models used for efficacy testing of experimental drugs against M. tuberculosis.* Antimicrob Agents Chemother, 2010.
219. Nuermberger, E., et al., *Combination chemotherapy with the nitroimidazopyran PA-824 and first-line drugs in a murine model of tuberculosis.* Antimicrob Agents Chemother, 2006. **50**(8): p. 2621-5.
220. Dayan, D., et al., *Are the polarization colors of picrosirius red-stained collagen determined only by the diameter of the fibers?* Histochemistry, 1989. **93**(1): p. 27-9.
221. Early, M.A., et al., *Non-invasive diagnosis of early pulmonary disease in PECAM-deficient mice using infrared pulse oximetry.* Exp Mol Pathol, 2009. **87**(2): p. 152-8.
222. Somoskovi, A., et al., *Lessons From a Proficiency Testing Event for Acid-Fast Microscopy.* Chest, 2001. **120**(1): p. 250-257.
223. Orme, I.M., *The mouse as a useful model of tuberculosis.* Tuberculosis (Edinb), 2003. **83**(1-3): p. 112-5.
224. Barry, C.E., H.I. Boshoff, and C.S. Dowd, *Prospects for Clinical Introduction of Nitroimidazole Antibiotics for the Treatment of Tuberculosis.* Current Pharmaceutical Design, 2004. **10**: p. 3239-3262.
225. Brooks, J.V., S.K. Furney, and I.M. Orme, *Metronidazole Therapy in Mice Infected with Tuberculosis.* Antimicrob Agents Chemother, 1999. **43**(5): p. 4.
226. Dhillon, J., et al., *Metronidazole has no antibacterial effect in Cornell model murine tuberculosis.* Int J Tuberc Lung Dis, 1998. **2**(9): p. 7.
227. Singh, P., et al., *Comparative evaluation of Lowenstein-Jensen proportion method, BacT/ALERT 3D system, and enzymatic pyrazinamidase assay for pyrazinamide susceptibility testing of Mycobacterium tuberculosis.* J Clin Microbiol, 2007. **45**(1): p. 76-80.
228. Li, M., et al., *Emergence of Fibroblasrs with A Proinflammatory Epigenetically Altered Phenotype in Severe Hypoxic Pulmonary Hypertension.* J Immunol, 2011. **187**(5): p. 2711-2722.
229. Schnoor, M., et al., *Production of Type VI Collagen by HUman Macrophages: A New Dimension in Macrophage Functional Heterogeneity.* J Immunol, 2008. **180**: p. 5707-5719.
230. Kim, M.J., et al., *Caseation of human tuberculosis granulomas correlates with elevated host lipid metabolism.* EMBO Mol Med, 2010. **2**(7): p. 258-274.

231. Basaraba, R.J., *Experimental tuberculosis: the role of comparative pathology in the discovery of improved tuberculosis treatment strategies.* Tuberculosis (Edinb), 2008. **88 Suppl 1**: p. S35-47.
232. Palanisamy, G.S., et al., *Clinical strains of Mycobacterium tuberculosis display a wide range of virulence in guinea pigs.* Tuberculosis (Edinb), 2009. **89**(3): p. 203-9.
233. Heifets, L. and P. Lindholm-Levy, *Pyrazinamide sterilizing activity in vitro against semidormant Mycobacterium tuberculosis bacterial populations.* Am Rev Respir Dis, 1992. **145**(5): p. 1223-5.
234. Wade, M.M. and Y. Zhang, *Anaerobic incubation conditions enhance pyrazinamide activity against Mycobacterium tuberculosis.* J Med Microbiol, 2004. **53**(Pt 8): p. 769-73.
235. Zhang, Y. and D. Mitchison, *The curious characteristics of pyrazinamide: a review.* Int J Tuberc Lung Dis, 2003. **7**(1): p. 6-21.
236. Crowle, A.J., J.A. Sbarbaro, and M.H. May, *Inhibition by pyrazinamide of tubercle bacilli within cultured human macrophages.* Am Rev Respir Dis, 1986. **134**(5): p. 1052-5.
237. Solotorovsky, M., et al., *Pyrazinoic acid amide; an agent active against experimental murine tuberculosis.* Proc Soc Exp Biol Med, 1952. **79**(4): p. 563-5.
238. Ahmad, Z., et al., *Dose-dependent activity of pyrazinamide in animal models of intracellular and extracellular tuberculosis.* Antimicrob Agents Chemother, 2011: p. 26.
239. Kjellsson, M.C., et al., *Penetration of anti-tuberculosis agents in rabbit pulmonary lesions: a pharmacokinetic evaluation.* Antimicrob Agents Chemother, 2011: p. 46.
240. Zhang, M., et al., *Treatments of Tuberculosis with Rifamycin-containing Regimens in Immune-deficient Mice.* Am J Respir Crit Care Med, 2011. **183**(9): p. 1254-1261.
241. Vernon, A., et al., *Acquired rifamycin monoresistance in patients with HIV-related tuberculosis treated with once-weekly rifapentine and isoniazid. Tuberculosis Trials Consortium.* Lancet, 1999. **353**(9167): p. 1843-7.
242. Burman, W., et al., *Acquired rifamycin resistance with twice-weekly treatment of HIV-related tuberculosis.* Am J Respir Crit Care Med, 2006. **173**(3): p. 350-6.
243. Ford, C.B., Philana Ling Lin, Michael R Chase, Rupal R Shah, Oleg Iartchouck, James Galagan, Nilofar Mohaideen, Thomas R Ioerger, James C Sacchettini, Marc Lipsitch, JoAnne L Flynn and Sarah M Fortune, *Use of whole genome sequencing to estimate the mutation rate of Mycobacterium tuberculosis during latent infection.* Nature Genetics, 2011. **43**(5): p. 482-486.
244. Larppanichpoonphol, P., et al., *Poor compliance makes treatment of latent tuberculosis infection unsatisfactory.* J Prim Care Community Health, 2012. **3**(4): p. 246-50.
245. Lin, P.L., et al., *CD4 T cell depletion exacerbates acute Mycobacterium tuberculosis while reactivation of latent infection is dependent on severity of tissue depletion in cynomolgus macaques.* AIDS Res Hum Retroviruses, 2012. **28**(12): p. 1693-702.
246. Smith, D.W. and G.E. Harding, *Animal model of human disease. Pulmonary tuberculosis. Animal model: Experimental airborne tuberculosis in the guinea pig.* Am J Pathol, 1977. **89**(1): p. 273-6.
247. Harper, J., et al., *Mouse model of necrotic tuberculosis granulomas develops hypoxic lesions.* J Infect Dis, 2012. **205**(4): p. 595-602.
248. Rosenthal, I.M., et al., *Dose-ranging comparison of rifampin and rifapentine in two pathologically distinct murine models of tuberculosis.* Antimicrob Agents Chemother, 2012. **56**(8): p. 4331-40.

249. Minion, J., et al., *Fading of auramine-stained mycobacterial smears and implications for external quality assurance.* J Clin Microbiol, 2011. **49**(5): p. 2024-6.
250. Gonzalez-Juarrero, M., et al., *Disruption of granulocyte macrophage-colony stimulating factor production in the lungs severely affects the ability of mice to control Mycobacterium tuberculosis infection.* J Leukoc Biol, 2005. **77**(6): p. 914-22.
251. Chandrasekhar, S. and M.K. Mukherjee, *Intracellular tubercle bacilli-alveolar macrophage lysosomal enzymes interaction in experimental tuberculosis.* Clin Immunol Immunopathol, 1990. **56**(2): p. 185-201.
252. Leong, F.J., V. Dartois, and T. Dick, *A Color Atlas of Comparative Pathology of Pulmonary Tuberculosis*. 2011, Boca Raton, FL: CRC Press Taylor and Francis Group.
253. Park, M.S., et al., *The role of chemotherapy in advanced solitary fibrous tumors: a retrospective analysis.* Clin Sarcoma Res, 2013. **3**(1): p. 7.
254. Chauhan, V.P., et al., *Angiotensin inhibition enhances drug delivery and potentiates chemotherapy by decompressing tumour blood vessels.* Nat Commun, 2013. **4**: p. 2516.
255. McIntyre, A., et al., *Carbonic anhydrase IX promotes tumor growth and necrosis in vivo and inhibition enhances anti-VEGF therapy.* Clin Cancer Res, 2012. **18**(11): p. 3100-11.
256. Hunter, R.L., et al., *Trehalose 6,6'-dimycolate and lipid in the pathogenesis of caseating granulomas of tuberculosis in mice.* Am J Pathol, 2006. **168**(4): p. 1249-61.
257. Behar, S.M., et al., *Apoptosis is an innate defense function of macrophages against Mycobacterium tuberculosis.* Mucosal Immunol, 2011. **4**(3): p. 279-87.
258. Blomgran, R., et al., *Mycobacterium tuberculosis inhibits neutrophil apoptosis, leading to delayed activation of naive CD4 T cells.* Cell Host Microbe, 2012. **11**(1): p. 81-90.
259. Chen, M., et al., *Lipid mediators in innate immunity against tuberculosis: opposing roles of PGE2 and LXA4 in the induction of macrophage death.* J Exp Med, 2008. **205**(12): p. 2791-801.
260. Ehlers, S. and U.E. Schaible, *The granuloma in tuberculosis: dynamics of a host-pathogen collusion.* Front Immunol, 2012. **3**: p. 411.
261. Hunter, R.L., *On the pathogenesis of post primary tuberculosis: the role of bronchial obstruction in the pathogenesis of cavities.* Tuberculosis (Edinb), 2011. **91 Suppl 1**: p. S6-10.
262. Hunter, R.L., *Pathology of post primary tuberculosis of the lung: an illustrated critical review.* Tuberculosis (Edinb), 2011. **91**(6): p. 497-509.
263. Calderon, V.E., et al., *A humanized mouse model of tuberculosis.* PLoS One, 2013. **8**(5): p. e63331.
264. Lowe, D.M., et al., *Neutrophils in tuberculosis: friend or foe?* Trends Immunol, 2012. **33**(1): p. 14-25.
265. Eum, S.Y., et al., *Association of antigen-stimulated release of tumor necrosis factor-alpha in whole blood with response to chemotherapy in patients with pulmonary multidrug-resistant tuberculosis.* Respiration, 2010. **80**(4): p. 275-84.
266. Mahajan, S., et al., *Mycobacterium tuberculosis modulates macrophage lipid-sensing nuclear receptors PPARgamma and TR4 for survival.* J Immunol, 2012. **188**(11): p. 5593-603.
267. Arko-Mensah, J., et al., *Resistance to mycobacterial infection: a pattern of early immune responses leads to a better control of pulmonary infection in C57BL/6 compared with BALB/c mice.* Vaccine, 2009. **27**(52): p. 7418-27.

268. Pokkali, S. and S.D. Das, *Augmented chemokine levels and chemokine receptor expression on immune cells during pulmonary tuberculosis.* Hum Immunol, 2009. **70**(2): p. 110-5.
269. den Hertog, A.L., et al., *Early specific host response associated with starting effective tuberculosis treatment in an infection controlled placebo controlled mouse study.* PLoS One, 2013. **8**(2): p. e57997.
270. Kozakiewicz, L., et al., *The role of B cells and humoral immunity in Mycobacterium tuberculosis infection.* Adv Exp Med Biol, 2013. **783**: p. 225-50.
271. Cavalcanti, Y.V., et al., *Role of TNF-Alpha, IFN-Gamma, and IL-10 in the Development of Pulmonary Tuberculosis.* Pulm Med, 2012. **2012**: p. 745483.
272. Cilfone, N.A., et al., *Multi-scale modeling predicts a balance of tumor necrosis factor-alpha and interleukin-10 controls the granuloma environment during Mycobacterium tuberculosis infection.* PLoS One, 2013. **8**(7): p. e68680.
273. Gordon, S., et al., *F4/80 and the related adhesion-GPCRs.* Eur J Immunol, 2011. **41**(9): p. 2472-6.
274. Balemans, W., et al., *Novel antibiotics targeting respiratory ATP synthesis in Gram-positive pathogenic bacteria.* Antimicrob Agents Chemother, 2012. **56**(8): p. 4131-9.
275. Diacon, A.H., et al., *Randomized pilot trial of eight weeks of bedaquiline (TMC207) treatment for multidrug-resistant tuberculosis: long-term outcome, tolerability, and effect on emergence of drug resistance.* Antimicrob Agents Chemother, 2012. **56**(6): p. 3271-6.
276. Jain, R., et al., *Treatment induced necrosis versus recurrent/progressing brain tumor: going beyond the boundaries of conventional morphologic imaging.* J Neurooncol, 2010. **100**(1): p. 17-29.
277. Quaia, E., et al., *Radiologic-pathologic correlations of intratumoral tissue components in the most common solid and cystic renal tumors. Pictorial review.* Eur Radiol, 2005. **15**(8): p. 1734-44.
278. Mueller, M.M. and N.E. Fusenig, *Friends or foes - bipolar effects of the tumour stroma in cancer.* Nat Rev Cancer, 2004. **4**(11): p. 839-49.
279. Radisky, D., C. Hagios, and M.J. Bissell, *Tumors are unique organs defined by abnormal signaling and context.* Semin Cancer Biol, 2001. **11**(2): p. 87-95.
280. Feig, C., et al., *The pancreas cancer microenvironment.* Clin Cancer Res, 2012. **18**(16): p. 4266-76.
281. Yun, C.O., *Overcoming the extracellular matrix barrier to improve intratumoral spread and therapeutic potential of oncolytic virotherapy.* Curr Opin Mol Ther, 2008. **10**(4): p. 356-61.
282. Vakoc, B.J., et al., *Three-dimensional microscopy of the tumor microenvironment in vivo using optical frequency domain imaging.* Nat Med, 2009. **15**(10): p. 1219-23.
283. Jain, R.K., *Determinants of tumor blood flow: a review.* Cancer Res, 1988. **48**(10): p. 2641-58.
284. Fang, J., H. Nakamura, and H. Maeda, *The EPR effect: Unique features of tumor blood vessels for drug delivery, factors involved, and limitations and augmentation of the effect.* Adv Drug Deliv Rev, 2011. **63**(3): p. 136-51.
285. Fang, J., T. Sawa, and H. Maeda, *Factors and mechanism of "EPR" effect and the enhanced antitumor effects of macromolecular drugs including SMANCS.* Adv Exp Med Biol, 2003. **519**: p. 29-49.

286. Seki, T., J. Fang, and H. Maeda, *Enhanced delivery of macromolecular antitumor drugs to tumors by nitroglycerin application.* Cancer Sci, 2009. **100**(12): p. 2426-30.
287. Maeda, H., et al., *Vascular permeability enhancement in solid tumor: various factors, mechanisms involved and its implications.* Int Immunopharmacol, 2003. **3**(3): p. 319-28.
288. Greish, K., et al., *Macromolecular therapeutics: advantages and prospects with special emphasis on solid tumour targeting.* Clin Pharmacokinet, 2003. **42**(13): p. 1089-105.
289. Jain, R.K. and T. Stylianopoulos, *Delivering nanomedicine to solid tumors.* Nat Rev Clin Oncol, 2010. **7**(11): p. 653-64.
290. Leunig, M., et al., *Angiogenesis, microvascular architecture, microhemodynamics, and interstitial fluid pressure during early growth of human adenocarcinoma LS174T in SCID mice.* Cancer Res, 1992. **52**(23): p. 6553-60.
291. Zhang, Y., et al., *Antimetastatic activities of pegylated liposomal doxorubicin in a murine metastatic lung cancer model.* J Drug Target, 2008. **16**(9): p. 679-87.
292. Torchilin, V.P., *Targeted pharmaceutical nanocarriers for cancer therapy and imaging.* AAPS J, 2007. **9**(2): p. E128-47.
293. Sagnella, S.M., et al., *Dextran-based Doxorubicin nanocarriers with improved tumor penetration.* Biomacromolecules, 2014. **15**(1): p. 262-75.
294. Li, Y., et al., *Delivery of nanomedicines to extracellular and intracellular compartments of a solid tumor.* Adv Drug Deliv Rev, 2012. **64**(1): p. 29-39.
295. Drummond, D.C., et al., *Pharmacokinetics and in vivo drug release rates in liposomal nanocarrier development.* J Pharm Sci, 2008. **97**(11): p. 4696-740.
296. Gordon, A.N., et al., *Recurrent epithelial ovarian carcinoma: a randomized phase III study of pegylated liposomal doxorubicin versus topotecan.* J Clin Oncol, 2001. **19**(14): p. 3312-22.
297. Gill, P.S., et al., *Randomized phase III trial of liposomal daunorubicin versus doxorubicin, bleomycin, and vincristine in AIDS-related Kaposi's sarcoma.* J Clin Oncol, 1996. **14**(8): p. 2353-64.
298. Noble, C.O., et al., *Development of ligand-targeted liposomes for cancer therapy.* Expert Opin Ther Targets, 2004. **8**(4): p. 335-53.
299. Sapra, P. and T.M. Allen, *Ligand-targeted liposomal anticancer drugs.* Prog Lipid Res, 2003. **42**(5): p. 439-62.
300. Nanopharmaceuticals.org/Liposomes.html. 2005.
301. Knight, C.B., P.C. Elwood, and B.A. Chabner, *Future directions for antifolate drug development.* Adv Enzyme Regul, 1989. **29**: p. 3-12.
302. Lee, R.J. and P.S. Low, *Delivery of liposomes into cultured KB cells via folate receptor-mediated endocytosis.* J Biol Chem, 1994. **269**(5): p. 3198-204.
303. Agrawal, A.K., et al., *Improved stability and antidiabetic potential of insulin containing folic acid functionalized polymer stabilized multilayered liposomes following oral administration.* Biomacromolecules, 2014. **15**(1): p. 350-60.
304. Drummond, D.C., et al., *Optimizing liposomes for delivery of chemotherapeutic agents to solid tumors.* Pharmacol Rev, 1999. **51**(4): p. 691-743.
305. Drummond, D.C., et al., *Development of a highly active nanoliposomal irinotecan using a novel intraliposomal stabilization strategy.* Cancer Res, 2006. **66**(6): p. 3271-7.
306. Kirpotin, D.B., et al., *Building and characterizing antibody-targeted lipidic nanotherapeutics.* Methods Enzymol, 2012. **502**: p. 139-66.

307. Reynolds, J.G., et al., *HER2-targeted liposomal doxorubicin displays enhanced anti-tumorigenic effects without associated cardiotoxicity.* Toxicol Appl Pharmacol, 2012. **262**(1): p. 1-10.
308. Marzo, E., et al., *Damaging role of neutrophilic infiltration in a mouse model of progressive tuberculosis.* Tuberculosis (Edinb), 2014. **94**(1): p. 55-64.
309. Lee, R.J. and P.S. Low, *Folate-mediated tumor cell targeting of liposome-entrapped doxorubicin in vitro.* Biochim Biophys Acta, 1995. **1233**(2): p. 134-44.
310. Welsh, K.J., et al., *Immunopathology of postprimary tuberculosis: increased T-regulatory cells and DEC-205-positive foamy macrophages in cavitary lesions.* Clin Dev Immunol, 2011. **2011**: p. 307631.
311. Yang, Q., et al., *Accelerated drug release and clearance of PEGylated epirubicin liposomes following repeated injections: a new challenge for sequential low-dose chemotherapy.* Int J Nanomedicine, 2013. **8**: p. 1257-68.
312. Zhao, Y., et al., *A frustrating problem: accelerated blood clearance of PEGylated solid lipid nanoparticles following subcutaneous injection in rats.* Eur J Pharm Biopharm, 2012. **81**(3): p. 506-13.
313. Suzuki, T., et al., *Accelerated blood clearance of PEGylated liposomes containing doxorubicin upon repeated administration to dogs.* Int J Pharm, 2012. **436**(1-2): p. 636-43.
314. Ishida, T., S. Kashima, and H. Kiwada, *The contribution of phagocytic activity of liver macrophages to the accelerated blood clearance (ABC) phenomenon of PEGylated liposomes in rats.* J Control Release, 2008. **126**(2): p. 162-5.
315. Doherty, T.M., *Immunotherapy for TB.* Immunotherapy, 2012. **4**(6): p. 629-47.
316. Feng, C.G., et al., *NK cell-derived IFN-gamma differentially regulates innate resistance and neutrophil response in T cell-deficient hosts infected with Mycobacterium tuberculosis.* J Immunol, 2006. **177**(10): p. 7086-93.
317. Lockhart, E., A.M. Green, and J.L. Flynn, *IL-17 production is dominated by gammadelta T cells rather than CD4 T cells during Mycobacterium tuberculosis infection.* J Immunol, 2006. **177**(7): p. 4662-9.
318. Diez, J., et al., *Losartan-dependent regression of myocardial fibrosis is associated with reduction of left ventricular chamber stiffness in hypertensive patients.* Circulation, 2002. **105**(21): p. 2512-7.
319. Noble, P.W., et al., *Pirfenidone in patients with idiopathic pulmonary fibrosis (CAPACITY): two randomised trials.* Lancet, 2011. **377**(9779): p. 1760-9.
320. Yoshiji, H., et al., *Losartan, an angiotensin-II type 1 receptor blocker, attenuates the liver fibrosis development of non-alcoholic steatohepatitis in the rat.* BMC Res Notes, 2009. **2**: p. 70.
321. Sookoian, S., M.A. Fernandez, and G. Castano, *Effects of six months losartan administration on liver fibrosis in chronic hepatitis C patients: a pilot study.* World J Gastroenterol, 2005. **11**(48): p. 7560-3.
322. Ma, T.K., et al., *Renin-angiotensin-aldosterone system blockade for cardiovascular diseases: current status.* Br J Pharmacol, 2010. **160**(6): p. 1273-92.
323. Cohn, R.D., et al., *Angiotensin II type 1 receptor blockade attenuates TGF-beta-induced failure of muscle regeneration in multiple myopathic states.* Nat Med, 2007. **13**(2): p. 204-10.

324. Sironi, L., et al., *Anti-inflammatory properties of drugs acting on the renin-angiotensin system.* Drugs Today (Barc), 2005. **41**(9): p. 609-22.
325. Diop-Frimpong, B., et al., *Losartan inhibits collagen I synthesis and improves the distribution and efficacy of nanotherapeutics in tumors.* Proc Natl Acad Sci U S A, 2011. **108**(7): p. 2909-14.
326. Lo, M.W., et al., *Pharmacokinetics of losartan, an angiotensin II receptor antagonist, and its active metabolite EXP3174 in humans.* Clin Pharmacol Ther, 1995. **58**(6): p. 641-9.
327. Stearns, R.A., et al., *Biotransformation of losartan to its active carboxylic acid metabolite in human liver microsomes. Role of cytochrome P4502C and 3A subfamily members.* Drug Metab Dispos, 1995. **23**(2): p. 207-15.
328. Molina-Molina, M., et al., *Losartan attenuates bleomycin induced lung fibrosis by increasing prostaglandin E2 synthesis.* Thorax, 2006. **61**(7): p. 604-10.
329. Keogh, K.A., et al., *Angiotensin II antagonism fails to ameliorate bleomycin-induced pulmonary fibrosis in mice.* Eur Respir J, 2005. **25**(4): p. 708-14.
330. Skerry, C., et al., *Adjunctive TNF inhibition with standard treatment enhances bacterial clearance in a murine model of necrotic TB granulomas.* PLoS One, 2012. **7**(6): p. e39680.
331. Comas, I. and S. Gagneux, *A role for systems epidemiology in tuberculosis research.* Trends Microbiol, 2011. **19**(10): p. 492-500.
332. Kato-Maeda, M., J.Z. Metcalfe, and L. Flores, *Genotyping of Mycobacterium tuberculosis: application in epidemiologic studies.* Future Microbiol, 2011. **6**(2): p. 203-16.
333. Ordway, D.J., et al., *Mycobacterium bovis BCG-mediated protection against W-Beijing strains of Mycobacterium tuberculosis is diminished concomitant with the emergence of regulatory T cells.* Clin Vaccine Immunol, 2011. **18**(9): p. 1527-35.
334. Borrell, S. and S. Gagneux, *Strain diversity, epistasis and the evolution of drug resistance in Mycobacterium tuberculosis.* Clin Microbiol Infect, 2011. **17**(6): p. 815-20.
335. Borrell, S., et al., *Epistasis between antibiotic resistance mutations drives the evolution of extensively drug-resistant tuberculosis.* Evol Med Public Health, 2013. **2013**(1): p. 65-74.
336. Gagneux, S. and P.M. Small, *Global phylogeography of Mycobacterium tuberculosis and implications for tuberculosis product development.* Lancet Infect Dis, 2007. **7**(5): p. 328-37.
337. Muller, B., et al., *The heterogeneous evolution of multidrug-resistant Mycobacterium tuberculosis.* Trends Genet, 2013. **29**(3): p. 160-9.
338. Homolka, S., et al., *Functional genetic diversity among Mycobacterium tuberculosis complex clinical isolates: delineation of conserved core and lineage-specific transcriptomes during intracellular survival.* PLoS Pathog, 2010. **6**(7): p. e1000988.
339. Barczak, A.K., et al., *In vivo phenotypic dominance in mouse mixed infections with Mycobacterium tuberculosis clinical isolates.* J Infect Dis, 2005. **192**(4): p. 600-6.
340. Bifani, P.J., et al., *Global dissemination of the Mycobacterium tuberculosis W-Beijing family strains.* Trends Microbiol, 2002. **10**(1): p. 45-52.
341. Tsolaki, A.G., et al., *Genomic deletions classify the Beijing/W strains as a distinct genetic lineage of Mycobacterium tuberculosis.* J Clin Microbiol, 2005. **43**(7): p. 3185-91.

342. Kato-Maeda, M., et al., *Differences among sublineages of the East-Asian lineage of Mycobacterium tuberculosis in genotypic clustering.* Int J Tuberc Lung Dis, 2010. **14**(5): p. 538-44.
343. Sreevatsan, S., et al., *Restricted structural gene polymorphism in the Mycobacterium tuberculosis complex indicates evolutionarily recent global dissemination.* Proc Natl Acad Sci U S A, 1997. **94**(18): p. 9869-74.
344. Manca, C., et al., *Hypervirulent M. tuberculosis W/Beijing strains upregulate type I IFNs and increase expression of negative regulators of the Jak-Stat pathway.* J Interferon Cytokine Res, 2005. **25**(11): p. 694-701.
345. Shang, S., et al., *Increased Foxp3 expression in guinea pigs infected with W-Beijing strains of M. tuberculosis.* Tuberculosis (Edinb), 2011. **91**(5): p. 378-85.
346. Manca, C., et al., *Virulence of a Mycobacterium tuberculosis clinical isolate in mice is determined by failure to induce Th1 type immunity and is associated with induction of IFN-alpha /beta.* Proc Natl Acad Sci U S A, 2001. **98**(10): p. 5752-7.
347. Henao-Tamayo, M.I., et al., *Phenotypic definition of effector and memory T-lymphocyte subsets in mice chronically infected with Mycobacterium tuberculosis.* Clin Vaccine Immunol, 2010. **17**(4): p. 618-25.
348. Palanisamy, G.S., et al., *Disseminated disease severity as a measure of virulence of Mycobacterium tuberculosis in the guinea pig model.* Tuberculosis (Edinb), 2008. **88**(4): p. 295-306.
349. Boon, A.C., et al., *Cross-reactive neutralizing antibodies directed against pandemic H1N1 2009 virus are protective in a highly sensitive DBA/2 mouse influenza model.* J Virol, 2010. **84**(15): p. 7662-7.
350. Soffler, C., et al., *Development and characterization of a caprine aerosol infection model of melioidosis.* PLoS One, 2012. **7**(8): p. e43207.
351. Smith, D.W., V. Balasubramanian, and E. Wiegeshaus, *A guinea pig model of experimental airborne tuberculosis for evaluation of the response to chemotherapy: the effect on bacilli in the initial phase of treatment.* Tubercle, 1991. **72**(3): p. 223-31.
352. Sathekge, M., et al., *Use of 18F-FDG PET to predict response to first-line tuberculostatics in HIV-associated tuberculosis.* J Nucl Med, 2011. **52**(6): p. 880-5.
353. Foss, C.A., et al., *Noninvasive molecular imaging of tuberculosis-associated inflammation with radioiodinated DPA-713.* J Infect Dis, 2013. **208**(12): p. 2067-74.
354. Foster, B., et al., *Segmentation of PET Images for Computer-Aided Functional Quantification of Tuberculosis in Small Animal Models.* IEEE Trans Biomed Eng, 2013.
355. Watanabe, S., et al., *Treatment monitoring with (18)F-FDG PET/CT in a patient with peritoneal tuberculosis.* Eur J Nucl Med Mol Imaging, 2014. **41**(1): p. 184.
356. Divangahi, M., S.M. Behar, and H. Remold, *Dying to live: how the death modality of the infected macrophage affects immunity to tuberculosis.* Adv Exp Med Biol, 2013. **783**: p. 103-20.
357. Morris, D., et al., *An elucidation of neutrophil functions against Mycobacterium tuberculosis infection.* Clin Dev Immunol, 2013. **2013**: p. 959650.
358. Cunningham, A.F. and C.L. Spreadbury, *Mycobacterial stationary phase induced by low oxygen tension: cell wall thickening and localization of the 16-kilodalton alpha-crystallin homolog.* J Bacteriol, 1998. **180**(4): p. 801-8.
359. Gonzalez-Juarrero, M., *Immunity to TB and targets for immunotherapy.* Immunotherapy, 2012. **4**(2): p. 187-99.

360. Rosas-Taraco, A.G., et al., *Local pulmonary immunotherapy with siRNA targeting TGFbeta1 enhances antimicrobial capacity in Mycobacterium tuberculosis infected mice.* Tuberculosis (Edinb), 2011. **91**(1): p. 98-106.
361. Mayanja-Kizza, H., et al., *Immunoadjuvant prednisolone therapy for HIV-associated tuberculosis: a phase 2 clinical trial in Uganda.* J Infect Dis, 2005. **191**(6): p. 856-65.
362. Wyser, C., et al., *Corticosteroids in the treatment of tuberculous pleurisy. A double-blind, placebo-controlled, randomized study.* Chest, 1996. **110**(2): p. 333-8.
363. Vilaplana, C., et al., *Ibuprofen therapy resulted in significantly decreased tissue bacillary loads and increased survival in a new murine experimental model of active tuberculosis.* J Infect Dis, 2013. **208**(2): p. 199-202.
364. Mitchison, D. and G. Davies, *The chemotherapy of tuberculosis: past, present and future.* Int J Tuberc Lung Dis, 2012. **16**(6): p. 724-32.
365. Grosset, J.H., et al., *Assessment of clofazimine activity in a second-line regimen for tuberculosis in mice.* Am J Respir Crit Care Med, 2013. **188**(5): p. 608-12.
366. Inomata, M., et al., *Pirfenidone inhibits fibrocyte accumulation in the lungs in bleomycin-induced murine pulmonary fibrosis.* Respir Res, 2014. **15**(1): p. 16.
367. Jain, R., et al., *In vivo correlation of tumor blood volume and permeability with histologic and molecular angiogenic markers in gliomas.* AJNR Am J Neuroradiol, 2011. **32**(2): p. 388-94.

LIST OF ABBREVIATIONS

TB – Tuberculosis

MTB – Mycobacterium tuberculosis

HIV – Human Immunodeficiency Virus

INH, H – Isoniazid

RIF, R – Rifampin

EMB, E – Ethambutol

PZA, Z – Pyrazinamide

BDQ, J – Bedaquiline

MET – Metronidazole

LZD, L – Linezolid

MXF, X – Moxifloxacin

DOTS – Directly Observed Therapy Short Course

MDR-TB – Multidrug Resistant Tuberculosis

XDR-TB – Extensively drug Resistant Tuberculosis

TDR-TB – Totally drug Resistant Tuberculosis

CMI – Cellular Mediated Immunity

DTH – Delayed Type Hypersensitivity

LTBI – Latent Tuberculosis Infection

Th1 – T cell Helper 1

Th2 – T cell Helper 2

Th17 – T cell Helper 17

Treg – T Regulatory cell

CD4 – Cluster of Differentiation 4

CD8 – Cluster of Differentiation 8

IFN-γ – Interferon-gamma

TNF-α – Tumor Necrosis Factor-alpha

IL-12 – Interleukin-12

IL-23 – Interleukin-23

IL-10 – Interleukin-10

IL-17 – Interleukin-17

IL-4 – Interleukin-4

IL-5 – Interleukin-5

IL-13 – Interleukin-13

MCP-1 – Monocyte Chemoattractant Protein -1

SCID – Severe Combined Immunodeficiency

iNOS – induced Nitric Oxide Synthase

ROS – Reactive Oxygen Species

RNI – Reactive Nitrogen Intermediates

NO – Nitric Oxide

KatG – Catalase Peroxidase

ICL – Isocitrate Lyase

TCA – Tricarboxylate acid

ACR – Alpha-crystallin

HSP – Heat-shock protein

DosR – Dormancy Survival Regulator

NRP – Non-replicating Persister

EHR – Enduring Hypoxic Response

RAD – Rapid Anaerobic Dormancy

Sst1 – Super Susceptibility to Tuberculosis -1

Ipr1 – Intracellular Pathogen Resistance -1

Ifi75 – Interferon Inducible 75 genes

PET – Positron Emission Tomography

MRI – Magnetic Resonance Imaging

TSPO – Translocator Protein

DMSO – Dimethylsulfoxide

CFU – Colony Forming Unit

OADC – Oleic Albumin Dextrose Catalase

AR – Auramine-Rhodamine

DAPI – 4’6-Diamidino-2-Phenylindole

PBS – Phosphate Buffered Saline

SEM – Standard Error of Measurement

ZN – Ziehl-Neelsen

ND – No bacterial colonies detected

PK – Pharmacokinetic

VEGF – Vascular Endothelial Growth Factor

GM-CSF – Granulocyte Macrophage Colony Stimulating Factor

ELISA – Enzyme Linked Immunosorbent Assay

CBA – Cytometric Bead Array

GKO – Gamma Interferon Knockout

NHP – Non-human Primate

IHC – Immunohistochemistry

CAF – Cancer-associated Fibroblasts

TAM – Tumor-associated Macrophages

TAN – Tumor-associated Neutrophils

EPR – Enhanced Permeability and Retention

FDA – Federal and Drug Administration

IFP – Interstitial Fluid Pressure

ABC – Accelerated Blood Clearance

MALDI-MRM-MS – Matrix Assisted Laser Desorption/Ionization-Multiple Reaction Monitoring-Mass Spectrometric

BCG – Bacillus Calmette-Guérin

RD – Region of Difference

LK – Losartan Potassium

siRNA – Small Interfering RNA

HSR – Homogeneously Staining Regions

RT-PCR – Reverse Transcription Polymerase Chain Reaction

PGE_2 – Prostaglandin E2

LXA_4 – Lipoxin A4

BAX – Bcl-2 Associated X protein

BAK – Bcl-2 Homologous Antagonist Killer